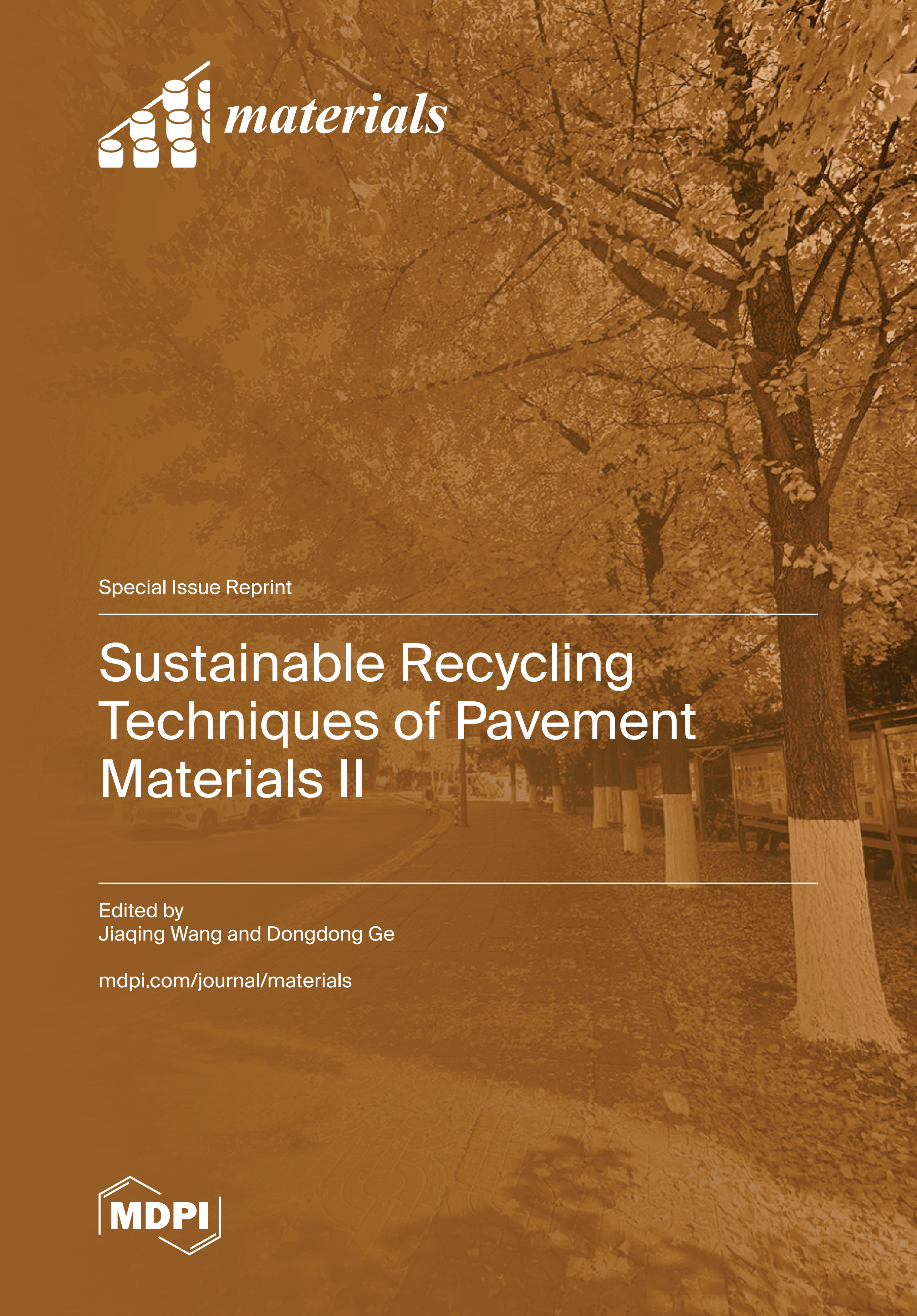

materials

Special Issue Reprint

Sustainable Recycling Techniques of Pavement Materials II

Edited by
Jiaqing Wang and Dongdong Ge

mdpi.com/journal/materials

MDPI

Sustainable Recycling Techniques of Pavement Materials II

Sustainable Recycling Techniques of Pavement Materials II

Guest Editors

Jiaqing Wang
Dongdong Ge

MDPI

Basel • Beijing • Wuhan • Barcelona • Belgrade • Novi Sad • Cluj • Manchester

Guest Editors

Jiaqing Wang
Nanjing Forestry University
Nanjing
China

Dongdong Ge
Changsha University of
Science and Technology
Changsha
China

Editorial Office
MDPI AG
Grossspeteranlage 5
4052 Basel, Switzerland

This is a reprint of the Special Issue, published open access by the journal *Materials* (ISSN 1996-1944), freely accessible at: https://www.mdpi.com/journal/materials/special_issues/PX7975FEEU.

For citation purposes, cite each article independently as indicated on the article page online and as indicated below:

Lastname, A.A.; Lastname, B.B. Article Title. *Journal Name* **Year**, *Volume Number*, Page Range.

ISBN 978-3-7258-2857-9 (Hbk)
ISBN 978-3-7258-2858-6 (PDF)
https://doi.org/10.3390/books978-3-7258-2858-6

Cover image courtesy of Jiaqing Wang

Contents

materials

MDPI

Article

Adhesion Properties of Recycled High-Viscosity Asphalt–Aggregate Interface under Dynamic Water Erosion

Kang Zhao, Shijie Song, Yang Wei *, Guofen Li * and Feng Guo

College of Civil Engineering, Nanjing Forestry University, Nanjing 210037, China; zkas@njfu.edu.cn (K.Z.); shijiesong@njfu.edu.cn (S.S.); 18816210278@163.com (F.G.)
* Correspondence: wy78@njfu.edu.cn (Y.W.); lgf@njfu.edu.cn (G.L.)

Abstract: The drainage of asphalt pavement requires the use of a large amount of high-viscosity-modified asphalt, which faces the service environment under dynamic water erosion. The feasibility of recycling high-viscosity-modified asphalt should be investigated to facilitate sustainable infrastructure construction. This study used ultrasonic equipment to simulate dynamic water erosion test conditions and tested the adhesion performance of different types of recycled high-viscosity asphalt at various environmental temperatures. The adhesion energy index and microstructure of recycled high-viscosity asphalt were analyzed using the contact angle test and AFM test. The results demonstrate that the higher the environmental temperature, the worse the anti-stripping performance of recycled high-viscosity asphalt. From the perspective of adhesion performance indicators, a 6% recycling agent dosage is more conducive to restoring the performance of aged high-viscosity -modified asphalt. The AFM test showed that the microstructure of high-viscosity -modified asphalt represented significant changes with an increase in the recycling agent content, and the change in the adhesion force of recycled high-viscosity -modified asphalt was consistent with the results of macroscopic adhesion performance tests. This study illustrates the applicability of implementing regeneration technology for the recycling of aged drainage asphalt pavement.

Keywords: drainage asphalt pavement; recycled high-viscosity asphalt; dynamic water erosion; ultrasonic numerical simulations; AFM; adhesion performance

Citation: Zhao, K.; Song, S.; Wei, Y.; Li, G.; Guo, F. Adhesion Properties of Recycled High-Viscosity Asphalt–Aggregate Interface under Dynamic Water Erosion. *Materials* **2023**, *16*, 6203. https://doi.org/10.3390/ma16186203

Academic Editor: Giovanni Polacco

Received: 29 August 2023
Revised: 7 September 2023
Accepted: 13 September 2023
Published: 14 September 2023

1. Introduction

In order to ensure the application effect of drainage asphalt pavement, researchers have developed different types of phase change materials to improve the high-temperature stability of the mixture on the one hand and used a high-viscosity asphalt binder to improve the overall road performance of the mixture on the other hand [1–6]. Generally speaking, improving asphalt viscosity can be realized by adding modifiers, among which Tafpack Super(TPS) high-viscosity-modified asphalt has been widely used because of its excellent high-temperature stability, low-temperature crack resistance, strong cohesion, and durability [7]. However, although higher viscous asphalt with better performance is used to drain asphalt pavements, due to the design concept of an open-graded and large void ratio (18–25%), pavements still have the disadvantage of rapid decay in surface function, low strength, and poor durability, and are prone to diseases such as void blockage, water damage, and fatigue cracking during service, and therefore, must be maintained periodically [8].

In China, up to 70 million tons of waste asphalt pavement materials are produced annually, and while the basalt aggregate used for the drainage of asphalt pavement has low reserves and the high-viscosity-modified asphalt cost is high, the use of recycled technology for pavement rehabilitation is particularly necessary [9–12]. On the one hand, researchers used the recycling agent to regenerate aged high-viscosity asphalt and evaluate the conventional performance of recycled asphalt. On the other hand, the mechanical properties and durability of recycled drainage asphalt mixtures were investigated at different old material mixing levels (15–93%) [13]. Xu et al. [14] developed a naphthenic asphalt rejuvenator for drainage asphalt pavements, which could improve the permeability and ductility of aged high-viscosity asphalt; however, the adhesion between asphalt and aggregate is insufficient, and asphalt can easily peel off from the surface of the aggregate in a humid environment. Frigio et al. [13] found that the use of an asphalt-based recycling agent could improve the strength and flexibility of recycled drainage asphalt mixtures, but the enhancement of its resistance to water damage was very limited. The road performance of reclaimed drainage asphalt mixtures with 30% old material basically meets the specification requirements, but its water stability is slightly poor, and its long-term performance needs to be further observed [15]. At present, recycled high viscous asphalt–aggregate interface adhesion performance research is limited, and the high viscous asphalt regeneration effect and adhesion performance recovery law have to be studied.

For vehicles traveling on the road surface, road surface water is under the action of the vehicle load constantly in the drainage of an asphalt mixture between the gap in the back and forth scouring, constantly abrading the asphalt in the connecting part between the aggregate and the aggregate, and ultimately resulting in the loss of asphalt's adhesion ability. It has been shown that the dynamic water action caused by vehicle loading is the main cause of water damage in asphalt mixtures, which is particularly significant in drained asphalt pavements [16]. Due to the huge difference between the hydrostatic test in the laboratory and the actual road used, many reclaimed roads experience different degrees of water damage within a short period of time after being put into operation. Therefore, in order to better investigate the scouring effect of vehicle loads on the asphalt–aggregate interface in the presence of water, simulation tests need to be designed in the laboratory [17,18]. A dynamic water pressure experimental simulator was designed for the test using the idea of the pneumatic pressure approach, and the final results obtained show that the main reason for the attenuation of the mechanical properties of asphalt mixtures is a decrease in asphalt viscosity under the condition that the dynamic water scour is directional and quantitative [19]. An ultrasonic dynamic water scour simulation device was used to simulate the scouring effect of water on the asphalt–aggregate interface in the open road and was combined with the image processing method to realize the quantitative description of the adhesion properties of the asphalt–aggregate interface [20]. The ultrasonic dynamic water scour simulation device is simple, and the ultrasonic cavitation phenomenon can simulate the extrusion and dynamic water scouring effect of the vehicle load on the road surface well on rainy days, which is especially suitable for the drainage of asphalt pavement.

In this paper, an ultrasonic dynamic water scour simulation device was used to study the effects of the high-viscosity agent dosage, recycling agent dosage, and temperature on the asphalt spalling rate on the aggregate surface and to analyze the anti-stripping performance of recycled high-viscosity asphalt under the dynamic water scour condition. The surface energies of asphalt and aggregate were measured and calculated using the lay-drop method, and the adhesion properties of a recycled high viscous asphalt–aggregate interface were evaluated using the parameters of the spreading coefficient, work of adhesion, and the work of spalling and energy ratio. An Atomic Force Microscope (AFM) (IBM, Armonk, NY, USA) was used to obtain the surface topography, force curve, and other microscopic information from the recycled high viscous asphalt to study the effects of the high viscous agent dosage and recycling agent dosage on the honeycomb structure, roughness, and adhesion force of asphalt, and to reveal the mechanism of changes to the adhesion properties of the recycled high viscous asphalt.

2. Materials Preparation and Test Methods

2.1. Materials

The technical indicators described in this paper for the study of matrix asphalt and which Alpha (Jiangyin) Asphalt Co., Ltd. (Nanjing, China) used to provide the ordinary 70# matrix asphalt are shown in Table 1. A high-viscosity modifier was selected for commonly used TPS materials the shape of the particle size was about 5 mm in the form of dark brown spherical particles and could be melted at 130 °C or more in the asphalt. The regeneration agent was the Anshan Shuangcheng brand asphalt regeneration agent, which is a yellow-brown liquid at room temperature. In this paper, a basalt aggregate above a 13.2 mm screen and below a 16 mm screen was obtained through the sieving test as the coarse aggregate used in the adhesion performance test.

Table 1. Technical indexes of base asphalt.

Evaluation Indicators	Test Results	Technical Requirement
25 °C pin man degree (mm)	69.0	60~80
Softening point (°C)	47.0	≥46
10 °C elongation (cm)	28.0	≥20
Solubility (%)	99.9	≥99.5
Density at 15 °C ($g \cdot cm^{-3}$)	1.02	-
Flash Point (°C)	272	≥260
135 °C rotational viscosity (Pa·s)	1.30	≤3
Film oven aging quality loss (%)	0.05	≤0.8
Film oven aging residual needle penetration ratio (%)	74.1	≥61
Film oven aging 10 °C residual elongation (cm)	10.0	≥6

2.2. Preparation of Recycled High-Viscosity Modified Asphalt

Since the TPS dosage varies in different projects: the dosage of a high-viscosity modifier was formulated as 10%, 12%, and 14% in this paper. In this paper, high-viscosity-modified asphalt was prepared using the shear method; first, the 70# base asphalt was heated to 140 °C and kept at a constant temperature; then, a specified dosage of the high-viscosity modifier was added and stirred evenly with a glass rod; finally, a high-speed shear was used to continuously shear for 30 min at a rate of 4000 r/min until the modifier was uniformly fused in the asphalt, and high-viscosity modified asphalt was obtained.

According to the “Standard test methods of bitumen and bituminous mixtures for highway engineering” (JTG E20-2011) in the T 0609-2011 and T 0630-2011 preparation of aging high-viscosity asphalt [21], at each time, 50 g of prepared high-viscosity asphalt was poured into the metal specimen dish in the film oven (TFOT) at 163 °C under the condition of 5 h of simulated asphalt with short-term aging. Short-term aging occurred after the end of the further in the pressure aging vessel (PAV) in a 100 °C and 2.1 MPa environment to maintain 20 h of simulated asphalt long-term aging.

In order to study the recovery effect of different rejuvenating agent dosages on the adhesive properties of aged high viscous asphalt, the aged high viscous asphalt was heated to a constant temperature of 170 °C, and then different ratios of the rejuvenating agent (4%, 6% and 8%) were added, and the rejuvenated high viscous asphalt was obtained using high-speed shear to mix at a rate of 2000 r/min for 30 min. The performance parameters for different types of recycled high-viscosity asphalt were measured, the results of which are shown in Table 2, and the recycled high-viscosity asphalt type named rules for R-high-viscosity modifier dosing-recycling agent dosing.

The preliminary analysis of the needle penetration index can be seen in the same regeneration agent dosage with an increase in the high-viscosity agent dosage; the needle penetration roughly showed a gradual decline in the trend, indicating that the amount of high-viscosity agent is directly proportional to the consistency of recycled high-viscosity asphalt. This is due to the TPS high-viscosity modifier as a thermoplastic elastomer where high temperatures and asphalt with full shear mixing occur in the fusion and dissolution, resulting in recycled high-viscosity asphalt in the components of the change, and the force between molecules increases, exhibiting high consistency and reduced fluidity [22]. Under the condition of the same high-viscosity agent dosage with an increase in the dosage of the reclaiming agent, the needle penetration roughly showed a gradual increase in the trend, indicating that the dosage of the reclaiming agent is inversely proportional to the consistency of recycled high-viscosity asphalt. This is due to the fact that the main component of the rejuvenating agent is light oils, which can supplement the aging of asphalt in missing saturated and aromatic components, thus reducing the consistency of recycled high-viscosity asphalt, increasing rheology as well as needle penetration.

Table 2. Basic performance parameter values for high-viscosity asphalt at different doses.

Type of Asphalt	Needle Penetration (0.1 mm)	Softening Point (°C)	10 °C Elongation (cm)
R-10-4	37.8	63.3	55.7
R-10-6	41.4	61.1	74.4
R-10-8	45.9	58.8	83.1
R-12-4	35.4	69.7	44.2
R-12-6	39.7	67.6	65.1
R-12-8	45.5	65.3	74.9
R-14-4	35.5	78.8	36.7
R-14-6	38.9	76.7	57.1
R-14-8	43.3	74.1	69.5

Taking the softening point as the analysis index, it can be found that under the condition of the same regenerant doping, the softening point increased with the increase in high-viscosity agent doping. Taking 4% regenerant doping as an example, the softening point increased from 63.3 °C to 78.8 °C with the increase in high-viscosity agent doping from 10% to 14%, and this increase was obvious. Taking the high-viscosity agent dosage of 10% as an example, with the increase in recycling agent dosage, the softening point of recycled high-viscosity asphalt decreases. Ductility is the main index to evaluate the plasticity of asphalt. The inclusion of a high-viscosity agent on asphalt ductility has a certain weakening effect, and the smaller the dosage of its ductility, the worse its plasticity is. On the contrary, the dosage of the regeneration agent has a certain enhancement effect on asphalt ductility.

2.3. Experimental Methods

2.3.1. Adhesion Test

In this paper, the YM-040PLUS (Fangao Microelectronics Co., Ltd., Shenzhen, China) ultrasonic generator was used for the test; the maximum capacity of the machine was 10 L, there were 6 ultrasonic vibrators, the heating power was 300 W, the ultrasonic power was 360 W, and the ultrasonic frequency was 40 KHz. Combined with the experimental experience of the predecessors, this paper set the dynamic water scouring time as 90 min in order to simulate the drained asphalt pavement in the harsh water damage environment in service for 3 years [20]. This study used this instrument to conduct ultrasonic asphalt aggregate adhesion tests on different types of recycled high-viscosity asphalt at temperatures of 20 °C, 50 °C, and 80 °C with reference to the test steps provided in reference [23]. Three parallel trials were conducted for each test condition. The spalling rate was used as the evaluation index to analyze the effects of three factors, namely, temperature, high-viscosity agent dosage, and recycling agent dosage, on the adhesion performance of a recycled high-viscosity asphalt–aggregate interface.

2.3.2. Contact Angle Test

(1) Test methods

This test was carried out using a KRUSSS-type contact angle tester (KRÜSS Scientific Instruments Co., Ltd., Hamburg, Germany), the main parts of which include an optical system, a sample conditioner, a video acquisition system, and an image analysis system, with a measurement range of 5° to 180° and an accuracy of ±0.1° [24]. Calculating the surface energy of asphalt and aggregate requires three liquids with known surface-free energy and its components. In this paper, distilled water, formamide, and glycerol were selected as the probing liquids, and the contact angles of the liquids on different recycled high-viscosity asphalt and aggregates were measured using the lay-drop method. Three parallel tests under equal conditions were performed for each measurement.

(2) Computational modeling

Surface energy is the work required to produce a new interface per unit area of a given material in a vacuum. It is known from the analysis in the literature that the surface energy of a substance (γ) is mainly composed of a polar component (γ^{AB}) and the dispersion component (γ^{LW}), while the polar component includes Lewis acid (γ^{+}) and Lewis base (γ^{-}), whose relationship is shown in Equation (1) [25].

$$\gamma = \gamma^{LW} + \gamma^{AB} = \gamma^{LW} + 2\sqrt{\gamma^{+}\gamma^{-}} \tag{1}$$

According to the surface physicochemical theory, the liquid wraps and adheres to the solid surface, and the surface energy change in the solid–liquid system is expressed by Equation (2):

$$W_{ls} = \gamma_l + \gamma_s - \gamma_{ls} \tag{2}$$

In this Equation, W_{ls} is the liquid-solid adhesion work, γ_l is the liquid surface energy, γ_s is the solid surface energy, and γ_{ls} is the interfacial energy on the contact surface of the solid–liquid system.

The free energy of the interface between a liquid and a solid is expressed by Equation (3):

$$\gamma_{ls} = \gamma_l + \gamma_s - 2\sqrt{\gamma_l^{AB}\gamma_s^{AB}} - 2\sqrt{\gamma_l^{LW}\gamma_s^{LW}} \tag{3}$$

In this Equation, γ_l^{LW} and γ_s^{LW} are the dispersion components for liquids and solids, respectively, while γ_l^{AB} and γ_s^{AB} are the polar components of the liquid and solid, respectively.

According to Young's equation, the relationship shown in Equation (4) is satisfied between the contact angle of a liquid with a solid surface and its surface-free energy and interfacial energy:

$$\gamma_l \cos\theta = \gamma_s - \gamma_{ls} \tag{4}$$

In this Equation, θ is the contact angle between the liquid and the solid.

Combining Equations (1)–(4) yields the Young–Dupre formula (Equation (5)):

$$W_{ls} = \gamma_l(1 + \cos\theta) = 2\sqrt{\gamma_l^{LW}\gamma_s^{LW}} + 2\sqrt{\gamma_l^{+}\gamma_s^{-}} + 2\sqrt{\gamma_l^{-}\gamma_s^{+}} \tag{5}$$

At room temperature, the asphalt is a solid. By measuring the contact angles between three types of liquids with known surface energy parameters and solid asphalt surfaces, a system of equations can be established according to Equation (5) to obtain the surface-free energy component value of asphalt before substituting it into Formula (1), which can be calculated from the surface free energy of asphalt where the solid surface energy calculation is the same [26].

(3) Evaluation indicators

a. Spreading factor

Wetting is the process by which a liquid droplet on a solid surface achieves contact with the solid and continues to spread. It can be seen that wettability can be used to evaluate the ability of bitumen to contact and spread on the aggregate surface; that is to say, it can reflect the ability of asphalt-coated aggregates. Wettability can be calculated by measuring the contact angle of a liquid on a solid. Meanwhile, the quantitative index to evaluate the wettability is the spreading coefficient, which is defined as the amount of surface-free energy reduction in a solid when it loses its bare surface and forms new solid–liquid and liquid–air interfaces, expressed as follows:

$$S_{a/s} = \gamma_s - \gamma_{as} - \gamma_a \tag{6}$$

where: $S_{a/s}$ is the spreading coefficient of asphalt (a denotes asphalt, s denotes aggregate), γ_s is the surface-free energy of the aggregate, γ_a is the surface-free energy of asphalt, and γ_{as} is the interface of free energy between asphalt and aggregate.

b. Adhesion

The work of adhesion is the free energy required to form a contact interface from the contact between a liquid and a solid. The work of adhesion between the asphalt and aggregate is expressed as follows:

$$W_{as} = 2\left(\sqrt{\gamma_a^{LW}\gamma_s^{LW}} + \sqrt{\gamma_a^{+}\gamma_s^{-}} + \sqrt{\gamma_a^{-}\gamma_s^{+}}\right) \tag{7}$$

where: W_{as} is the adhesion work between the asphalt and aggregate, γ_a^{LW}, γ_a^{+}, γ_a^{-} are the dispersion component, polar acid component, and polar alkali component of free energy on the asphalt surface, respectively, γ_s^{LW}, γ_s^{+}, γ_s^{-} represent the dispersion component, polar acid component, and polar alkali component for the surface-free energy of aggregates, respectively.

c. Flaking work

The flaking work can be expressed in detail as:

$$W_{aws} = 2\gamma_w + 2\begin{pmatrix} \sqrt{\gamma_a^{LW}\gamma_s^{LW}} + \sqrt{\gamma_a^{+}\gamma_s^{-}} + \sqrt{\gamma_a^{-}\gamma_s^{+}} - \sqrt{\gamma_a^{LW}\gamma_w^{LW}} - \\ \sqrt{\gamma_a^{+}\gamma_w^{-}} - \sqrt{\gamma_a^{-}\gamma_w^{+}} - \sqrt{\gamma_s^{LW}\gamma_w^{LW}} - \sqrt{\gamma_s^{+}\gamma_w^{-}} - \sqrt{\gamma_s^{-}\gamma_w^{+}} \end{pmatrix} \tag{8}$$

where: γ_w is the surface-free energy of water, γ_w^{LW}, γ_w^{+}, γ_w^{-} are the dispersion component, the polar acid component, and a polar base component of the surface-free energy of water.

d. Energy ratio parameters

The adhesion between asphalt and aggregate increases with the increase in the spreading factor $S_{a/s}$ and work of adhesion W_{as} and decreases with the increase in the work of spalling W_{aws}. As a result, researchers introduced the energy ratio parameter and the energy ratio parameter to synthesize the adhesion between the asphalt and aggregate [27]:

$$E_1 = \frac{W_{as}}{|W_{aws}|} \tag{9}$$

$$E_2 = \frac{S_{a/s}}{|W_{aws}|} \tag{10}$$

2.3.3. AFM Test

AFM has been widely used to determine the nanomechanical properties of soft matter systems with success [28]. The continuously recorded force–distance curves reveal the adhesion properties between the tip and the most external sample surface and the energy dissipation [29,30]. In this paper, *Ra* was calculated using the Nanoscope analysis software 2.0 in the AFM technique as an indicator to assess asphalt surface roughness on a microscopic scale. The test was carried out using Dimension Icon AFM produced by Bruker, Germany, with the probe model RTESPA, the Quantitative Nanomechanical (QNM)-SADER method was used to calibrate the probe, and the elasticity constant of the probe was 5 N/m. The array of sampling points was set to 256 pixels × 256 pixels, the sampling frequency was set to 1 Hz, and the constant peak force was set to 1 nN, with a scanning range of 10 µm × 10 µm [31]. Three parallel tests under equal conditions were performed for each measurement. The AFM test temperature was about 20 °C at room temperature, and the asphalt specimens were prepared using the hot casting method.

3. Test Results and Discussion

3.1. Study on the Interfacial Spalling Performance of Recycled High-Viscosity Asphalt Aggregate under Dynamic Water Erosion Conditions

This paper uses the more common commercially available TPS high-viscosity modifiers that improve high and low temperatures as well as the fatigue resistance properties of asphalt and provide a sufficiently large bond between the aggregate and the aggregate. As the performance of high-viscosity asphalt decreased during the service period, it is important to use recycling agents to effectively restore its performance. In this paper, we used the Anshan Shuangcheng brand asphalt rejuvenator, which is a mixture of various resins, solvents, and multifunctional additives with low viscosity, stable properties, and rich in lightweight components. In addition, the asphalt viscosity is greatly affected by temperature; the asphalt viscosity at different test temperatures changes, which inevitably leads to changes in the adhesion of asphalt and the aggregate surface. Therefore, this paper simulated different weather temperature conditions on different recycled high-viscosity asphalt dynamic water flushing tests to spalling rates as an evaluation index to quantitatively analyze the effect of adhesion damage under different influencing factors, the test results of which are shown in Figure 1. This figure shows the recycled high-viscosity asphalt naming rules for the high-viscosity dosage-regeneration agent dosage.

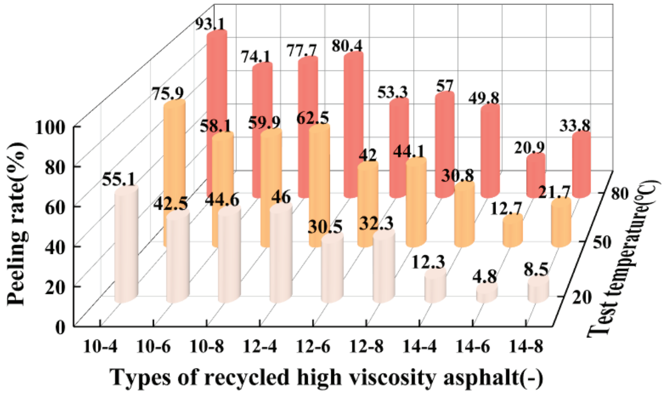

Figure 1. Peeling rate test results.

As can be seen from Figure 1, there is a certain negative correlation between the flaking rate and high-viscosity agent dosage when the recycling agent dosage is certain; that is to say, the higher the high-viscosity agent dosage, the smaller the flaking rate of the reclaimed high-viscosity asphalt–aggregate, which indicates that the increase in the high-viscosity modifier could enhance asphalt adhesion. Taking the ambient temperature of 80 °C and the recycling agent dosage of 6% as an example, with the increase in a high-viscosity modifier dosage from 10% to 14%, the flaking rate of the recycled high-viscous asphalt–aggregate interface decreased from 74.1% to 20.9%, which was a decrease of up to 71.8%. For the reclaimed drainage pavement, whether the performance of aged asphalt could be effectively restored or not, the dosage of its reclaimer in aged asphalt had a significant impact. From the above figure, it can be seen that at a 20 °C, 50 °C, and 80 °C test temperature, when the amount of high-viscosity agent was constant, the influence of the amount of regenerant on the peeling rate showed a V-shaped distribution, indicating that the recycling agent dosage of 6% for recycling high-viscous asphalt–aggregate interface adhesion is the best. The reason for this may be that the insufficient dosage of the rejuvenating agent affects the recovery effect of high-viscosity asphalt performance, while the excessive dosage of a rejuvenating agent leads to an increase in the lightweight component of reclaimed asphalt, which has an unfavorable effect on the adhesion of asphalt. With the increase in the test temperature, the flaking rate of the recycled high-viscosity asphalt–aggregate interface gradually increased, indicating that the adhesion between asphalt–aggregate decreases with the increase in temperature. This is mainly due to the fact that temperature affects the viscosity of asphalt. The rheology of recycled high-viscosity asphalt gradually increases with increasing temperature, and the viscosity of asphalt becomes smaller, resulting in smaller adhesion between asphalt and asphalt and between the asphalt and aggregate, and in the process of dynamic water flushing, asphalt is more likely to be stripped from aggregate under the vibration of ultrasonic waves and cavitation, which ultimately leads to the destruction and spalling of the recycled high-viscosity asphalt–aggregate interface.

3.2. Research on the Adhesion Performance of Regenerated High Viscous Asphalt Based on Surface Energy Principle

3.2.1. Surface Free Energy Measurement

Based on the surface-free energy introduction in Section 2.3.2 of this paper, the set of Equation (11) for calculating the surface-free energy of asphalt could be obtained by combining Equation (5) and the three known liquid surface energy parameters:

$$\begin{cases} \gamma_{l1}(1+cos\theta_1) = 2\sqrt{\gamma_{l1}^{LW}\gamma_a^{LW}} + 2\sqrt{\gamma_{l1}^{+}\gamma_a^{-}} + 2\sqrt{\gamma_a^{+}\gamma_{l1}^{-}} \\ \gamma_{l2}(1+cos\theta_2) = 2\sqrt{\gamma_{l2}^{LW}\gamma_a^{LW}} + 2\sqrt{\gamma_{l2}^{+}\gamma_a^{-}} + 2\sqrt{\gamma_a^{+}\gamma_{l2}^{-}} \\ \gamma_{l3}(1+cos\theta_3) = 2\sqrt{\gamma_{l3}^{LW}\gamma_a^{LW}} + 2\sqrt{\gamma_{l3}^{+}\gamma_a^{-}} + 2\sqrt{\gamma_a^{+}\gamma_{l3}^{-}} \end{cases} \tag{11}$$

In the formula, $\sqrt{\gamma_a^{LW}}$, $\sqrt{\gamma_a^{-}}$, $\sqrt{\gamma_a^{+}}$ is the unknown quantity, substituting the surface-free energy of distilled water, formamide, and glycerol, and each component, solving the ternary system of equations, where the solution obtained is the surface-free energy component of asphalt, where the results of the calculations are shown in Table 3:

Table 3. Asphalt surface-free energy and its components (mJ/m^2).

Recycled High-Viscosity Asphalt Types	Asphalt Surface Free Energy	Asphalt Dispersion Fraction	Asphalt Polarity Component	Asphalt Polar Acid Fraction	Asphalt Polar Base Fraction
R-10-4	23.95	21.96	1.99	0.23	4.32
R-10-6	28.85	25.84	3.01	0.49	4.65
R-10-8	25.84	25.14	0.70	0.05	2.52
R-12-4	25.29	21.51	3.77	0.50	7.14
R-12-6	32.67	28.02	4.65	1.02	5.30
R-12-8	38.19	33.89	4.30	1.47	3.13
R-14-4	47.02	39.26	7.76	3.54	4.25
R-14-6	51.01	44.53	6.47	3.44	3.05
R-14-8	57.60	49.66	7.93	5.21	3.02

From Table 3, it can be seen that no matter which kind of asphalt is used, the value of the nonpolar component accounts for about 85% of the free energy of the surface of the asphalt, and the remaining polar component accounts for only 15%. Continuing to analyze the two parts of the polar component, it can be found that the alkaline component accounted for a very small percentage, only about 5%.

According to the same calculation method, the surface-free energy and components of basalt aggregate can be obtained, and the results are shown in Table 4.

Table 4. Basalt aggregate surface-free energy and fraction (mJ/m^2).

Aggregates	Aggregates Surface Free Energy	Aggregates Dispersion Fraction	Aggregates Polarity Component	Aggregates Polar Acid Fraction	Aggregates Polar Base Fraction
Basalt	233.01	56.61	176.40	15.82	491.73

From Table 4, it can be seen that the surface energy of basalt aggregate was high, as high as 233.01 mJ/m^2, and when analyzing its surface energy component, it was found that the polar component accounted for the main part, close to 75.7%. In the polar component, it could be seen that the polar alkali component was as high as 491.7 mJ/m^2, which is consistent with the nature of basalt as an alkaline aggregate.

3.2.2. Evaluation of Interfacial Adhesion between Recycled High-Viscosity Asphalt and Aggregate

(1) Spreading factor

There is a significant correlation between the wettability of asphalt on the basalt aggregate and its adhesion effect. If the wettability of asphalt and aggregate is good and its spreading coefficient is high, asphalt can spread well on the aggregate surface, resulting in better adhesion performance between the two. On the contrary, if the wettability of asphalt and the aggregate is poor, and it is more difficult for asphalt to spread on the aggregate surface, then the spreading coefficient of the two is lower, and the adhesion performance of the two becomes worse. From an energetic point of view explanation, asphalt is in the process of wetting aggregate release energy where the size of the released energy is the spreading coefficient $S_{a/s}$, the index of which can be quantitatively analyzed on the wettability of the abstract. In this study, the spreading coefficient of nine types of recycled high-viscosity asphalt on the surface of basalt aggregate is determined by Equation (6), and the calculation results are shown in Figure 2.

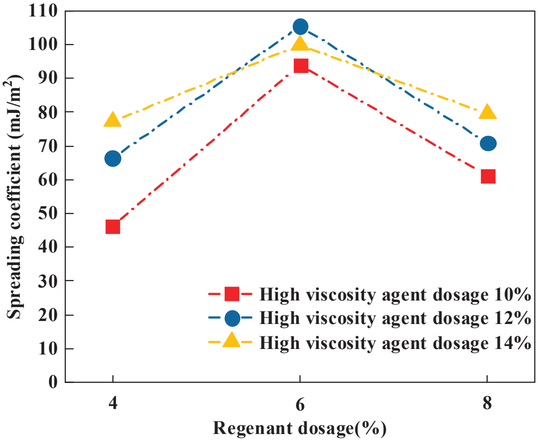

Figure 2. Test results of spreading coefficient calculation.

As can be seen from Figure 2, the case of the high-viscosity agent dosage was unchanged, with the increase in rejuvenating agent dosage, where the spreading coefficient between the recycled high-viscosity asphalt and basalt first increased and then decreased, all in the rejuvenating agent dosage of 6% to achieve the maximum value, which indicates that, at this time, the recycled high-viscosity asphalt and basalt aggregates had the best adhesion between the aggregates. The main reason for this is that, in a certain range, a greater dosage of the recycling agent increases the recycled high-viscosity asphalt of lightweight components in the content, improving the asphalt mobility and increasing the spreading coefficient. However, an excessive amount of the rejuvenating agent may form a gelatinous substance, resulting in a decrease in the spreading coefficient of recycled high-viscosity asphalt. In addition, with the increase in the high-viscosity agent, the spreading factor of reclaimed high-viscosity asphalt generally showed an increasing trend. However, the spreading coefficient of recycled high-viscosity asphalt with 12% high-viscosity agent at 6% recycling agent dosage is greater than that with 14% dosage, which might be due to the fact that the combination of the recycling agent and high-viscosity agent produces better wettability and fluidity at a specific dosage ratio.

(2) Adhesion function

The energy required to strip asphalt from the asphalt–aggregate interface under dry and anhydrous conditions is the work of adhesion. The work of adhesion can be calculated from the parameters of surface energy and the fraction of bitumen as well as the aggregate. If the work of adhesion is higher, it represents the greater adhesion strength between the asphalt and aggregate. The work of adhesion between the asphalt and aggregate can be determined by Equation (7), which is calculated, as shown in Figure 3.

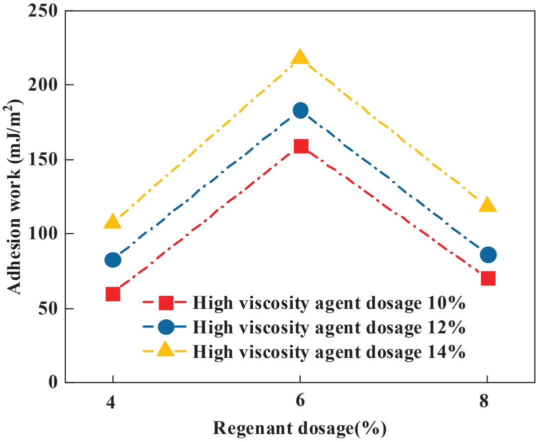

Figure 3. Adhesion work calculation results.

From Figure 3, it can be seen that similar to the rule of change in the spreading coefficient, when high viscous agent doping was certain, with the increase in rejuvenator doping, the adhesion function increased first and then decreased. The reason for this situation is that for the rejuvenating agent in a certain dosage range, the aging high-viscosity asphalt performance has a good recovery effect, the adhesion performance increases and the rejuvenating agent's dosage further increases, leading to the rejuvenating agent in the asphalt diffusion not being uniform, resulting in the components of the miscibility appearing nonhomogeneous with damaged adhesion strength and the adhesion function becomes smaller [32]. In addition, under different conditions, the adhesion function of recycled high-viscosity asphalt becomes larger with the increase in a high-viscosity modifier dosage. The reason for this is that the increase in the dosage of a high-viscosity modifier can significantly increase the asphalt viscosity, thus improving asphalt's adhesion.

(3) Flaking work

Water is one of the most important factors contributing to asphalt spalling, and the spalling function measures the likelihood of adhesion failure due to asphalt stripping from the aggregate in the presence of water. When water is present, there is a high likelihood that asphalt can be replaced by water at the asphalt–aggregate interface, resulting in the stripping of asphalt from the aggregate. From an initial asphalt–aggregate interface to a later water–aggregate interface, the overall surface energy of the system is reduced. The spalling work can be calculated by Equation (8), which is shown in Figure 4.

From Figure 4, it can be seen that the maximum value of the spalling work of the recycled high-viscosity asphalt and aggregate appeared in the case of 10% high-viscosity agent doping and 4% recycling agent doping for 156.01 mJ/m^2 at the time that asphalt was most prone to spalling. The curve shows that there was an optimum value for the recycling agent dosage, and it was more difficult for the recycled high-viscous asphalt and aggregate at the inflection point to be spalled and damaged under the water environment. At a 6% recycling agent dosage, the spalling work of recycled high-viscosity asphalt and aggregate was the smallest, and the adhesion performance was the best. Further analysis can be found with an increase in the high-viscosity agent dosage where the absolute value of the spalling work between recycled high-viscosity asphalt and basalt aggregates gradually decreased, indicating better-recycled high-viscosity asphalt—aggregate adhesion. This was due to the increase in the high-viscosity agent, which enhanced asphalt's adhesion performance.

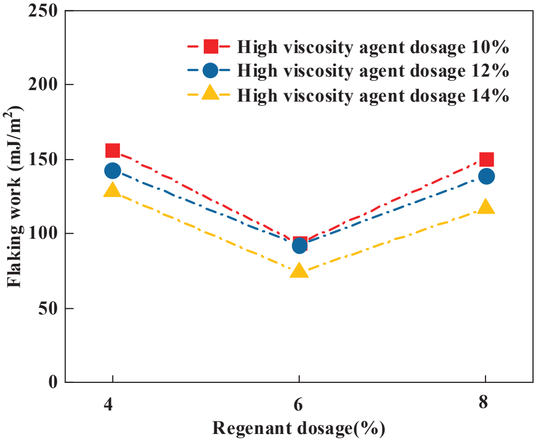

Figure 4. Calculation results of flaking work.

(4) Energy ratio parameters

The spreading coefficient, the adhesion work, and the spalling work of different types of recycled high-viscosity asphalt on basalt are calculated above. The adhesion function is an indicator for evaluating the adhesion effect of asphalt–aggregate in the absence of water, while the spalling function is an indicator to evaluate the adhesion effect of asphalt–aggregate in the presence of water. However, in the actual use of the road, the two extreme states of extremely dry or sufficient water seldom occur but appear more in the exchange cycle of water and waterless conditions, so a single adhesion function or a single flaking function cannot reasonably characterize the actual adhesion effect of the recycled high-viscosity asphalt–aggregate interface. Therefore, in this paper, we need to comprehensively consider the adhesion performance indexes under aqueous and anhydrous conditions; therefore, two energy ratio parameters E_1 and E_2 are introduced for evaluation. The energy ratio parameter E_1 is the ratio of the adhesion work to the flaking work, and the energy ratio parameter E_2 is the ratio of the spreading coefficient to the flaking work, which are calculated according to Equations (9) and (10), and the results are shown in Figure 5.

From Figure 5a, it can be clearly seen that the energy ratio E_1 of different recycled high-viscous asphalt was the smallest at 4% of the recycling agent dosage, which indicates that the adhesion between long-term aged asphalt and aggregate was extremely poor, and a sufficient recycling agent was needed to supplement the missing lightweight component of recycled high-viscous asphalt. In addition, under the condition of high viscous agent dosage determination, with the increase in the reclaiming agent, the energy ratio parameters, E_1 and $E_{2,}$ increased and then decreased, which indicates that the optimal reclaiming agent dosage selection should be paid attention to in the recycling of high-viscous aging asphalt. Through the energy ratio parameters of recycled high viscous asphalt, the high viscous agent dosage on the adhesion effect was not regular; the reason for this might be that the regeneration agent and high viscous agent on the recycled high viscous asphalt adhesion performance recovery effect had a synergistic effect.

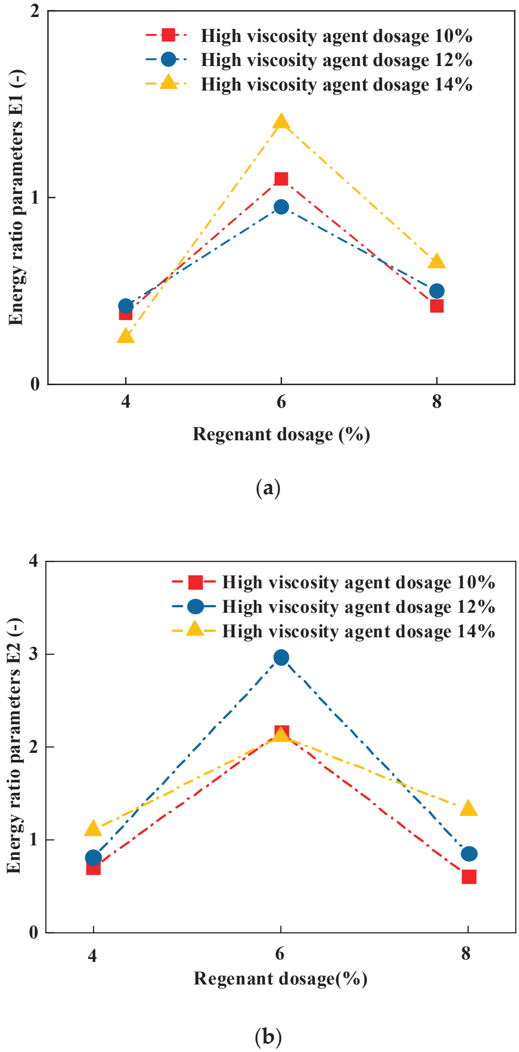

Figure 5. Calculation results of energy ratio parameters. (**a**) Calculation results of energy ratio parameter E_1. (**b**) Calculation results of energy ratio parameter E_2.

3.3. Adhesion Characteristics of Recycled High-Viscosity Asphalt Aggregate Interface Based on AFM

3.3.1. Microscopic Surface Feature Analysis

The two-dimensional surface morphology of the in-rejuvenated high-viscous asphalt with different high-viscosity agent and rejuvenator dosages is shown in Figure 6.

The 2D scanning image obtained by AFM clearly shows that the image consists of two main parts, namely the "bee-like structure" and the matrix phase. The area with alternating black and white bee-like shapes is called the "bee-like structure", and the area around the "bee-like structure" is the matrix phase [33]. The number, maximum individual area, average area, total area, and area ratio of the bee-like structures in the 2D scans were counted using Image Pro-plus (IPP) software 6.0, and the results are shown in Table 5.

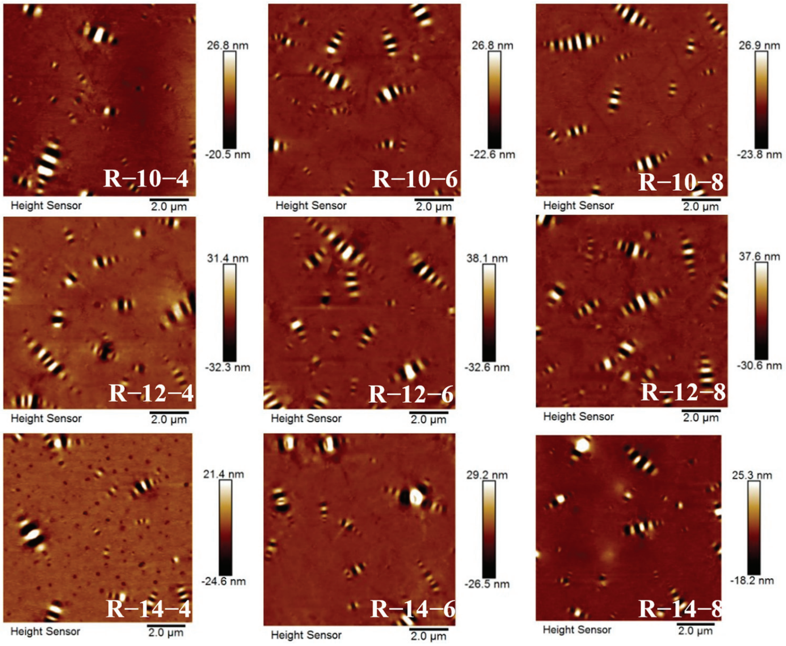

Figure 6. Surface micromorphology of different types of regenerated high viscous asphalt.

Table 5. Statistical results of "bee-like structure" data of 2D images.

Asphalt Type	Total Number	Total Area (μm^2)	Individual Maximum Area (μm^2)	Average Area (μm^2)	Area Share (%)
R-10-4	58	5.381	1.228	0.118	5.4
R-10-6	44	4.886	1.062	0.132	4.8
R-10-8	51	5.022	1.218	0.158	5.1
R-12-4	50	6.878	0.568	0.118	6.8
R-12-6	54	6.848	0.608	0.156	6.8
R-12-8	48	6.751	0.512	0.132	6.8
R-14-4	46	7.522	0.880	0.150	7.6
R-14-6	37	9.384	0.734	0.172	9.4
R-14-8	32	8.411	0.800	0.174	8.8

Analyzing the data in Table 5, it can be seen that with the increase in the high-viscosity agent, the number of honeycomb structures in the recycled high-viscosity asphalt roughly showed a decreasing trend, the total area of the honeycomb structure roughly showed an increasing trend, the maximum area of a single honeycomb structure showed a roughly decreasing trend, the average honeycomb structure area showed a gradually increasing trend, and the proportion of the total area also showed an increasing trend. This indicates that the adhesion capacity between the asphalt and aggregate was greatly enhanced with the increase in the high-viscosity agent dosage.

3.3.2. Roughness

Asphalt surface roughness is related to asphalt adhesion and its self-healing properties. The higher the surface roughness, the better the adhesion between the asphalt and aggregate [34]. The *Ra* results obtained from the AFM test are shown in Figure 7.

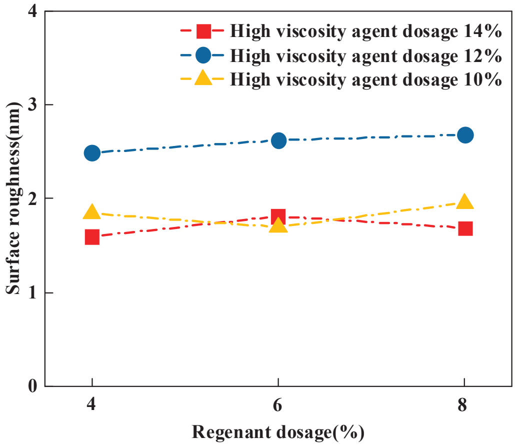

Figure 7. Surface roughness of different types of recycled high-viscosity asphalt.

From Figure 7, it can be found that under the condition of 12% and 14% of high-viscosity agent doping, the surface roughness of the recycled high-viscosity asphalt increased from 5.7 nm and 3.91 nm to 6.24 nm and 4.35 nm, respectively, which increased by 0.54 nm and 0.44 nm, and the change fluctuation was very small. Under the condition of 10% high-viscosity agent dosing, the roughness decreased first and then increased with the increase in reclaimer dosing and finally changed by only 0.39 nm. Therefore, it was judged that the correlation between the reclaimer dosing and the roughness of the surface of reclaimed high-viscosity asphalt was not obvious. In addition, as a whole, the surface roughness was the largest at 12% high-viscosity agent dosing, and this roughness was similar at 10% and 14% dosing, which is obviously inconsistent with the actual situation. Therefore, this paper concludes that the use of roughness as an indicator for evaluating the adhesion performance of recycled high-adhesion asphalt needs to be further investigated.

3.3.3. Adhesion

In order to further analyze the mechanical properties of recycled high-viscosity asphalt, the properties of its mechanical images were quantified using NanoScope Analysis software 2.0, and the statistical results of the adhesion of different recycled high-viscosity asphalt were obtained, as shown in Figure 8.

It can be seen from Figure 8, in the case of a certain amount of the high-viscosity agent, with the increase in recycling agent dosage, that the adhesion of recycled high-viscosity asphalt greatly increased and then slowly reduced. Taking the high-viscosity agent dosage R = 14% as an example with the recycling agent dosage from 4% to 6% in the process, the adhesion of the recycled high-viscosity asphalt increased by 56.1%; when the recycling agent increased dosage from 6% to 8% of the process, the adhesion of the recycled high-viscosity asphalt decreased by 0.81%. From this, the optimum rejuvenator dosage was judged to be 6% based on the adhesion. In the case of a certain amount of the recycling agent, the adhesion of recycled high-viscosity asphalt was positively correlated with the increase in high-viscosity agent dosage. The higher the viscous agent dosage, the denser the TPS high viscous agent in the uniform dispersion of matrix asphalt in the formation of a crosslinked network structure, showing a more stable state; at the same time, the network structure is also based on asphalt rheology's ability to produce a damping effect, thereby improving asphalt adhesion, and further increasing the viscosity of asphalt.

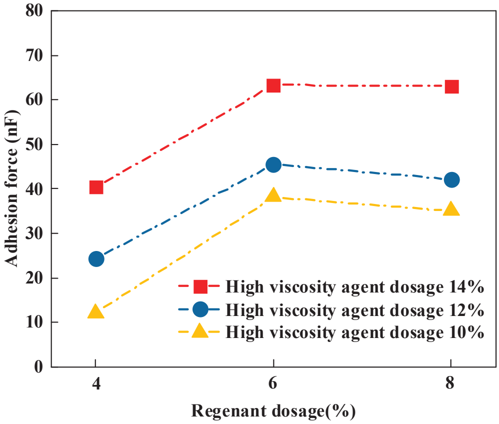

Figure 8. Adhesion of different types of recycled high-viscosity asphalt.

3.4. Significance Analysis

The test results were analyzed using ANOVA using SPSS software 27 at a 95% confidence level to compare the significance of the effect of different factors on the adhesion performance parameters of the recycled high-viscosity asphalt, and the results are shown in Table 6. It was found that the modifier dosage and high-viscosity agent dosage had no significant effect on the energy ratio parameters E_1 and E_2 of the recycled high-viscosity asphalt, while almost all of the other adhesion performance parameters showed a significant effect. This suggests that the energy ratio parameter itself might not be applicable to the study of the adhesion characteristics of asphalt.

Table 6. Results of variance analysis.

Factor	Sum of Squared Deviations	Degrees of Freedom	Mean Square Error	F-Value	*p*-Value
(1) Spreading coefficient					
Dosage of regeneration agent	2252	2	1126	25.33	0.005
Dosage of high-viscosity agent	553.8	2	276.9	6.229	0.059
(2) Adhesion work					
Dosage of regeneration agent	1.979×10^4	2	9897	693.5	0.000
Dosage of high-viscosity agent	3988	2	1994	139.7	0.000
(3) Flaking work					
Dosage of regeneration agent	5548	2	2774	153.0	0.000
Dosage of high-viscosity agent	1142	2	571.0	31.51	0.003
(4) Energy ratio parameter E_1					
Dosage of regeneration agent	1.560	2	0.780	4.274	0.174
Dosage of high-viscosity agent	3.552	2	1.776	4.402	0.021
(5) Energy ratio parameter E_2					
Dosage of regeneration agent	4.568	2	2.284	17.20	0.010
Dosage of high-viscosity agent	0.280	2	0.140	1.054	0.428
(6) Surface roughness					
Dosage of regeneration agent	0.026	2	0.013	1.072	0.423
Dosage of high-viscosity agent	1.415	2	0.707	57.98	0.001
(7) Adhesion force					
Dosage of regeneration agent	1001	2	500.7	170.7	0.000
Dosage of high-viscosity agent	1153	2	576.6	196.6	0.000

4. Conclusions

(1) In the ultrasonic equipment, simulated dynamic water scour test conditions, different high-viscous agent dosages of aging high-viscous asphalt with the addition of a rejuvenating agent, the rate of spalling on the aggregate surface with the increase in rejuvenating agent dosage decreased first and then increased. A 6% rejuvenating agent dosage of the aging high-viscous asphalt was used with the anti-stripping performance of the best restoration effect. In addition, simulating the adhesion performance test under different weather temperatures, it was found that the higher the temperature, the worse the anti-spalling performance of reclaimed high-viscous asphalt.

(2) Through the contact angle test, it was found that the spreading coefficient and adhesion work of recycled high-viscous asphalt on the surface of the basalt aggregate increased and then decreased with the dosage of the rejuvenating agent under anhydrous conditions, and the spalling work decreased and then increased under aqueous conditions, which is consistent with the conclusion of the kinetic water scour test. By calculating the adhesion performance indexes E_1 and E_2, it was found that the adhesion performance of recycled high-viscous asphalt increased and then decreased with the increase in the rejuvenating agent under the combined consideration of the state of water and no water, while the influence of high-viscous agent dosage on the adhesion effect was not regular, which could be due to the synergistic effect of the rejuvenating agent and the high-viscous agent in the recovery of adhesion performance of recycled high-viscous asphalt.

(3) The AFM test on different kinds of recycled high-viscosity asphalt "bee-like structure" morphology had some differences with the increase in high-viscosity agent mixing; its "bee-like structure" showed a number of reductions, the area of the trend increased, and there was no obvious change pattern as the amount of regenerant increased. There was no obvious connection between the roughness of recycled high-viscosity asphalt and its adhesion performance, and the pattern of change in adhesion was consistent with the results of the macro-adhesion performance test.

Author Contributions: Conceptualization, K.Z.; Data curation, F.G.; Methodology, Y.W.; Resources, Y.W. and G.L.; Writing—original draft, K.Z.; Writing—review and editing, S.S. All authors have read and agreed to the published version of the manuscript.

Funding: This research received no external funding.

Institutional Review Board Statement: Not applicable.

Informed Consent Statement: Not applicable.

Data Availability Statement: All the original data in this article can be obtained by contacting the corresponding author.

Conflicts of Interest: The authors declare no conflict of interest.

References

1. Duan, M.J.; Suo, X.C.; Dong, F.H.; Li, J.H.; Li, G.F. Research on the Control Method for the Reasonable State of Self-Anchored Symmetry Suspension Bridge Stiffening Girders. *Symmetry* **2022**, *14*, 935. [CrossRef]
2. Langa, E.; Buonocore, G.; Squillace, A.; Muiambo, H. Effect of Vegetable Oil on the Properties of Asphalt Binder Modified with High Density Polyethylene. *Polymers* **2023**, *15*, 749. [CrossRef] [PubMed]
3. Mongkol, K.; Chaturabong, P.; Suwannaplai, A. Effect of Bagasse and Coconut Peat Fillers on Asphalt Mixture Workability. *Coatings* **2020**, *10*, 1262. [CrossRef]
4. Shah, P.M.; Mir, M.S. Investigating the influence of carbon nanotube on the performance of asphalt binder. *Prog. Rubber Plast. Recycl. Technol.* **2021**, *37*, 422–440. [CrossRef]
5. Zeiada, W.; Liu, H.Q.; Al-Khateeb, G.G.G.; Shanableh, A.; Samarai, M. Evaluation of test methods for measurement of zero shear viscosity (ZSV) of asphalt binders. *Constr. Build. Mater.* **2022**, *325*, 126794. [CrossRef]
6. Bhat, F.S.; Mir, M.S. Investigating the effects of nano Al_2O_3 on high and intermediate temperature performance properties of asphalt binder. *Road Mater. Pavement Des.* **2021**, *22*, 2604–2625. [CrossRef]

7. Kiselev, A.; Zhang, H.T.; Liu, Z.Q. The effect of two-phase mixing on the functional and mechanical properties of TPS/SBS-modified porous asphalt concrete. *Constr. Build. Mater.* **2021**, *270*, 121841. [CrossRef]
8. Jiang, J.W.; Leng, Z.; Yang, B.; Lu, G.Y.; Tan, Z.F.; Han, M.Z.; Dong, Z.J. Penetration mechanism of the emulsion-based rejuvenator in damaged porous asphalt mixture: Microstructure characterization and 3D reconstruction. *Mater. Des.* **2022**, *221*, 111014. [CrossRef]
9. Duan, M.J.; Zou, X.X.; Bao, Y.; Li, G.F.; Chen, Y.W.; Li, Z.Z. Experimental investigation of headed studs in steel-ultra-high performance concrete (UHPC) composite sections. *Eng. Struct.* **2022**, *270*, 114875. [CrossRef]
10. Kawakami, A.; Sasaki, I.; Nitta, H.; Yabu, M. Mixture Design for Recycled Porous Asphalt Pavement and Results of Follow-up Survey for Ten Years. *Lect. Notes Civ. Eng.* **2020**, *48*, 460–469.
11. Bozkurt, T.S.; Karakas, A.S. Investigation of Asphalt Pavement to Improve Environmental Noise and Water Sustainability. *Sustainability* **2022**, *14*, 14901. [CrossRef]
12. Duan, M.J.; Zhang, S.Y.; Wang, X.; Dong, F.H. Mechanical Behavior in Perfobond Rib Shear Connector with UHPC-Steel Composite Structure with Coarse Aggregate. *KSCE J. Civ. Eng.* **2020**, *24*, 1255–1267. [CrossRef]
13. Frigio, F.; Pasquini, E.; Partl, M.N.; Canestrari, F. Use of Reclaimed Asphalt in Porous Asphalt Mixtures: Laboratory and Field Evaluations. *J. Mater. Civ. Eng.* **2015**, *27*, 04014211. [CrossRef]
14. Xu, B.; Ding, R.D.; Yang, Z.H.; Sun, Y.R.; Zhang, J.C.; Lu, K.J.; Cao, D.W.; Gao, A.D. Investigation on performance of mineral-oil-based rejuvenating agent for aged high viscosity modified asphalt of porous asphalt pavement. *J. Clean. Prod.* **2023**, *395*, 136285. [CrossRef]
15. Kawakami, A.; Kubo, K.; Sasaki, L.; Kano, T. Study on the Recycling Method for Drainage Asphalt pavement and Evaluation for its Durability. *Adv. Mater. Res.* **2013**, *723*, 664–669. [CrossRef]
16. Zheng, C.F.; Xu, J.P.; Zhang, T.; Tan, G.J. Study on the microscopic damage of porous asphalt mixture under the combined action of hydrodynamic pressure and ice crystal frost heave. *Constr. Build. Mater.* **2021**, *303*, 124489. [CrossRef]
17. Xiong, R.; Chu, C.; Qiao, N.; Wang, L.; Yang, F.; Sheng, Y.P.; Guan, B.W.; Niu, D.Y.; Geng, J.G.; Chen, H.X. Performance evaluation of asphalt mixture exposed to dynamic water and chlorine salt erosion. *Constr. Build. Mater.* **2019**, *201*, 121–126. [CrossRef]
18. Chen, W.X.; Wang, Z.Y.; Guo, W.; Dai, W.T. Measurement and Evaluation for Interbedded Pore Water Pressure of Saturated Asphalt Pavement under Vehicle Loading. *Appl. Sci.* **2020**, *10*, 1416. [CrossRef]
19. Hu, X.D.; Jiang, M.; Bai, T.; Pan, P.; Walubita, L.F. Development and validation of an enhanced test setup for assessing HMA stripping potential under hydrodynamic pressure. *Road Mater. Pavement Des.* **2020**, *21*, 2024–2039. [CrossRef]
20. Guo, M.; Yin, X.; Du, X.L.; Tan, Y.Q. Effect of aging, testing temperature and relative humidity on adhesion between asphalt binder and mineral aggregate. *Constr. Build. Mater.* **2023**, *363*, 129775. [CrossRef]
21. *JTG E20-2011*; RIOH, Standard Test Methods of Bitumen and Bituminous Mixtures for Highway Engineering. China Communications Press: Beijing, China, 2011; Volume JTG E20-2011.
22. Jiao, Y.B.; Zhang, Y.; Fu, L.X.; Guo, M.; Zhang, L.D. Influence of crumb rubber and tafpack super on performances of SBS modified porous asphalt mixtures. *Road Mater. Pavement Des.* **2019**, *20*, S196–S216. [CrossRef]
23. Peng, C.; Huang, S.F.; You, Z.P.; Xu, F.; You, L.Y.; Ouyang, H.; Li, T.J.; Guo, C.; Ma, H.C.; Chen, P.X.; et al. Effect of a lignin-based polyurethane on adhesion properties of asphalt binder during UV aging process. *Constr. Build. Mater.* **2020**, *247*, 118547. [CrossRef]
24. Yang, M.; Huang, T.; Lv, S.T.; Zheng, J.L. Effect and mechanism of acidic aggregate surface silane modification on water stability of asphalt mixture. *Road Mater. Pavement Des.* **2021**, *22*, 1654–1666. [CrossRef]
25. Zeng, Z.; Zhang, D.R.; Liu, H.Q. Development of an energy-based framework to determine the surface free energy of asphalt binder: Theoretical models. *Mater. Struct.* **2021**, *54*, 241. [CrossRef]
26. Fang, Y.; Zhang, Z.Q.; Zhang, H.J.; Li, W.Y. Analysis of wetting behavior and its influencing factors of rejuvenator/old asphalt interface based on surface wetting theory. *Constr. Build. Mater.* **2022**, *314*, 125674. [CrossRef]
27. Hajj, R.; Bhasin, A. The search for a measure of fatigue cracking in asphalt binders—A review of different approaches. *Int. J. Pavement Eng.* **2018**, *19*, 205–219. [CrossRef]
28. Magazzu, A.; Marcuello, C. Investigation of Soft Matter Nanomechanics by Atomic Force Microscopy and Optical Tweezers: A Comprehensive Review. *Nanomaterials* **2023**, *13*, 963. [CrossRef]
29. Anczykowski, B.; Gotsmann, B.; Fuchs, H.; Cleveland, J.P.; Elings, V.B. How to measure energy dissipation in dynamic mode atomic force microscopy. *Appl. Surf. Sci.* **1999**, *140*, 376–382. [CrossRef]
30. Lostao, A.; Lim, K.; Pallares, M.C.; Ptak, A.; Marcuello, C. Recent advances in sensing the inter-biomolecular interactions at the nanoscale—A comprehensive review of AFM-based force spectroscopy. *Int. J. Biol. Macromol.* **2023**, *238*, 124089. [CrossRef]
31. Sader, J.E.; Larson, I.; Mulvaney, P.; White, L.R. Method for the calibration of atomic force microscope cantilevers. *Rev. Sci. Instrum.* **1995**, *66*, 3789–3798. [CrossRef]
32. Jacobs, G.; Couscheir, K.; Hernando, D.; Moins, B.; Vansteenkiste, S.; Tanghe, T.; Duerinckx, B.; van den Bergh, W. Mechanical performance of asphalt base layers with high RAP content and recycling agents. *Road Mater. Pavement Des.* **2023**, 1–11. [CrossRef]

33. Ouyang, Q.J.; Xie, Z.W.; Liu, J.H.; Gong, M.H.; Yu, H.Y. Application of Atomic Force Microscopy as Advanced Asphalt Testing Technology: A Comprehensive Review. *Polymers* **2022**, *14*, 2851. [CrossRef] [PubMed]
34. Li, M.C.; Liu, L.P.; Yang, R.K.; Liu, L.X. Investigation of the Influence of Aging on the Nanoscale Adhesion of Asphalt from the Perspective of AFM-IR-Based Chemical Properties. *J. Mater. Civ. Eng.* **2022**, *34*, 04022240. [CrossRef]

materials

MDPI

Article

Effective Notch-Stress-Based Stress Concentration Factors of the Rib–Deck Weld in Orthotropic Steel Decks Considering the Effect of Asphalt Surfacing

Qiudong Wang [1,*], Shanchun Shi [1], Yue Yao [2], Zhiqiang Wang [1] and Zhongqiu Fu [3]

[1] College of Civil Engineering, Nanjing Forestry University, Nanjing 210037, China; 15052610385@163.com (S.S.); wzq010302@163.com (Z.W.)
[2] College of Construction Engineering, Jiangsu Open University, Nanjing 210000, China; jsouyaoyue@163.com
[3] College of Civil and Transportation Engineering, Hohai University, Nanjing 210098, China; fuzhongqiu@hhu.edu.cn
* Correspondence: qdwang@njfu.edu.cn

Abstract: Effective notch stress (ENS) approaches have many application prospects in fatigue damage assessments; however, an ENS can only be obtained by conducting complex and time-consuming numerical analyses, deterring many engineers from applying such an approach. In terms of the rib–deck weld in orthotropic steel decks (OSDs), predictive formulae for determining the ENS concentration factors (ENS-based SCFs) have been proposed; however, the effect of asphalt surfacing is not involved, which limits their applications in practical engineering. In the present study, refined finite element (FE) models, including asphalt surfacing, were developed to obtain the ENS-based SCFs which could be applied to practical engineering. Parametric analyses were conducted to investigate the effect of the transverse loading position, the combined effect of the transverse loading position and asphalt surfacing, and the effect of the temperature of the asphalt surfacing. The amplification coefficients (k_{SCF}, k_{SCF1}, and k_{SCF2}) were introduced to determine the ENS-based SCFs on the basis of the predictive formulae without considering the effect of asphalt surfacing. Results show that the ENS-based SCFs of the rib–deck weld is considerably affected by the transverse position of wheel loading and the asphalt surfacing. The cubic polynomial function could be employed to fit the numerical results of the ENS-based SCFs and amplification coefficients (k_{SCF}, k_{SCF1}, and k_{SCF2}) with high fitting precision. Predictive formulae for determining the ENS-based SCFs corresponding to arbitrary transverse loading position and temperature of asphalt surfacing are proposed. The validation investigation turns out that the relative error of the proposed formulae is within 10%, indicating the feasibility of using this approach for engineering applications.

Keywords: orthotropic steel deck; rib–deck weld; effective notch stress; concentration factor; predictive formula

Citation: Wang, Q.; Shi, S.; Yao, Y.; Wang, Z.; Fu, Z. Effective Notch-Stress-Based Stress Concentration Factors of the Rib–Deck Weld in Orthotropic Steel Decks Considering the Effect of Asphalt Surfacing. *Materials* **2023**, *16*, 6760. https://doi.org/10.3390/ma16206760

Academic Editor: Paulo Santos

Received: 19 September 2023
Revised: 7 October 2023
Accepted: 17 October 2023
Published: 19 October 2023

1. Introduction

Orthotropic steel decks (OSDs) are easily subjected to fatigue cracking under cyclic traffic loads [1]. As welded steel structures, there are various fatigable details in OSDs, e.g., rib–deck welds, butt welds, diaphragm–rib welds, and arc-sharped notches [2]. Among them, the rib–deck weld has generated significant concern in recent years [3]; this is because the propagation of fatigue cracks thereat will further threaten the durability of asphalt surfacing [4–6]. In this case, fatigue damage assessments and life predictions have become a hot issue in bridge engineering. For these purposes, several stress-based approaches have been widely employed, e.g., the nominal stress approach, the hotspot stress approach, and the effective notch stress approach [7]. The nominal stress approach is the simplest; however, the assessing accuracy is limited since the structure-related stress concentration is not considered [8–10]. Comparatively, the hotspot stress (HSS) approach has higher accuracy;

however, such approach is limited to applications to the weld root, where most fatigue cracks of the rib–deck welds are initiated [11]. Additionally, the notch stress induced by the weld bead cannot be considered by employing the hotspot stress approach. Alternatively, the effective notch stress (ENS) approach has broad application prospects as the notch stress could be precisely considered. However, effective notch stress can only be obtained by conducting numerical simulations (e.g., finite element modeling) [12], which deters many engineers from applying such approaches in practical engineering. Exploring feasible ways to efficiently determine the effective notch stress without conducting numerical simulations is of great significance, which warrants further investigations.

Instead of complex and time-consuming finite element modeling, empirical formulae obtained using parametric and regression analysis provide a feasible way to quickly determine effective notch stress [13]. Some researchers have proposed various parametric formulae to predict the effective notch stress concentration factor (SCF), which is defined by the ratio of the effective notch stress to nominal stress. For instance, formulae for predicting the ENS-based SCFs of the butt–weld joint [13,14], the welded cruciform joint [15], and the T-butt welded joint [16,17] have been reported. ENS-based SCFs could be quickly obtained by employing these formulae for implementing accurate assessment of fatigue damage or life. In recent years, artificial neural networks (ANNs) and machine leaning have also been employed to develop accurate predictive models [18,19]. In terms of the rib–deck welded joint, Wang et al. [20] proposed predictive formulae for predicting ENS-based SCFs, corresponding to three typical fatigue-cracking modes (i.e., root–toe, root–deck, and toe–deck cracking modes) to improve the efficiency of the ENS approach. More details will be introduced in Section 2; these form the basis of the present research. Notably, the proposed formulae in [20] are only applicable and efficient when all of the geometric parameters of the rib–deck weld are accessible, while might be inapplicable due to the absence of critical geometric parameters in practical engineering, e.g., the weld leg lengths. In this case, predictive formulae for determining the ENS-based SCFs have been proposed through an integration of the HSS measurements to improve the efficiency of applying an ENS approach [21]. However, in these investigations, the effect of the asphalt surfacing is not considered, which might affect the accuracy of assessments in practical engineering applications.

This study focuses on the parametric formulae for predicting ENS-based while SCFs considering the effect of asphalt surfacing. Firstly, predictive formulae for predicting the ENS-based SCFs of a rib–deck weld, without considering the effect of the asphalt surfacing, were reviewed; these form the basis of the present study. Subsequently, a refined finite element model was developed to conduct the parametric analysis of the effect of the asphalt surfacing, wheel loading position, and temperature. Next, new predictive formulae were proposed based on the results of parametric analysis. Finally, the application of the proposed formulae was presented to validate the feasibility and accuracy.

2. Review of Equations for Predicting the SCF

Rib–deck welds in OSDs are easily subjected to fatigue cracking, as shown in Figure 1, where the crack has penetrated the deck plate and subsequent leakage and corrosion were observed. To propose the predictive formulae for predicting the ENS-based SCFs, finite element (FE) models simulating the rib–deck welded detail were developed. For detailed geometric sizes of the FE model, please refer to [20]. Since the ENS-based SCF at a weld root was the focus of the present study, the stress 20 mm away from the weld root was selected to be the nominal stress [20]. Regarding the geometric parameters of the rib–deck weld, six parameters were considered in the FE modeling, namely the thickness of the deck plate (t_d), the thickness of the rib wall (t_r), the angle between the deck plate and rib wall (θ), the weld penetration rate ($1 - t_p/t_r$), the length of the weld leg at the deck plate ($l_{w,d}$), and the length of the weld leg at the rib wall ($l_{w,r}$). For more details of the geometric parameters, please refer to [20]. In parametric analysis, the t_r was valued at 6, 8, and 10 mm, while the relative value of t_d/t_r was set to be 1.8, 2.0, and 2.5 to take in account the effect of the thickness of the deck plate and rib wall. The value of ($1 - t_p/t_r$) was increased from 0 (i.e., no penetration) to 0.8 at intervals of 0.1. The relative length of the weld leg (i.e., $l_{w,d}/t_r$ and $l_{w,r}/t_r$) was valued from 0.8 to 1.2 at intervals of 0.2. Additionally, the value of θ increased from 70° to 80° at intervals of 5°. Based on the results of the parametric analysis, a database of the ENS-based SCFs in the presence of different geometric parameters was developed. Finally, predictive formulae for determining the ENS-based SCFs were proposed based on regression analysis, as expressed by Equation (1).

$$SCF_{\mathrm{ENS}} = \sum_{i=1}^{28} c_i \times f_i(X_1, X_2, X_3, X_4, X_5, X_6) \tag{1}$$

where SCF_{ENS} represents the ENS-based SCF at the weld root; $X_1 = 1 - t_p/t_r$; $X_2 = t_r/10$; $X_3 = l_{w,d}/t_r$; $X_4 = l_{w,r}/t_r$; $X_5 = 2\theta/180°$; and $X_6 = t_d/t_r$. c_i is the coefficient determined by the regression analysis as listed in [20]. Results of the parametric analysis in [20] show that the SCF is considerably affected by the weld penetration rate ($X_1 = 1 - t_p/t_r$), the relative thickness of the deck plate ($X_6 = t_d/t_r$), and the relative length of the weld leg at the rib wall ($X_4 = l_{w,r}/t_r$). Accordingly, the SCF is less affected by the thickness of the rib wall ($X_2 = t_r/10$), the relative length of the weld leg at the deck plate ($X_3 = l_{w,d}/t_r$), and the angle between the deck plate and rib wall ($X_5 = 2\theta/180°$). It is noted that the effect of asphalt surfacing on the values of SCF_{ENS} is not considered in Equation (1), which is to be investigated in the following sections.

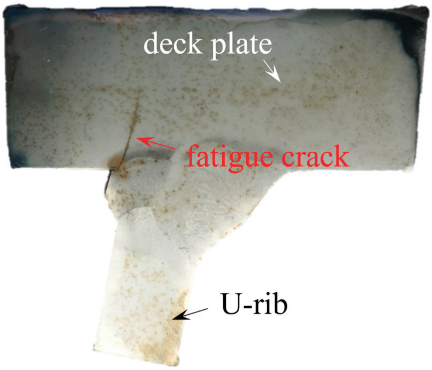

Figure 1. The rib–deck weld with fatigue crack penetrating the deck plate (imaged by Q.W.).

3. Finite Element Model for Parametric Analysis

To investigate the effect of the asphalt surfacing on the ENS-based SCFs of the rib–deck weld, refined finite element models, including the global model and sub model, were developed using ANSYS (Canonsburg, PA, USA), as shown in Figure 2. The global model was composed of seven U-ribs (labelled from R1 to R7) and three diaphragms (labelled from D1 to D3). Previous investigations have already shown that such FE model could be employed to obtain the stress characteristics of the OSDs in practical engineering with high accuracy. The thickness of the asphalt surfacing was set to be 60 mm which was in accordance with the value in extensive practical engineering. Other main geometric parameters were shown in Figure 3. The longitudinal length of the global model was 9000 mm, while the length between either two diaphragms was 3000 mm. The sub model included the U-rib labelled R4 and half of R3 and R5 (see Figure 2). The rib–deck weld of R4 was selected as the objective, and the notch with a radius of 1 mm was arranged at the weld root for obtaining the ENS, following the recommendations by the IIW [7], to account for the variation in the weld shape parameters, as well as the nonlinear material behavior at the notch root.

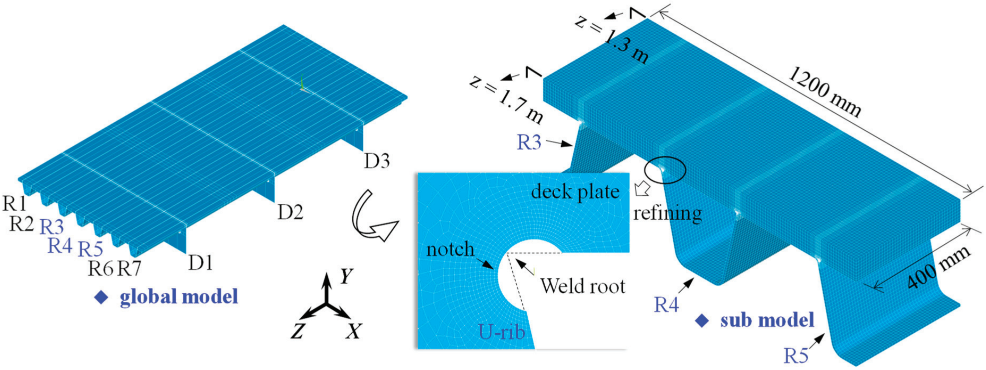

Figure 2. Finite element model simulating the OSD and asphalt surfacing.

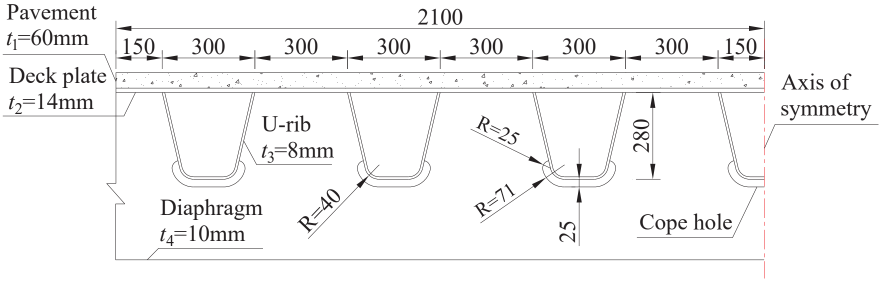

Figure 3. Main geometric parameters of the FE model (unit: mm).

The SOLID186-typed element, which was defined by 20 nodes having three degrees of freedom per node, was employed to simulate both the OSD and asphalt surfacing with a meshing size of 10 mm [2]. To improve the evaluating accuracy, the mesh of the objective weld (i.e., arranged with a notch) was refined (see Figure 2), and the refined meshing size around the notch was nearly 0.2 mm [20,21]. The elastic modulus and Poisson's ratio of the material of the OSD were 210 GPa and 0.3, respectively. As previous research has revealed, the stress characteristics of the OSD were less affected by the Poisson's ratio of the asphalt surfacing; this was valued as 0.3 in the present study. While the elastic modulus of the asphalt surfacing was to be assigned with different values to simulate the effect of the temperature, as will be introduced in the following sections.

In terms of the boundary conditions, the displacement of nodes on the longitudinal end of the deck plate and the U-rib was constrained to simulate the continuous structure that is present in real-world engineering. The displacement of nodes on the transverse end of the deck plate and diaphragm were also constrained. The displacement of nodes at the bottom of the diaphragm was also constrained to simulate the continuous structure.

4. Modified Formulae for Predicting the SCFs

As illustrated before, the effect of the asphalt surfacing is not considered in the results of the ENS-based SCFs predicted by Equation (1). Therefore, parametric analysis of the effect of the asphalt surfacing, including the effect of transverse loading position and temperature, was carried out in the present study to clarify the effect of the asphalt surfacing on the ENS-based SCFs predicted by Equation (1). Notably, the effect of the transverse loading position should be taken into account because vehicles generally pass through the same cross-section following different transverse in-lane positions. As will be pointed out in Section 4.1, the ENS-based SCF determined by Equation (1) corresponds to the same transverse loading position, which cannot be directly applied to the evaluation in practical engineering as the real transverse loading position is unclear. In this case, an additional parametric analysis on the effect of the transverse loading position on the SCF should be carried out based on the FE model. Once the modified formulae were proposed, the ENS-based SCFs considering the effect of the asphalt surfacing could be efficiently obtained.

Furthermore, previous study reveals that the ENS concentration position is independent of the transverse loading position, while being sensitive to the temperature of the asphalt surfacing [2]. However, in terms of the full-penetrated rib–deck weld, the root–deck crack (i.e., the target crack in the present study) will be generated due to fatigue damage accumulation regardless of the variation in the transverse loading position and temperature of the asphalt surfacing. In the following sections, parametric analysis was performed based on the FE models with fully penetrated rib–deck welds. Therefore, the predicted ENS-based SCF could be employed to evaluate the fatigue damage in the corresponding concentration position, i.e., the proposed predictive formulae are applicable to the fatigue evaluation of the root–deck crack.

4.1. Effect of the Transverse Loading Position

Firstly, to investigate the effect of single factor (i.e., the transverse loading position), an additional FE model without the asphalt surfacing was developed. The double wheel load model, with a loading area of 600 mm (transverse) × 200 mm (longitudinal), was employed according to the Chinese standard "Specifications for Design of Highway Steel Bridge" [22]. Five transverse loading positions were considered: $x = 0$, $x = \pm 0.1$ m, and $x = \pm 0.2$ m. $x = 0$ meant that the wheel loading was applied right above the U-rib labelled R4, as shown in Figure 4; $x = 0.1$ m meant that the wheel loading was 0.1 m right of the symmetric axis of the sub model; $x = -0.2$ m meant that the wheel loading was 0.2 m left.

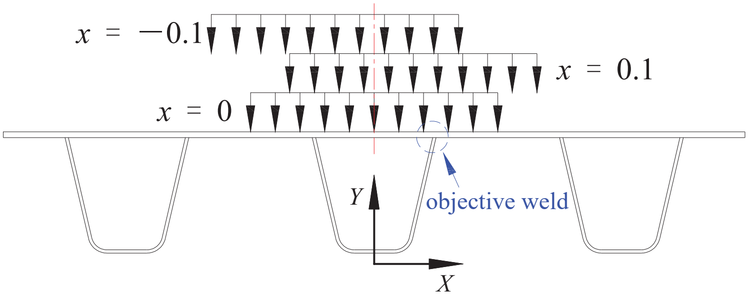

Figure 4. Schematic diagram of the transverse loading position (unit: m).

Both the effective notch stress (ENS) and nominal stress were obtained using the FE analysis; subsequently, the ENS-based SCF could be determined by the ratio of the ENS to the nominal stress. Based on the FE analysis, values of the ENS-based SCFs corresponding to different transverse loading positions were plotted in Figure 5a. Additionally, the SCFs predicted by Equation (1) was also plotted. Based on the geometric sizes of the rib–deck weld in FE model (i.e., $t_d = 14$ mm, $t_r = 8$ mm, $1 - t_p/t_r = 1.0$, $l_{w,d} = l_{w,r} = 6$ mm, $\theta = 78°$), the predicted value was calculated to be 3.496.

As can be seen from Figure 5a, the ENS-based SCF is considerably affected by the transverse loading position. The ENS-based SCF reaches the greatest value when the wheel load is applied at the position of $x = -0.1$ m. The cubic polynomial function was employed to fit the results with a final correlation coefficient (R^2) of 0.997, as expressed by Equation (2).

$$SCF_{\mathrm{ENS}} = 7.28829 - 28.63279x - 79.15843x^2 + 484.32571x^3 \tag{2}$$

where x represents the position of the wheel loading, as shown in Figure 4.

It can also be seen that the ENS-based SCF is consistent with the value predicted by Equation (1) when $x = 0.125$ m. On this basis, it is feasible to modify Equation (1) by introducing the amplification coefficient (k_{SCF}) to take into account the effect of the transverse loading position. The k_{SCF} could be determined by Equation (3).

$$k_{SCF} = SCF_{\text{ENS},x} / SCF_{\text{ENS},x=0.125} \tag{3}$$

where $SCF_{\text{ENS},\,x}$ is the ENS-based SCF at arbitrary position of the wheel loading; $SCF_{\text{ENS},\,0.125}$ is the ENS-based SCF corresponding to the position of $x = 0.125$ m.

Values of k_{SCF} were plotted in Figure 5b. The cubic polynomial function was also employed to fit the results with a final correlation coefficient (R^2) of 0.997, as expressed by Equation (4). Clearly, the ENS-based SCF corresponding to arbitrary weld geometry and transverse loading position could be determined by using Equations (1)–(4). Notably, the obtained results are only applicable to the OSDs without considering the asphalt surfacing.

$$k_{SCF} = 2.08475 - 8.19016x - 22.64257x^2 + 138.53711x^3 \tag{4}$$

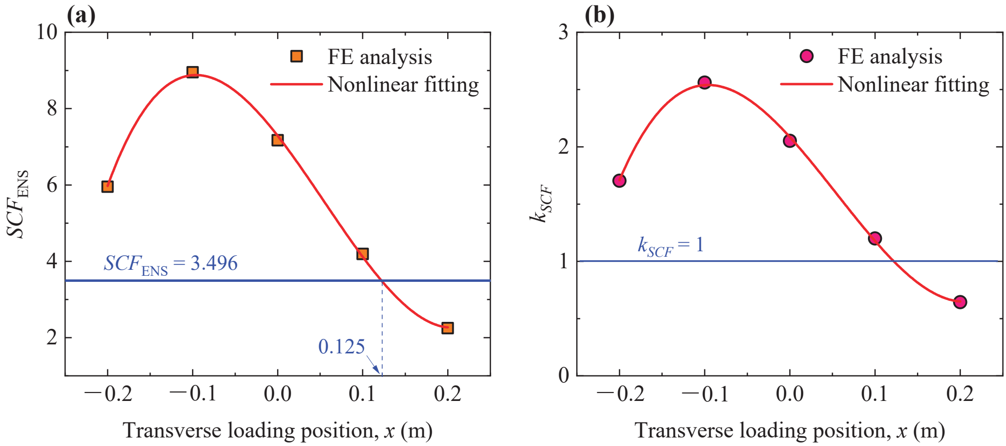

Figure 5. Effect of the transverse loading position on the ENS-based SCFs: (**a**) variation in the ENS-based SCFs; (**b**) variation in the amplification coefficient k_{SCF}.

4.2. Combined Effect of the Transverse Loading Position and Asphalt Surfacing

In practical engineering, the effect of asphalt surfacing is considerable. To investigate the combined effect of the transverse loading position and asphalt surfacing, FE models with a 60 mm thick asphalt surfacing were developed. The elastic modulus and Poisson's ratio of the asphalt surfacing were assumed to be 5058 MPa and 0.3, without considering the variation in temperature. Values of the ENS-based SCF and k_{SCF1} were obtained, as plotted in Figure 6. The cubic polynomial function was also employed to fit the results, as expressed by Equations (5) and (6), and the final correlation coefficients (R^2) were both 0.927. It could be seen that the ENS-based SCF considering the effect of asphalt surfacing is generally greater than the one without considering such effect. This further demonstrates that Equation (1) cannot be directly applied to practical engineering as the effect of asphalt surfacing is not involved. Notably, while considering the effect of the asphalt surfacing, there is no conflict between the increase in the ENS-based SCF and the decrease in the weld stress. The reason is that the ENS-based SCF is defined as the ratio of the ENS to the nominal stress, and both the ENS and nominal stress decrease when considering the effect of the asphalt surfacing but the decrease in the nominal stress is more obvious. For instance, when the wheel loading was applied at the position of $x = 0.10$ m, the ENS and nominal stress were 31.8 and 7.6 MPa without considering the effect of the asphalt surfacing, while the values decreased to be 25.0 and 5.1 MPa considering an such effect.

It is obvious that both the ENS and nominal stress decrease, while the ENS-based SCF increases (increased from 4.18 to 4.90 in terms of this example) when considering the effect of the asphalt surfacing.

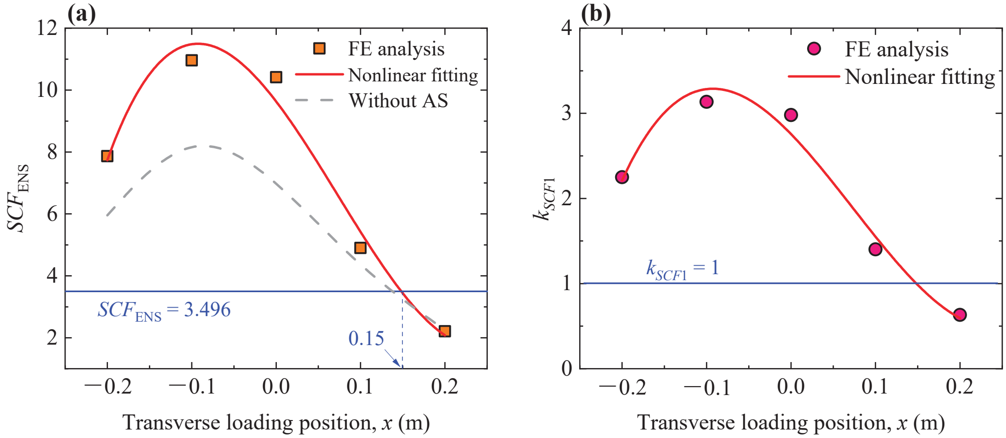

Figure 6. Combined effect of the transverse loading position and asphalt surfacing: (**a**) variation in the values of the ENS-based SCF, where AS represents the asphalt surfacing; (**b**) variation in the amplification coefficient k_{SCF1}.

It can also be seen that the ENS-based SCF, considering the combined effect of the transverse loading position and asphalt surfacing, is consistent with the value predicted by Equation (1) when x = 0.15 m. On this basis, another amplification coefficient (k_{SCF1}) was introduced to take into consideration the combined effect of the transverse loading position and asphalt surfacing, as expressed by Equation (7). On this basis, an ENS-based SCF which corresponds with arbitrary weld geometry and transverse loading positions, used in practical engineering, could be determined by using Equations (1) and (5)–(7).

$$SCF_{\text{ENS}} = 9.63401 - 35.68153x - 118.19119x^2 + 538.58958x^3 \tag{5}$$

$$k_{SCF1} = 2.75572 - 10.20639x - 33.80755x^2 + 154.05881x^3 \tag{6}$$

$$k_{SCF1} = SCF_{\text{ENS},x} / SCF_{\text{ENS},x=0.15} \tag{7}$$

4.3. Effect of the Temperature of Asphalt Surfacing

In Section 4.2, the elastic modulus of the asphalt surfacing was valued as 5058 MPa, which corresponded to a temperature of 20 °C according to Equation (8). Additionally, the elastic modulus was set to be 16,290, 11,031, 2320, 1064, and 488 MPa to simulate the effect of temperatures of −10, 0, 40, 60, and 80 °C, respectively. The loading position remained unchanged (the wheel load was applied right above the U-rib, i.e., x = 0.0) to investigate the effect of the temperature of asphalt surfacing. Values of the ENS-based SCF in presence of different temperatures were determined by the FE analysis, as plotted in Figure 7a. It could be seen that the ENS-based SCF decreases with the increasing temperature of asphalt surfacing. Notably, the asphalt surfacing has a greater elastic modulus at lower temperatures, decreasing fatigue stress. At low temperatures, even though the rib–deck weld has a higher stress concentration, the stress range will be much smaller due to the strengthened composite stiffness of the asphalt surfacing and OSD. Furthermore, since the ENS-based SCF is sensitive to the transverse loading position (see Figure 6a), it is believed that the curve in Figure 7a changes with the variation in the transverse loading position. However, it is unnecessary to perform additional FE simulations to conduct the parametric analysis, since the predictive formulae for determining the ENS-based SCFs, corresponding to an arbitrary transverse loading position and the temperature of the asphalt surfacing, could be proposed based on the current database. If additional simulations can be performed to expand the database of the ENS-based SCFs, the only result would be that the relative error of the proposed formulae will decrease.

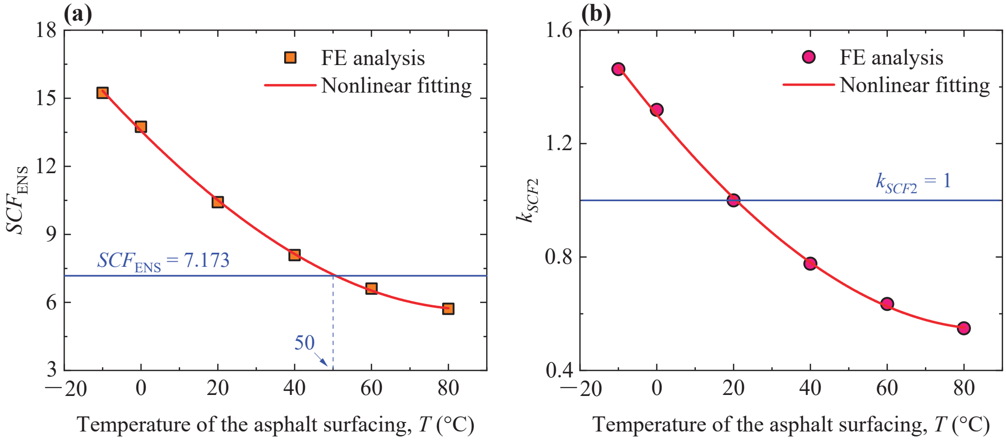

Figure 7. Effect of the temperature of the asphalt surfacing: (**a**) variation in the values of the ENS-based SCF; (**b**) variation in the amplification coefficient k_{SCF2}.

The cubic polynomial function was also employed to fit the results, as expressed by Equation (9), with a final correlation coefficient (R^2) of 0.998. Taking the ENS-based SCF at 20 °C (i.e., SCF_{ENS} = 7.173) as the reference, another amplification coefficient (k_{SCF2}) was introduced to determine the ENS-based SCF at arbitrary temperatures of the asphalt surfacing, as expressed by Equation (10). The values of k_{SCF2} are plotted in Figure 7b. The cubic polynomial function was also employed for nonlinear fitting, as expressed by Equation (11). The final correlation coefficient (R^2) was 0.998. To this end, the ENS-based SCF corresponding to arbitrary weld geometry and temperatures in practical engineering could be determined by using Equations (1) and (8)–(11).

$$E = 11031 \times 10^{-0.01693T} \tag{8}$$

where E is the elastic modulus of asphalt surfacing and T is the temperature.

$$SCF_{\mathrm{ENS}} = 13.56537 - 0.16886T + 7.66876 \times 10^{-4}T^2 + 1.52388 \times 10^{-6}T^3 \tag{9}$$

$$k_{SCF2} = SCF_{\mathrm{ENS},T} / SCF_{\mathrm{ENS},T=20} \tag{10}$$

$$k_{SCF2} = 1.30223 - 0.01621T + 7.36178 \times 10^{-5}T^2 + 1.46288 \times 10^{-7}T^3 \tag{11}$$

4.4. Validation of the Proposed Formulae

To validate the feasibility and reliability of the proposed formulae, an additional five cases were considered, as listed in Table 1. Corresponding FE models were developed to obtain the FE results, and predictive results were also obtained by employing Equations (5)–(11). Both the numerical and predictive results were plotted in Figure 8 and Table 2. As can be seen, the ENS-based SCFs obtained using FE analysis were 7.73, 11.08, 3.01, 8.85, and 7.31, respectively, while those obtained by employing the proposed formulae were 8.12, 11.89, 3.25, 8.74, and 6.69, respectively. The relative errors between the numerical and predictive results were 5.14%, 7.34%, 8.36%, −1.27%, and −8.48%, which were all within 10%. Therefore, it is believed that the proposed formulae are acceptable for engineering applications.

Additionally, to minimize the adverse effects of the relative error, the relative error should be reasonably considered so as to obtain the distributing range of the evaluating results of the fatigue damage.

Table 1. Cases for validation.

Case	Transverse Loading Position (m)	Temperature of the Asphalt Surfacing (°C)
1	$x = 0.05$	$T = 5$
2	$x = -0.05$	$T = 15$
3	$x = 0.15$	$T = 25$
4	$x = -0.15$	$T = 35$
5	$x = 0$	$T = 50$

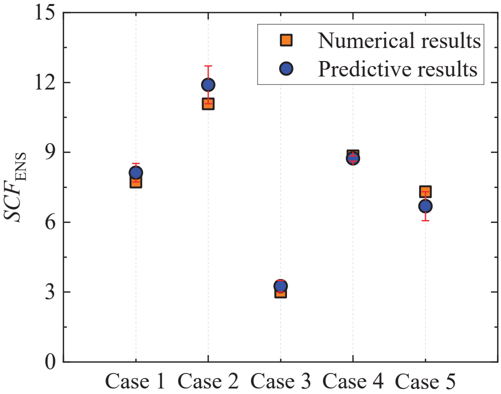

Figure 8. Comparison of the numerical and predictive results of SCF_{ENS}.

Table 2. Comparison of the numerical and predictive results.

Case	Numerical Results	Predictive Results	Relative Error (%)
1	7.73	8.12	5.14
2	11.08	11.89	7.34
3	3.01	3.25	8.36
4	8.85	8.74	−1.27
5	7.31	6.69	−8.48

5. Conclusions

The prediction of ENS-based SCFs of a rib–deck weld in an OSD, considering the effect of asphalt surfacing, was the focus of the present study. Based on the refined FE models, parametric analysis was conducted to investigate the effect of the transverse loading position, the combined effect of the transverse loading position and asphalt surfacing, and the effect of the temperature of asphalt surfacing. On this basis, predictive formulae for determining ENS-based SCFs for engineering applications were proposed by integrating the parametric equations without considering the effect of asphalt surfacing. The following conclusions can be drawn.

(1) ENS-based SCFs of rib–deck welds are sensitive to transverse loading positions, and the greatest value corresponds to the loading position of $x = -0.1$ m. The ENS-based SCF increases when considering the combined effect of the asphalt surfacing, while the variation trend remains unchanged.

(2) ENS-based SCFs are considerably affected by the temperature of asphalt surfacing. The lower the temperature is, the greater the ENS-based SCF is. And the ENS-based SCF decreases with an increase in temperature.

(3) Based on the numerical results of ENS-based SCFs, predictive formulae are proposed to determine the ENS-based SCFs corresponding to arbitrary weld geometry, transverse loading position, and the temperature of the asphalt surfacing. Validation research shows that the proposed formulae could provide reliable results with a relative error within 10% (namely 5.14%, 7.34%, 8.36%, −1.27%, and −8.48% for the five cases, respectively), which is believed to be acceptable for real-world engineering applications.

In future investigations, more cases considering variations in weld geometry, transverse loading position, and temperature should be simulated to extend the database of the ENS-based SCF so as to improve the predictive accuracy of the regressive formulae. Additionally, the artificial neural network (ANN) and machine leaning method should also be employed to propose more reliable models for the prediction of ENS-based SCFs.

Author Contributions: Q.W. developed the methodology; S.S. was in charge of the formal analysis; Z.W. was responsible for data curation; Z.F. and Y.Y. mainly worked on investigation and validation. All authors have read and agreed to the published version of the manuscript.

Funding: This work is sponsored by the National Natural Science Fundation of China (No. 52308176), the Natural Science Foundation of Jiangsu Province (Grant No. BK20220422) and the Natural Science Foundation of the Jiangsu Higher Education Institutions of China (Grant No. 22KJB560008). The assistances are gratefully acknowledged.

Institutional Review Board Statement: Not applicable.

Informed Consent Statement: Informed consent was obtained from all subjects involved in this study.

Data Availability Statement: The data that support the findings of this study are available from the corresponding author upon reasonable request.

Conflicts of Interest: The authors declare no conflict of interest.

References

1. Tsakopoulos, P.A.; Fisher, J.W. Full-scale fatigue tests of steel orthotropic decks for the Williamsburg bridge. *J. Bridge Eng.* **2003**, *8*, 323–333. [CrossRef]
2. Wang, Q.D.; Ji, B.H.; Fu, Z.Q.; Yao, Y. Effective notch stress approach-based fatigue evaluation of rib-to-deck welds including pavement surfacing effects. *Int. J. Steel Struct.* **2020**, *20*, 272–286. [CrossRef]
3. Fisher, J.W.; Barsom, J.M. Evaluation of Cracking in the Rib-to-Deck Welds of the Bronx–Whitestone Bridge. *J. Bridge Eng.* **2016**, *21*, 04015065. [CrossRef]
4. Xue, J.W.; Wang, J.Q.; Yi, J.Y.; Wei, Y.; Huang, K.J.; Ge, D.M.; Sun, R.Y. Optimal parking path planning and parking space selection based on the entropy power method and Bayesian network: A case study in an indoor parking lot. *Sustainability* **2023**, *15*, 8450. [CrossRef]
5. Wang, J.Q.; Li, Q.; Huang, K.J.; Ge, D.M.; Gong, F.Y. Sustainable recycling techniques of pavement materials. *Materials* **2022**, *15*, 8710. [CrossRef] [PubMed]
6. Su, P.F.; Li, M.M.; Dai, Q.L.; Wang, J.Q. Mechanical and durability performance of concrete with recycled tire steel fibers. *Constr. Build. Mater.* **2023**, *394*, 132287. [CrossRef]
7. Hobbacher, A. *Recommendations for Fatigue Design of Welded Joints and Components*; Springer International Publishing: Berlin, Germany, 2016.
8. Esderts, A.; Willen, J.; Kassner, M. Fatigue strength analysis of welded joints in closed steel sections in rail vehicles. *Int. J. Fatigue* **2012**, *34*, 112–121. [CrossRef]
9. Duan, M.J.; Wang, F.; Wu, Y.T.; Tao, H.; Zhang, D.P. Sensitivity analysis of structural parameters of unequal-span continuous rigid frame bridge with corrugated steel webs. *Appl. Sci.* **2023**, *13*, 10024. [CrossRef]
10. Duan, M.J.; Zhu, J.T.; Gu, Z.; Fang, Z.J.; Xu, J.Y. Analysis of the temperature field effect on the thermal stress of the main tower of long-span suspension bridges. *Appl. Sci.* **2023**, *13*, 8787. [CrossRef]
11. Lotsberg, I.; Sigurdsson, G. Hot spot stress S-N curve for fatigue analysis of plated structures. *J. Offshore Mech. Arct. Eng. Trans. ASME* **2006**, *128*, 330–336. [CrossRef]
12. Radaj, D.; Lehrke, H.P.; Greuling, S. Theoretical fatigue-effective notch stresses at spot welds. *Fatigue Fract. Eng. Mater. Struct.* **2001**, *24*, 293–308. [CrossRef]
13. Pachoud, A.J.; Manso, P.A.; Schleiss, A.J. New parametric equations to estimate notch stress concentration factors at butt welded joints modeling the weld profile with splines. *Eng. Fail. Anal.* **2017**, *72*, 11–24. [CrossRef]
14. Luo, Y.X.; Tsutsumi, S.; Han, R.; Ma, R.L.; Dai, K.S. Parametric formulas for stress concentration factor and clamping-induced stress of butt-welded joints under fatigue test condition. *Weld. World* **2022**, *66*, 1897–1913. [CrossRef]

15. Yung, J.L.; Lawrence, F.V. Analytical and graphical aids for the fatigue design of weldments. *Fatigue Fract. Eng. Mater. Struct.* **1985**, *8*, 223–241. [CrossRef]
16. Terán, G.; Albiter, A.; Cuamatzi-Meléndez, R. Parametric evaluation of the stress concentration factors in T-butt welded connections. *Eng. Struct.* **2013**, *56*, 1484–1495. [CrossRef]
17. Brennan, F.P.; Peleties, P.; Hellier, A.K. Predicting weld toe stress concentration factors for T and skewed T-joint plate connections. *Int. J. Fatigue* **2000**, *22*, 573–584. [CrossRef]
18. Oswald, M.; Mayr, C.; Rother, K. Determination of notch factors for welded cruciform joints based on numerical analysis and metamodeling. *Weld. World* **2019**, *63*, 1339–1354. [CrossRef]
19. Wang, B.X.; Zhao, W.G.; Du, Y.L.; Zhang, G.Y.; Yang, Y. Prediction of fatigue stress concentration factor using extreme learning machine. *Comput. Mater. Sci.* **2016**, *125*, 136–145. [CrossRef]
20. Wang, Q.D.; Ji, B.H.; Fu, Z.Q.; Yao, Y. Parametric equations for notch stress concentration factors of rib-deck welds under bending loading. *Front. Struct. Civ. Eng.* **2021**, *15*, 595–608. [CrossRef]
21. Wang, Q.D.; Fu, Z.Q.; Wei, Y.; Wang, Y.X.; Yao, Y. Predicting the ENS-based SCFs of rib-deck welds by integrating HSS measurement. *J. Constr. Steel Res.* **2023**, *203*, 107828.
22. *JTG D64-2015*; Specifications for Design of Highway Steel Bridges. China Communications Press: Beijing, China, 2015.

materials

MDPI

Article

Repairing Behaviors of Cracked Steel Plates Based on Bolted Fiber-Reinforced Polymer Plates

Jie Liu [1], Haobo Wang [1], Yang Wei [1,*], Daguang Han [2] and Yunfei Xiang [1]

[1] College of Civil Engineering, Nanjing Forestry University, Nanjing 210037, China; jieliu@outlook.com (J.L.); whb20230426@163.com (H.W.); yfxiang@njfu.edu.cn (Y.X.)
[2] School of Civil Engineering, Southeast University, Nanjing 210096, China; daguanghan@seu.edu.cn
* Correspondence: wy78@njfu.edu.cn

Abstract: The use of FRP materials to repair cracked/damaged steel structures has gradually been adopted by researchers. This paper investigates the repairing effect of bolted FRP plates for cracked steel plates based on experimental and numerical simulation methods. In the experimental investigation, the tensile strengths of six specimens, including three repaired specimens and three pure cracked steel specimens, were evaluated. The test outcomes indicated that the bolt repairing method significantly enhanced the tensile strengths of the cracked steel plates. As an example, the failure of a pure steel plate with a 1 mm width crack occurred at 813 N, whereas after being repaired, a tensile strength of 1298 N was observed. Based on finite element (FE) analysis, the influence of bolt preloads and interfacial friction coefficients were verified. The stress-relative ratio for specimens was contingent on the bolt preload magnitude and gradually decreased as the preload was augmented. By exploring the repairing effect for varied friction coefficients, it was concluded that using a higher bolt preload can aid in eliminating the performance discrepancy of the overall component caused by interface treatment errors.

Keywords: cracked steel plate; fiber-reinforced polymer; repair; stress; pre-tightening force

Citation: Liu, J.; Wang, H.; Wei, Y.; Han, D.; Xiang, Y. Repairing Behaviors of Cracked Steel Plates Based on Bolted Fiber-Reinforced Polymer Plates. *Materials* **2023**, *16*, 6773. https://doi.org/10.3390/ma16206773

Academic Editor: Paulo Santos

Received: 8 September 2023
Revised: 14 October 2023
Accepted: 17 October 2023
Published: 19 October 2023

1. Introduction

Steel elements are extensively employed in diverse fields, such as aerospace engineering, civil engineering, marine engineering, etc. During practical application, owing to external loads and working environment conditions, steel members are inevitably prone to damage, cracks, and even failures [1–3]. In practical applications, preventing cracks from spreading and evolving into through-thickness cracks is of the utmost importance, particularly in the fields of bridge engineering, aerospace engineering, transportation pipelines, and pressure vessels [4–6]. Recently, fiber-reinforced polymer (FRP) has been increasingly used in the aviation industry, civil engineering, and energy industry sectors because of its light weight, high strength, super fatigue resistance, and corrosion resistance [7–11]. The technology of repairing/reinforcing structures with FRP materials has attracted more and more scholars' attention [12,13].

Typically, there are two techniques for repairing steel structures with FRP, namely external bonding and bolting methods. For the bonding method, high-performance bonding materials are employed to affix the FRP material onto the surface of the base material, allowing both to distribute the force. On the other hand, the bolt connection method utilizes bolts to establish a connection between the FRP and the base structure, resulting in the FRP material being secured together with the structure as a whole [14–18]. For actual reinforcement, considering the low durability and high-temperature sensitivity of the bonding material and the fragility of the interface, the bolted connection method can be regarded as a significant practical and competitive reinforcement method.

The study of bolted FRP-reinforced/repaired structures has been an area of research interest. Hai and Mutsuyoshi [19] researched the structural behavior of double-lap joints composed of steel splice plates bolted and bonded to pultruded hybrid CFRP/GFRP laminates, revealing that the bolted joint's failure strength and failure mode were predominantly influenced by the bolt-end distance. Feroldi and Russo [20] conducted experimental research on the structural performance of FRP beam–column–plate bolted connections by determining the initial stiffness and ultimate bending capacity for each connection and the rotation in relation to ultimate strength. These results were then compared to numerical predictions obtained through commercial code utilizing finite element analysis. Sweedan et al. [21] investigated the interfacial behavior of mechanically anchored FRP laminates for strengthening steel beams. The failure of test components was primarily controlled by using a combination of various mechanisms, including bearing in FRP laminates, bending in connecting bolts, folding in washers, and tearing of FRP laminates. Later, Satasivam et al. [22] conducted an experimental study on the composite actions present in steel-FRP composite beam systems utilizing novel blind bolt shear connections. They quantified the shear stiffness, also known as the slip modulus, of the shear connection by subjecting steel-FRP joints to tension loads. Abdelkerim et al. [23] investigated the static and fatigue performance of FRP bolted joints and proposed a new hybrid steel-FRP bolt to prolong the fatigue life of the composite joints. Recently, Olivier et al. [24] investigated the feasibility of bolted connectors in hybrid FRP-steel structures via experimental analysis. The authors confirmed the great application prospect of the bolted FRP-steel composite structure for engineering structures and proposed novel preloaded connectors injected with steel-reinforced resin for the bolted connections. The above-mentioned researchers undertook extensive studies on the performance of FRP-steel bolted connections. These studies demonstrate the enormous potential of FRP bolted repair/reinforcement of steel components.

However, the existing research mainly focuses on the conventional reinforcement connection performance of typical components, and there is little research on FRP bolted repair of cracked steel specimens in engineering. The research results introduced previously have proven that FRP bolted technology has great potential for repairing/strengthening steel components. The specific efficiency and influencing factors of this repair technology need further research. Therefore, this study investigated the repair of cracked steel plate specimens using the bolt connection method through experimental and simulating analysis. It comprehensively analyzed the effects of crack size and bolt preload on the repairing performance, providing a solid scientific basis for the application of FRP bolted steel specimens.

2. Repair Experiment

2.1. Materials

In this study, 3 mm thick Q355b steel, with a yield strength and Young's modulus measuring 364 MPa and 203 GPa, respectively, according to the manufacturer's specifications, was the primary material used for constructing the steel plates. The outer contour size of the slotted steel plate was 150 mm × 100 mm. Prefabricated at specified positions, two bolt holes featuring a 7 mm diameter were included on each steel plate. For this research study, 6 mm diameter stainless-steel screw arbors were utilized. The Young's modulus and shear strength of the stainless-steel bolts were provided by the manufacturer, measuring 202 GPa and 645 MPa, respectively. Tabulated in Table 1 are the material properties adopted throughout the research, including those of the pultruded GFRP plates, reinforced adhesive, and steel. These GFRP plates, possessing a thickness of 3 mm, were constructed from E-glass fibers and unsaturated polyester resin.

Table 1. Mechanical properties of the GFRP, adhesive, and steel.

Mechanical Property	GFRP	Steel Plates	Steel Bolts
Young's modulus (GPa)	20.22 (longitudinal direction) 12.39 (transversal direction) 13.66 (thickness direction)	203	202

Table 1. *Cont.*

Mechanical Property	GFRP	Steel Plates	Steel Bolts
Strength (MPa)	537.86 (longitudinal direction) 303.24 (transversal direction) 327.43 (thickness direction)	364 (yield strength) 542 (tensile strength)	645 (shear strength)
Poisson's ratio	0.37	0.30	0.30

2.2. Manufacturing and Repairing Mechanism

Table 2 presents information regarding the tested specimens—consisting of three repaired specimens (type I, II, and III)—and three reference specimens (reference I, II, and III), which were pure cracked steel plates. To construct the repaired specimens, a cracked steel plate, two FRP plates, and two steel bolts were integrated into their structural design, as illustrated by the geometric features shown in Figure 1 and Table 2. It is worth noting that no initial preload (i.e., pre-tightening force) was imposed on the bolts of the three bolted repaired specimens analyzed in this study. To analyze the strain development throughout the quasi-static tensile test, strain sensors were placed on the steel plates' surface adjacent to the crack tip. The test was carried out using displacement control mode at a constant rate of 1 mm/min. Additionally, to monitor the stress changes in the region around the crack tip during the stretching process, a strain gauge was positioned 3 mm in front of the tip, as depicted in Figure 1. Furthermore, the tensile strength and failure characteristics of the six specimens were obtained based on the quasi-static experiments, as illustrated in Table 2.

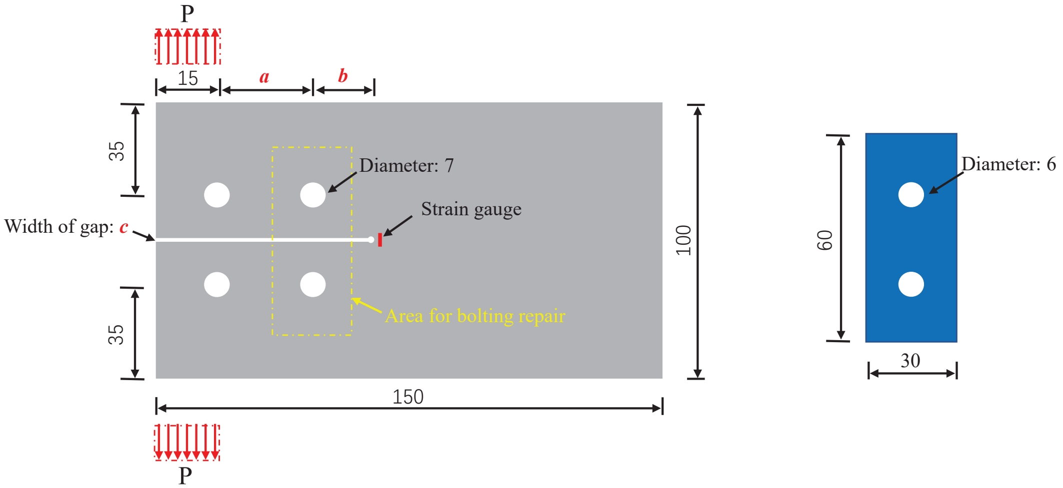

(**a**) (**b**)

Figure 1. Geometry and load graph of the FRP steel bolted repaired specimen (unit: mm). (**a**) Cracked steel plate. (**b**) FRP plate.

Table 2. Parameters for the specimens.

Specimen	a and b and c/mm	Tensile Strength/N	Failure Mode
Type I	40 and 20 and 1	1298	Cracking of steel plate +shear-out failure of FRP
Type II	40 and 20 and 2	1573	Cracking of steel plate +shear-out failure of FRP
Type III	40 and 20 and 3	1750	Cracking of steel plate +shear-out failure of FRP

Table 2. *Cont.*

Specimen	a and b and c/mm	Tensile Strength/N	Failure Mode
Reference I	40 and 20 and 1	813	Cracking of steel plate
Reference II	40 and 20 and 2	1038	Cracking of steel plate
Reference III	40 and 20 and 3	1204	Cracking of steel plate

Under tensile loading P, the repaired specimen experienced shear force (P) and a bending moment (M) in the left section proximate to the reinforcement area (comprising the upper and lower sections). Meanwhile, the local bolted area was subjected to surface friction (F_f) between the FRP and steel plate as well as extrusion force (F_e) between the screw and steel plate screw hole wall (which may occur only after slippage of the FRP and steel plate), as shown in Figure 2. Based on the force transmission mechanism in Figure 3, it is easy to conclude that the repaired specimen utilized the new force transmission path (offered by the bolted combination area) to transfer a portion of the internal load. By using this technique, the stress on the cracked area can be reduced, ultimately leading to the safeguarding and reinforcement of the cracking region. The greater the internal loads transferred, the more effective the repair/reinforcement will prove to be.

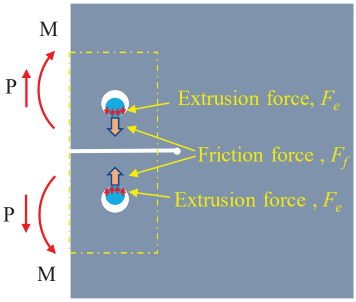

Figure 2. Load transfer diagram of the repaired specimen.

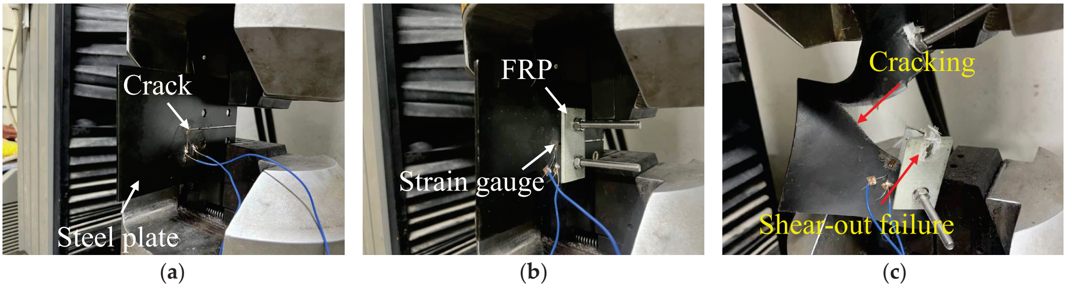

(**a**) (**b**) (**c**)

Figure 3. Test setup and failure modes. (**a**) For reference specimen. (**b**) For repaired specimen. (**c**) Composite failure modes.

3. Repair Performance Analysis

3.1. Testing Results

Figure 3 plots the tests and failure modes of the specimens, and the results of the specimens labeled as reference I, II, and III in Table 2 reveal that the width of the steel plate crack affected the specimen's failure strength, with the narrower crack width resulting in lower failure strength of the specimen. For instance, reference I had a tensile strength of 813 N, whereas 1204 N was adopted by reference III. A similar trend was observed in types I, II, and III. This demonstrated that the crack width exerted a vital influence on the specimen's cracking strength. By comparing the reference specimen and its corresponding repaired specimen, it was found that the adopted repairing method could significantly improve the tensile specimen of the cracked steel plates. For example, the failure of the specimen for reference I occurred at 813 N, whereas 1298 N of the tensile specimen was adopted by the specimen of repairing type I. For the reference specimens, during the loading process, because of the stress concentration effect in the crack area, the reference specimen cracked rapidly, and as the load continued to be applied, the crack gradually expanded until the overall failure of the plate. However, the damage of the repaired specimens exhibited distinct characteristics: during the initial loading stage, due to the bolting and anchoring effect of the FRP plate, the load-bearing capacity of the repaired specimen was mainly supported by the FRP plate. As the external load gradually increased to a certain value, shear-out failure of the FRP plate occurred and eventually caused the failure of the steel plate due to cracking. Figure 4 plots the load–displacement curves of specimens type I and reference I.

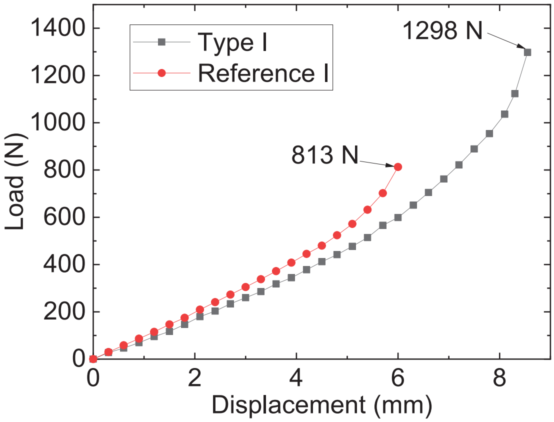

Figure 4. Load–displacement curves of specimens type I and reference I.

3.2. Finite Element Models

Three-dimensional (3-D) finite element (FE) analysis using ABAQUS was employed to investigate the repair efficiency of the bolted FRP method for cracked steel plates. The bolted repaired model comprised one cracked steel plate, two FRP plates, and two bolts, while the steel plate and steel bolt were assumed to be homogeneous and linearly elastic, based on Table 1 values. Concurrently, the orthotropic linear elastic material model for the FRP laminate plate referenced the longitudinal, transverse, and thickness modulus values in Table 1. The sizes of the steel, FRP, and bolt models were established based on the actual sizes of the bolted repaired specimens. The steel plate's screw hole diameter was 7 mm, and the FRP screw hole diameter was 6 mm, with a 6 mm diameter screw arbor and 9 mm outer diameter nut. The steel plate, FRP plate, and bolt component (i.e., nuts and screw arbors) were simulated using eight-node linear brick elements (C3D8R) suitable for complex nonlinear analyses of bolted specimens, as evidenced in Mandal and Anupam [25] and Yang et al. [26]. Moreover, wedge elements were implemented to mesh the prefabricated crack's tip region and the center core portion of the bolting zones of the steel plates. Finer wedge elements were applied near the bolt holes of the FRP plates due to the high stress concentration. Each screw hole was divided into 32 units along the perimeter. The mesh size of the overall model was approximately 2 mm, while hexahedral elements represented the crack area of the steel plate with a mesh size of 0.1 mm to capture the stress distribution of the crack tip accurately. Figure 5 illustrates one of the repaired FE models' layouts, and the model's constraints were established according to actual stress and deformation conditions.

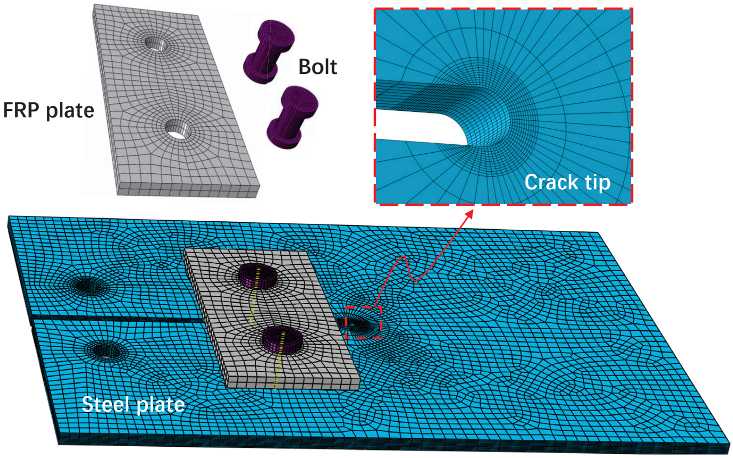

Figure 5. Repaired FE model.

An in-built master–slave algorithm was used to define the contact relationships among various components of the repaired model. This study encompassed different contact behaviors, such as the contact between the bolt and FRP, the contact between the bolt and the steel plate, and the contact between the steel and FRP. These behaviors were primarily characterized by their tangential and normal properties. The contact behaviors in the normal direction were referred to as “hard contact” in this study, while the contact behaviors in the tangential direction were expressed through the application of “Coulomb friction force”. The finite sliding surface-to-surface discretization method was utilized to simulate the relative sliding of different components and to prevent stress concentration. McCarthy et al.’s [27] coefficients of friction of 0.1 and 0.3 for the bolt-to-FRP and steel-to-FRP interfaces, respectively, were adopted.

To validate the accuracy of the FE model method, the results from the 3-D FE model of the repaired specimen for type II (repaired by FRP plates without preload) and reference II (pure steel plate with 2 mm crack) were compared with the results from experiments. Figure 6 shows the comparison of the stresses of the measuring point of the crack tip (the measuring location of the strain gauges is shown in Figure 1) under different tensile loads. Upon comparison of the 3-D FE simulation analysis and experimental test stress values, it can be observed that the results are substantially consistent. For instance, the monitored stress level for the reference specimen under a 1000 N load was 126.88 MPa, whereas the model stress for the same load was 119.13 MPa, with a relative error of 5.5%. Furthermore, for the repaired specimen, the experimental stress under a 1000 N load was 79.61 MPa, whereas the corresponding model analysis stress level was 81.78 MPa, with the relative error amounting to roughly 2.7%. The comparison outcomes demonstrate that the 3-D FE analysis approach employed can effectively and precisely capture the loading information of the actual specimen.

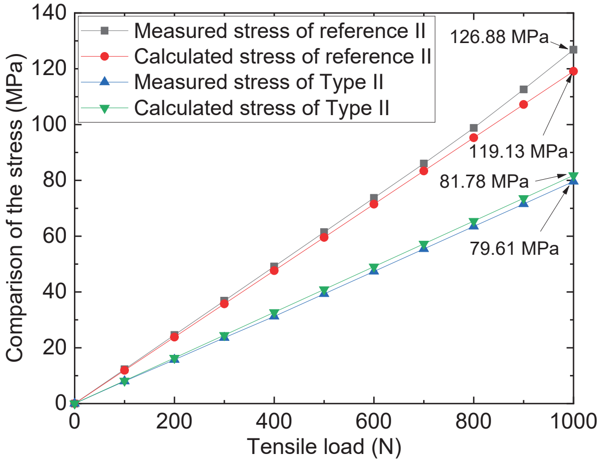

Figure 6. Comparison of the stresses of tests and FE models.

3.3. Stress Distribution of Reference II

Figure 7 exemplifies the stress distribution of reference II, which was subjected to a tensile force of 1000 N. The stress cloud diagram reflects significant stress concentration in the cracking tip, thereby suggesting that the specimen's failure under tensile load was initiated in the crack tip area. To facilitate a thorough analysis of the stress distribution within the fracture tip region, the local polar coordinate system of the tip area was established, and the stress values of the edge nodes in this region were extracted. Specifically, the coordinate origin was defined as the center of the gap area (point O in Figure 7), while the middle plane of the crack gap served as the coordinate plane.

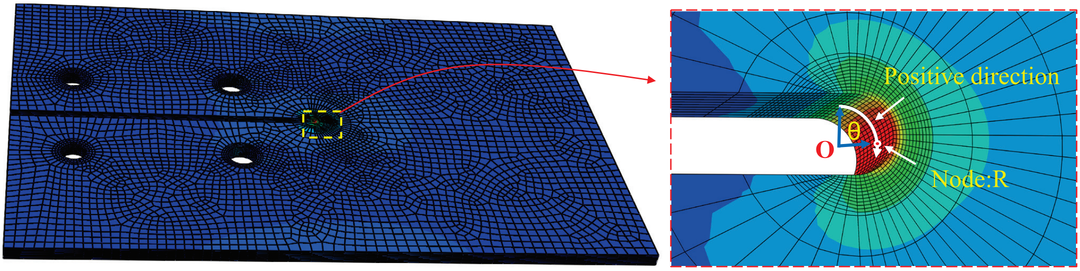

Figure 7. Stress distribution and location of calculated nodes.

Drawing on the calculated path's definition in Figure 7, the stress of crack tip nodes could be ascertained and are depicted in Figure 8. A detailed analysis of Figure 8 reveals substantial variation in the stress value at the crack tip with the azimuth angle's augmentation. Specifically, for $0° < \theta < 90°$, the stress steadily increased with the increase in angle, and an incremental increase in the stress value was observed with the augmentation in the azimuth angle's magnitude. For $90° < \theta < 180°$, the stress value displayed an opposite trend, with a gradual decrease in the stress values observed alongside an increase in azimuth angle. Notably, for the node (referred to as node "R") with an azimuth angle of 90°, the stress value reached its maximum of 358.15 MPa. According to the stress distribution law of the crack notch, node R was used as the stress control point, and the subsequent analysis was based on the stress information of this node.

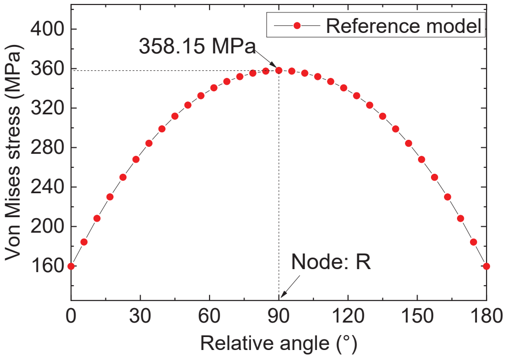

Figure 8. Stress distribution of the crack tip nodes for the reference model.

Figure 9 illustrates a stress comparison between the type II repaired specimen and the reference I specimen under a tension of 1000 N. Upon examining the data from Figure 9, it becomes apparent that the variation in the stress at the crack tip following repairing/strengthening with double-sided FRP plates mirrors that of the reference specimen. Nevertheless, upon scrutinizing the joint stresses of the two models at identical positions (for instance, the node, R), it becomes evident that the bolt repair of the FRP plates effectively mitigates the stress concentration at the crack tip in the specimen. As a consequence, the extreme stress level occurring near the tip following strengthening measures amounts to 238.68 MPa, which is significantly lower than the value of the reference specimen model (358.15 MPa), and the reduction range of 119.47 MPa was calculated accordingly.

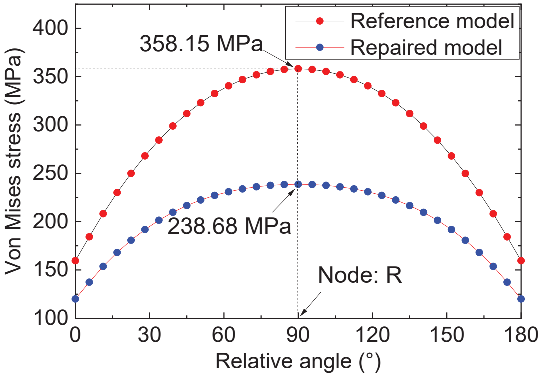

Figure 9. Comparison of the stress distribution of the repaired and reference model.

3.4. Effect of Preload of the Bolts

It is worth noting that the tested specimens were manufactured without preload of the bolts; therefore, to investigate the pre-tightening effect of the bolts on the repaired specimens, FE analysis was carried out. To effectively simulate the pre-tightening effects of bolts on repairing efficiency, researchers adopted the in-built Bolt Load option in ABAQUS. Figure 10a offers an insightful comparison of the stresses of node R in the repaired specimen with various preload conditions under a 1000 N tensile load. It is essential to mention that the reinforced specimens shared the same type II steel plate. The valuable insights in Figure 8 demonstrate that the pre-tightening force of bolts played a crucial role in influencing the stress magnitude within a specimen's crack area. As the pre-tightening force increases, the stress levels within the crack area gradually trend upwards. For instance, for specimens possessing 5000 N preloads, the maximum stress values at point R approximate 110.84 MPa, yet when the preload is augmented to 10,000 N, the maximum stress reduces to 91.54 MPa. The change in the von Mises stress for node R can be modeled kinetically with a cubic function curve, as Figure 10a shows, where S is the von Mises stress of node R and P_t is the pre-tightening force of the bolts.

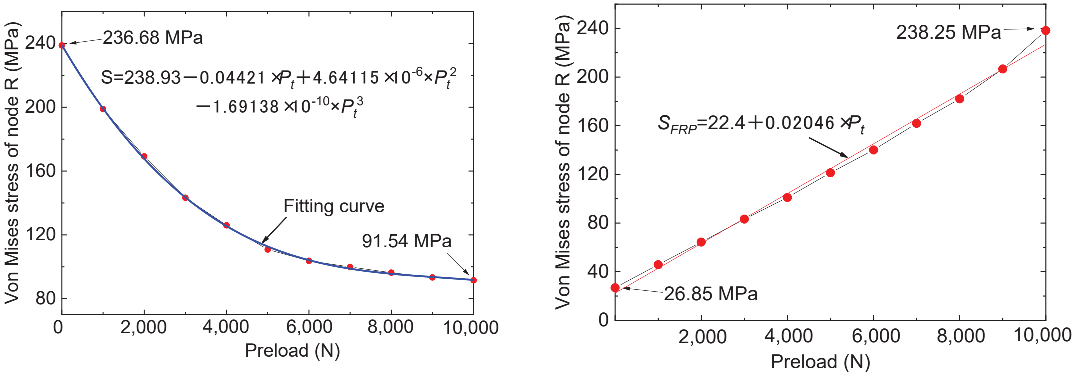

(**a**) (**b**)

Figure 10. Comparison of the stresses for different preload conditions. (**a**) Stresses of node R. (**b**) Stresses of FRP plates.

Figure 10b plots the comparison of the stresses of FRP plates for different preload conditions. From Figure 10b, it is discovered that, despite the effectiveness of bolt pre-tensioning in reducing stress concentration in the steel plate crack area, it inadvertently leads to stress concentration within the FRP plate itself, notably in the bolt hole region. Stress concentration in the FRP plate stems from two factors: firstly, the robust pre-tensioning action of the bolts, whereby the FRP plate bears more tensile load, and secondly, the initial pre-tensioning of the bolts increases the stress in the hole of the bolt. However, despite the stress concentration of the FRP plates, the magnitude of the forces involved does not surpass the failure strength of the FRP material itself. For instance, the stress threshold for the FRP plate in the 10,000 N preloaded specimen was about 238.25 MPa, which is considerably smaller than the failure strength of the FRP plate. Therefore, it may be deduced that within the predefined preloading limit (preloading force should not exceed 10,000 N), a higher preloading force will help repair and reinforce cracks in steel plates.

3.5. Effect of Crack Size

Previous research [28,29] has established the significance of crack size (mainly referring to the crack width) in defining the fracture performance of steel components. As a result, we conducted an analysis of repair/reinforcement based on FRP materials for steel plates with varying crack widths while simultaneously scrutinizing the impact of bolted connection repair under different pre-tightening forces on the failure performance of the specimens. Based on the test results for the repaired specimens in Table 2, the tensile strengths of the joints were significantly influenced by the crack widths, with a narrower crack width implying larger tip stress intensity. Figure 11 plots the stress of node R for the repaired model with different crack widths under a 1000 N tensile load. Based on the results in Figure 11, the stress of the crack tips was found to be significantly affected by the crack widths. For instance, for the type I specimen (1 mm width crack prefabricated in the steel plate) with 0 N pre-tightening force, the stress of node R was calculated as 324.35 MPa, whereas a stress of 217.66 MPa was found for type III. In addition, when the larger pre-tightening force (for example, 10,000 N) was applied through the bolts, the reinforcement effect of FRP on the steel plate was quite prominent, so the stresses at the crack tips of steel plates with different crack widths were close to each other; for example, the stresses of the three types of specimens were 94.67 (type I), 91.54 (type II), and 89.67 MPa (type III).

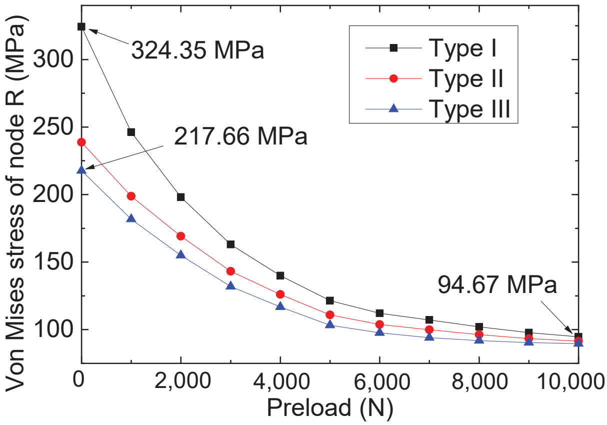

Figure 11. Stresses for node R for the three repaired models.

3.6. Effect of Interfacial Friction Coefficient

Taking into account that the bolted repaired specimens studied previously were based on a coefficient of friction of 0.3 for the steel-to-FRP interfaces, this coefficient was confirmed by a study on bolted structures on conventional surfaces [27]. However, considering that surface treatment can be used to change the friction properties of a steel structure during the repair/strengthening process, it is necessary to investigate the effect of the friction coefficient of the interface on the mechanical performance of bolted repair components. Therefore, to explore the impact of the steel-FRP interfacial friction characteristics of type II repaired specimens on its tensile performance, a study on the mechanical properties of the specimens under varying friction coefficients was conducted. Three friction coefficients of 0.3, 0.5, and 0.7 were adopted, and the corresponding stresses of node R for each repaired specimen under a 1000 N tensile load are plotted in Figure 12.

Based on Figure 12, the mechanical performance of the specimen will be affected by the interface friction coefficient. For example, for the repaired specimen under the same preload (for example, a preload of 5000 N), as the interface friction coefficient increased (from 0.3 to 0.7), the stress of node R gradually decreased from 110.84 to 86.03 MPa accordingly, indicating that a larger interface friction coefficient is more conducive to the unloading of the steel plate, which means that a larger interface friction coefficient of FRP-steel plates is more conducive to repair the cracked steel plates. Therefore, for the application of bolted FRP plates to repair cracked steel plates, it is advisable to increase the friction coefficient of the interface as much as possible through surface treatment.

In addition, by examining the data presented in Figure 12, it is evident that the performance of the repaired specimens was significantly influenced by changes in the friction coefficient at lower preloads (for preloads below 4000 N). For instance, at a preload of 1000 N, the analysis results for the three friction coefficients were 198.78 (0.3), 153.06 (0.5), and 125.85 MPa (0.7), respectively. Yet, for the working conditions featuring higher preloads (such as when the preloads were 10,000 N), closed values of 91.54 (0.3), 86.75 (0.5), and 81.06 MPa (0.7) were calculated. This phenomenon shows that under the higher preload, slip movement between the FRP and steel plates did not occur. Therefore, it can be concluded that for bolted reinforcement/repair structures, the use of a higher bolt preload can help to eliminate the performance difference of the overall component caused by interface treatment errors. That is to say, to ensure the performance safety of the bolted repair structure, it is advisable to increase the pre-tightening force of the bolts (preferably using high-strength pre-tightening bolts).

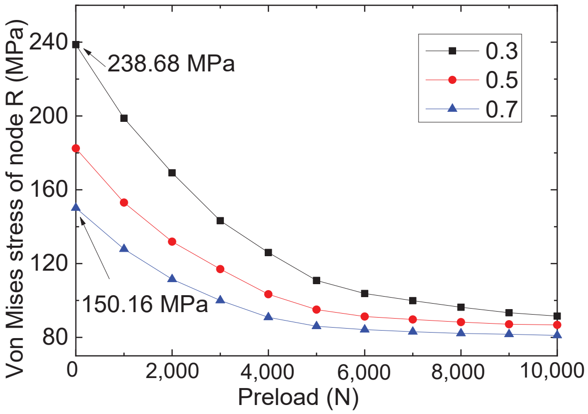

Figure 12. Stresses of node R for different friction coefficients.

4. Conclusions

This study provides insights into the repairing behaviors of cracked steel plates based on bolted FRP plates through experiments and FE analysis. The results of this study reveal the repair effectiveness and the influence factors (i.e., pre-tightening forces and friction coefficients) of this repair method. The results highlight the importance of considering preloads and friction coefficients in the design of bolted repair for steel components. The following conclusions can be drawn:

1. By comparing the reference specimen (i.e., the pure cracked steel plate) and its corresponding repaired specimen (which was bolted with FRP plates), it was found that the bolted repairing method could significantly improve the tensile strengths of the cracked steel plates. Moreover, by examining the failure characteristics of the six specimens, composite failure modes—which included the cracking of the steel plate and bearing failure of the FRP—were observed in the repaired specimens.
2. The bolt repair of the FRP plates effectively mitigated the stress concentration at the crack tip in the specimen. As a consequence, the extreme stress level occurring near the tip following strengthening measures amounted to 238.68 MPa for the bolted specimen with a 2 mm width crack, which is significantly lower than that of the reference specimen (pure cracked specimen with a 2 mm width crack).
3. The discussion of the effect of the preloads of the bolts revealed that the pre-tightening force of bolts played a crucial role in influencing the stress magnitude within a specimen's crack area. As the pre-tightening force increases, the stress levels within the crack area gradually trend upwards, and the change in the von Mises stress for node R can be modeled kinetically with a cubic function curve.
4. The mechanical performance of the specimen will be affected by the interface friction coefficient, and as the interface friction coefficient increases (from 0.3 to 0.7), the stress of node R gradually decreases accordingly. In addition, based on the discussion on the working conditions featuring higher preloads (such as when the preloads were 10,000 N), it was concluded that the use of a higher bolt preload can help to eliminate the performance difference of the overall component caused by interface treatment errors. It is worth noting that this study mainly studied the repairing/strengthening effects of bolted specimens of FRP and cracked steel plates; however, the relaxation effects of bolted structures under vibrational loads may result in different performances, and the influences of relaxation effects require additional investigation in future studies.

Author Contributions: Conceptualization, J.L.; Methodology, J.L.; Software, H.W.; Validation, H.W. and Y.W.; Investigation, J.L.; Writing—original draft, J.L.; Writing—review & editing, Y.W. and D.H.;

Visualization, J.L.; Supervision, D.H.; Project administration, Y.X.; Funding acquisition, J.L. and Y.X. All authors have read and agreed to the published version of the manuscript.

Funding: This research was funded by the National Natural Science Foundation of China (grant number: 52108151) and the foundation of Basic Science (Natural Science) Research Project for Colleges and Universities of Jiangsu Province (grant number: 22KJB420002).

Institutional Review Board Statement: Not applicable.

Informed Consent Statement: Not applicable.

Data Availability Statement: Data will be made available on request.

Conflicts of Interest: The authors declare no conflict of interest.

References

1. Wang, Q.; Wang, L.; JI, B.; Fu, Z. Modified effective notch stress method for fatigue evaluation of rib-deck welds integrating the critical distance approach. *J. Constr. Steel Res.* **2022**, *196*, 107373.
2. Duan, M.; Zhang, S.; Wang, X.; Dong, F. Mechanical behavior in perfobond rib shear connector with UHPC-steel composite structure with coarse aggregate. *KSCE J. Civ. Eng.* **2020**, *24*, 1255–1267. [CrossRef]
3. Duan, M.; Zou, X.; Bao, Y.; Li, G.; Chen, Y.; Li, Z. Experimental investigation of headed studs in steel-ultra-high performance concrete (UHPC) composite sections. *Eng. Struct.* **2022**, *270*, 114875. [CrossRef]
4. Liu, J.; Guo, T.; Feng, D.; Liu, Z. Fatigue Performance of Rib-to-Deck Joints Strengthened with FRP Angles. *ASCE's J. Bridge Eng.* **2018**, *23*, 04018060. [CrossRef]
5. Rashnooie, R.; Zeinoddini, M.; Ahmadpour, F.; Aval, S.B.; Chen, T. A coupled XFEM fatigue modelling of crack growth, delamination and bridging in FRP strengthened metallic plates. *Eng. Fract. Mech.* **2023**, *279*, 109017. [CrossRef]
6. Mohan, A.; Poobal, S. Crack detection using image processing: A critical review and analysis. *Alex. Eng. J.* **2018**, *57*, 787–798. [CrossRef]
7. Hollaway, L.C. A review of the present and future utilisation of FRP composites in the civil infrastructure with reference to their important in-service properties. *Constr. Build. Mater.* **2010**, *24*, 2419–2445. [CrossRef]
8. Wei, Y.; Zhang, Y.; Chai, J.; Wu, G.; Dong, Z. Experimental investigation of rectangular concrete-filled fiber reinforced polymer (FRP)-steel composite tube columns for various corner radii. *Compos. Struct.* **2020**, *244*, 112311. [CrossRef]
9. Cristescu, N.D.; Craciun, E.M.; Soós, E. *Mechanics of Elastic Composites*; CRC Press: Boca Raton, FL, USA, 2003; Volume 1.
10. Lepretre, E.; Chataigner, S.; Dieng, L.; Gaillet, L. Stress intensity factor assessment for the reinforcement of cracked steel plates using prestressed or non-prestressed adhesively bonded CFRP. *Materials* **2021**, *14*, 1625. [CrossRef]
11. Craciun, E.M. Energy criteria for crack propagation in pre-stressed elastic composites. In *Lecture Notes on Composite Materials: Current Topics and Achievements*; Springer: Dordrecht, The Netherlands, 2009; pp. 193–237.
12. Shi, X.; Guo, T.; Song, L.; Yang, J. Cyclic load tests and finite element modeling of self-centering hollow-core FRP-concrete-steel bridge columns. *Alex. Eng. J.* **2023**, *70*, 301–314. [CrossRef]
13. Wei, Y.; Bai, J.; Zhang, Y.; Miao, K.; Zheng, K. Compressive performance of high-strength seawater and sea sand concrete-filled circular FRP-steel composite tube columns. *Eng. Struct.* **2021**, *240*, 112357. [CrossRef]
14. Bocciarelli, M. A new cohesive law for the simulation of crack propagation under cyclic loading. Application to steel-and concrete-FRP bonded interface. *Theor. Appl. Fract. Mech.* **2021**, *114*, 102992. [CrossRef]
15. Zhao, X.-L.; Zhang, L. State-of-the-art review on FRP strengthened steel structures. *Eng. Struct.* **2007**, *29*, 1808–1823. [CrossRef]
16. Yun, Y.; Wu, Y.F.; Tang, W.C. Performance of FRP bonding systems under fatigue loading. *Eng. Struct.* **2008**, *30*, 3129–3140. [CrossRef]
17. Wang, J.; Xiong, Y.; Li, Q.; Jin, D.; Hu, Y.; Che, T. Experimental investigation on the preparation and surface treatment of biomass fibers for stone mastic asphalt mixtures modification. *Constr. Build. Mater.* **2023**, *408*, 133667. [CrossRef]
18. Saleem, M. Multiple crack extension model of steel anchor bolts subjected to impact loading. *Constr. Build. Mater.* **2018**, *180*, 364–374. [CrossRef]
19. Hai, N.D.; Mutsuyoshi, H. Structural behavior of double-lap joints of steel splice plates bolted/bonded to pultruded hybrid CFRP/GFRP laminates. *Constr. Build. Mater.* **2012**, *30*, 347–359. [CrossRef]
20. Feroldi, F.; Russo, S. Structural behavior of all-FRP beam-column plate-bolted joints. *J. Compos. Constr.* **2016**, *20*, 04016004. [CrossRef]
21. Sweedan, A.M.I.; El-Sawy, K.M.; Mohammed, M.A.A. Interfacial behavior of mechanically anchored FRP laminates for strengthening steel beams. *J. Constr. Steel Res.* **2013**, *80*, 332–345. [CrossRef]
22. Satasivam, S.; Feng, P.; Bai, Y.; Caprani, C. Composite actions within steel-FRP composite beam systems with novel blind bolt shear connections. *Eng. Struct.* **2017**, *138*, 63–73. [CrossRef]
23. Abdelkerim, D.S.; Wang, X.; Ibrahim, H.A.; Wu, Z. Static and fatigue behavior of pultruded FRP multi-bolted joints with basalt FRP and hybrid steel-FRP bolts. *Compos. Struct.* **2019**, *220*, 324–337. [CrossRef]

24. Olivier, G.; Csillag, F.; Christoforidou, A.; Tromp, L.; Veltkamp, M.; Pavlovic, M. Feasibility of bolted connectors in hybrid FRP-steel structures. *Constr. Build. Mater.* **2023**, *383*, 131100. [CrossRef]
25. Mandal, B.; Anupam, C. Numerical failure assessment of multi-bolt FRP composite joints with varying sizes and preloads of bolts. *Compos. Struct.* **2018**, *187*, 169–178. [CrossRef]
26. Yang, K.; Bai, Y.; Ding, C.T.; Kong, S.Y. Comparative study on·mechanical performance of bolted joints with steel and fibre-reinforced polymer bolts. *J. Build. Eng.* **2021**, *41*, 102457. [CrossRef]
27. McCarthy, C.T.; McCarthy, M.A.; Stanley, W.F.; Lawlor, V.P. Experiences with modeling friction in composite bolted joints. *J. Compos. Mater.* **2005**, *39*, 1881–1908. [CrossRef]
28. Meresht, E.S.; Farahani, T.S.; Neshati, J. Failure analysis of stress corrosion cracking occurred in a gas transmission steel pipeline. *Eng. Fail. Anal.* **2022**, *18*, 963–970. [CrossRef]
29. Mohtadi-Bonab, M.A.; Ghesmati-Kucheki, H. Important factors on the failure of pipeline steels with focus on hydrogen induced cracks and improvement of their resistance. *Met. Mater. Int.* **2019**, *25*, 1109–1134. [CrossRef]

materials

MDPI

Article

The Mechanical Properties and Water-Reducing and Retarding Mechanism of a Xylonic Cement Admixture

Feng Han [1], Kaijian Huang [1,*], Yang Wei [1], Jian Han [2] and Yong Xu [2]

[1] College of Civil Engineering, Nanjing Forestry University, Nanjing 210037, China; hanfeng2678@sina.com (F.H.); wy78@njfu.edu.cn (Y.W.)
[2] Jiangsu Co-Innovation Center of Efficient Processing and Utilization of Forest Resources, College of Chemical Engineering, Nanjing Forestry University, Nanjing 210037, China; nl_hanjian@njfu.edu.cn (J.H.); xuyong@njfu.edu.cn (Y.X.)
* Correspondence: huangkaijian@njfu.edu.cn; Tel.: +86-138-1386-6459; Fax: +86-025-84498336

Abstract: This study explores the mechanical properties, as well as the water-reducing and setting delay mechanism, of a novel xylonic acid-based water reducer applied to cementitious materials. Four xylonic acid water reducers were synthesized in this study: XACa (PX) from pure xylose, XACa (HS) from hemicellulose hydrolysate, XANa (PX) from pure xylose, and XANa (HS) from hemicellulose hydrolysate. These were generated through the whole-cell catalysis of Gluconobacter oxydans bacteria, using pure xylose and hemicellulose hydrolysate as substrates. The findings indicate that the xylonic acid-based water reducer can attain a water-reducing capability between 14% and 16% when the dosage (expressed as a mass fraction of cement) is roughly 0.2%. In initial and final setting tests, XACa (PX) demonstrated a pronounced retarding influence at admixture levels below 0.15%, reaching its apex at 0.10%. This delayed the initial setting time by 76% and the final setting time by 136% relative to the control group. However, a slight pro-setting effect was noted beyond a 0.2% dosage. In the compressive and flexural tests of concrete, under the same slump, the XA group improved its mechanical properties by 5% to 10% compared to the SodiuM lignosulfonate (SL) group. In the air content and chloride ion migration resistance tests, the XA group reduced the air content by 38% compared to the SL group, but also increased the data of rapid chloride migration (D_{RCM}) by 16%. Characterization studies revealed that the carboxyl and hydroxyl groups in xylonic acid undergo chemisorption with the Si-O bonds on the surface of cement particles. These groups interact with the Si-O bonds on cement particles, contributing to water-reducing effects and delaying the setting process by impeding Ca^{2+} ion aggregation in the calcium-silicate-hydrate gel. Its significant water-reducing effect, adjustable setting time, and excellent mechanical and durability properties suggest its viability as an alternative to lignosulfonate series water-reducing agents.

Keywords: xylonic acid; water reducer; slow setting mechanism; water reducing mechanism

Citation: Han, F.; Huang, K.; Wei, Y.; Han, J.; Xu, Y. The Mechanical Properties and Water-Reducing and Retarding Mechanism of a Xylonic Cement Admixture. *Materials* **2023**, *16*, 7096. https://doi.org/10.3390/ma16227096

Academic Editor: Geo Paul

Received: 12 October 2023
Revised: 31 October 2023
Accepted: 8 November 2023
Published: 9 November 2023

1. Introduction

The use of concrete admixtures is one of the most effective and widely adopted strategies for enhancing the workability of concrete [1,2]. At present, the widely used concrete water reducing agents on the market are mostly naphthalene-based water reducing agents, polycarboxylic acid water reducing agents, and simple combinations of the two with other admixtures such as early strength agents, with a small portion being lignosulfonate-based water reducing agents. The dispersion mechanism of a polycarboxylate water-reducing agent on cement is a dual mechanism of electrostatic repulsion and steric hindrance [3]. Although the effect is outstanding, its cost is high, and there is no unified standard for its compound formula, which has mixed quality. With respect to the naphthalene-based water-reducing agents, hydrophilic groups dissociated from them are directionally adsorbed on the surface of cement particles [4], making it easy to associate with water molecules in the form of hydrogen bonds to form water, prevent direct contact between cement particles, and provide lubrication between particles. Although naphthalene-based water-reducing agents are relatively cheap, with the rise of large-scale construction such as highway bridges, mechanical mixing and pumping of concrete have exposed a fatal drawback: rapid loss of slumps. Both production processes will pollute the environment to varying degrees. Environmentally friendly lignosulfonate, as an anionic surfactant, has good adsorption and dispersion properties. When added to cement slurry, it can dissociate into macromolecular anions and metal cations. Anions with negative charges adsorb on the surface of positively charged cement particles [5–9], which can generate a certain electrostatic repulsion and disperse the cement particles. As "low-carbon development" has gradually become a global consensus for economic development, which has led to heightened demands for environmentally friendly additives in terms of raw materials and production processes.

Currently, the predominant biomass water reducer in use is lignosulfonate. Derived as a by-product of the sulfite process in wood pulp papermaking, lignosulfonate carries the advantages of being environmentally friendly and cost-effective. Nevertheless, it is not without its shortcomings, such as a low water-reducing efficiency and a high level of air entrainment and retardation, factors that constrain its broader application.

In addition, Maimaiti [10] treated waste cellulose to obtain microcrystalline cellulose (MCC), then with BS to obtain SBC, which was experimentally proved to be a retarded water reducer. As the degree of polymerization (DP) of MCC rises, the degree of substitution of SBC and concrete fluidity decrease, but the fluidity of concrete is not negatively correlated with the DP of MCC. Only when the DP of MCC < 96 and the degree of substitution > 0.375, SBC has the water-reducing ability, and the water-reducing and dispersing effect is best when DP = 45. The retardation effect may be due to the fact that the BS in SBC did not react completely with the -OH in cellulose, which made these groups form complexes with the inorganic particles in cement to cover the surface of the cement particles, and it is also possible that the -OH in cellulose is bonded with the water molecules to form hydrogen bonds, which formed a solventized water film on the surface of the cement particles and prevented the hydration reaction from proceeding. Rouzi [11] prepared a cellulose-based water reducer (CS) in a dichloromethane solution using cellulose cotton paddle meal as the base material and chlorosulfonic acid as the sulfonating agent. When the tension of the ratio of sulfonating agent and cellulose is 0.6, the water reducer obtained at room temperature for 3 h has the best performance. The surface CS aqueous solution decreases with an increase in the concentration of CS water reducer, and it has a certain air-entraining effect on the concrete. CS water reducer is adsorbed on the surface of cement particles, which makes the surface of cement particles have the same charge and then produces a repulsive effect resulting in the dispersion of cement particles, resulting in a water-reducing and dispersing effect. All of the above biomass water reducers have the problems of low water-reducing efficiency (no more than 10%) and difficulty going into production. Finding more efficient and environmentally friendly water-reducing agents is still necessary.

In the current research on xylonic acid-based (XA) water-reducing agents, Zhou's [12] experiment roughly explored the water-reducing efficiency and setting time of XA. Compared with Zhou's experimental results on water-reducing efficiency and air content after the addition of XA water-reducing agent, the relevant data are roughly the same as in this article. However, in terms of setting time, Zhou obtained experimental results that the setting time increases to 15 h with the increase of the addition amount between 0 and 0.40%. In the initial stage of this article, the initial and final setting times of cement paste are different from the results of Zhou, which makes it necessary to conduct more accurate and systematic experiments on the XA water-reducing agent to verify its performance.

Lignocellulose, a biomass resource with an approximate global annual yield of 180 billion tons [13], chiefly comprises cellulose, hemicellulose, and lignin. It possesses benefits such as carbon neutrality, economic viability, and broad availability. In order to fully exploit the potential of straw-based biomass resources, it is imperative to transform cellulose and hemicellulose into their corresponding monosaccharides for microbial conversion into resource-derived products [12,14–18]. This study employed sulfuric acid treatment as a means to eliminate lignin, thus liberating more cellulose and hemicellulose, disrupting the straw structure, augmenting the contact surface between microorganisms or enzymes and straw, and enhancing the conversion efficiency of straw-like biomass.

In this investigation, the studied xylonic acid (XA) water reducers were synthesized using pure xylose (PX) and xylose-rich hemicellulose hydrolysate (HS) as substrates. XA bears a chemical structure akin to gluconate, a well-known water-reducing and retarding agent in the cement and concrete industries. Consequently, XA, with its hydroxyl and carboxyl groups, offers potential as a novel concrete admixture. Characteristically, the xylonic acid water reducer is non-toxic, non-hazardous, eco-friendly, and biodegradable throughout its entire production process, inclusive of both raw materials and catalysts. When contrasted with lignosulfonate-based biomass water reducers, the xylonic acid water reducer presents remarkable benefits such as low gassing, minimal admixture requirement, high efficiency, control over setting time, and extensive application prospects [19–21].

This manuscript offers a succinct overview of the production methodology of xylonic acid water reducers and probes their water-reducing efficiency and optimal admixture quantity through experimental investigation. The outcomes hint at the potential substitutability of sodium lignosulfonate (SL) water reducers with these new developments.

2. Experiment

2.1. Experimental Materials

The cement is P.O 42.5 Hailuo brand ordinary silicate cement, which is produced by Nanjing Longtan Town Cement Factory; its specific gravity is 3.1. The fine aggregate is medium sand with a fineness modulus of 2.8, and the coarse aggregate is basalt with a grain size of 15–25 mm.

In the compressive strength test of mortar, which is to select the better reducers, W/C is 0.284. In the compressive and flexural strength tests of concrete, the ratio of cement, fine aggregate, and coarse aggregate in the concrete mixture is 1:1.5:2.55. Maintaining uniformity of slumps by varying the dose of water-reducing agent and the amount of water used. The water absorption of coarse aggregate is 1.24%.

Four distinct xylonic acid water reducers, specifically XACa (PX), XACa (HS), XANa (PX), and XANa (HS), were generated via whole-cell fermentation of the strain Gluconobacter oxydans after neutralization with NaOH and $Ca(OH)_2$ to reach a pH conducive to the strain's survival. The hemicellulose hydrolysate was derived from the treatment of agricultural residues such as corn stover and corn cobs with sulfuric acid. Gluconobacter oxydans, a bacterium of significant industrial relevance, is known for its production of aldehydic acids like xylogluconic acid (XA), which are utilized in this investigation. The pH of XA water reducers is 7~8. The specific gravity of XA water reducers is 0.35.

Water-reducing agents are listed in Table 1:

Table 1. The water reducers.

Particulars	XACa (PX)	XANa (PX)	XACa (HS)	XANa (HS)	SL
Category	Xlonic acid				Sodium lignosulfonate
Molecular formula	$C_5H_{10}O_6$				$C_{20}H_{24}Na_2O_{10}S_2$
Reaction materials	Pure xylose		Hemicellulose hydrolysate		Lignin + Na_2SO_3
Reaction environment	$Ca(OH)_2$	NaOH	$Ca(OH)_2$	NaOH	NaOH
Recommended dose	0~0.2%				0~0.3%
Efficiency of water reduction	0~16%				0~11%
Other functions	Promoting/retarding hydration, air-entraining				Retarding hydration, air-entraining

The basic properties and mineral composition of the cement are shown in Tables 2 and 3. The particle size distribution of aggregates is listed in Tables 4 and 5.

Table 2. Chemical composition and content of cement.

Component	LOI	Al_2O_3	CaO	MgO	Fe_2O_3	SO_2	SO_3
Content (%)	2.98	5.85	70.45	1.24	2.97	19.00	2.83

Table 3. Physical and mechanical properties of cement.

Water Consumption of Standard Consistency (%)	Setting Time (min)		Compressive Strength (MPa)		Flexural Strength (MPa)	
	Initial	Final	3 d	28 d	3 d	28 d
28.6%	328	362	27.8	54.2	5.4	8.6

Table 4. Particle size distribution of coarse aggregates.

Material Specifications	Proportion (%)	Percentage Passing (%)							
		31.5	26.5	19	16	13.2	9.5	4.75	2.36
20~30 mm	45	98	67.4	3.9	0.8	-	-	-	-
10~20 mm	55	100	100	96.9	75.0	6.9	5.3	0.6	-

Table 5. Particle size distribution of fine aggregates.

Material Specifications	Fineness Modulus	Percentage Passing (%)					
		2.0	1.6	1.0	0.5	0.16	0.08
Medium sand	2.8	100	93	67	23	13	1

2.2. Methods

2.2.1. Determination of Water Consumption and Setting Time for Standard Consistency of Cement Paste

The determination of the setting time for the cement paste adhered to the GB 1346-2001 (Chinese Standard) [22], The initial setting standard was defined when the probe of the Automatic Vicatometer descended by (34 ± 2) mm, and the final setting was marked when the probe penetrated the cement surface by (3 ± 1) mm.

2.2.2. Characterization of Cement Paste Samples

The cement paste with the same standard consistency was prepared and cured for 24 h in a constant temperature and humidity curing oven. A small portion was taken out and immersed in ethanol for an additional 24 h to halt the hydration reaction. Subsequently, it was transferred to an oven for drying. The surface appearance of the cement was observed using an environmental scanning electron microscope (Environmental Scanning Electron Microscope, Quanta 200, FEI, Hillsborough, OR, USA). Another portion was pulverized, milled to a 200-mesh consistency, and similarly placed in ethanol to stop the hydration process for 24 h. Subsequently, the XRD patterns of cement hydrates were measured using a multifunctional X-ray diffractometer (XRD Ultima IV, Rigaku, Tokyo, Japan)after an additional 24 h of suspension in ethanol.

2.2.3. Compressive Strength Test of Mortar

The experiment was conducted adhering to the guidelines of JGJ/I 70-2009 (Chinese Standard) [23]. The samples were prepared to a size of 70.7 mm × 70.7 mm × 70.7 mm for the test, with a lateral compression test being executed (Pressure Testing Machine, HTC-1068, Shenzhen Wance Test Equipment Co., Shenzhen, China) following a maintenance period of 7 days.

2.2.4. Compressive and Flexural Strength Test of Concrete

The experiment was conducted adhering to the guidelines of GB 50204-2015 (Chinese Standard) [24]. The samples were prepared to sizes of 100 mm × 100 mm × 100 mm for the compressive test, and 100 mm × 100 mm × 400 mm for the flexural test, with the lateral test being executed (Pressure Testing Machine, HTC-1068, Shenzhen Wance Test Equipment Co., Shenzhen, China) following a maintenance period of 7 and 28 days.

2.2.5. Concrete Air Content Test

In alignment with GB 50203-2011 (Chinese Standard) [25], a concrete air content meter(Direct Reading Concrete Air Content Tester, LC-615A, Jianyanhuace (Hangzhou) Technology Co., Hangzhou, China) was utilized. The concrete mix was evenly loaded into the measurement bowl and vibrated for 15–30 s until it became compact. The surface was then scraped to be flat, ensuring no air bubbles were present. The bowl was covered and filled with water until it reached the outlet, at which point the tap and exhaust valve were closed. The bowl was pressurized with air until the gauge pressure exceeded 0.1 MPa, precisely regulated with a trimmer valve. After actuating the valve lever 1–2 times, the pressure gauge reading was recorded. Utilizing the calibration curve, the value of air content A_1 was ascertained, and the aggregate air content C was determined using the water pressure method. The final air content A was calculated as $A = A_1 - C$.

2.2.6. Concrete Resistance to Chloride Ion Permeability Test

The examination was conducted in conformity with GB/T 50082-2009 (Chinese Standard) [26], utilizing the Rapid Chloride Migration Coefficient Method (RCM)(Concrete Chloride Ion Diffusion Coefficient Tester, CABR-RCM, Jianyan Building Materials Co., Beijing, China). A cylindrical specimen with a diameter of (100 ± 1) mm and a height $L = (50 \pm 2)$ mm was initially placed in a $Ca(OH)_2$ vacuum saturator for 24 h. Subsequently, it was enclosed in a rubber sleeve and introduced into the RCM experimental apparatus. Each sleeve was injected with 300 mL of NaOH solution with a concentration of 0.3 mol/L, while the cathodic experimental tank was filled with 12 L of NaCl solution with a concentration of 10%. Upon connecting the power supply's positive and negative terminals and energizing for $t = 24$ h, the energizing voltage U and temperature T were recorded. The specimen was dissected along the diameter of the circular surface, followed by the application of an $AgNO_3$ solution. The average value of chloride ion penetration depth Xd was noted, and the non-stationary chloride ion migration coefficient D_{RCM} of the concrete was calculated using the prescribed Equation (1).

$$D_{RCM} = \frac{0.239 * (273 + T)L}{(U - 2)t}\left(X_d - 0.238\sqrt{\frac{(273 + T)LX_d}{U - 2}}\right) \tag{1}$$

3. Results and Discussion

3.1. Influence of Different Xylonic Acid Water Reducer on Water Consumption

XACa (PX), XACa (HS), XANa (PX), and XANa (HS) were prepared using pure xylose and hydrolysate as reaction substrates, with calcium carbonate and sodium hydroxide as neutralizing substances, respectively. The water-reducing effects were evaluated based on the water consumption required to reach standard consistency, and the results are presented in Figure 1.

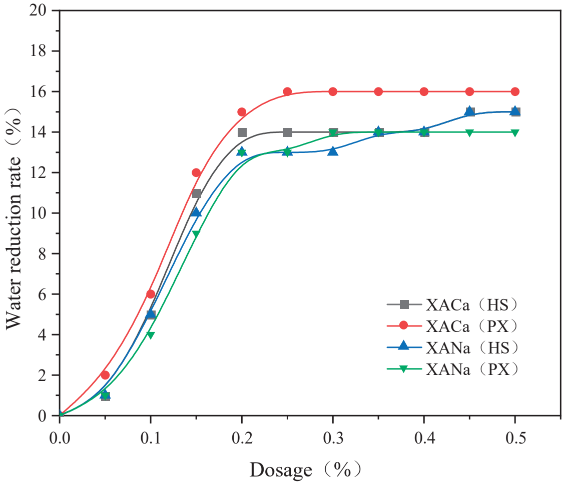

Figure 1. Effect of XA dosage on the water reduction rate.

From Figure 1, it is evident that the water-reducing capacity of xylonic acid water reducer gradually increases with higher dosages until reaching a saturation point. When the dosage is below 0.2%, the water consumption of cement to achieve standard consistency decreases with an increasing dosage of xylonic acid water reducer. However, at dosages ranging from 0.2% to 0.3%, the rate of increase in water-reducing capacity slows down. Beyond 0.3% dosage, all four water reducers exhibit maximum water-reducing effects. The water-reducing effects of the four xylonic acid water reducers are comparable, with XACa (HS), obtained by neutralizing $Ca(OH)_2$ with hydrolysate as the substrate, exhibiting the highest water-reducing effect. However, considering the effective content determination of the powder formulation and test errors, the effects of the four xylonic acid water reducers were considered equivalent for the time-setting.

3.2. Impact of Xylonic Acid (HS) Water Reducer Dosage on the Setting Time of Cement Paste

The initial and final setting times of cement paste were investigated by introducing xylonic acid water reducers at dosage levels ranging from 0% to 0.30% in increments of 0.05%. The tests were conducted using standard consistency water consumption (water-cement ratio of 0.284), 99% humidity in the curing chamber, and 20 °C. The results are presented in Figure 2.

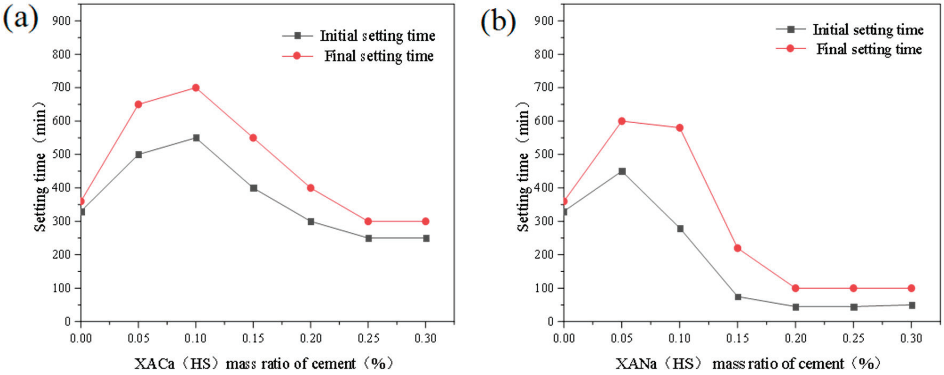

Figure 2. Effect of XA dosage on setting time: (**a**) XACa (HS); (**b**) XANa (HS).

From Figure 2, it can be observed that both XACa (PX) and XANa (PX) exhibit a retarding effect on the cement paste at a dosage of 0.05%. The retarding effect of XACa (PX) reaches its peak at 0.10%, increasing the initial setting time by approximately 76%. Conversely, the retarding effect of XANa (PX) shows a decreasing trend, and at 0.15%, it demonstrates a pro-setting effect, reducing the initial setting time by around 79%. With increasing dosage, the retarding effect of XANa (PX) remains consistent, while the retarding effect of XACa (PX) gradually diminishes and ceases after reaching 0.20%.

3.3. Impact of Xylonic Acid (PX) Water Reducer on the Setting Time of Cement Paste

Similarly, the effects of XACa (PX) and XANa (PX) on the final setting time of cement slurry are shown in Figure 3.

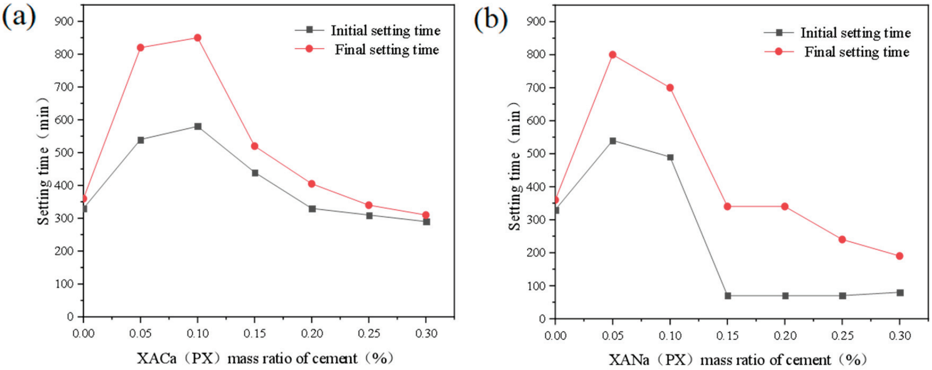

Figure 3. Effect of XA dosage on setting time: (**a**) XACa (PX); (**b**) XANa (PX).

Align with their initial setting effects. At a dosage of 0.05%, both water reducers extend the final setting time by approximately 128%. At a dosage of 0.10%, XACa (PX) exhibits a slightly improved retarding effect, while the retarding effect of XANa (PX) starts to decrease. With further dosage increases, XANa (PX) demonstrates a setting-promoting ability at 0.15%, followed by XACa (PX) at 0.25%. Additionally, XANa (PX) exhibits coagulation-promoting ability at 0.25%. Notably, XANa (PX) displays a stronger pro-setting ability, reducing the final setting time of cement paste by 47% at 0.30%. Zhou [12] obtained experimental results that the addition amount is between 0% and 0.40%, and the final setting time extends to 15 h with the increase of the addition amount. This may be due to the different purity of xylic acid compared to this article.

When the dosage of xylonic acid is sufficiently high, it promotes the generation of a large amount of Ettringaite (referred to as AFt), consumes a significant amount of mixing water, rapidly thickens the slurry, and, together with the bridging effect of AFt, accelerates cement setting. Conversely, with lower dosages of xylonic acid, the generation of AFt is limited, resulting in delayed formation of tricalcium silicate (C_3S) hydration and calcium silicate hydrate (CSH) gel, thus slowing down the cement setting process. This hypothesis was verified in subsequent characterization experiments.

The test results of xylonic acid obtained using hydrolysate as the substrate raw material demonstrate similar effects, where low dosages retard coagulation and high dosages promote coagulation. However, the coagulation time of both hydrolysate groups is slightly shorter than that of the pure xylose group. This can be attributed to trace impurities present in the hydrolysate, including but not limited to acids (formic acid, acetic acid, levulinic acid, butyric acid, and 4-hydroxybenzoic acid) and aldehydes (5-hydroxymethyl furfural, furfural, vanillin, butyraldehyde, and 5-hydroxybenzaldehyde), which hinder the reaction between xylonic acid and cement mineral components, thereby partially inhibiting the promoting effect of xylonic acid on C_3A hydrolysis.

Comparing the retarding effect of xylonic acid with lignosulfonate water reducers with certain retarding effects (Figure 4), it was found that the retarding effect is similar, but the dosing stage of the performance is different. With the increase in SL dosing, the retarding effect also increases.

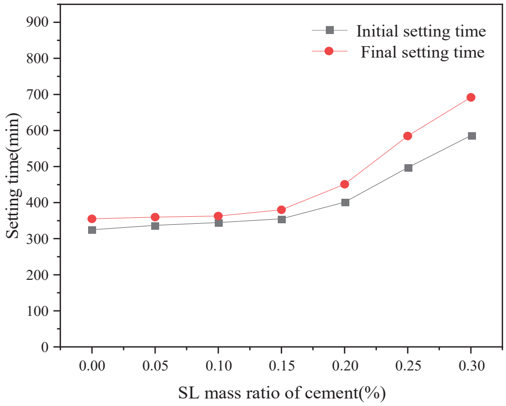

Figure 4. Effect of SL dosage on setting time.

SL has been utilized as a retarding agent for oil well cement for decades. Although the exact mechanism by which lignosulfonate delays silicate formation is not yet clear, it is speculated that this mechanism is a combination of adsorption and nucleation [27]. According to studies, sulfonates and hydroxyl groups can be adsorbed on the CSH gel layer of hydrated cement. This means the sulfonates and hydroxyl groups existing in the lignosulfonate can be mixed into the CSH gel layer, resulting in changes in the morphology of the CSH gel and a more impermeable structure. This will result in a waterproof effect, slowing down further hydration. The more sulfonates and hydroxyl groups it provides, the tardier the hydration proceeds, which led to the proportional linear result in the figure above.

3.4. Effect of XA Dosage on the Compressive Strength of Mortar

The influence of four xylonic acid water reducers on the compressive strength of test blocks with mortar exhibited varied performance, as depicted in Figure 5. At a low admixture of 0.05%, the compressive strength improved; however, it decreased to some extent as the admixture increased. At the optimal admixture of 0.2%, the hydrolysate group demonstrated superior performance with minimal strength reduction. Notably, XACa (HS) even exhibited a slight increase in compressive strength. This can be attributed to the retardation effect of xylonic acid at low to medium doping levels, which slows down the hydration rate and leads to lower 7-day strength formation. Considering the results of the aforementioned experiments, it is evident that the HS group outperformed the others. Therefore, subsequent experiments in this study employed two hydrolysates as xylonic acid water reducers.

In the case of the SL group, the compressive strength of mortar consistently decreased with increasing dosage. At its optimal admixture of 0.2~0.3%, the 7-day compressive strength decreased by approximately 30%. This decrease can be attributed to the air entrainment side effect of SL, which inversely impacts the compressive strength of mortar as air content rises.

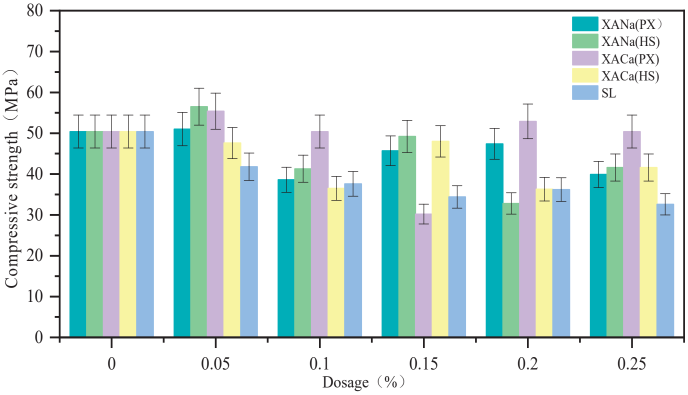

Figure 5. Effect of XA dosage on compressive strength.

3.5. Effect of Different Water Reducers on the Compressive and Flexural Properties of Concrete

Concrete compressive and flexural tests were conducted at 7 days and 28 days, using the water-reducing capacity of each water reducer obtained from the previous cement paste experiments (XA for 0.2% and SL for 0.3%), while maintaining a concrete mix slump of 100 mm. Analysis of the data in Figure 6 reveals significant improvements in the mechanical properties of concrete with XANa (HS) and XACa (HS) at the same slump level. Compared to the blank group, the xylonic acid water reducer demonstrated enhancements of approximately 35% and 27% in the 7-day and 28-day compressive strengths of concrete, respectively. Moreover, the flexural strength of concrete exhibited improvements of approximately 25% and 8% at 7 days and 28 days, respectively. Comparatively, the overall improvement over the SL water reducer ranged from 5% to 10%. In terms of compressive strength, the results are not compared with Zhou's results due to different concrete mix ratios.

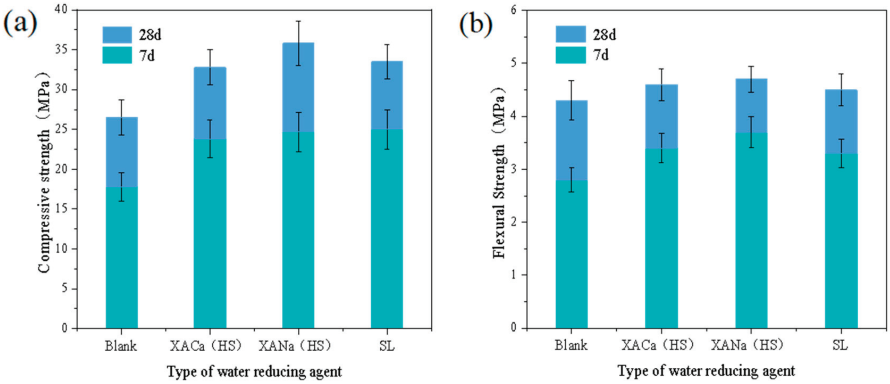

Figure 6. Effect of different reducers on the compressive and flexural strengths: (**a**) compressive strength; (**b**) flexural strength.

The improvement of compressive strength and flexural strength of concrete by three types of water-reducing agents is an inevitable result of the reduction of the water-cement ratio, and the enhancement of compressive strength is more obvious than the enhancement of flexural strength. This is because there are many cracks in the normal microscopic level of the concrete, and this kind of crack is unavoidable and randomly distributed [28]. The damage to concrete is due to the development of cracks, which tend to close instead of developing under compression, while cracks develop under tension, leading to concrete damage. This effect can be significantly improved by adding reinforcement.

3.6. Effect of Various Water Reducers on Air Content and Resistance to Chloride Ion Penetration in Concrete

The entrainment of air in concrete serves as a vital parameter that receives differential evaluation across distinct application contexts. On one side, the deliberate inclusion of gas can subtly augment the flexural strength of concrete and notably enhance its durability. This process, which introduces a myriad of minute air bubbles uniformly distributed at an optimal gas content and suitably spaced, effectively elongates the migration route of chloride ions, thereby establishing a blockade against chloride ion penetration. As a result, the concrete's resistance to chloride ion infiltration is fortified [29,30]. Furthermore, its resilience against freeze–thaw cycles also sees significant improvement. However, on the flip side, the presence of excessive entrapped air can precipitously diminish the concrete's strength and potentially instigate engineering mishaps.

As illustrated in the accompanying Figure 7, the xylonic acid water reducer consistently introduces less air into the concrete compared to the SL group as the admixture level increases. This reduction in air content subsequently leads to a decrease in the resistance to chloride ion penetration during the chloride ion penetration resistance experiments [29,31]. The results are basically consistent with Zhou.

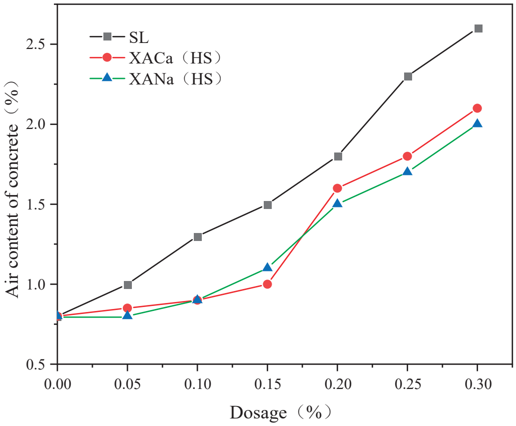

Figure 7. Effect of reducer type and dosage on the air content of concrete.

In the experiment assessing the resistance to chloride ion penetration (Table 6), the rapid chloride migration coefficient method (RCM) was employed. The results indicated that the migration coefficient of xylonic acid, dosed at 0.2%, was significantly lower than that of the control group and slightly lower than that of the SL group. Thus, the xylonic acid water reducer can be considered a viable alternative to SL as a water reducer in environments where a water reducer with a lower chloride ion content is required.

Table 6. Effect of different additives on the air content and D_{RCM} of concrete.

Additive Dosing (%)	Slumps (mm)	W/C	Air Content (%)	D_{RCM} ($\times 10^{-12}$ m^2/s^{-1})
Blank	100	0.60	0.8	20.18
0.1%XACa(HS)	100	0.57	1.2	18.02
0.2%XACa(HS)	100	0.52	1.6	14.71
0.1%XANa(HS)	100	0.57	1.2	17.98
0.2%XANa(HS)	100	0.52	1.6	14.57
0.15%SL	100	0.57	1.5	17.33
0.3%SL	100	0.54	2.6	12.38

3.7. Microscopic Characterization

The intensity of the characteristic peak of calcium hydroxide (CH) in the control group demonstrated similar levels to the 0.2% XANa (HS)-doped samples, while it was significantly higher than that observed in the 0.05% XANa (HS) samples, as indicated by the XRD plots (Figure 8).

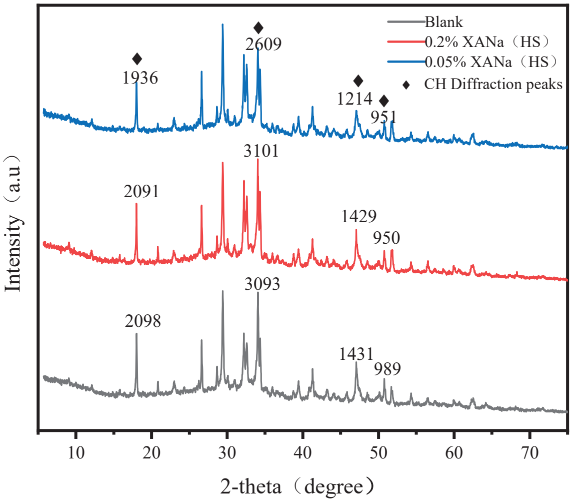

Figure 8. XRD of three dosage XANa(HS).

Electron micrographs further confirmed these findings (Figure 9), revealing increased formation of AFt and CH in the 1-d cement paste with 0.2% XANa (HS) compared to the control group. Conversely, the 1-d cement paste with 0.05% XANa (HS) exhibited considerably less AFt, and no CH formation was observed.

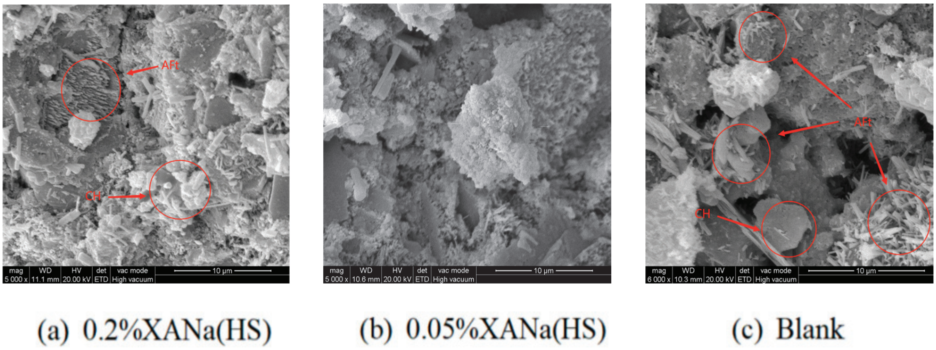

Figure 9. SEM of three dosage XANa(HS): (**a**) 0.2%; (**b**) 0.05%; (**c**) blank.

Based on the micro-level characterization conducted through SEM and XRD analyses, it was determined that the addition of a higher dosage of xylonic acid water reducer accelerated the formation of AFt and CH during the 1-d cement hydration process in comparison to the control group. Conversely, the addition of a lower dosage of xylonic acid water reducer slowed down AFt formation and hindered the formation of CH [32,33]. This effect was attributed to the inhibitory role of the lower xylonic acid dosage on the hydration of C_3S and its binding with Ca^{2+} ions, preventing the formation of CH as a crystalline nucleation agent. In contrast, the higher xylonic acid dosage promoted the initial hydration process of C_3A, accelerating AFt formation and enabling the rapid development of a certain strength within three hours. Additionally, it facilitated the formation of an AFt-phase film on the surface of cement particles. As the AFt-phase film thickened and generated crystallization pressure, it eventually ruptured, leading to the subsequent formation of a new AFt phase in the damaged region. This cyclic process resulted in a denser structure. The early end of the induction period accelerates the formation of CH. Consequently, the cement paste with 0.2% xylonic acid water reducer exhibited higher compressive strength compared to the control group, despite having the same water-cement ratio. Conversely, the lower dosage of xylonic acid delayed AFt formation and interacted with Ca^{2+} ions in the CSH gel [34], preventing their aggregation and retarding CSH growth, thereby requiring more than 600 min to achieve initial setting.

According to Figure 10 (based on the Pellenq model [35]), carboxyl and hydroxyl groups exhibit a propensity to chemically adsorb to the Si-O bonds present on the surface of cement particles [34,36]. Additionally, hydrophilic groups combine with water molecules [33–35], resulting in cement particles and water sharing similar groups. This interaction between identical groups provides a lubricating effect among cement particles, while the hydrophilic end of the xylonic acid molecule interacts with water, reducing surface tension [37–39]. Consequently, water molecules diffuse and disperse more effectively in the concrete mixture, improving the fluidity of the cement slurry and acting as a water-reducing agent.

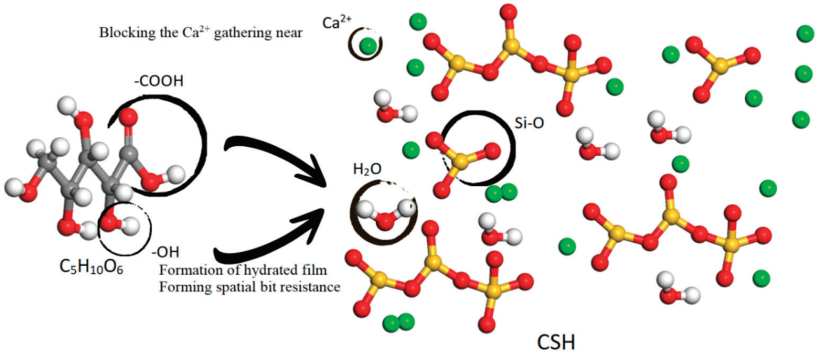

Figure 10. Schematic diagram of the water reduction and retarding mechanism.

4. Conclusions

In the present investigation, four variants of xylonic acid-based water-reducing agents—XACa (PX), XACa (HS), XANa (PX), and XANa (HS)—were synthesized leveraging whole-cell catalysis of Gluconobacter oxydans, employing pure xylose and hemicellulose hydrolysate as substrates. The main conclusions obtained can be summarized as follows:

(1) Findings demonstrated that these xylonic acid water-reducing agents delivered a water reduction efficiency in the range of 14% to 16% when the dosage approximated 0.2%. Experiments determining the initial and final setting times of cement paste demonstrated that XA manifested a significant retarding influence at doses below 0.15%, peaking at 0.10%. It extended the initial setting time by 76% and the final setting time by 136% relative to the control group. However, at dosages of 0.2% and beyond, it demonstrated a minor acceleration effect.

(2) In tests assessing the mechanical properties of mortar, the XA(HS) group exhibited superior compressive strength compared to the XA(PX) group at equivalent dosages. Moreover, the XA(HS) group exhibited commendable performance in compressive and flexural, air-entrainment, and chloride ion penetration resistance experiments, showcasing performance akin to SL.

(3) The adsorption of the carboxyl and hydroxyl groups in xylonic acid onto the Si-O bonds on the cement particle surface escalated the fluidity of the cement paste.

Moreover, the chemisorption of hydroxyl and carboxyl groups with the Si-O bonds on the cement particle surface provided water-reducing functionality, thereby influencing the formation of CSH and delaying the setting process.

(4) The XA(HS) group demonstrated significant water-reducing effects, the capacity to regulate setting time, and satisfactory outcomes in mechanical durability tests, thus indicating its potential to supplant lignosulfonate-based water-reducing agents.

Given that the experiments conducted in this article are very limited, more application experiments are needed in the future to verify the practical application feasibility of XA water-reducing agent, such as the dry shrinkage of concrete after addition and its compatibility with steel bars or steel fiber composite materials.

Author Contributions: Conceptualization, K.H.; Methodology, K.H.; Software, J.H. and Y.X.; Investigation, F.H.; Resources, J.H. and Y.W.; Writing—original draft, F.H.; Supervision, Y.W. and Y.X. All authors have read and agreed to the published version of the manuscript.

Funding: This research received no external funding.

Data Availability Statement: Data are contained within the article.

Conflicts of Interest: The authors declare no conflict of interest.

References

1. Şahin, H.G.; Mardani, A.; Özen, S.; Emin, A. Utilization of high-range water reducing admixture having air-entraining agents in cementitious systems. *J. Build. Eng.* **2023**, *64*, 105565. [CrossRef]
2. Lokesh, G.; Nantha Kumar, P.; Aishwarya, N.; Parthiban, P.; Ponshanmugakumar, A. Experimental study of the effect of water reducing admixtures on concrete. *Mater. Today Proc.* 2023, *in press*. [CrossRef]
3. Karakuzu, K.; Kobya, V.; Mardani-Aghabaglou, A.; Felekolu, B.; Ramyar, K. Adsorption properties of polycarboxylate ether-based high range water reducing admixture on cementitious systems: A review. *Constr. Build. Mater.* **2021**, *312*, 125366. [CrossRef]
4. Liu, Y.; Li, H.; Wang, K.; Wu, H.; Cui, B. Effects of accelerator–water reducer admixture on performance of cemented paste backfill. *Constr. Build. Mater.* **2020**, *242*, 118187. [CrossRef]
5. Johnson, A.T.; Sosa, D.; Arredondo, R.; Li, H.; Yuan, Z.; Xu, C. Production of Bio-based Concrete Water Reducers from Renewable Resources—A Review. *Biofuels Bioprod. Biorefin.* **2023**, *17*, 1425–1444. [CrossRef]
6. Topçu, İ.B.; Ateşin, Ö. Effect of high dosage lignosulphonate and naphthalene sulphonate based plasticizer usage on micro concrete properties. *Constr. Build. Mater.* **2016**, *120*, 189–197. [CrossRef]
7. Ruviaro, A.S.; Dos Santos Lima, G.T.; Silvestro, L.; Barraza, M.T.; Rocha, J.C.; De Brito, J.; Gleize, P.J.P.; Pelisser, F. Characterization and investigation of the use of oat husk ash as supplementary cementitious material as partial replacement of Portland cement: Analysis of fresh and hardened properties and environmental assessment. *Constr. Build. Mater.* **2023**, *363*, 129762. [CrossRef]
8. Badgujar, K.C.; Bhanage, B.M. Factors governing dissolution process of lignocellulosic biomass in ionic liquid: Current status, overview and challenges. *Bioresour. Technol.* **2015**, *178*, 2–18. [CrossRef]
9. Cao, F.; Qiao, H.; Li, Y.; Shu, X.; Cui, L. Effect of highland barley straw ash admixture on properties and microstructure of concrete. *Constr. Build. Mater.* **2022**, *315*, 125802. [CrossRef]
10. Maimaiti, H.; Aerken, X. The structure and properties of sulfo-butylated celluluse ether (SBC) based water-reducing agents. *Appl. Mech. Mater.* **2014**, *556*, 433–440. [CrossRef]
11. Kurbanjian, R.; Maliya, M. Performance of sulfonated cellulose based water-reducing agent for cement. *Hunningtu(Concrete)* **2012**, 74–76.
12. Zhou, X.; Zhou, X.; Tang, X.; Xu, Y. Process for calcium xylonate production as a concrete admixture derived from in-situ fermentation of wheat straw pre-hydrolysate. *Bioresour. Technol.* **2018**, *261*, 288–293. [CrossRef] [PubMed]
13. Zhu, Z.; Huang, R.; Yao, S.; Liu, Y.; Zhang, Q.; Zhou, X.; Jiang, K. An integrated process for co-producing fermentable sugars and xylonate from sugarcane bagasse based on xylonic acid assisted pretreatment. *Bioresour. Technol.* **2023**, *369*, 128464. [CrossRef]
14. Hou, W.; Bao, J. Evaluation of cement retarding performance of cellulosic sugar acids. *Constr. Build. Mater.* **2019**, *202*, 522–527. [CrossRef]
15. Zhang, H.; Han, X.; Wei, C.; Bao, J. Oxidative production of xylonic acid using xylose in distillation stillage of cellulosic ethanol fermentation broth by Gluconobacter oxydans. *Bioresour. Technol.* **2017**, *224*, 573–580. [CrossRef]
16. Han, J.; Hua, X.; Zhou, X.; Xu, B.; Wang, H.; Huang, G.; Xu, Y. A cost-practical cell-recycling process for xylonic acid bioproduction from acidic lignocellulosic hydrolysate with whole-cell catalysis of Gluconobacter oxydans. *Bioresour. Technol.* **2021**, *333*, 125157. [CrossRef]
17. Han, J.; Han, F.; Wang, J.; Wei, Y.; Kuznetsov, B.N.; Xu, Y. In-situ sodium percarbonate assisting and intensifying the aerobic whole-cell catalysis and bio-oxidation of lignocellulosic xylose, glucose and glycerol. *Ind. Crops Prod.* **2023**, *195*, 116482. [CrossRef]

18. Magina, S.; Barros-Timmons, A.; Evtuguin, D.V. Synthesis of Lignosulfonate-Based Dispersants for Application in Concrete Formulations. *Materials* **2021**, *14*, 7388. [CrossRef]
19. Ouyang, X.; Ke, L.; Qiu, X.; Guo, Y.; Pang, Y. Sulfonation of Alkali Lignin and Its Potential Use in Dispersant for Cement. *J. Dispers. Sci. Technol.* **2009**, *30*, 1–6. [CrossRef]
20. Aro, T.; Fatehi, P. Production and Application of Lignosulfonates and Sulfonated Lignin. *ChemSusChem* **2017**, *10*, 1861–1877. [CrossRef]
21. Breilly, D.; Fadlallah, S.; Froidevaux, V.; Colas, A.; Allais, F. Origin and industrial applications of lignosulfonates with a focus on their use as superplasticizers in concrete. *Constr. Build. Mater.* **2021**, *301*, 124065. [CrossRef]
22. *GB 1346-2001*; Standard Consistency of Cement Water Consumption, Setting Time, Stability Test Methods. China Construction Industry Press: Shanghai, China, 2001.
23. 23. *JGJ/T 70-2009*; Basic Experimental Performance Standards for Construction Mortar. China Construction Industry Press: Beijing, China, 2009.
24. *GB 50204-2015*; Code for Quality Acceptance of Concrete Structural Construction. China Construction Industry Press: Shanghai, China, 2015.
25. *GB 50203-2011*; Masonry Structural Engineering Construction Quality Acceptance Specification. China Construction Industry Press: Beijing, China, 2011.
26. *GB/T 50082-2009*; Standard Test Method for Long-Term Performance and Durability of Ordinary Concrete. China Construction Industry Press: Beijing, China, 2009.
27. Bishop, M.; Barron, A.R. Cement Hydration Inhibition with Sucrose, Tartaric Acid, and Lignosulfonate: Analytical and Spectroscopic Study. *Ind. Eng. Chem. Res.* **2006**, *45*, 7042–7049. [CrossRef]
28. El Afandi, M.; Yehia, S.; Landolsi, T.; Qaddoumi, N.; Elchalakani, M. Concrete-to-concrete bond Strength: A review. *Constr. Build. Mater.* **2023**, *363*, 129820. [CrossRef]
29. Shi, X.; Xie, N.; Fortune, K.; Gong, J. Durability of steel reinforced concrete in chloride environments: An overview. *Constr. Build. Mater.* **2012**, *30*, 125–138. [CrossRef]
30. Angst, U.; Elsener, B.; Larsen, C.K.; Vennesland, Ø. Critical chloride content in reinforced concrete—A review. *Cem. Concr. Res.* **2009**, *39*, 1122–1138. [CrossRef]
31. Mao, J.; Liu, Y.; Xu, J.; Wang, Q.; Lou, Y. Desorption behavior and mechanism of chloride ions in fresh concrete mixtures under electromigration. *Constr. Build. Mater.* **2023**, *362*, 129680. [CrossRef]
32. Goyal, R.; Verma, V.K.; Singh, N.B. Hydration of Portland slag cement in the presence of nano silica. *Constr. Build. Mater.* **2023**, *394*, 132173. [CrossRef]
33. Chen, L.; Jiang, L.; Jin, W.; Guo, M.-Z.; Niu, Y.; Chu, H.; Song, Z. Effect of citrate retarders on the expansion property and hydration behavior of light-burned magnesia cement-based materials. *J. Build. Eng.* **2022**, *61*, 105265. [CrossRef]
34. Neubauer, J.; Pöllmann, H. Alinite—Chemical composition, solid solution and hydration behaviour. *Cem. Concr. Res.* **1994**, *24*, 1413–1422. [CrossRef]
35. Petersen, T.; Valdenaire, P.-L.; Pellenq, R.; Ulm, F.-J. A reaction model for cement solidification: Evolving the C–S–H packing density at the micrometer-scale. *J. Mech. Phys. Solids* **2018**, *118*, 58–73. [CrossRef]
36. Klyusov, A.A. $3CaO \cdot SiO_2$ hydration under decreased temperatures. *Cem. Concr. Res.* **1994**, *24*, 127–132. [CrossRef]
37. Zhou, L.; Jiang, Y.; Wang, J.; Shao, Z.; Luo, Y.; Qian, B.; Li, Y.; Zang, J.; Wang, H.; Ma, B.; et al. Effect of steel slag on pores and strength of fly-ash-based adsorbent geopolymers. *Proc. Inst. Civ. Eng.-Eng. Sustain.* **2023**, 1–11. [CrossRef]
38. Wang, J.; Xiong, Y.; Li, Q.; Jin, D.; Hu, Y.; Che, T. Experimental investigation on the preparation and surface treatment of biomass fibers for stone mastic asphalt mixtures modification. *Constr. Build. Mater.* **2023**, *408*, 133667. [CrossRef]
39. Wang, Q.D.; Shi, S.C.; Yao, Y.; Wang, Z.Q.; Fu, Z.Q. Effective Notch-Stress-Based Stress Concentration Factors of the Rib–Deck Weld in Orthotropic Steel Decks Considering the Effect of Asphalt Surfacing. *Materials* **2023**, *16*, 6760. [CrossRef] [PubMed]

materials

MDPI

Article

Strengthening Cracked Steel Plates with Shape Memory Alloy Patches: Numerical and Experimental Investigations

Zhiqiang Wang [1], Libin Wang [1,2], Qiudong Wang [1,*], Bohai Ji [3], Jie Liu [1] and Yue Yao [4]

[1] College of Civil Engineering, Nanjing Forestry University, Nanjing 210037, China; wzq010302@163.com (Z.W.); jhwlb@163.com (L.W.); jieliu@outlook.com (J.L.)
[2] Faculty of Architecture and Civil Engineering, Huaiyin Institute of Technology, Huai'an 223001, China
[3] College of Civil and Transportation Engineering, Hohai University, Nanjing 210098, China; bhji@hhu.edu.cn
[4] College of Construction Engineering, Jiangsu Open University, Nanjing 210000, China; jsouyaoyue@163.com
* Correspondence: qdwang@njfu.edu.cn

Abstract: To investigate the retarding effect of bonding the shape memory alloy (SMA) patches on crack propagation in steel plates, both numerical and experimental analyses were conducted in the present study. A compact tension (CT) model was developed to clarify the feasibility of bonding the SMA patch to the reinforcement of the mode I, mode II, and mode III cracks. On this basis, parametric analysis was conducted to investigate the strengthening parameters, i.e., the bonding area, the thickness, and the strengthening angle of the SMA patch. Subsequently, fatigue tests on the unreinforced steel plate and cracked steel plate strengthened by the SMA patches were conducted. The monitored stress variation, crack propagation behavior, and fatigue fracture surfaces were analyzed. Findings are meaningful to the application of the SMA reinforcement method in practical engineering.

Keywords: steel plate; fatigue crack; strengthening; SMA; fatigue life

1. Introduction

Steel structures (e.g., marine steel structures and steel bridges) are easily subjected to fatigue cracking under cyclic dynamic loading [1]. Fatigue cracks are permanent damage to steel members, which significantly threaten the durability, service performance, and safety of steel structures [2]. It is necessary to take effective measures to strengthen or repair the cracked steel components once the crack has been detected.

Many strengthening measures have been developed to retard the crack propagation in steel structures, such as drilling stop-hole [3,4], hammer peening [5,6], attaching additional steel patches [7], etc. In bridge engineering, bonded/bolted steel plate reinforcement and bonded carbon/glass fiber reinforced polymer (CFRP/GFRP) reinforcement have been widely used [8–11]. In terms of the strengthening methods by attaching additional elements, the theoretical basis of these solutions is that a second load path could be obtained by the additional elements attached to the cracked steel components. Subsequently, the load transferred by the cracked steel component could be considerably reduced, thus reducing the stress intensity factor (SIF) at the crack tip and retarding the crack propagation. On this basis, it is obvious that the crack propagation rate would be further reduced if the prestress was applied to the attached element. Furthermore, it has already been proved that a complete crack arrest could be achieved in the presence of the introduction of an adequately high level of prestressing.

However, cracked steel components are usually relatively small, and it is rather difficult to conduct the prestressing process of attached elements (e.g., fiber-reinforced polymer (FRP) plates). In recent years, the investigation and application of shape memory alloys (SMA) in civil engineering have raised great concern [12,13]. In contrast to the traditional strengthening method (e.g., attaching the steel or FRP elements), the prestressing

Citation: Wang, Z.; Wang, L.; Wang, Q.; Ji, B.; Liu, J.; Yao, Y. Strengthening Cracked Steel Plates with Shape Memory Alloy Patches: Numerical and Experimental Investigations. *Materials* **2023**, *16*, 7259. https://doi.org/10.3390/ma16237259

Academic Editor: Alessandro Pirondi

Received: 30 October 2023
Revised: 14 November 2023
Accepted: 20 November 2023
Published: 21 November 2023

effect could be achieved by taking advantage of the SMA materials. The SMA material has a unique thermomechanical response in which deformed SMA patches can return to their original geometry after thermal activation [14]. Once the deformed SMA element (before thermal activation) is attached to the cracked component, the prestress, induced by the recovery forces after thermal activation, could be applied to the cracked component; thus, the crack could be retarded or even arrested by the prestressing effect of the SMA element [15].

Some investigations have been conducted to investigate the performance of cracked components reinforced by the SMA materials. Wang et al. [16] conducted fatigue tests on cracked steel plates strengthened by CFRP and iron-based SMA (Fe-SMA) strips, revealing that the bonded prestressed Fe-SMA strips are much more effective than CFRP strips, extending the fatigue crack growth life by a factor of 3.51. Izadi et al. [17] revealed that a prestressing level within the range of 330–410 MPa could be achieved, resulting in compressive stresses within the range of 35–72 MPa in the cracked steel plates. Results also demonstrated that considerable compressive stresses could be applied to the cracked steel plate, reducing the tensile stresses and SIFs at the crack tip, subsequently resulting in a significant decrease in the crack propagation and a complete crack arrest in some cases. Chen et al. [18] investigated the durability of steel structures strengthened by Fe-SMAs when subjected to harsh service conditions via fatigue tests. Wang et al. [19] investigated the behavior of the Fe-SMA-to-steel bonded joints through lap-shear tests, revealing that no debonding or degradation was observed for the adhesively bonded Fe-SMA-strengthened specimen and demonstrating the reliable performance of the strengthening solution under service loads. Vujtech et al. [20] conducted an application of an iron-based SMA (Fe-SMA) for the prestressed strengthening of a bridge, revealing that the recovery stress of the Fe-SMA strips resulted in a compressive stress of approximately -33 MPa in the lower flange of the bridge girder. Additionally, the long-time monitoring showed that the main loss of the prestressing force caused by relaxation occurred within the first 30 days after activation and was approximately 20% of the original prestress. Li et al. [21] conducted a systematic study on the static behavior of adhesively-bonded Fe-SMA-to-steel joints in applications adopting iron-based Shape Memory Alloys (SMAs).

At the same time, CFRP/SMA composite patches have been proposed to improve the reinforcement effect on cracked components further. For instance, Qiang et al. [22] proposed to repair the fatigue crack at the diaphragm arc-shape cutout by employing SMA/CFRP composite patches, indicating that the fatigue notch factor was reduced by 30.76% after bonding SMA/CFRP composite patches, and the initiation and propagation of fatigue cracks could be effectively postponed. Fatigue tests conducted by Deng et al. [23] indicated that the crack propagation rate could be considerably reduced by applying the SMA/CFRP composite strengthening, and the load capacity and stiffness of notched steel beams could be significantly improved. Kean et al. [24] performed a numerical study of the fatigue life of SMA/CFRP patches retrofitted to central-cracked steel plates, indicating that the increase in the Young's modulus, prestress level, and width could significantly improve the fatigue life of central-notched steel plates. Similar investigations have also been reported [25,26].

In general, some investigations have been conducted, focusing on the fatigue performance of cracked steel components strengthened by the SMA patches or the SMA/FRP composited layers. The retarding effect of attaching SMA elements on cracked steel components is proved. However, the mode I crack condition is considered in most of the investigations, while fewer investigations have focused on the retarding effect on different cracking types, which is the focus of the present study. In terms of the experimental investigations, the crack propagation behavior and the fatigue life before and after strengthening are the main focus. However, the stress variation in the SMA and reinforced steel component and the fatigue fracture surfaces of the reinforced steel plates were not clear.

In this study, numerical and experimental investigations were performed to illustrate the performance of cracked steel plates strengthened by Fe-SMA patches. CT models were first developed to clarify the retarding effect on different types of fatigue cracks. On this basis, parametric analyses were conducted to investigate the effects of strengthening area, thickness, and position of the Fe-SMA patch and the strengthening angle. Finally, fatigue tests were conducted to investigate the stress variation, crack propagation, and fatigue failure characteristics of cracked steel plates strengthened by the Fe-SMA patches.

2. CT Model-Based Feasibility Analysis

2.1. Finite Element Model

The fatigue crack could be divided into three basic types: mode I cracks subjected to in-plane tension, mode II cracks subjected to in-plane shear, and mode III cracks subjected to out-plane shear. Under different loading conditions, the SIF at the crack tip could be adopted to identify the mode I, mode II, and mode III cracks, namely labeled K_{I}, K_{II}, and K_{III}. To investigate the feasibility of attaching Fe-SMA reinforcement to different cracking types, the CT model recommended by the American Society for Testing and Materials (ASTM) was developed by ABAQUS 6.14 Documentation (Dassault Systemes Simulia Corp, Providence, RI, USA) since the basic three types of fatigue cracks could be easily simulated. The extended finite element method (XFEM) embedded in ABAQUS was employed to obtain the SIF at the crack tip. A mesh size of 5 mm was employed to model the CT model, and the Fe-SMA patch was modeled with a mesh size of 2 mm [27]. The element type of C3D8R, including 8 Gaussian integral points with a size of 0.5 mm, was used to deal with the stress concentration at the crack tip, considering the accuracy and efficiency of the calculation. The geometric sizes of the CT model are plotted in Figure 1. The thickness of the CT model was set to 5 mm. The crack was simplified to be a rectangle with a length of 50 mm.

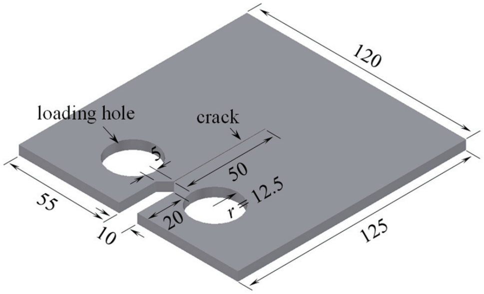

Figure 1. Schematic view of the CT model (unit: mm).

Steel and Fe-SMA are usually strain-hardening materials; thus, elastic/plastic properties should be considered in practical engineering. However, in this section, the CT model was considered to be in a linear elastic state, and the steel and Fe-SMA were simply assigned a linear elastic constitutive relation. The elastic modulus and Poisson's ratio of the steel were set to be 2.06×10^5 MPa and 0.3, and values of the Fe-SMA patch were set to be 1.70×10^5 MPa and 0.36, respectively. It is difficult to simulate the thermal activation process of the Fe-SMA patch using finite element (FE) modeling. As an alternative method, the prestressing level of the Fe-SMA patch was modeled by introducing a predefined stress field in the initial step. The predefined stress field was then redistributed in the subsequent load step in ABAQUS, leading to the compressive stress in the strengthened component and a prestressing loss in the Fe-SMA patch owing to the contraction of the strengthened component. For more details regarding the modeling of the prestressing level of the SMA patch, please refer to [27]. In the present study, a prestress level of 0.075 MPa was employed for qualitative analysis.

2.2. Simulation of Different Fatigue Types

To simulate the mode I crack, the uniform area loads with a magnitude of 10 MPa were applied at the upper and lower semicircular surfaces of the loading hole (see Figure 2a). The same loads were applied at the left and right semicircular surfaces to simulate the mode II crack. At the same time, in terms of the CT model simulating the modes I and II cracks, the displacement of nodes at the top and bottom surfaces was fixed at the thickness direction to avoid the bulking effect. To simulate the mode III crack, the loading hole was not simulated, and a uniform area load of 0.4 MPa was applied at the corresponding surface (see Figure 2a). Additionally, nodes at the right end of the model were fixed. Based on the J integral and XFEM, the SIF corresponding to the mode I, mode II, and mode III cracks could be calculated. Since the crack was simplified to be a rectangle penetrating along the thickness direction of the CT model, the SIF at the middle point of the crack front was extracted, as plotted in Figure 2b. For the mode I crack, the value of SIF K_{I} was calculated to be 390 MPa·mm$^{1/2}$, while the values of SIF K_{II} and K_{III} could be neglected. For the mode II crack, the value of SIF K_{II} was calculated to be 124 MPa·mm$^{1/2}$, while the values of SIF K_{I} and K_{III} could be neglected. Similarly, the value of SIF K_{III} was calculated to be 108 MPa·mm$^{1/2}$ for the mode III crack, while the values of SIF K_{I} and K_{II} could be neglected. The results indicate that the mode I, mode II, and mode III cracks could be well simulated by the developed CT models.

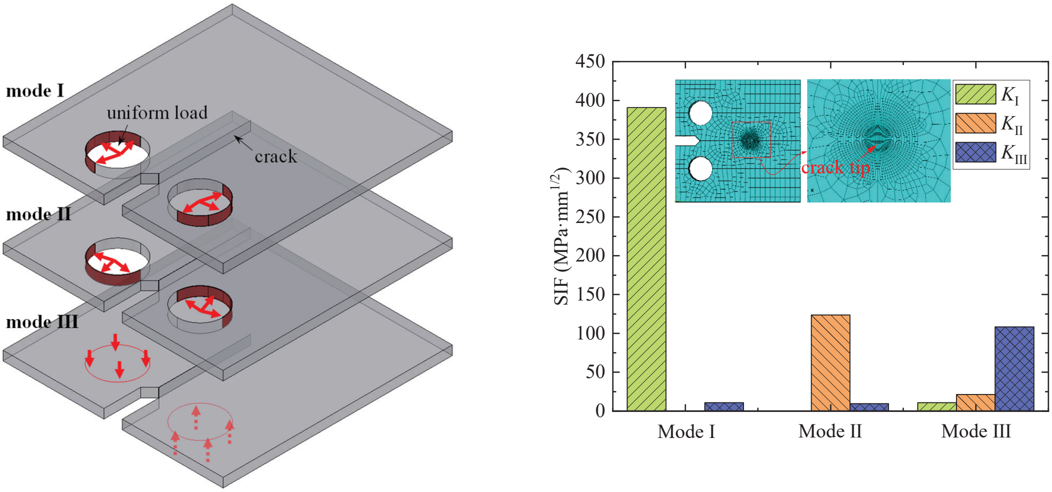

(**a**) (**b**)

Figure 2. CT model and numerical results of the SIFs corresponding to the modes I, II, and III cracks. (**a**) CT model simulating the modes I, II, and III crack. (**b**) SIFs corresponding to the modes I, II, and III cracks.

2.3. Variation in the SIFs

To investigate the retarding effect of attaching the Fe-SMA patch on the mode I, mode II, and mode III cracks, the CT model strengthened by the Fe-SMA patch was simulated. For the feasibility analysis, the geometric size of the Fe-SMA patch was set to be 30 × 55 × 0.5 mm, as shown in Figure 3a. The influence of the geometry of the Fe-SMA patch was to be discussed in the following Section 3. The SIFs corresponding to the CT model and the CT model strengthened by the Fe-SMA patch were compared, as plotted in Figure 3b. The SIF corresponding to the CT model strengthened by the steel patch was also added for comparison. The geometry of the steel patch was the same as the Fe-SMA patch, and the elastic modulus and Poisson's ratio were the same as the material properties of the CT model. It can be seen from Figure 3b that, after bonding the steel and Fe-SMA patch, the SIF decreased by 12.1% and 37.3%, respectively. It indicates that attaching the Fe-SMA patch has a better reinforcement effect than attaching the steel patch. Regarding the mode II and mode III crack, the SIF has only decreased by 9.2% and 10.2%, respectively. It indicates that other strengthening methods should be taken for retarding the propagation of mode II and mode III crack instead of attaching the Fe-SMA patch.

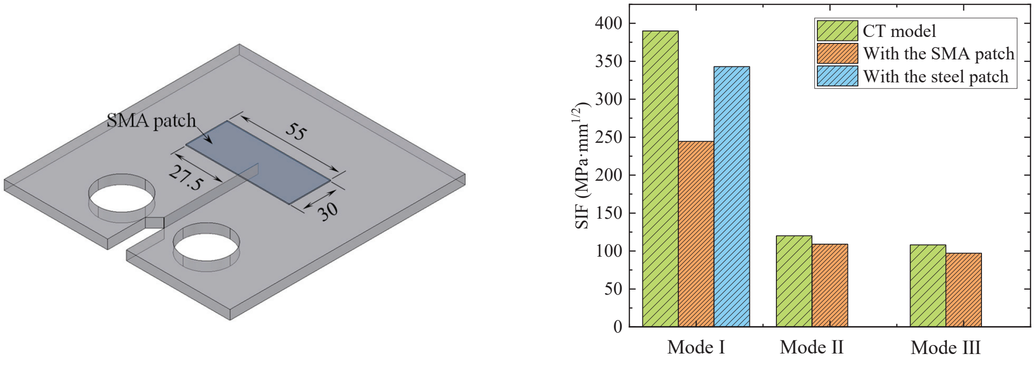

(**a**) (**b**)

Figure 3. Comparison of the values of K_I corresponding to the CT model, CT model strengthened by the Fe-SMA patch, and CT model strengthened by the steel patch. (**a**) CT model strengthened by the Fe-SMA patch. (**b**) Comparison of the values of K_I.

3. Parametric Analyses on the Strengthening Method

3.1. Effect of the Bonding Area

In practical engineering, it is difficult to bolt the small-sized Fe-SMA patch to the cracked component. Alternatively, the Fe-SMA patch could be bonded to the cracked component using a cementing compound, such as that employed in the present study. In this case, the strengthening effect might be affected by the bonding area (as illustrated in Figure 4a). To investigate the effect of the bonding area, half of the length of the bonding area along the lengthwise direction of the Fe-SMA patch (labeled x) was set to be 5.5 (1/10 of the length of the Fe-SMA patch), 11.0, 16.5, 22.0, and 27.5 mm (half of the length of the Fe-SMA patch), respectively. The width of the bonding area was the same as that of the Fe-SMA patch. The mode I crack was simulated, and the results were plotted in Figure 4b. The value of the SIF K_I decreased from 305.3 to 298.5 MPa·mm$^{1/2}$ as the value of x increased from 5.5 to 22.0 mm. The smallest value of the SIF K_I (257.6 MPa·mm$^{1/2}$) was obtained when the Fe-SMA patch was completely bonded to the CT model (i.e., x = 27.5 mm). However, in terms of the experimental investigations, it is not suggested that the Fe-SMA patch be completely bonded to the cracked component. The reason is that the bonding property of the bonding layer within the thermally activated region might be affected by the high activation temperature; however, it is difficult to quantify such an effect. To eliminate the influence of uncertain factors on the experimental results, a limited area of the Fe-SMA patch was bonded to the cracked component in the present study, as to be introduced in the following Section 4.

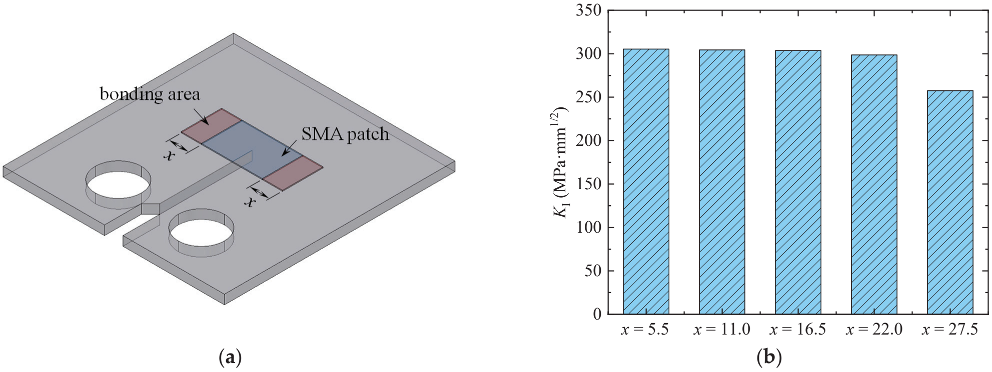

(**a**) (**b**)

Figure 4. Variation in the SIFs in the presence of different bonding areas. (**a**) Illustration for the bonding area. (**b**) Variation in the SIFs.

3.2. Effect of the Thickness of the SMA Patch

The prestressing force could be generated by the thermomechanical response of the Fe-SMA patch. To investigate the effect of the thickness of the Fe-SMA patch on the retarding effect, the thickness was set to be 0.5, 1.0, and 1.5 mm, respectively. The mode I crack was simulated, and the results were plotted in Figure 5. It could be seen that the value of the SIF K_I decreased from 305.3 to 161.1 MPa·mm$^{1/2}$ while the thickness of the Fe-SMA patch increased from 0.5 to 1.5 mm. It can be concluded that the thicker the Fe-SMA patch, the greater the prestressing force.

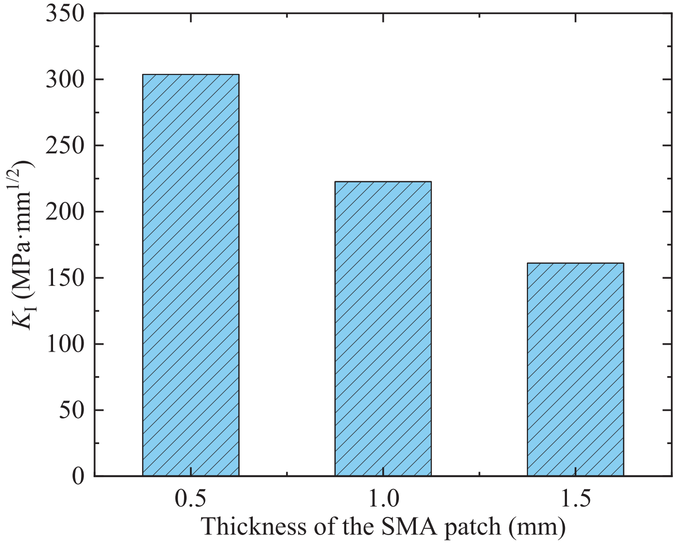

Figure 5. Variation in the SIFs in the presence of different thicknesses of the SMA patch.

3.3. Effect of the Strengthening Angle

Due to the possible manual error during the bonding process, the lengthwise direction of the Fe-SMA patch may not be perpendicular to the crack propagation direction. To clarify such an effect, the strengthening angle (as illustrated in Figure 6a) was set to be 0°, 15°, 30°, and 45°, and the numerical results were plotted in Figure 6b. Similarly, the mode I crack was also simulated here. It could be seen that the SIF K_I increased from 305.3 to 351.5 MPa·mm$^{1/2}$ while the strengthening angle (θ) varied from 0° to 45°. The results are readily comprehensible as a horizontal component of the prestressing force (parallel to the crack propagation direction) will be generated once the strengthening angle is greater than zero. Nevertheless, the SIF K_I has increased by merely 1.7% (increased from 305.3 to 310.4 MPa·mm$^{1/2}$) while the strengthening angle (θ) varies from 0° to 15°. Therefore, it is acceptable that the bonded Fe-SMA patch is not strictly perpendicular to the crack propagation direction in practical engineering.

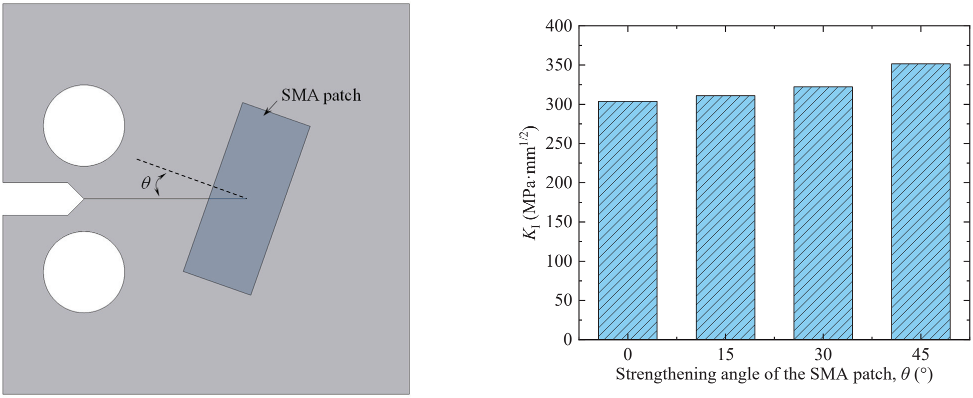

(**a**) (**b**)

Figure 6. Variation in the SIFs in the presence of different strengthening angles. (**a**) Illustration for the strengthening angle. (**b**) Variation in the SIFs.

4. Experimental Investigations

4.1. Specimens and Fe-SMA Patches

A series of fatigue tests on unreinforced and reinforced steel plates with artificial cracks was performed to investigate the efficiency of retarding the fatigue crack propagation by bonding the Fe-SMA patches. Three specimens were included in the fatigue tests: a bare steel plate was tested to obtain the reference data of the crack propagation behavior of the steel plate, labeled SP-1; two cracked specimens were strengthened by the prestrained Fe-SMA patches to obtain the data of crack propagation behavior after strengthening, labeled SP-2 and SP-3. The bare steel plates were manufactured by the China Railway Baoqiao (Yangzhou, China) Co., Ltd., and the Fe-SMA patches were manufactured by Suzhou Haichuan Rare Metal Products Co., Ltd. (Suzhou, China). The material properties of the steel and Fe-SMA were listed in Tables 1 and 2, respectively. Notably, the material Q345qD possesses the same properties and composition as ASTM A572 [28] Gr 50 steel. The main geometric sizes of the steel plate and Fe-SMA patch are presented in Figure 7. The thickness of the steel plate and Fe-SMA patch were 14 and 3 mm, respectively.

Table 1. Mechanical properties and chemical composition of the Q345qD material.

Elastic Modulus (MPa)	Yield Strength (MPa)	Ultimate Tensile Strength (MPa)	Chemical Composition (%)				
			C	Si	Mn	P	S
2.1 × 105	345	490	0.14	0.31	1.46	0.016	0.006

To generate a fatigue crack at the objective position of the steel plate, each steel plate was cut first to induce a crack in the middle (see Figure 7a), and the crack length was 120 mm. Subsequently, the steel plate with an artificial crack was pre-tested under cyclic fatigue loading to generate real fatigue cracks at both ends of the artificial crack. During this stage, two strain gauges were arranged at both sides of the artificial crack, 5 mm away from the crack tip, to monitor the initial crack propagation. Once the strain gauge was broken, indicating that the fatigue crack had propagated below the strain gauge, the crack length was measured every five minutes. Once the fatigue crack at one side had propagated to 15 mm, the pre-test was stopped. Then, two cracked steel plates were strengthened by the deformed SMA patches at both sides of the fatigue cracks. In the present study, since the steel plate with artificial crack, fatigue load, and boundary conditions were symmetric, the propagation of fatigue cracks at two tips of the artificial crack was almost the same during the pre-testing process. When the fatigue crack at one side has propagated to 15 mm, the fatigue crack at the other side has commonly propagated to a length between 14 and 15 mm. In general, the total length of the fatigue crack after pre-testing was about 150 mm.

Table 2. Mechanical properties and chemical composition of the Fe-SMA material.

Elastic Modulus (MPa)	Yield Strength (MPa)	Ultimate Tensile Strength (MPa)	Chemical Composition (%)						
			Cr	C	V	Si	Mn	Ni	S
1.73 × 105	546	1015	8	≤0.4	≤4	5	15	5	0.006

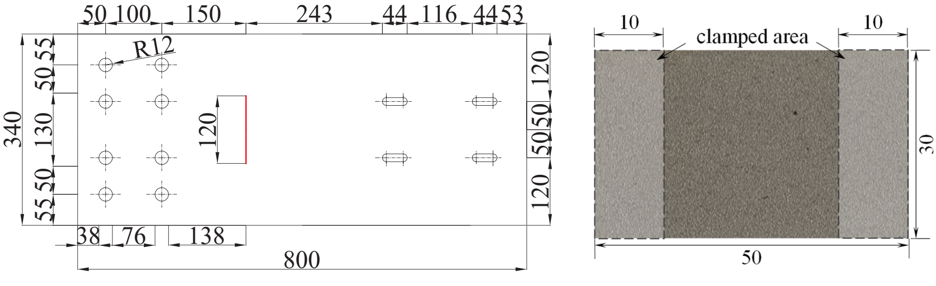

(**a**) (**b**)

Figure 7. Geometric sizes of the specimen and Fe-SMA patch (unit: mm). (**a**) Tested specimen. (**b**) Fe-SMA patch.

Before being adopted for strengthening, the undeformed Fe-SMA patches were annealed to obtain the best shape memory effect: the Fe-SMA patches were heated at 900 °C for 20 min, then removed and naturally cooled to room temperature. The prestressing force (i.e., the recovery force) is related to the prestrain of the Fe-SMA patch. Before bonding to the cracked steel plate, the Fe-SMA patches were prestrained to a strain of 5% and then unloaded to a free-stress state at room temperature. The clamped area of the Fe-SMA patches is shown in Figure 7b. The clamped area was fixed to the anchorage, and the rest part (i.e., 30 mm in the lengthwise direction) was stretched to 31.5 mm in this study.

4.2. Activation of the Fe-SMA Patch

Regarding the specimens labeled SP-2 and SP-2, the prestrained Fe-SMA patches were adhesively bonded to the cracked steel plate. Notably, only the clamped area (see Figure 7b) was bonded to the steel plate, while the deformed area remained unbonded. A two-part epoxy adhesive (typed Ergo 1309) was adopted to bond the Fe-SMA patch to the cracked steel plate. During the fatigue loading, no debonding failure of the adhesive layer was detected, indicating that this type of two-part epoxy adhesive could be adopted for experimental investigation.

After strengthening, a ceramic heating element (produced by Shanghai Yidu Electronics Co., Ltd., Shanghai, China) was adopted to activate the prestrained Fe-SMA patches, as shown in Figure 8. The maximum temperature heated by the ceramic heating element is

250 °C. The temperature along the Fe-SMA patch was monitored by a contact temperature detector (typed TM902C) (see Figure 8). As soon as the temperature in the Fe-SMA patch reached the available activation temperature of 250 °C, the electric current was cut off, and the thermal-activated Fe-SMA patch was naturally cooled down to room temperature.

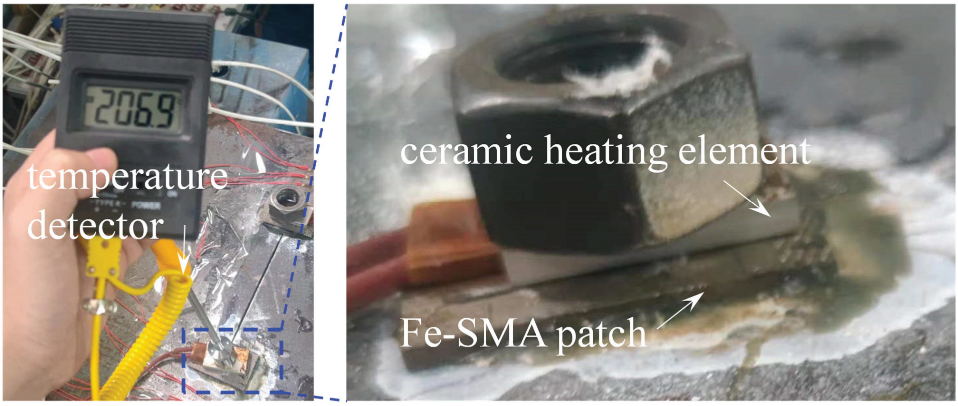

Figure 8. Thermal activation of the prestrained Fe-SMA patch.

Before thermal activation, a strain gauge (typed 120-3AA) was arranged at the surface of the Fe-SMA patch to monitor the variation in strain during the heating process, and the monitored strain data were plotted in Figure 9. It can be seen that considerable compressive strain was induced during thermal activation, and the maximum compressive strain was 690 με (corresponding to a compressive stress of 119.37 MPa) after heating for approximately 20 s. Notably, the real compressive strain induced by the shape memory effect was greater than 690 με because the measured results were significantly affected by the thermal expansion (generating tensile strain) of the strain gauge and the adhesive layer bonding the strain gauge to the Fe-SMA patch. It could be observed that, after heating for 20 s, the compressive strain gradually reduced and then turned into tensile. Subsequently, the strain gauge was debonded because of continuous heating. Generally, the monitoring results indicated that considerable compressive stress (greater than 119.37 MPa) was induced by the shape memory effect of the Fe-SMA patch; thus, considerable prestress was applied to the cracked steel plate for retarding the fatigue crack propagation.

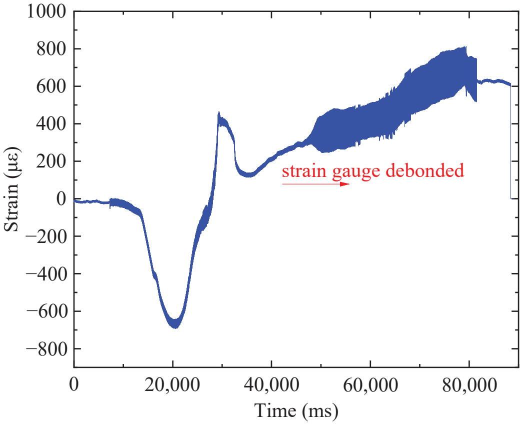

Figure 9. Monitored strain-time curve of the Fe-SMA patch during thermal activation.

4.3. Fatigue Test Setup

In the process of the fatigue pre-test, eight strain gauges (labeled from G1 to G8) were arranged at the extension of the artificial crack, as shown in Figure 10a. The resistance of the strain gauge is 120 Ω, and the sensitivity ratio is 2.0 ± 1.0%. The G4 and G5 were 5 mm away from the crack tip, and G6 (G3), G7 (G2) and G8 (G1) were 60, 70, and 80 mm away from the crack tip, respectively. Once G4 or G5 was broken, indicating the fatigue crack propagating below the strain gauge, the crack length was measured every five minutes. The pre-test was stopped while the fatigue crack at one side propagated to 15 mm. Then, the G4 and G5 were removed, and the corresponding position was polished. Subsequently, the SMA patches were bonded to the cracked steel plate, and the other two strain gauges were bonded to the activated SMA patches at the same position (i.e., 5 mm away from the artificial crack tip).

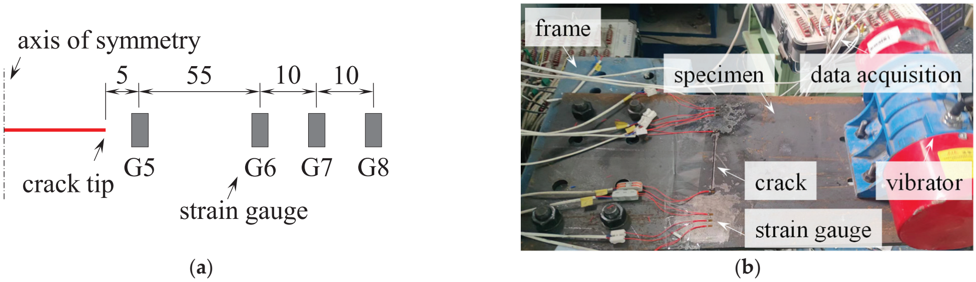

Figure 10. Illustration for the fatigue test. (**a**) Schematic drawing of the arrangement of the strain gauges (unit: mm). (**b**) Fatigue test setup.

For applying the fatigue load, one side of the specimen was bolted to the rigid frame, and the other was bolted to the fatigue test machine (see Figure 10b). A bending-type load was then generated by the rotation of an eccentric block inside the vibrator. The G8 was selected as the reference point, and the applied stress range was controlled to be 180 MPa (with a stress ratio of −1). For SP-1, SP-2, and SP-3, the loading frequency was 31.5, 32.7, and 33.0 Hz, respectively. Once the fatigue crack had propagated to the lateral side of the specimen, the fatigue test was stopped. The fatigue crack propagation was recorded, and the fracture surface was also obtained, as to be introduced in the following section.

5. Test Results and Discussions

5.1. Strain Variation during Fatigue Testing

Given the large amount of monitored strain data and the similarity of the strain variation among the three specimens, the strain data of SP-2 were plotted for analysis. The strain gauges G4 and G5 were employed to monitor the strain at the surface of SMA patches, as plotted in Figure 11a,b. It could be seen that the surface strain was up to 700 με while the fatigue crack propagated below the SMA patch. Subsequently, a sharp decline in the strain-time curve was observed, and the subsequent strain was compressive. Integrating the experimental phenomenon, it was found that the occasion for the sharp decline corresponded to the fact that the fatigue crack propagated to the edge of the SMA plate. Therefore, it could be supposed that the fatigue load transferred by the SMA patch was significantly reduced once the fatigue crack propagated to the edge of the SMA patch. Meanwhile, since the prestress force (i.e., the recovery force) remained stable, the monitored strain turned into compressive. It could also be concluded that the strain variation characteristics bonded to the SMA patch could be employed to predict whether the fatigue crack has propagated to the edge of the SMA patch. Additionally, the strain-time curve of G4 and G5 stayed out to the end of the fatigue test, indicating that there was no debonding failure of the adhesive layer between the SMA patch and steel plate.

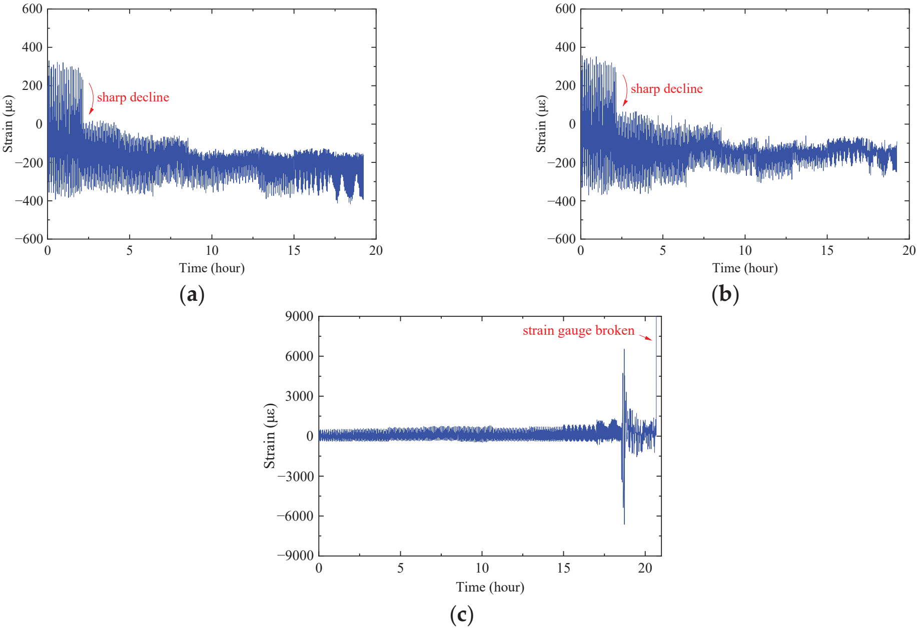

Figure 11. Strain-time curves of G4, G5, and G6 of SP-2 during the fatigue test. (**a**) G4. (**b**) G5. (**c**) G6.

Except for the G8 adopted as the reference point, the other strain gauges arranged at the surface of the cracked steel plate were adopted to assist in observing the fatigue crack propagation. Taking the G6 plotted in Figure 11c, for example, it could be observed that the strain range gradually increased as the fatigue test went on. The monitored strain increased sharply once the fatigue cracks propagated close to the strain gauge. For the SP-2, the G6 was debonded rather than broken when the fatigue crack propagated below the strain gauge, and it could be seen from Figure 11c that the G6 kept working for several hours after the sharp increase in strain; however, the monitored strain at this time no longer represented the real strain of the steel plate, and it could be supposed to be broken.

5.2. Crack Propagation

The fatigue crack propagation life (i.e., fatigue life), as well as the crack propagation curve, were presented in this section. Regarding the fatigue life, the values corresponding to the crack propagating to 15 mm in the pre-test and corresponding to the crack propagation in the subsequent fatigue test were compared, as shown in Figure 12. It could be observed that there are few differences among the fatigue lives of SP-1, SP-2, and SP-3 in the pre-test. Compared to the fatigue life of SP-1, the one of SP-2 is 11.8% longer while the one of SP-3 is 0.7% shorter. After strengthening with the SMA patches, a considerable retarding effect on the crack propagation was obtained. The fatigue life of SP-1 in the subsequent fatigue test is 110×10^4 cycles, while the one of SP-2 and SP-3 has increased by 188.9% and 168.3% (see Figure 12), respectively. It indicates that bonding the SMA patches is feasible to strengthen the crack steel plate subjected to fatigue bending loading.

Since it is difficult to measure the crack length when the crack propagates below the SMA patch, the crack length is not recorded until the crack propagates beyond the edge of the SMA patch. The crack propagation curves of SP-1, SP-2, and SP-3 were plotted in Figure 13. It is observed that the propagating rate of the fatigue crack increases with the increasing loading cycle and crack length. However, there are no significant differences among the crack propagation curves corresponding to the same side of the specimen. It indicates that the crack propagation life is less affected by the bonded SMA patch once the crack propagates out of the cover range. Therefore, integrating the data plotted in Figure 12, it could be concluded that the fatigue crack could be retarded only if it propagates within the cover range of the bonded SMA patch, whether there is debonding failure between the SMA patch and cracked steel plate or not.

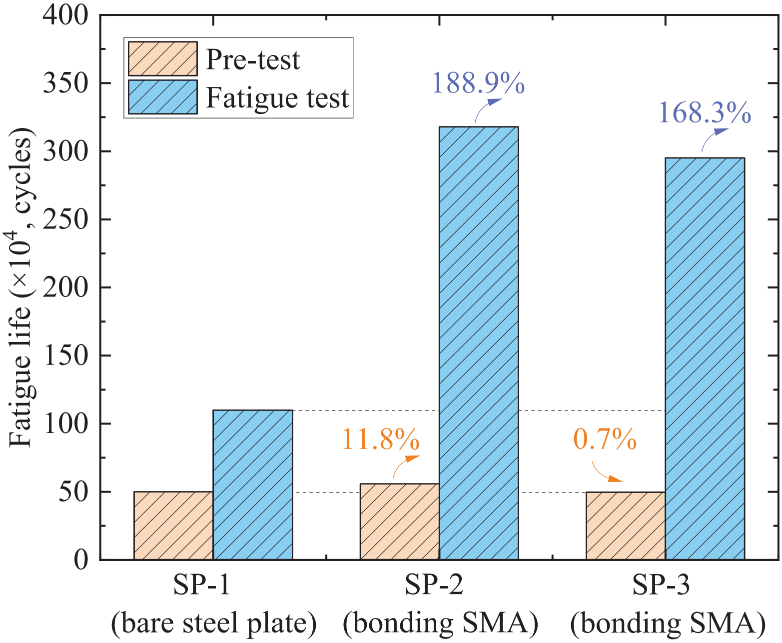

Figure 12. Fatigue life comparison.

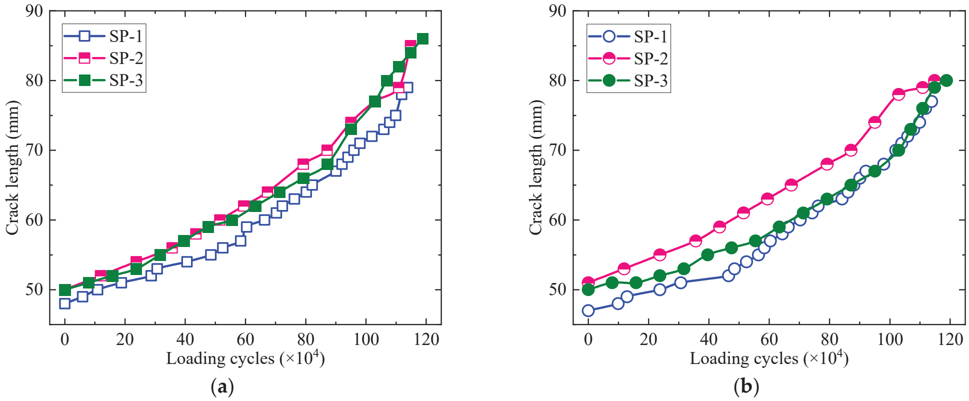

(**a**) (**b**)

Figure 13. Crack propagation curves. (**a**) On the left side of the specimen. (**b**) On the right side of the specimen.

5.3. Fracture Surface Analysis

The fatigue fracture surfaces of SP-1, SP-2, and SP-3 were obtained after fatigue tests. Figure 14 shows the fracture surface of SP-1 and SP-2 for comparison. As can be seen in Figure 14, the original place where the crack was initiated is observed on both the top and bottom surfaces of the cracked steel plate on the edge of the artificial cutting surface. However, the top crack propagation dominates the final fatigue failure. The benchmarks (i.e., the progression marks), generated by the variations in the crack growth rate, could be clearly seen in the fracture surface because the crack growth rate increases with the increasing crack length (see Figure 13).

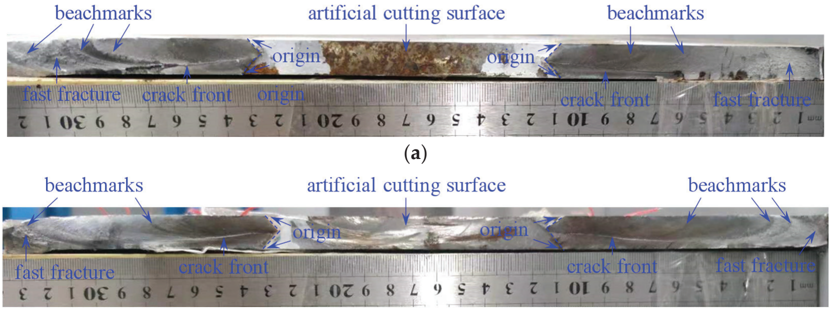

(**a**)

(**b**)

Figure 14. Fatigue fracture surfaces. (**a**) SP-1. (**b**) SP-2.

Additionally, the fast fracture zone (i.e., the overload zone), generated when the crack reached the point where the remaining material was overstressed, could be clearly seen on both sides of the fracture surface. Regarding SP-1, the crack propagation surface in the latter stage of the fatigue life is macroscopically brittle, especially on the left side, as shown in Figure 14a: the crack propagation surface is rough, and the benchmarks can be clearly seen. It is supposed that the rough surface is generated by only a few stress cycles in the latter stage of the fatigue life. However, regarding the SP-2, the crack propagation surface is generally smooth, and the fast fracture zone is relatively small. This could be attributed to the reinforcement effect of the SMA patch, which decreases the magnitude of the load sustained by the cracked steel plate when the final fracture occurs.

6. Conclusions

In the present study, the feasibility of attaching the SMA patches to the reinforcement of the mode I, mode II, and mode III cracks was investigated. Finite element analysis-based parametric analysis was conducted to investigate the effect of the bonding area, the thickness of the SMA patch, and the strengthening angle on the reinforcement effect. Fatigue tests were also conducted to investigate the reinforcement effect by bonding the SMA patch. The following conclusions can be drawn.

(1) Bonding the SMA patch is applicable to the mode I crack while inapplicable to both mode II and mode III cracks. Compared to the strengthening method by bonding the steel patch, bonding the SMA patch could further decrease the SIF at the crack tip because of the prestress force (i.e., the recovery force).

(2) The SIF has decreased 144.2 MPa·mm$^{1/2}$ in the presence of every 1 mm thickening of the SMA patch. It is recommended that the SMA patch be arranged with the direction of the recovery force perpendicular to the possible crack propagation direction. Comparatively, the reinforcement effect is less affected by the bonding area of the SMA patch.

(3) Experimental results demonstrate the retarding effect on the crack growth by bonding the SMA patches. Compared with the bare steel plate, the fatigue life of SMA patch-strengthened specimens has increased by 188.9% and 168.3%, respectively. However, the retarding effect could be neglected when the fatigue crack propagates out the cover range of the SMA patch.

Author Contributions: Z.W. and L.W. mainly worked on investigation and validation; Q.W. developed the methodology; B.J. was in charge of the formal analysis; J.L. was responsible for data curation; Y.Y. mainly worked on investigation and validation. All authors have read and agreed to the published version of the manuscript.

Funding: This work is sponsored by the National Natural Science Fund of China (No. 52308176), the Natural Science Foundation of Jiangsu Province (Grant No. BK20220422) and the Natural Science Foundation of the Jiangsu Higher Education Institutions of China (Grant No. 22KJB560008). The assistances are gratefully acknowledged.

Institutional Review Board Statement: Not applicable.

Informed Consent Statement: Informed consent was obtained from all subjects involved in this study.

Data Availability Statement: The data that support the findings of this study are available from the corresponding author upon reasonable request.

Conflicts of Interest: The authors declare that there are no conflict of interest regarding the publication of this paper.

Nomenclature

SMA	shape memory alloy
CT	compact tension
CFRP	carbon fiber reinforced polymer
GFRP	glass fiber reinforced polymer
SIF	stress intensity factor
FE	finite element
XFEM	extended finite element method

References

1. Fustar, B.; Lukacevic, I.; Dujmovic, D. Review of fatigue assessment methods for welded steel structures. *Adv. Struct. Eng.* **2018**, *2018*, 3597356.
2. Wang, J.Q.; Xiong, Y.K.; Li, Q.; Jin, D.Z.; Hu, Y.Y.; Che, T.K. Experimental investigation on the preparation and surface treatment of biomass fibers for stone mastic asphalt mixtures modification. *Constr. Build. Mater.* **2023**, *408*, 133667. [CrossRef]
3. Murdani, A.; Makabe, C.; Saimoto, A.; Irei, Y.; Miyazaki, T. Stress concentration at stop-drilled holes and additional holes. *Eng. Fail. Anal.* **2008**, *15*, 810–819. [CrossRef]
4. Fang, L.; Fu, Z.Q.; Ji, B.H.; Wang, Q.D. Interference of cracking and drilling on opposite side of steel deck components. *J. Constr. Steel Res.* **2023**, *208*, 107996. [CrossRef]
5. Liu, Q.; Chen, S.L.; Xu, X.W.; Jin, S.Y.; Li, Y.P.; Wang, Y.Q.; Shen, B. Multi-objective optimization of the subsurface residual stress field of TC4 alloy in machine hammer peening. *J. Manuf. Process.* **2023**, *104*, 98–107. [CrossRef]
6. YuanZhou, Z.Y.; Ji, B.H.; Fu, Z.Q.; Kainuma, S.; Tsukamoto, S. Fatigue crack retrofitting by closing crack surface. *Int. J. Fatigue* **2019**, *119*, 229–237. [CrossRef]
7. Li, A.B.; Xu, S.H.; Wang, Y.D.; Wu, C.; Nie, B. Fatigue behavior of corroded steel plates strengthened with CFRP plates. *Constr. Build. Mater.* **2021**, *314*, 125707. [CrossRef]
8. Bu, L.T.; Hou, Q.; Zhou, J. Mechanical behaviour of H-shaped steel columns reinforced with bonded steel plates and anchor bolts. *Structures* **2023**, *51*, 544–559. [CrossRef]
9. Duan, M.J.; Tang, Y.; Wang, Y.S.; Wei, Y.; Wang, J.Q. Compressive performance of longitudinal steel-FRP composite bars in concrete cylinders confined by different type of FRP composites. *Polymers* **2023**, *20*, 4051. [CrossRef]
10. Liu, J.; Guo, T.; Wei, Y.; Wang, L.B.; Zou, X.X. Investigation of the effect of pre-tightening forces on bolted connection for FRP-steel joints. *Case Stud. Constr. Mater.* **2023**, *19*, 02348. [CrossRef]
11. Miao, K.T.; Wei, Y.; Zheng, K.Q.; Zhang, S.C. Eccentric compression behavior of concrete-filled steel tube columns strengthened by CFRP/steel strip. *Eng. Struct.* **2023**, *287*, 116191. [CrossRef]
12. Zareie, S.; Issa, A.S.; Seethaler, R.J.; Zabihollah, A. Recent advances in the application of shape memory alloys in civil infrastructures: A review. *Structures* **2020**, *27*, 1535–1550. [CrossRef]
13. Muntasir, B.; Raham, J.; Zhang, Q. Shape memory alloys (SMAs) for resilient bridges: A state-of-the-art review. *Structures* **2022**, *37*, 514–527. [CrossRef]
14. Fritsch, E.; Izadi, M.; Ghafoori, E. Development of nail-anchor strengthening system with iron-based shape memory alloy (Fe-SMA) strips. *Constr. Build. Mater.* **2019**, *229*, 117042. [CrossRef]
15. Ghafoori, E.; Hosseini, E.; Leinenbach, C.; Michels, J.; Motavalli, M. Fatigue behavior of a Fe-Mn-Si shape memory alloy used for prestressed strengthening. *Mater. Des.* **2017**, *133*, 349–362. [CrossRef]

16. Wang, W.D.; Li, L.Z.; Hosseini, A.; Ghafoori, E. Novel fatigue strengthening solution for metallic structures using adhesively bonded Fe-SMA strips: A proof of concept study. *Int. J. Fatigue* **2021**, *148*, 106237. [CrossRef]
17. Izadi, M.R.; Ghafoori, E.; Motavalli, M.; Maalek, S. Iron-based shape memory alloy for the fatigue strengthening of cracked steel plates: Effects of re-activations and loading frequencies. *Eng. Struct.* **2018**, *176*, 953–967. [CrossRef]
18. Chen, Z.Y.; Gu, X.L.; Zhao, X.L.; Ghafoori, E.; Yu, Q.Q. Fatigue tests on Fe-SMA strengthened steel plates considering thermal effects. *J. Struct. Eng.* **2023**, *149*, 04022255. [CrossRef]
19. Wang, S.Z.; Li, L.Z.; Su, Q.T.; Jiang, X.; Ghafoori, E. Strengthening of steel beams with adhesively bonded memory-steel strips. *Thin-Walled Struct.* **2023**, *189*, 110901. [CrossRef]
20. Vujtech, J.; Ryjacek, P.; Matos, J.C.; Ghafoori, E. Iron-Based shape memory alloy for strengthening of 113-Year bridge. *Eng. Struct.* **2021**, *248*, 113231. [CrossRef]
21. Li, L.Z.; Wang, W.D.; Chatzi, E.; Ghafoori, E. Experimental investigation on debonding behavior of Fe-SMA-to-steel joints. *Constr. Build. Mater.* **2022**, *364*, 129857. [CrossRef]
22. Qiang, X.H.; Wu, Y.P.; Jiang, X.; Xu, G.W. Fatigue performance of cracked diaphragm cutouts in steel bridge reinforced employing CFRP/SMA. *J. Constr. Steel Res.* **2023**, *211*, 108136. [CrossRef]
23. Deng, J.; Fei, Z.Y.; Li, J.H.; Huang, H.F. Flexural capacity enhancing of notched steel beams by combining shape memory alloy wires and carbon fiber-reinforced polymer sheets. *Adv. Struct. Eng.* **2023**, *26*, 1525–1537. [CrossRef]
24. Kean, V.; Chen, T.; Li, L.Z. Numerical study of fatigue life of SMA/CFRP patches retrofitted to central-cracked steel plates. *Constr. Build. Mater.* **2021**, *284*, 122845. [CrossRef]
25. Zheng, B.T.; El-Tahan, M.; Dawood, M. Shape memory alloy-carbon fiber reinforced polymer system for strengthening fatigue-sensitive metallic structures. *Eng. Struct.* **2018**, *171*, 190–201. [CrossRef]
26. Russian, O.; Belarbi, A.; Dawood, M. Effect of surface preparation technique on fatigue performance of steel structures repaired with self-stressing SMA/CFRP patch. *Compos. Struct.* **2021**, *280*, 114968. [CrossRef]
27. Izadi, M.R.; Ghafoori, E.; Shahverdi, M.; Motavalli, M.; Maalek, S. Development-of an iron-based shape memory alloy (Fe-SMA) strengthening system for steel plates. *Eng. Struct.* **2018**, *174*, 433–446. [CrossRef]
28. *ASTM E21-09*; Standard Test Methods for Elevated Temperature Tension Tests of Metallic Materials. ASTM International: West Conshohocken, PA, USA, 2009.

materials

Article

Research on the Properties of Steel Slag with Different Preparation Processes

Xingbei Liu [1], Chao Zhang [1], Huanan Yu [1,*], Guoping Qian [1], Xiaoguang Zheng [2], Hongyu Zhou [1], Lizhang Huang [1], Feng Zhang [1] and Yixiong Zhong [1,*]

[1] School of Traffic and Transportation Engineering, National Engineering Research Center of Highway Maintenance Technology, Changsha University of Science & Technology, Changsha 410114, China; l11191815148@126.com (X.L.); zc11@stu.csust.edu.cn (C.Z.); guopingqian@csust.edu.cn (G.Q.); zhouhongyu23@126.com (H.Z.); huanglz@stu.csust.edu.cn (L.H.); zhangfeng122333@163.com (F.Z.)

[2] Shanghai Municipal Engineering Design & Research Institute (Group) Co., Ltd., Shanghai 200092, China; zhengxiaoguang@smedi.com

* Correspondence: huanan.yu@csust.edu.cn (H.Y.); yixiongzhong@stu.csust.edu.cn (Y.Z.)

Citation: Liu, X.; Zhang, C.; Yu, H.; Qian, G.; Zheng, X.; Zhou, H.; Huang, L.; Zhang, F.; Zhong, Y. Research on the Properties of Steel Slag with Different Preparation Processes. *Materials* **2024**, *17*, 1555. https://doi.org/10.3390/ma17071555

Academic Editor: Miguel Ángel Sanjuán

Received: 16 February 2024
Revised: 6 March 2024
Accepted: 13 March 2024
Published: 28 March 2024

Abstract: To promote the resource utilization of steel slag and improve the production process of steel slag in steelmaking plants, this research studied the characteristics of three different processed steel slags from four steelmaking plants. The physical and mechanical characteristics and volume stability of steel slags were analyzed through density, water absorption, and expansion tests. The main mineral phases, morphological characteristics, and thermal stability of the original steel slag and the steel slag after the expansion test are analyzed with X-ray diffractometer (XRD), scanning electron microscope (SEM), and thermogravimetric analysis (TG) tests. The results show that the composition of steel slag produced by different processes is similar. The main active substances of other processed steel slags are dicalcium silicate (C_2S), tricalcium silicate (C_3S), CaO, and MgO. After the expansion test, the main chemical products of steel slag are $CaCO_3$, $MgCO_3$, and calcium silicate hydrate (C-S-H). Noticeable mineral crystals appeared on the surface of the steel slag after the expansion test, presenting tetrahedral or cigar-like protrusions. The drum slag had the highest density and water stability. The drum slag had the lowest porosity and the densest microstructure surface, compared with steel slags that other methods produce. The thermal stability of steel slag treated by the hot splashing method was relatively higher than that of steel slag treated by the other two methods.

Keywords: preparation process; steel slag; expansion test; XRD; microscopic morphology; thermal stability

1. Introduction

Steel slag is a lumpy substance that combines the residual solvent and metal oxides in the steelmaking furnace after cooling, iron removal, crushing, etc. It is a by-product of the steelmaking process. Steel slag emissions make up about 8–15% of crude steel [1,2]. China's crude steel production exceeded 1 billion tons and the amount of slag discharge exceeded 120 million tons in 2021, with the strong growth of China's iron and steel industry [3]. However, the physical mechanics, morphology, and volumetric stability of steel slag are limited by the production equipment, preparation process, and geographical environment, resulting in the overall utilization rate of steel slag being less than 30% [4]. Most steel slag is treated as industrial waste and piled up in the mountains, resulting in land occupation, environmental pollution, resource waste, and other issues [5,6]. In the context of "carbon peak, carbon neutral", promoting the efficient utilization of steel slag resources is an urgent need to ensure the stable development of China's society [7].

The research on the material properties of steel slag is the primary problem of its utilization. Experts have made some progress focusing on its physical and chemical properties, mechanical properties, morphological characteristics, and other properties. In terms of the physical and chemical properties of steel slag, experts believe that, through the analysis of the vast majority of steel slag, the main components can be identified as calcium, magnesium, silicon, and iron oxides, so the steel slag can be regarded as a $CaO–SiO_2–MgO–FeO$ tetrameric system [8,9]. Calcium, silicon, and phosphorus oxide content were used to indicate the alkalinity of steel slag [10]. According to the differences in alkalinity, steel slag can be divided into three categories: high-alkalinity steel slag ($M > 2.5$), medium-alkalinity steel slag ($1.8 < M < 2.5$), and low-alkalinity steel slag ($M < 1.8$). It has been pointed out that the alkalinity of steel slag can reflect its hydration activity [11]. However, it is more reliable to evaluate the hydration activity of steel slag using the activity index rather than alkalinity [12,13]. In addition, Li et al. [14] attempted to evaluate the hydration activity of steel slag materials using chemical methods, and the experimental process operation was more difficult to control. The experts affirmed the physical and mechanical properties of steel slag materials, and the hardness, adhesion, and roughness of steel slag became advantages for certain applications. In addition, some researchers used two-dimensional and three-dimensional image analysis techniques to characterize the morphology of steel slag aggregates [15]. Scanning electron microscopes can also be used to observe the micro-morphological characteristics of steel slag; steel slag has a rough surface texture, and steel slag contains a lot of pores, making it a somewhat porous material [16].

The material properties of steel slag determine its resource uses and application effects. Steel slag contains CaO, Fe, MnO, MgO, Fe_2O_3, etc. It can be used as raw material for iron and steel sintering, and its magnesium and calcium composition means it can be used as a solid solution, which can replace part of magnesite, limestone, and other fluxes [17–19]. Steel slag contains about 10% of the metal iron, which, after crushing, screening, magnetic separation, and other processing, can be sorted into different particle sizes, of slag steel and magnetically separated powder, for reuse [20]. Steel slag's main composition is CaO, Al_2O_3, SiO_2, and MgO, which is similar to the raw materials for the traditional construction of tiles; therefore, steel slag can be used as a raw material in the preparation of ceramics [21]. Steel slag contains many alkaline oxides, such as CaO and other compositions, which can be used to treat pollutants in wastewater through chemical reactions [22,23]. Steel slag contains high levels of Si, Mn, and P and various trace elements, which can provide nutrients needed for crop growth. At the same time, CaO in steel slag can also slowly neutralize soil, so it can be used as farmland fertilizer and for improvement purposes [24,25]. Steel slag contains dicalcium silicate and tricalcium silicate, and, as silicate cement clinker has a similar mineral phase, steel slag can be used as a raw material for the production of cement, but also can be applied to concrete admixture, dry mortar, and so on. However, the low content of practical cementitious components in steel slag and its high formation temperature of up to 1600 °C, which results in more crystallization of the mineral phase, limit the broad application of steel slag in cement and concrete [26,27]. Steel slag, crushed stone, and its natural aggregates have similar physico-mechanical properties [28,29]. The density of steel slag is high, generally above 3.2 g/cm^3, while the density of natural aggregates is about 2.6–2.9 g/cm^3; steel slag has the advantage of physico-mechanical indices, which show that its crushing value and Los Angeles abrasion are higher than that of natural aggregates by 4.7–20.5% and 12.0–52.7%, respectively. The porous nature of steel slag results in high water absorption levels of steel slag aggregate, generally between 1% and 2% [30,31]. Steel slag crushed stone is suitable for road material requirements, as it can be used for the road base layer, the surface layer, and the bedding, and can also be used as engineering backfill material [32–35]. The common uses of steel slag are shown in Table 1. Many studies have shown that using steel slag as a road construction material is the most effective means of resource utilization [36–38]. However, the volumetric stability of steel slag materials, preparation process limitations, distribution of iron and steel enterprises, policies, and other reasons still limit the use of steel slag in road construction [28,39,40].

Table 1. Common applications of steel slag [41–44].

Active Ingredients	Application	Advantages and Disadvantages
C_2S, C_3S, C_4AF, and C_3A	Replace natural aggregate in concrete	Good durability. Poor water stability
C_3S and β-C_2S	Steel slag powder as supplementary cementitious materials	Improve mechanical properties and durability. Potential expansion problem
$CaCO_3$, C_2S and C_3S	Replace natural aggregate in asphalt mixture	Higher mechanical behavior of mixtures with steel slag aggregate. But require a higher asphalt content

Meanwhile, the treatment processes of different steel slags result in significant differences in their performance. Analyzing and comparing the steel slag produced by various methods will be beneficial for promoting the resource utilization of steel slag. Therefore, this study investigates the properties of steel slag (XG/PG/BG/WG) with different preparation processes. In this research, XG and PG are produced using the thermal smothering method, WG is produced using the hot splashing method, and BG is made using the drum method. Hot smothering and drum method steel slag are in a high-temperature steam environment. At the same time, the hot splashing method of steel slag is in a natural environment. Different processing techniques lead to differences in the performance of steel slags. Thus, this study further analyzes steel slags' physicomechanical characteristics and volumetric stability by density, water absorption, crushing value, and swelling tests. The main mineral phases, morphological characteristics, and thermal stability of steel slags are analyzed using XRD, SEM, and TG tests before and after expansion tests. The results can provide a reliable reference for the application selection of steel slag.

2. Materials and Methods

2.1. Materials

Steel slags from four steel mills are used in this research: XG, PG, BG, and WG. XG has been stored for more than 12 months, and PG, BG, and WG have been stored for about 3–6 months. After sieving, particle sizes of steel slag range from 4.75 to 16 mm and are classified into 4.75–9.5 mm, 9.5–13.2 mm, and 13.2–16 mm. We take classified steel slags as the test material. The chemical element composition of the four types of steel slag is shown in Table 2. The picture of four kinds of steel slag is shown in Figure 1.

Table 2. Chemical element composition of the four types of steel slag.

	CaO (%)	Fe_2O_3 (%)	SiO_2 (%)	MgO (%)	MnO (%)	Al_2O_3 (%)	P_2O_5 (%)	TiO_2 (%)	Cr_2O_3 (%)	SO_3 (%)
BG	40.80	33.51	13.59	4.39	2.91	1.99	0.99	0.75	0.39	0.23
WG	45.33	31.63	10.46	4.37	3.32	1.51	1.38	0.99	0.43	0.10
PG	46.13	29.85	11.66	4.08	3.65	1.39	1.33	0.93	0.49	0.18
XG	43.36	26.53	13.02	3.92	5.15	0.87	3.68	1.37	0.63	0.74

XG and PG steel slags are produced using the hot smothering method. The production process of hot smothering slags is to introduce high-temperature liquid steel slags into a special hot slag pond, cool them with water spray, cover the slag pond to maintain pressure, and use the thermal stress generated by the rapid cooling of steel slags and saturated high-temperature steam to penetrate steel slags. Thus, free calcium oxide in steel slags can be digested to generate calcium hydroxide, resulting in volume expansion and tiny steel slag particles conducive to recovery [45].

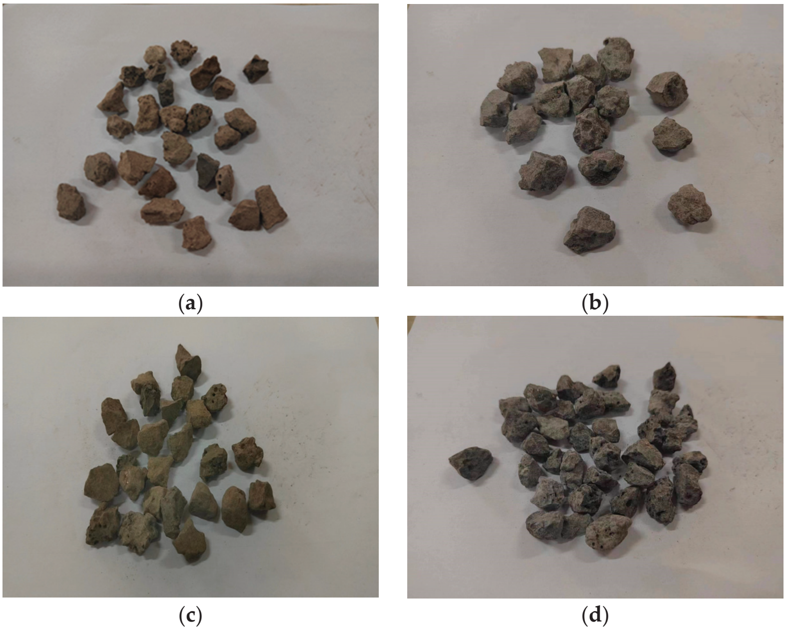
(**a**) (**b**)
(**c**) (**d**)

Figure 1. Pictures of steel slags. (**a**) PG; (**b**) BG; (**c**) WG; (**d**) XG.

BG steel slag is produced using the drum method. The drum slag process involves the granulation of molten slag into the drum at an appropriate flow rate, under rapid cooling conditions, under centrifugal force, spray water, and the squeezing friction of steel balls inside the drum [46]. This process has the advantages of small pollution, clean site, high treatment efficiency, uniform particle size of treated steel slag, stable free calcium oxide, and direct utilization of steel slag. However, the requirements for the iron content of the treated steel slag are strict, and the slag with molten steel is prone to explosion. The equipment is severely worn, and the cost of slag treatment is high [47]. Additionally, there are requirements for the block size of the treated steel slag. Although drum slag equipment capable of handling solid slag has been developed, limitations still exist, and converter steel slag cannot be fully processed.

WG steel slag is produced using the hot splashing method. The production process of hot splashing slag is to load liquid high-temperature steel slag into a tank, lift the tank with a crane, and evenly pour the liquid steel slag into a shallow plate. After filling the shallow plate with water, spray water for 8–45 h and filter for another 2 h. The average temperature of the steel slag can be cooled to around 50 degrees and then sent to crush and classify [48,49].

2.2. Experiments

2.2.1. Density Test

In order to compare the basic physical indexes of different steel slag, the density and water absorption of steel slag are tested. The test process was carried out according to the JTGE42-2005 Code for Testing Aggregates in Highway Engineering [50].

2.2.2. Volume Expansion Test

The expansion test was carried out using GB/T 24765-2009 steel slag for wearing asphalt pavement [51] to compare the volume stability of different steel slags. The four kinds of steel slag are 4.3 kg each, and the proportions of particle size 4.75–9.5 mm, 9.5–13.2 mm, and 13.2–16 mm were 48.63%, 44.52%, and 6.85%, respectively. After the water bath temperature reaches 90 ± 1 °C, the constant temperature is maintained for 6 h, and then the heating and cooling are naturally stopped for 10 cycles. The data were recorded and the expansion rate was calculated.

2.2.3. XRD, SEM, and TG Test

Grind XG, PG, BG, and WG steel slags into powder with a ball mill. The powder of four kinds of steel slag is used to conduct the XRD and TG tests. The crystal structure of the sample was characterized by Rigak SmartLab 9KW X-ray Diffraction (XRD) (Rigaku, Auburn Hills, MI, USA). The wavelength of the X-ray is 1.54 Å (CuKa). The test voltage and current are 45 kV and 200 mA, respectively. The scanning range is 5–75°, the scanning frequency is 10°/min, and the step size is 0.02°. Thermogravimetric analysis (TG) of steel slag material is carried out by the Netzsch STA449F3 synchronous thermal analyzer produced in Selb, Germany. The test atmosphere was a nitrogen environment. The test temperature is from room temperature to 1200 °C, and the heating rate is 5 °C/min. Scanning electron microscopy is used to characterize the surface microstructure of the original steel slag produced by different processes and the steel slag after the expansion test. The electrical signals generated by the photoactive focused electron beam on the sample's surface were converted into images for on-site measurement. The experimental equipment for the XRD, SEM, and TG tests is shown in Figure 2.


(**a**) (**b**) (**c**)

Figure 2. Experimental equipment: (**a**) SEM test device; (**b**) TG test device; (**c**) XRD test device.

3. Results and Discussion

3.1. Density and Water Absorption

The density and water absorption are shown in Table 3.

Table 3. Density and water absorption.

Types	Parameter	4.75–9.5 mm	9.5–13.2 mm	13.2–16 mm
XG	Density (g/cm^3)	3.498	3.393	3.377
	Apparent density (g/cm^3)	3.281	3.192	3.224
	Water absorption (%)	1.89%	1.85%	1.41%
PG	Density (g/cm^3)	3.488	3.437	3.110
	Apparent density (g/cm^3)	3.321	3.333	2.865
	Water absorption (%)	1.45%	0.90%	2.75%
BG	Density (g/cm^3)	3.579	3.628	3.628
	Apparent density (g/cm^3)	3.351	3.456	3.450
	Water absorption (%)	1.90%	1.38%	1.42%
WG	Density (g/cm^3)	3.523	3.478	3.512
	Apparent density (g/cm^3)	3.327	3.343	3.387
	Water absorption (%)	1.67%	1.16%	1.05%

It can be seen from Table 3 that BG has the highest density compared to the other three kinds of steel slags. It can be found that the density of particle size of 4.75–9.5 mm decreases in the order of BG, WG, XG, and PG. The density of particle size of 9.5–13.2 mm decreases in the order of BG, WG, PG, and XG. The density of particle size of 13.2–16 mm decreases in the order of BG, WG, XG, and PG. The apparent density of XG, PG, BG, and

WG varies from 3.192 to 3.456. The apparent density of four kinds of steel slag is 19.0–28.9% higher than natural aggregate; the average apparent density of four kinds of steel slag is relatively close to the steel slag from Baotou, with a variation of less than 10% [52].

According to the density of steel slag, it can be found that the steel slag produced by the drum method from BG has the highest apparent density. Relative to drum method slag, the rougher production process of hot smothering steel slag and hot splashing slag reduces the density of steel slag.

3.2. Volume Expansion

The expansion test results of four kinds of steel slag can be seen in Figure 3.

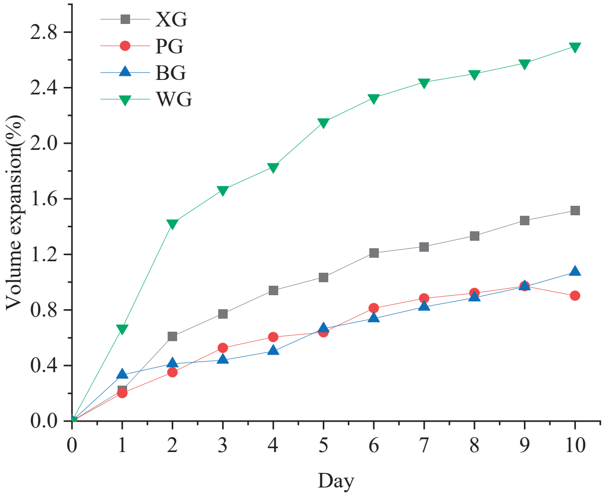

Figure 3. The expansion test results.

It can be seen from Figure 3 that the volume expansion of steel slag is continuously increasing. Based on the expansion rate of the volume of steel slag specimens on the tenth day, the expansion rate of WG is the highest, at 2.7%, followed by XG, at 1.52%. The expansion rates of BG and PG are relatively close, and both are around 1%. The volume expansion of steel slag varies from 0.5 to 3.5% in the present research; it can be found that the expansion rates of XG, PG, and BG are at a low level, while the volume expansion rate of WG is relatively high [53,54].

3.3. Mineral Changes

XRD analysis is conducted on the steel slags before and after the expansion test to study the mineral phase, as shown in Figure 4. In this case, the suffix 0 is the initial steel slag, and the suffix 10 is the steel slag after the expansion test.

Due to the more substantial alkalinity of CaO compared to MgO, a small amount of SiO_2 will preferentially form dicalcium silicate or tricalcium silicate with CaO at high temperatures [55]. It can be observed from the XRD diffraction patterns of four different steel slags in Figure 3 that the original steel slag contains elements presenting prominent peaks such as C_2S, C_3S, CaO, and MgO. These substances are the main active components in steel slag that participate in the aging reaction. It can be observed that the mineral elements in the four types of steel slag have undergone significant changes. $CaCO_3$ and C-S-H in XRD peak patterns show an obvious increase after expansion tests. Meanwhile, C_2S, C_3S, CaO, MgO, and other alkaline elements show an apparent decrease.

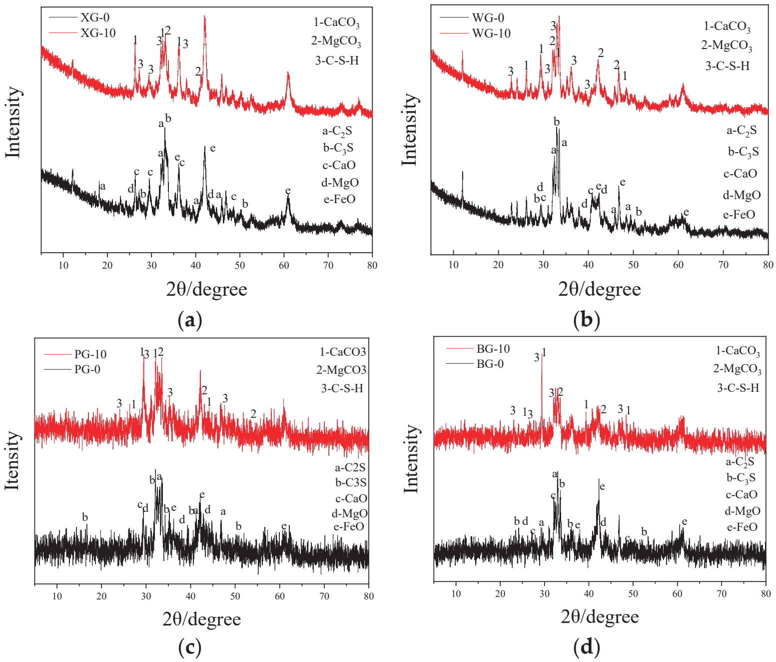

(**a**) (**b**) (**c**) (**d**)

Figure 4. XRD results of steel slags. (**a**) XG steel slag; (**b**) WG steel slag; (**c**) PG steel slag; (**d**) BG steel slag.

In addition to these similar mineral changes, there are also changes in some elements that are worth exploring. Considering the minimum density of WG in the previous density experiment, although the peak heights of C-S-H and $CaCO_3$ in WG vary less, the lower density results in more significant volume expansion of WG in the expansion rate experiment. Considering the maximum density of BG in the previous density experiment, although the peak heights of C-S-H and $CaCO_3$ in BG are very high, the higher density results in less volume expansion of BG in the expansion rate experiment. It is worth noting that the peak around the FeO position of BG steel slag decreased after the expansion test. Because the peak around 42° contains MgO and FeO, MgO reacts with CO_2 to generate $MgCO_3$, and the iron element oxidizes to form iron oxide with higher FeO peaks. Although the peaks of MgO and FeO are relatively close, FeO cannot decrease after the expansion test. The MgO content of BG steel slag is much higher than the other three types of steel slag.

The above analysis shows that the main elements of steel slag produced by different steel mills have similar mineral phases, with the main mineral phases being C_2S, C_3S, ferrite, and a small amount of CaO and MgO. The iron oxide content in the steel slag produced by XG and PG using the hot smothering process is significantly higher than that produced by WG and BG. Considering the differences in iron recovery processes, this may indicate that there is still room for modification in the iron recovery processes of XG and PG steel plants. WG and BG contain fewer ferrite compounds, suggesting that steel slag's production process and supporting recovery measures are better. It can be concluded after XRD analysis that the initial steel slag contains a certain content of unstable elements composed of MgO and CaO in the RO phase. After hydration, the main products of the steel slag are still $CaCO_3$ and C-S-H.

3.4. Simple Quantitative Analysis

A simple quantitative analysis of C2S, C3S, CaO, and MgO mineral phases is performed using Jade software (version 6.0) on the XRD spectra of four initial steel slag types [56]. Simple quantitative analysis is a built-in quantitative analysis function in Jade software. This function calculates the percentage of selected minerals based on parameters such as peak, angle, and area. It is worth noting that the sum of selected mineral proportions in simple quantitative analysis is 100%. The analysis results mainly consider the four elements C_2S, C_3S, CaO, and MgO, which account for a relatively large proportion of steel slag, so these four compounds are mainly considered. The sum of the four elements in the figure is 100%. The analysis results are shown in Figure 5.

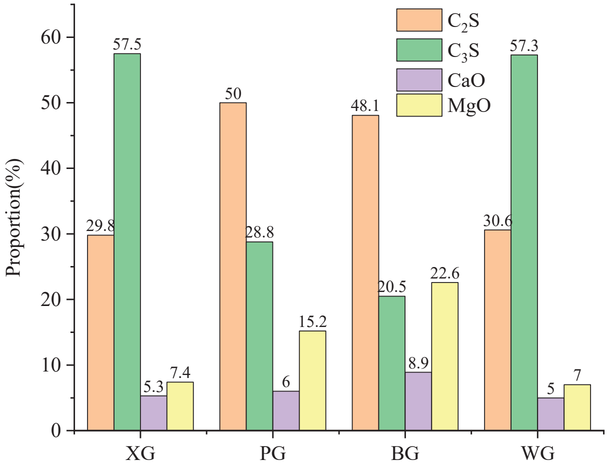

Figure 5. Initial steel slag simple quantitative analysis.

A simple quantitative analysis is conducted on the main products of the four types of steel slag after the expansion test, and the analysis results are shown in the figure. It can be seen from the graph that the content of C_2S and C_3S is the highest, accounting for over 60% of these four minerals, with the content of C_2S and C_3S in XG and WG exceeding 80%. Next is PG, which contains 78.8% of C_2S and C_3S. The lowest content of C_2S and C_3S is BG, accounting for 68.6%. The analysis of the four main alkaline active minerals in steel slag also reveals interesting results, with C_3S in XG and WG significantly higher than C_2S by about two times, while in contrast, C_2S in BG and PG is significantly higher than C_3S by about two times. Considering the differences between different steel slags and the influence of various factors, such as other raw materials, the impact of the steel slag production process on the differences in C_3S and C_2S content deserves further research.

The main components of the RO phase in steel slag are CaO and MgO. From the simple quantitative analysis chart, it can be found that the content of MgO is greater than that of CaO, with the highest MgO content in BG, followed by PG, XG, and WG. The content of CaO decreases in the order of BG, PG, XG, and WG. The content of MgO decreases in the order of BG, PG, XG, and WG.

Figure 6 shows that the most common mineral composition of the main reaction products of PG, BG, and WG steel slag is hydrated calcium silicate after the expansion test. It can be found that among the four types of steel slag, only XG has the highest proportion of $CaCO_3$, exceeding the proportion of hydrated calcium silicate. In the three types of steel slag, PG, BG, and WG, the content of hydrated calcium silicate is the highest, accounting for over 50%. The proportion of hydrated calcium silicate after the BG expansion test is the highest, at 61.4%. The high proportion of hydrated calcium silicate indicates that BG has the highest degree of volcanic ash reaction, with more dicalcium silicate and tricalcium silicate participating in the volcanic ash reaction, because the alkalinity of CaO is higher than that of MgO, and the hydroxyl activity in $Ca(OH)_2$ of the hydration product is higher than that in $Mg(OH)_2$. Figure 5 shows that the proportion of CaO in BG is the highest, indicating this phenomenon.

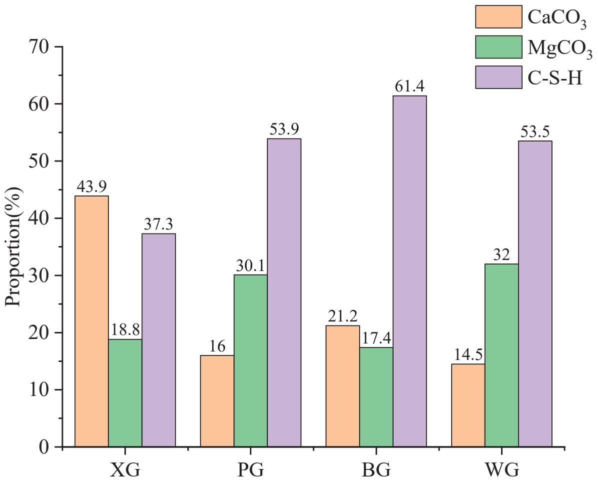

Figure 6. Steel slag simple quantitative analysis after expansion test.

The above analysis shows that C_2S and C_3S are important alkali-active compounds in steel slag, accounting for 70% to 80% of the total. However, further research on the proportion of C_2S and C_3S shows no obvious connection with the steel plant process. The specific differences in production processes, temperatures, and raw materials among different steel plants make it difficult to control variables and specifically study the generation conditions of C_2S and C_3S. The generation of C-S-H is not related to the content of water-active products such as C_2S and C_3S but rather to the alkaline substance CaO in the environment. XG's higher alkaline environment is conducive to the generation of C-S-H.

3.5. Microstructure Changes

Scanning Electron Microscope (SEM) analysis is performed on the surfaces of four types of untreated steel slag and steel slag after expansion testing, and the results are shown in Figure 7. The suffix 0 represents the initial steel slag, while the suffix 10 represents the steel slag after expansion tests.

Figure 7 shows that the initial microstructure of the steel slag surface is similar, with a rough surface and no noticeable mineral crystals visible. However, after the expansion test, obvious mineral crystals appear on the surface of the steel slag, with most of the mineral crystal structures showing tetrahedral or cigar-like protrusions. Based on comprehensive XRD analysis, the main hydration products of steel slag after the expansion test are $CaCO_3$ and C-S-H compounds. It can be inferred that this part of the crystal is mainly C-S-H crystal, and $CaCO_3$ is mostly a needle-like structure rather than a polyhedral or protruding crystal structure [57].

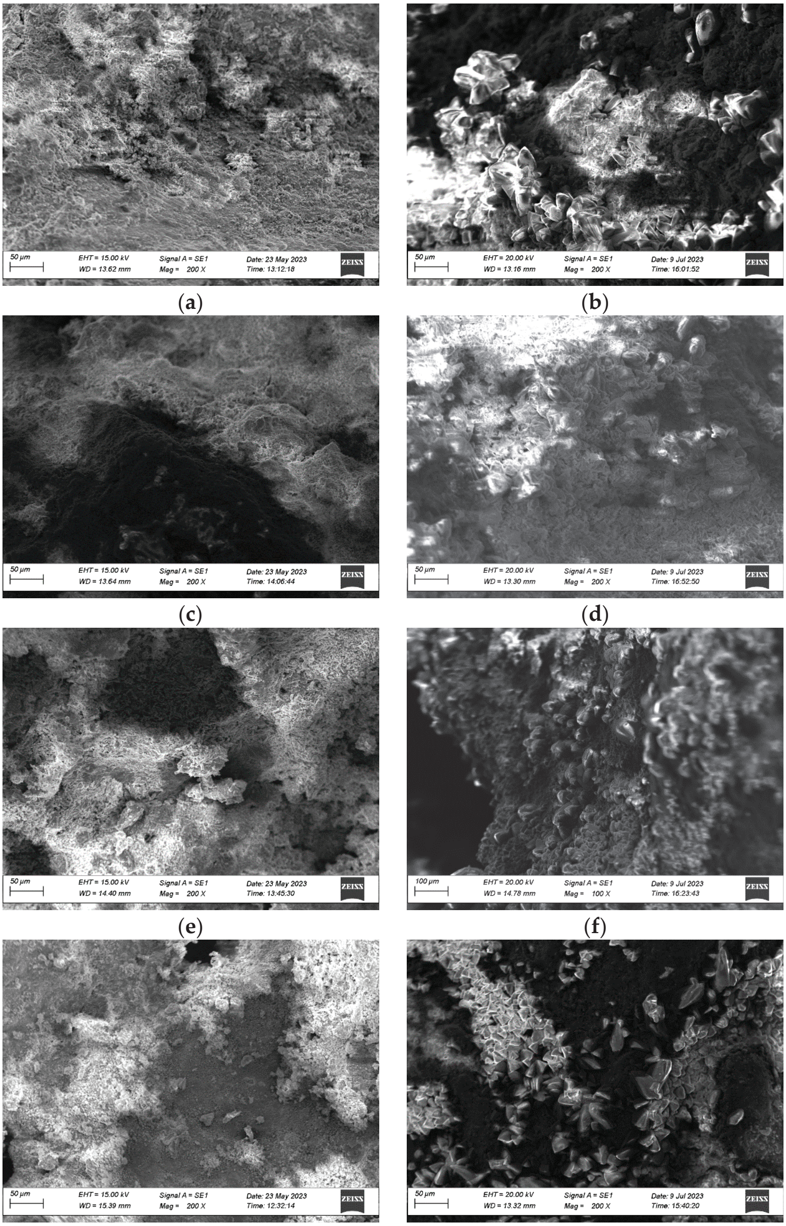

(**a**) (**b**)
(**c**) (**d**)
(**e**) (**f**)
(**g**) (**h**)

Figure 7. Before and after the expansion test of four kinds of steel slag. (**a**) XG-0; (**b**) XG-10; (**c**) PG-0; (**d**) PG-10; (**e**) BG-0; (**f**) BG-10; (**g**) WG-0; (**h**) WG-10.

3.6. Thermogravimetric Analysis

The TG results of the four initial steel slags are shown in Figure 8. Figure 8a is the TG data curve, and Figure 8b is the gradient of TG data (DTG). Figure 8a shows that the mass of PG-0, BG-0, XG-0, and WG-0 continues to decrease with the increased temperature. It can be observed that the rapidly decreasing mass in Figure 8a corresponds to the two weight loss peaks around 100 °C and 700 °C in Figure 8b, where a large amount of mass loss occurs near these temperatures. Figure 8b also shows a third weight loss peak around 400 °C. Only the WG-0 sample shows a significant weight loss peak in Figure 8b, as the sample continuously absorbs water to form $Ca(OH)_2$ during storage. At around 400 °C, $Ca(OH)_2$ will continuously dehydrate to form CaO. The weight loss peak around 400 °C is not apparent due to the small amount of $Ca(OH)_2$, which slows the reaction between CaO and water. WG exhibits a more significant weight loss peak at 400 °C compared to other samples due to the highest CaO content. The most substantial weight loss peak is around 700 °C due to the decomposition of $CaCO_3$ at high temperatures to generate CaO and CO_2, which causes weight loss [58].

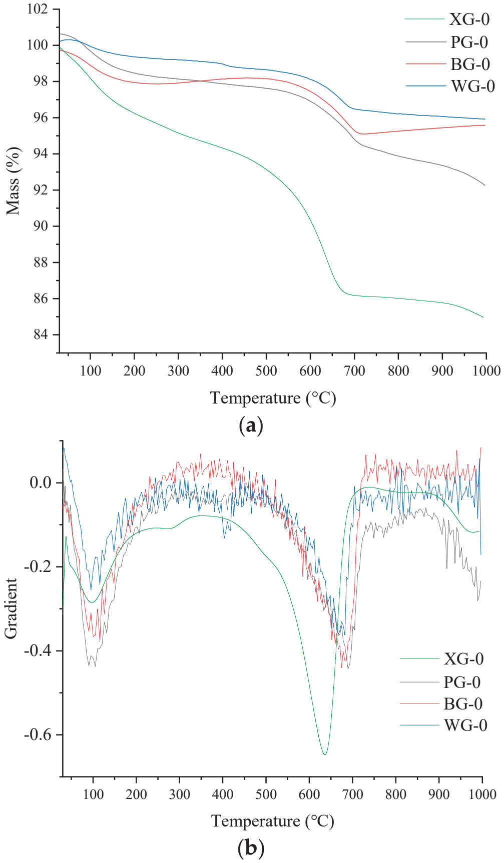

(**a**)

(**b**)

Figure 8. Initial steel slag TG and DTG results. (**a**) TG curve; (**b**) DTG curve.

The minimum mass loss rate of WG steel slag indicates higher CaO and lower $CaCO_3$ content. The higher CaO and lower $CaCO_3$ content suggests that the mineral phase is stable at high temperatures, followed by BG and PG steel slag in the middle position. XG steel slag has the highest mass loss rate because the $CaCO_3$ in XG is the highest. The mass loss and mass loss rate are the highest in the 600–750 °C range. Through comprehensive comparison, it can be found that the mass loss rates of four initial steel slags were ranked from small to large: WG > BG > PG > XG.

The TG and DTG results of the steel slags after the expansion test are shown in Figure 9. It can be found from Figure 9a that the mass loss increases from small to large and is classified as WG, BG, PG, and XG. Figure 9a shows that the mass of the four types of steel slag after the expansion test continues to decrease as the temperature increases.

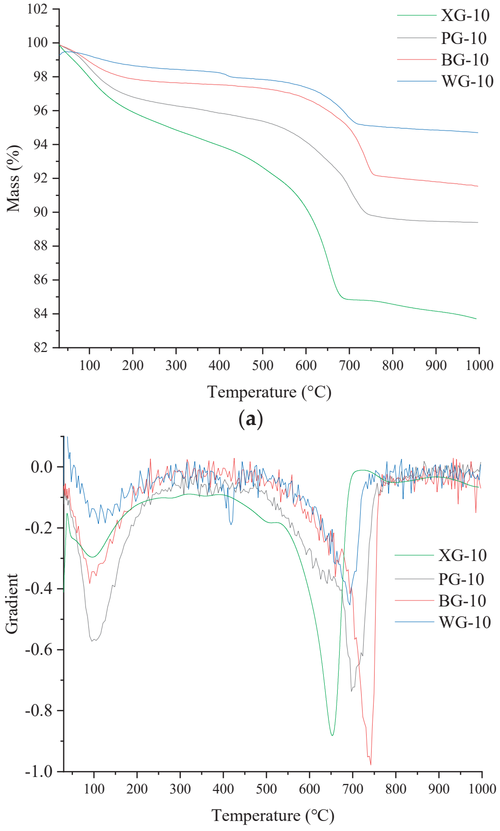

(**a**)

(**b**)

Figure 9. TG and DTG results after expansion test. (**a**) TG curve; (**b**) DTG curve.

In Figure 9a, it can be seen that the maximum mass loss peak occurs around 700 °C. It can also be observed from Figure 9b that there is a maximum decrease rate in the range of 600–750 °C. The mass loss in this part is composed of $CaCO_3$. The second peak of weight loss is between 100 and 200 °C, and the mass loss in this part is mainly free water. Figure 9b shows that a small weight loss peak appears at 400 °C, which is smaller than at 100 °C. The mass loss around 400 °C decomposes $Ca(OH)_2$ into solid CaO and gas state H_2O. Only WG exhibits a relatively small weight loss peak at 400 °C, indicating that the steel slag of WG generates more $Ca(OH)_2$ during hydrolysis and reaction. More $Ca(OH)_2$ demonstrates that WG steel slag contains more CaO, consistent with the highest WG expansion rate in the expansion test results.

The mineral content in the steel slag has changed after expansion testing. The mass loss and mass loss rate are relatively higher than the results compared to the TG results of the initial steel slag. During the expansion experiment, more $CaCO_3$ and C-S-H were generated, which released CO_2 and bound water during thermal decomposition. Based on the TG test of the initial steel slag and steel slag after the expansion test, it can be concluded that WG steel slag has the highest thermal stability performance, followed by PG, BG, and XG.

Considering that TG and DTG curves can only qualitatively analyze the quality loss of four types of steel slag, they cannot quantitatively analyze the quality changes of steel slag at different temperatures. Therefore, a quantitative analysis was conducted on the mass loss in the three mass loss peak temperature ranges of steel slag before and after the expansion experiment. The temperature range of the weightlessness peak and the mass loss rate was calculated in three intervals: 100–200 °C, 400–500 °C, and 600–750 °C. The statistical data results are shown in Table 4.

Table 4. Weigh loss rate of initial steel slag in the specific temperature range.

Temperature (°C)	XG (%)	PG (%)	BG (%)	WG (%)
100–200	1.927	1.228	0.953	0.581
400–500	1.199	0.264	−0.013	0.337
600–750	4.216	2.674	2.314	1.791

The maximum mass loss of XG steel slag occurs between 100 and 200 °C due to the larger pore structure of XG, which has higher voids and water absorption. The mass loss rate of XG steel slag is the highest in the temperature range of 400–500 °C due to the high CaO content in XG steel slag, which generates the most $Ca(OH)_2$ in the hydration reaction. The 600–750 °C temperature range mainly involves the decomposition of $CaCO_3$ into CaO and CO_2. The maximum mass loss rate of XG steel slag in this temperature range indicates the highest content of $CaCO_3$, followed by PG and BG steel slag, respectively. In the original sample, XG steel slag has the highest $CaCO_3$ content and water absorption rate; WG has the lowest water absorption and $CaCO_3$ content; PG and BG are in the middle.

It can be seen from Table 5 that XG has the highest mass loss rate in the range of 100–200 °C, indicating that XG steel slag has the highest water absorption rate, followed by PG, BG, and WG. The 400–500 °C temperature range has the highest $Ca(OH)_2$ content in XG, followed by PG, WG, and BG. XG has the highest weight loss rate in the 600–750 °C range, followed by PG, BG, and WG. Compared with other research [59,60], it can be found that the thermal stability of four kinds of steel slag is enough for construction. From TG, DTG, and qualitatively analyzed results, it can be concluded that WG has the highest thermal stability, followed by BG, PG, and XG.

Table 5. The mass loss rate of steel slag in a specific temperature range after the expansion test.

Temperature (°C)	XG (%)	PG (%)	BG (%)	WG (%)
100–200	2.035	1.736	1.015	0.589
400–500	1.289	0.498	0.223	0.398
600–750	5.467	4.336	4.268	2.273

4. Conclusions

This study compared the physical and chemical properties of steel slag produced by three different methods from four different steel mills. We compared the changes in mineral phases, microstructure, water stability, and thermal stability of steel slag before and after the expansion test. The research results are of great significance for the resource utilization of steel slag and the improvement of steel slag treatment methods in steelmaking plants. The conclusions of this research can be drawn as follows:

(1) The steel slag produced by the drum method has the highest density and lower expansion rate than the other three steel slags. It was also found that although BG has the highest content of free calcium oxide, the higher density of steel slag particles helps to resist the volume expansion caused by water contact.

(2) The composition elements of steel slag produced by different processes are very similar, with the primary active materials being C_2S, C_3S, CaO, and MgO. After the expansion test, the main chemical products of steel slag are $CaCO_3$, $MgCO_3$, and C-S-H. C-S-H is generated by hydrolysis and a combination of C_2S and C_3S, and the content of CaO and MgO mainly influences the amount generated. This means a higher degree of alkalinity can promote the generation of C-S-H. Most C-S-H is generated on the surface of steel slag, forming clusters of mineral crystals.

(3) The thermal stability of the two types of steel slag treated by the hot smothering method is relatively lower than that of steel slag treated by the hot splashing and

drum methods. Additionally, it was found that the storage time may be related to the thermal stability of steel slag particles.

(4) This research considers the density, volume stability, and thermal stability of the four types of steel slag. XG, PG, and BG are recommended as alternative coarse aggregates for road and building construction. Meanwhile, WG is unsuitable as a building material due to its high expansion, and further treatment should be carried out to reduce its expansion before testing. Among them, BG steel slag has the best comprehensive performance.

There are still some shortcomings in existing research, and in future research, more steel slag produced by existing processes and stricter variable control will be adopted.

Author Contributions: Conceptualization, H.Y.; methodology, G.Q.; validation, C.Z.; formal analysis, X.L.; investigation, X.Z., F.Z. and L.H.; resources, H.Z.; writing original draft preparation, X.L.; writing review and editing, Y.Z.; supervision, G.Q.; project administration, H.Y.; funding acquisition, X.L. and H.Y. All authors have read and agreed to the published version of the manuscript.

Funding: This research was funded by the 2022 National College Students' Innovative Entrepreneurial Training Plan Program (grant number: 202210536001); The National Natural Science Foundation of China (grant number: 52227815; 52178414; 52078065; 52008043); and the Science and Technology Innovation Program of Hunan Province (grant number: 2020RC4048); and the Postgraduate Scientific Research Innovation Project of Hunan Province (grant number: CX20220865).

Institutional Review Board Statement: Not applicable.

Informed Consent Statement: Not applicable.

Data Availability Statement: Data are contained within the article.

Conflicts of Interest: Author Xiaoguang Zheng was employed by the company Shanghai Municipal Engineering Design & Research Institute (Group) Co., Ltd. The remaining authors declare that the research was conducted in the absence of any commercial or financial relationships that could be construed as a potential conflict of interest.

References

1. Shaopeng, W.; Peide, C.; Jun, X.; Quantao, L.; Ling, P. Expansive Inhibition Method of Steel Slag Aggregate and Volume Stability of Mixture: A Review. *China J. Highw. Transp.* **2021**, *34*, 166–179. [CrossRef]
2. Roque, A.J.; Rodrigues, G.M.; da Silva, P.F. Re-cycling of construction and demolition waste and steel slag: Characterization of the durability. *J. Mater. Cycles Waste Manag.* **2020**, *22*, 1699–1711. [CrossRef]
3. Gao, W.; Zhou, W.; Lyu, X.; Liu, X.; Su, H.; Li, C.; Wang, H. Comprehensive utilization of steel slag: A review. *Powder Technol.* **2023**, *422*, 118449. [CrossRef]
4. Tozsin, G.; Oztas, T. Utilization of Steel Slag as a Soil Amendment and Mineral Fertilizer in Agriculture: A Review. *J. Agric. Sci. Tarim Bilim. Derg.* **2023**, *29*, 906–913. [CrossRef]
5. O'Connor, J.; Nguyen, T.B.T.; Honeyands, T.; Monaghan, B.; O'Dea, D.; Rinklebe, J.; Vinu, A.; Hoang, S.A.; Singh, G.; Kirkham, M.B.; et al. Production, characterisation, utilisation, and beneficial soil application of steel slag: A review. *J. Hazard. Mater.* **2021**, *419*, 126478. [CrossRef]
6. Mal, U.; Adhikari, K.; Tripathi, A. Steel plant slag dumps: A potential source of groundwater contamination. *J. Earth Syst. Sci.* **2022**, *131*, 45. [CrossRef]
7. Zhang, C.; Yu, H.; Zhu, X.; Yao, D.; Peng, X.; Fan, X. Unified Characterization of Rubber Asphalt Mixture Strength under Different Stress Loading Paths. *J. Mater. Civ. Eng.* **2024**, *36*, 04023498. [CrossRef]
8. Baalamurugan, J.; Kumar, V.G.; Padmapriya, R.; Raja, V.K.B. Recent applications of steel slag in construction industry. *Environ. Dev. Sustain.* **2024**, *26*, 2865–2896. [CrossRef]
9. Masilamani, A.; Ramalingam, M.; Kathirvel, P.; Murali, G.; Vatin, N.I. Mechanical, Physico-Chemical and Morphological Characterization of Energy Optimised Furnace (EOF) Steel Slag as Coarse Aggregate in Concrete. *Materials* **2022**, *15*, 3079. [CrossRef] [PubMed]
10. Edgar, M.; Hamdan, N.; Morales, D.; Boyer, T.H. Phosphorus removal by steel slag from tile drainage water: Lab and field evaluations. *Chemosphere* **2022**, *307*, 135850. [CrossRef] [PubMed]
11. Angst, U.M. Steel corrosion in concrete-Achilles' heel for sustainable concrete? *Cem. Concr. Res.* **2023**, *172*, 107239. [CrossRef]
12. Stefanini, L.; Ghorbani, S.; De Schutter, G.; Matthys, S.; Walkley, B.; Provis, J.L. Evaluation of copper slag and stainless steel slag as replacements for blast furnace slag in binary and ternary alkali-activated cements. *J. Mater. Sci.* **2023**, *58*, 12537–12558. [CrossRef]

13. Baalamurugan, J.; Kumar, V.G.; Prasad, B.; Padmapriya, R.; Karthick, V.; Govindaraju, K. Recycling of induction furnace steel slag in concrete for marine environmental applications towards ocean acidification studies. *Int. J. Environ. Sci. Technol.* **2022**, *19*, 5039–5048. [CrossRef]
14. Zaibo, L.; Tusheng, H.; Xuguang, Z.; Sanyin, Z. Cementitious Activity Evaluation of Steel Slag by EDTA-NaOH Solution Extraction Method. *Mater. Sci. Forum* **2017**, *893*, 389–394.
15. Ramezani, A.; Modaresi, S.; Dashti, P.; GivKashi, M.R.; Moodi, F.; Ramezanianpour, A.A. Effects of Different Types of Fibers on Fresh and Hardened Properties of Cement and Geopolymer-Based 3D Printed Mixtures: A Review. *Buildings* **2023**, *13*, 945. [CrossRef]
16. Neubert, L.; Kovtun, O.; Kreschel, T.; Volkova, O. Phosphorus Partition Between Liquid Crude Steel and High-Basicity Basic Oxygen Furnace Slags Containing V_2O_5. *Metall. Mater. Trans. B Process Metall. Mater. Process. Sci.* **2023**, *54*, 1524–1531. [CrossRef]
17. Gencel, O.; Karadag, O.; Oren, O.H.; Bilir, T. Steel slag and its applications in cement and concrete technology: A review. *Constr. Build. Mater.* **2021**, *283*, 122783. [CrossRef]
18. Al-Saedi, M.; Sabbar, A.S. Treatment of Expansive Soils with Slag: A Review Study. *Soil Mech. Found. Eng.* **2024**, *60*, 574–580. [CrossRef]
19. Devarangadi, M.; Shankar, M.U. Correlation studies on geotechnical properties of various industrial byproducts generated from thermal power plants, iron and steel industries as liners in a landfill-a detailed review. *J. Clean. Prod.* **2020**, *261*, 121207. [CrossRef]
20. Yuan, S.; Xiao, H.; Wang, R.; Li, Y.; Gao, P. Improved iron recovery from low-grade iron ore by efficient suspension magnetization roasting and magnetic separation. *Miner. Eng.* **2022**, *186*, 107761. [CrossRef]
21. Schneider, R.; Wiesinger, V.; Gelder, S.; Reiter, G. Effect of the Slag Composition on the Process Behavior, Energy Consumption, and Nonmetallic Inclusions during Electroslag Remelting. *Steel Res. Int.* **2023**, *94*, 2200483. [CrossRef]
22. Chowdhury, S.R. Recycled Smelter Slags for In Situ and Ex Situ Water and Wastewater Treatment-Current Knowledge and Opportunities. *Processes* **2023**, *11*, 783. [CrossRef]
23. Kurniati, E.O.; Pederson, F.; Kim, H.J. Application of steel slags, ferronickel slags, and copper mining waste as construction materials: A review. *Resour. Conserv. Recycl.* **2023**, *198*, 107175. [CrossRef]
24. Deus, A.C.F.; Büll, L.T.; Guppy, C.N.; Santos, S.D.M.C.; Moreira, L.L.Q. Effects of lime and steel slag application on soil fertility and soybean yield under a no till-system. *Soil Tillage Res.* **2020**, *196*, 104422. [CrossRef]
25. Singh, S.K.; Rekha, P.; Surya, M. Utilization of Linz-Donawitz slag from steel industry for waste minimization. *J. Mater. Cycles Waste Manag.* **2020**, *22*, 611–627. [CrossRef]
26. Kourounis, S.; Tsivilis, S.; Tsakiridis, P.E.; Papadimitriou, G.D.; Tsibouki, Z. Properties and hydration of blended cements with steelmaking slag. *Cem. Concr. Res.* **2007**, *37*, 815–822. [CrossRef]
27. Hajiaghamemar, M.; Mostofinejad, D.; Bahmani, H. A high-strength concrete resistant to elevated temperatures using steel slag aggregates. *Struct. Concr.* **2023**, *24*, 3162–3177. [CrossRef]
28. Yildirim, I.Z.; Prezzi, M. Chemical, Mineralogical, and Morphological Properties of Steel Slag. *Adv. Civ. Eng.* **2011**, *2011*, 463638. [CrossRef]
29. Alex, T.C.; Mucsi, G.; Venugopalan, T.; Kumar, S. BOF Steel Slag: Critical Assessment and Integrated Approach for Utilization. *J. Sustain. Metall.* **2021**, *7*, 1407–1424. [CrossRef]
30. Pathak, S.; Choudhary, R.; Kumar, A. Effect of Long-Term Binder Draindown on Performance of Open Graded Asphalt Friction Courses with BOF Steel Slag Aggregates. *J. Mater. Civ. Eng.* **2022**, *34*, 04021383. [CrossRef]
31. Ghorbani, S.; Sun, Y.B.; Mohan, M.K.; Matthys, S. Effect of copper and stainless steel slags on fresh, mechanical and pore structure properties of alkali activated ground granulated blast furnace slag. *Case Stud. Constr. Mater.* **2023**, *18*, e01981. [CrossRef]
32. Pasetto, M.; Baliello, A.; Giacomello, G.; Pasquini, E. Sustainable solutions for road pavements: A multi-scale characterization of warm mix asphalts containing steel slags. *J. Clean. Prod.* **2017**, *166*, 835–843. [CrossRef]
33. Tozsin, G.; Yonar, F.; Yucel, O.; Dikbas, A. Utilization possibilities of steel slag as backfill material in coastal structures. *Sci. Rep.* **2023**, *13*, 4318. [CrossRef] [PubMed]
34. Meshram, S.; Raut, S.P.; Ansari, K.; Madurwar, M.; Daniyal, M.; Khan, M.A.; Katare, V.; Khan, A.H.; Khan, N.A.; Hasan, M.A. Waste slags as sustainable construction materials: A compressive review on physico mechanical properties. *J. Mater. Res. Technol.* **2023**, *23*, 5821–5845. [CrossRef]
35. Aziz, I.H.; Abdullah, M.M.A.; Salleh, M.; Ming, L.Y.; Li, L.Y.; Sandu, A.V.; Vizureanu, P.; Nemes, O.; Mahdi, S.N. Recent Developments in Steelmaking Industry and Potential Alkali Activated Based Steel Waste: A Comprehensive Review. *Materials* **2022**, *15*, 1948. [CrossRef] [PubMed]
36. Evans, J.P. Return of results to the families of children in genomic sequencing: Tallying risks and benefits. *Genet. Med.* **2013**, *15*, 435–436. [CrossRef] [PubMed]
37. Xue, Y.; Wu, S.; Hou, H.; Zha, J. Experimental investigation of basic oxygen furnace slag used as aggregate in asphalt mixture. *J. Hazard. Mater.* **2006**, *138*, 261–268. [CrossRef] [PubMed]
38. Motz, H.; Geiseler, J. Products of steel slags an opportunity to save natural resources. *Waste Manag.* **2001**, *21*, 285–293. [CrossRef] [PubMed]
39. Kumar, H.; Varma, S. A review on utilization of steel slag in hot mix asphalt. *Int. J. Pavement Res. Technol.* **2020**, *14*, 232–242. [CrossRef]

40. Rajesh, A.A.; Senthilkumar, S.; Samson, S. Optimal proportional combinations of rubber crumbs and steel slag for enhanced concrete split tensile strength. *Mater. Rio De Jan.* **2023**, *28*, e2023020. [CrossRef]
41. Ren, Z.Y.; Li, D.S. Application of Steel Slag as an Aggregate in Concrete Production: A Review. *Materials* **2023**, *16*, 5841. [CrossRef] [PubMed]
42. Jiang, Y.; Ling, T.-C.; Shi, C.; Pan, S.-Y. Characteristics of steel slags and their use in cement and concrete—A review. *Resour. Conserv. Recycl.* **2018**, *136*, 187–197. [CrossRef]
43. Loureiro, C.D.A.; Moura, C.F.N.; Rodrigues, M.; Martinho, F.C.G.; Silva, H.; Oliveira, J.R.M. Steel Slag and Recycled Concrete Aggregates: Replacing Quarries to Supply Sustainable Materials for the Asphalt Paving Industry. *Sustainability* **2022**, *14*, 5022. [CrossRef]
44. Liu, J.Z.; Xu, J.; Liu, Q.; Wang, S.Y.; Yu, B. Steel Slag for Roadway Construction: A Review of Material Characteristics and Application Mechanisms. *J. Mater. Civ. Eng.* **2022**, *34*, 03122001. [CrossRef]
45. Nugmanova, A.; Shon, C.S.; Kim, J.R.; Rossi, C.O. Characterizing Chronologically Aged Basic Oxygen Furnace Slags as Aggregates and Their Use in Asphalt Concrete Mix as Filler. *Appl. Sci.* **2023**, *13*, 10126. [CrossRef]
46. Wang, X.; Zhang, M.; Li, S. Research and Application of Drum Method Stainless Steel Slag Treatment Technology. *Baosteel Technol.* **2020**, 73–77. Available online: https://kns.cnki.net/kcms2/article/abstract?v=1fhXvtqifPLIRZfH5frPT9ewWMGkVTVocbaRZQHn5UMlDUW6v_5au5Pa3uaUa_Ncd7FxfLHmoLesMPaJh4bRsNq65Uv76SewK8XcqVCcEEN8tS7kEF60TQt6dCABqCR9JsQJUNlyiQNqeskM2jehAA==&uniplatform=NZKPT&language=CHS (accessed on 15 January 2024).
47. Dilbas, H. Optimizing the Treatment of Recycled Aggregate (>4 mm), Artificial Intelligence and Analytical Approaches. *Materials* **2023**, *16*, 2994. [CrossRef]
48. Zhou, Y.; Ji, Y.; Zhang, Z.; Ma, Z.; Gao, F.; Xue, Q.; Xu, Z. Effect of acid-activation on CaO existential state and reactive properties of hot-splashed steel slag in cement-based materials. *Struct. Concr.* **2022**, *23*, 3819–3833. [CrossRef]
49. Teo, P.T.; Zakaria, S.K.; Salleh, S.Z.; Taib, M.A.A.; Sharif, N.M.; Abu Seman, A.; Mohamed, J.J.; Yusoff, M.; Yusoff, A.H.; Mohamad, M.; et al. Assessment of Electric Arc Furnace (EAF) Steel Slag Waste's Recycling Options into Value Added Green Products: A Review. *Metals* **2020**, *10*, 1347. [CrossRef]
50. *JTG E42-2005*; Test Code for Aggregate in Highway Engineering. Ministry of Communications Highway Science Research Institute: Beijing, China, 2005.
51. *GB/T 24765-2009*; Steel Slag for Wearing Asphalt Pave. China Iron and Steel Association: Beijing, China, 2010.
52. Fu, Q.; Xue, G.; Xu, S.; Li, J.J.; Dong, W. Mechanical performance, microstructure, and damage model of concrete containing steel slag aggregate. *Struct. Concr.* **2023**, *24*, 2189–2207. [CrossRef]
53. Hussain, A.; Hussaini, S.K.K. Use of steel slag as railway ballast: A review. *Transp. Geotech.* **2022**, *35*, 100779. [CrossRef]
54. Hassan, K.E.; Attia, M.I.E.; Reid, M.; Al-Kuwari, M.B.S. Performance of steel slag aggregate in asphalt mixtures in a hot desert climate. *Case Stud. Constr. Mater.* **2021**, *14*, e00534. [CrossRef]
55. Yu, H.M.; Wang, Q. *Steel Slag Treatment and Resource Utilization*; Metallurgical Industry Press: Beijing, China, 2015.
56. Kang, H.; Lee, Y.; Lee, J.; Moon, J. Importance of amorphous content, surface energy, and preferred orientation on the accurate quantification of cement minerals in clinkers. *J. Build. Eng.* **2023**, *66*, 105887. [CrossRef]
57. Xiaogang, Z. Synthesis, Composition, Structure, and Morphology of Hydrated Calcium Silicate. Master's Thesis, Wuhan University of Technology, Wuhan, China, 2010.
58. Zhang, H. *Preparation and Performance Study of Cement-Based Active Powder Concrete for 3D Printing*; North University of China: Taiyuan, China, 2020. [CrossRef]
59. Yao, D.; Yu, H.A.; Chen, X.; Yu, X.L.; Yao, J.L.; Zheng, X.G.; Zhang, C.; Gong, L.J. Effect of surface modification on properties of steel slag aggregate and mixture. *Constr. Build. Mater.* **2023**, *402*, 133058. [CrossRef]
60. Kaya, G.G.; Yilmaz, E.; Deveci, H. Synthesis of sustainable silica xerogels/aerogels using inexpensive steel slag and bean pod ash: A comparison study. *Adv. Powder Technol.* **2020**, *31*, 926–936. [CrossRef]

materials

MDPI

Article

Influence of Curing Temperature on the Performance of Calcined Coal Gangue–Limestone Blended Cements

Wenguang Zhang [1,†], Hao Zhou [2,†], Yueyang Hu [3], Jiaqing Wang [4], Jian Ma [1,*], Ruiyu Jiang [1] and Jinfeng Sun [1,*]

[1] Key Laboratory for Advanced Technology in Environmental Protection of Jiangsu Province, Yancheng Institute of Technology, Yancheng 224051, China; wenguangzhang1997@163.com (W.Z.); jiangry@ycit.edu.cn (R.J.)
[2] Nanjing Institute of Environmental Sciences, Ministry of Ecology and Environment of the People's Republic of China, Nanjing 210042, China; zhouhao@nies.org
[3] College of Materials Science and Engineering, Yancheng Institute of Technology, Yancheng 224051, China; huyueyang1989@163.com
[4] College of Civil Engineering, Nanjing Forestry University, Nanjing 210037, China; jiaqingw@njfu.edu.cn
* Correspondence: jian_ma@njtech.edu.cn (J.M.); jinfengsun1990@163.com (J.S.)
† These authors contributed equally to this work.

Abstract: The utilization of calcined coal gangue (CCG) and limestone for the preparation of blended cement is an efficient approach to address the issue of coal gangue disposal. However, the compressive strength development of blended cement is slow, particularly at high substitution levels of CCG. Therefore, this study aimed to promote the hydration and mechanical properties of the calcined coal gangue–limestone blended cements by increasing the curing temperature. In this study, the samples were cured at two different temperatures, namely 20 and 40 °C. The four groups of samples contained 15 wt.%, 30 wt.%, 45 wt.% and 60 wt.% cement substitutions using CCG and limestone (2:1 mass ratio). The compressive strength, hydration and microstructure were investigated at the ages of 1 to 28 d. X-ray diffraction (XRD) and thermogravimetry (TG) were used to study the hydration behavior of samples. Mercury intrusion porosimetry (MIP) and scanning electron microscopy (SEM) were used to determine the microstructure of the samples. The results indicate that an increase in curing temperature significantly promotes the compressive strength of the calcined coal gangue–limestone blended cements from 1 to 28 d. The microstructural analysis indicates that increasing the curing temperature not only promotes cement hydration but also facilitates the reaction of CCG, which precipitated more hydrates such as C-A-S-H gel, Hc and Mc. These hydrates are conducive to refining the pore structures and densifying the microstructure, which sufficiently explains the enhanced compressive strength of the calcined coal gangue–limestone blended cements.

Keywords: calcined coal gangue; limestone; curing temperature; hydration; microstructure; compressive strength

Citation: Zhang, W.; Zhou, H.; Hu, Y.; Wang, J.; Ma, J.; Jiang, R.; Sun, J. Influence of Curing Temperature on the Performance of Calcined Coal Gangue–Limestone Blended Cements. *Materials* **2024**, *17*, 1721. https://doi.org/10.3390/ma17081721

Academic Editor: Danuta Barnat-Hunek

Received: 4 March 2024
Revised: 21 March 2024
Accepted: 7 April 2024
Published: 9 April 2024

1. Introduction

Coal is an important energy resource in many countries. The top five countries holding proved coal reserves globally are the United States (22%), Russia (15%), Australia (14%), China (14%), and India (11%) [1]. Coal gangue (CG) is one of the largest industrial wastes, which is mainly discharged in the process of coal mining and washing. China has large reserves of about 6 billion tons of CG and is expected to increase by approximately 500–800 million tons for each year [2]. However, its utilization rate is less than 20%. CG is mainly composed of SiO_2 and Al_2O_3 (50–70% wt.%), even though its chemical compositions vary with different sources [3]. Such high SiO_2 and Al_2O_3 contents make it possible to be used as a potential SCM in cement-based materials [4]. The current research has demonstrated that CG can be used as a potentially active SCM to partially replace cement after calcination at appropriate temperatures (usually 700–900 °C) [5]. In the calcination process, kaolinite ($Al_2O_3{\cdot}2SiO_2{\cdot}H_2O$, AS_2H_2) would dehydroxylate to form metakaolin ($Al_2O_3{\cdot}2SiO_2$, AS_2) [6,7], which was the main source of the pozzolanic reactivity of calcined coal gangue (CCG) [8].

Extensive studies indicate incorporating an appropriate amount of CCG as a partial replacement of cement can maintain a relatively high long-term mechanical strength [9,10]. This is because as the curing time increased, the amorphous metakaolin with high pozzolanic reactivity in CCG gradually started to react with portlandite (CH) to form additional C-A-S-H gel [11], which resulted in a higher strength growth rate as compared with the pure cement especially from 7 days onwards [12]. In this process, pore structure distributions in the hydrated binder have also been refined [13], which is reflected in the reduction in the large pores and formation of more gel pores with lower size. More importantly, the pore structure refinement and ion consolidation ability of C-A-S-H gel are also favorable for resisting the penetration and transmission of corrosive ions, such as Cl^- and SO_4^{2-} [14]. Therefore, CCG-blended cement also secure satisfactory long-term durabilities in severe environments as compared with the corresponding reference samples. Additionally, the pozzolanic reactivity [15], fineness [16], and replacement level of CCG were also found to influence the performance of the CCG-blended cement. The application of CCG is generally limited to 10–20 wt.%. However, with a higher replacement amount, the performance of composites cement would decrease remarkably.

In recent years, some researchers have begun to introduce limestone to the binary system of calcined coal gangue-cement [17,18], which is originated from limestone calcined clay cement (LC^3) [19]. In LC^3, the high pozzolanic reactivity of calcined kaolinite clay (metakaolin) and the synergistic effect between metakaolin and limestone produce C-A-S-H gel, hemicarboaluminate (Hc) and monocarboaluminate (Mc) [20], which allows a higher cement replacement of up to 50 wt.% in LC^3 without comprising its compressive strength [21]. Given that kaolinite is also one of the major minerals in CG, it is theoretically feasible to use CCG instead of calcined kaolinite clay in LC^3. Liu et al. [18] reported that the co-utilization of CCG (with kaolinite content of 28.4%) and limestone maximized the level of substitution of cement up to 30% (2:1 mass ratio). The ternary binder comprising 10% CCG and 5% limestone achieved comparable compressive strength to the reference mortar at 7 d. Moreover, for a given replacement level, the limestone can enhance the compressive strength of CCG blended cement by approximately 5–12% from 7 d onwards. The authors [18] attribute this observation to the synergistic effect between CCG and limestone, forming more hydrates (C-A-S-H gel, Hc and Mc) and refining the pore structure. As shown by Jiu et al. [17], compared with the reference cement paste, the paste with 40–50% partial replacement of cement by combined CCG and limestone (1:1, 2:1 and 3:1 mass ratio) exhibited a 14–35% increase in the 28-day compressive.

The limestone calcined coal gangue composite provides satisfactory late-strength advantages. However, the existing research also concluded that both calcined coal gangue-blended cements and the limestone-calcined coal gangue composite present characteristic of much slower compressive strength development compared to the reference Portland cement, especially at higher replacement levels. Take the work of Liu et al. [18] as an example: the mortar prepared with 20% CCG and 10% limestone showed a 46.6% decrease in the 1-day compressive strength compared with the reference mortar. This is also similar to other SCM-blended cements [22,23]. Most of these observations can be related to the significant lower reaction kinetics of SCMs than that of clinker phases [24]. In practical engineering, the slow early-strength development usually limits the large-scale utilization of SCMs.

It has been reported that approximately increasing the curing temperature is beneficial for achieving a higher early compressive strength of cement-based materials [25,26]. When the curing temperature is increased, the hydration kinetics of cement is greatly enhanced, which is reflected in the increased cement hydration degree [25] and is also supported by the classical boundary nucleation and growth (BNG) model [27,28]. More hydrates such as C-S-H gel are precipitated and effectively contributed to the early compressive strength development of pure cement mortar [29]. As for the SCMs-blended cement, especially a higher 30% substitution of SCMs for cement [30,31], these promotional effects are more significant. Many of the results indicate that the reactions of SCMs were also enhanced apart from cement hydration [32,33], which were also the main contributors to the compressive strength development at early and later curing ages. However, no relevant studies have reported the effect of curing temperature on the performance of calcined coal gangue–limestone blended cements so far. This part of the study should be paid attention to, because if the early strength of this blended cement can be improved by increasing the curing temperature, the application of calcined coal gangue in cement-based cementitious materials can be greatly promoted. In addition, the resource treatment of coal gangue can be accelerated to a certain extent.

Based on the research gaps of the existing studies, this research aimed at investigating the effect of curing temperature on hydration and the microstructure properties of calcined coal gangue–limestone blended cements. Four groups of samples with 15 wt.%, 30 wt.%, 45 wt.% and 60 wt.% cement substitutions using calcined coal gangue and limestone (2:1 mass ratio) were designed for the experimental investigations. The curing temperatures were set at 20 and 40 °C up to 28 d. These temperature are usually set as the curing temperature in the current research, which can cover ranges representative of common practice in a place of perennial heat [33]. The evolution in the compressive strength of the mortars was first examined. Then, the X-ray diffraction (XRD), thermogravimetry (TG), mercury intrusion porosimetry (MIP) and scanning electron microscopy (SEM) tests were performed on the corresponding pastes to disclose the mechanism of compressive strength development.

2. Materials and Methods

2.1. Starting Materials

The Portland cement (P.I. 42.5) used in this study was obtained from Fushun Cement Co., Ltd. (Fushun, China) Limestone with a purity of 85% and was provided by Zaozhuang Building Materials Co., Ltd. (Zaozhuang, China). The coal gangue was collected from Huainan City, Anhui Province. Table 1 summarizes the chemical composition of each material. After being received, the coal gangue was further dried, crushed, ground and finally calcined at 800 °C for 2 h. Figure 1a shows the XRD patterns of the coal gangue before and after calcination. As observed, mica, kaolinite, quartz, and siderite are the major minerals in CG. After calcination, the characteristic peaks for kaolinite (2θ = 12.29°, 24.85°, 28.75°, 34.96°, 37.73°, 62.18°) disappeared by calcining at 800 °C, which clearly indicates a complete decomposition of kaolinite. It can be calculated from TG curves (Figure 1b) using the tangent method that the kaolinite content of coal gangue was approximately 14.1%. Additionally, the sand complied with GB/T 17671-2021 [34] and provided by Xiamen ISO Standard Sand Co., Ltd. (Xiamen, China) was used for the mortars' preparation.

Table 1. Chemical compositions of raw materials (wt.%).

	CaO	SiO_2	Al_2O_3	Fe_2O_3	MgO	SO_3	Na_2O	K_2O	TiO_2	P_2O_5	LOI
Cement	54.0	17.6	3.7	3.3	2.4	2.9	0.1	0.7	0.3	0.1	14.6
Limestone	55.6	5.2	2.4	1.3	2.7	0.2	0.03	0.6	0.1	0.3	31.6
CG	1.2	43.6	19.3	2.6	0.4	0.1	0.3	1.1	0.7	0.1	16.5

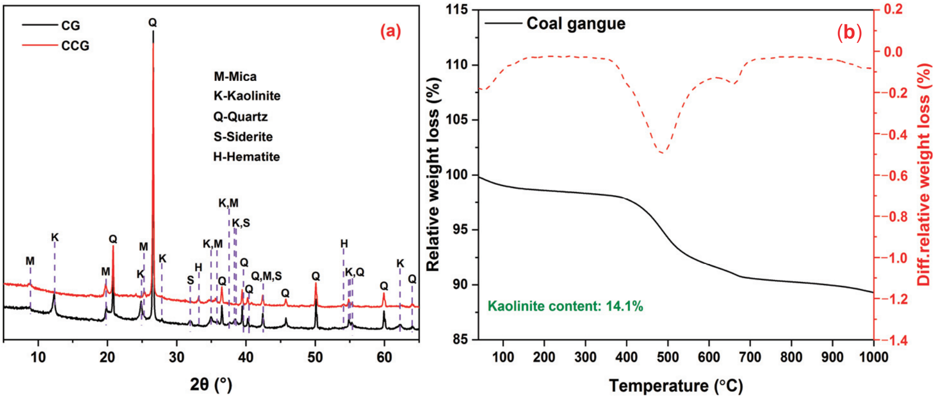

Figure 1. (**a**) XRD patterns and (**b**) TG/DTG curves of CG and CCG.

2.2. Mixture Proportions

The detailed mixture proportions of mortars are displayed in Table 2. Mortars were prepared with a constant water to binder (w/b, binder = cement + limestone + calcined coal gangue) ratio of 0.5 and a constant sand to binder ratio of 3. The pure Portland cement mortar was used as the reference sample. Four different limestone and calcined coal gangue combinations were designed, and they were, respectively, at total OPC replacement levels of 15%, 30%, 45% and 60% by mass. The mass ratio between calcined coal gangue and limestone was fixed at 2:1. Specially, additional gypsum was added to achieve an adequate sulfate balance of the systems. As shown in Table 2, the notation was given according to the curing temperatures, constituents and the corresponding weight percentage in the binders. Take T40-CCGL60 as an example; it refers to the sample consisting of 40 wt.% CCG and 10 wt.% limestone, which was cured at the temperature of 40 °C.

Table 2. Detailed mix proportions of the mortar (g, 100 g base for binder).

T	Notation	OPC	CCG	LS	Gypsum	Water	Sand
20 °C	T20-OPC	100	0	0	0	50	300
20 °C	T20CCGL15	84.8	10	5	0.2	50	300
20 °C	T20CCGL30	69.6	20	10	0.4	50	300
20 °C	T20CCGL45	54.4	30	15	0.6	50	300
20 °C	T20CCGL60	39.2	40	20	0.8	50	300
40 °C	T40-OPC	100	0	0	0	50	300
40 °C	T40-CCGL15	84.8	10	5	0.2	50	300
40 °C	T40-CCGL30	69.6	20	10	0.4	50	300
40 °C	T40-CCGL45	54.4	30	15	0.6	50	300
40 °C	T40-CCGL60	39.2	40	20	0.8	50	300

2.3. Mortars and Pastes Preparation

They were prepared according to the Chinese standard GB/T 50081-2019 [35]. All materials involved in Table 2 were respectively pre-cured at the target temperatures for 1 d. Cement, CCG, limestone and gypsum were weighed according to Table 2, and they were uniformly mixed using a high-shear mixer. After this, the above mixtures, sand and water (or PCE if needed) were mixed to prepare the mortar. The fresh mortar was cast into cubic samples with a size of 40 × 40 × 40 mm^3 followed by being, respectively, cured at the temperatures of 20 and 40 °C for 1 d. Then, the samples were removed from the molds and transferred to a water curing tank with the same temperatures as that of the fresh mortar for the compressive strength test at the designated curing ages.

Pastes were used for better revealing the mechanism of compressive strength changes resulted from altering the curing temperatures. Their mix proportions were referred to Table 2 without taking sand and PCE into consideration. The procedure of paste preparations and the curing conditions are the same as that of the mortar. Once at the required testing ages, the samples were crushed into small pieces and then were immersed in ethanol for 7 d to stop the hydration. Afterwards, the ethanol was decanted, and part of the piece samples was directly dried in a vacuum drying oven at 40 °C for 48 h. Finally, these samples were used for the MIP and SEM analysis. Another part of the pieces without being dried was finely ground to <75 μm, which was followed by the same drying regime in the vacuum-drying oven for XRD and TG tests. It is notable that all hydration-stopped samples were always kept in the vacuum-drying oven to avoid being carbonated until the tests.

2.4. Analytical Techniques

The compressive strength test followed GB/T 50081-2019, and it was performed on a YYW-300 DS hydraulic testing machine (Zhejiang Yiyu Instrument Equipment Co., Ltd., Shaoxing, China) with a 300 kN capacity. Mortars were tested at the required curing ages of 1 day, 3, 7 and 28 days. The applied loading rate on the samples was 2400 N/s. For each group of the sample, the average of the three tests is considered as the final compressive strength.

A Rigaku SmartLab 3000A X-ray diffractometer (Rigaku, Tokyo, Japan) equipped with CuKα X-rays was used to determine the mineralogical composition of the hydrated pastes. The 2θ scan range was 5–65° with a scan speed of 5°/min, and the operating conditions were 15 KV and 40 mA.

A NETZSCH STA 449F3 differential thermal analyzer (NETZSCH Analyzing & Testing, Selb, Germany) was used for the TG-DTG analysis of the hydrated paste samples with samples subjected to a temperature range of 40 °C to 1000 °C and a temperature increase rate of 10 °C/min.

A PoreMaster GT produced by Quantachrome (Boynton Beach, FL, USA) is used for analysis of the pore structure of the paste samples. The intrusion pressure was gradually increased from 0.10 to 60 psia, and the pores ranging from 3.6 nm to 950 μm can be probed.

A Nova NanoSEM 450 scanning electron microscope (FEI, Hillsboro, OR, USA) was used to observe the morphology of the hydrated paste samples. All samples were coated with a layer of gold to increase the conductivity of samples.

3. Results and Discussion

3.1. Compressive Strength

Figure 2 displays the compressive strength of the mortars cured at 20 and 40 °C up to 28 d. As shown in Figure 2a, the compressive strength of mortars at 1 d decreased with the increase in the replacement level of cement regardless of the curing temperature. This is expected and can be explained by the dilution of cement with an increased content of limestone and CCG and a much lower reaction activity of limestone and CCG than that of cement, which resulted in a significant reduction in the compressive strength. On the contrary, it can be clearly seen that the increased curing temperature evidently promoted the 1-day compressive strength. For the reference mortar, its 1-day compressive strength achieved 13.1 MPa at 20 °C, while this value increased to 19.4 MPa at 40 °C with an increase of about 48.7%. Similar trends can also be observed in the mortars with adding CCG and limestone, but their strength development tends to be more sensitive to curing temperature, especially for higher coupled limestone and CCG content. Take CCGL15 as an example, the curing temperature of 40 °C resulted in an increase in the compressive strength by approximately 51% as compared to 20 °C. Similarly, for CCGL15, the corresponding growth rate increased up to about 420%.

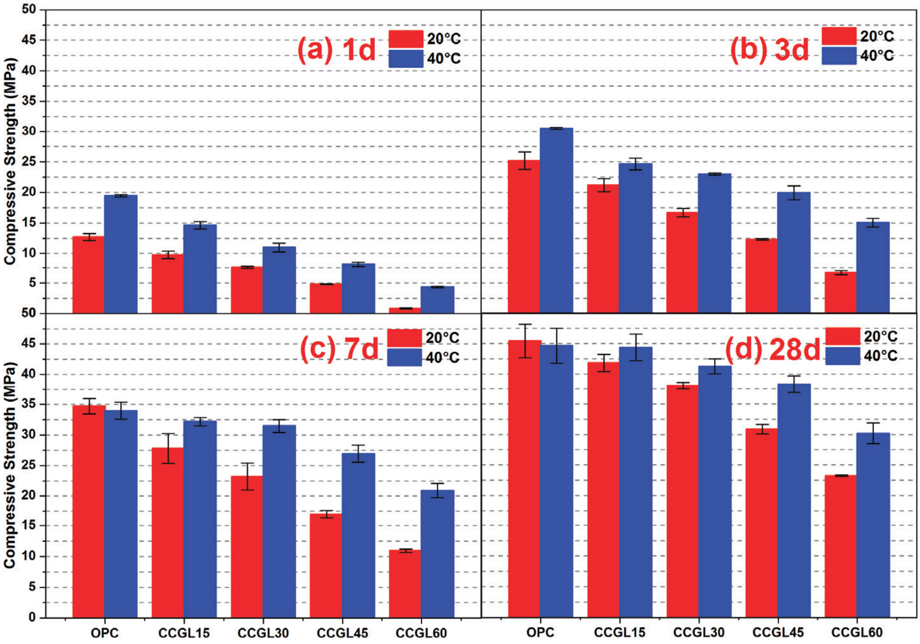

Figure 2. Compressive strength of mortar samples cured at 20 and 40 °C up to 28 d.

Similarly, the strength development of the mortars at 3 (Figure 2b) and 7 d (Figure 2c) also displays a close dependence on the curing temperatures. In the case of the reference mortar, the compressive strength at 3 d increased by 5.1 MPa from 20 to 40 °C, but it was comparable at 7 d. Studies have shown that increasing the curing temperature could accelerate the early age of cement hydration and promote early strength development [26]. Unlike the reference mortar, the increase in curing temperature from 20 to 40 °C enhanced the compressive strength of CCGL15, CCGL30, CCGL45 and CCGL60, respectively, by 3.5, 6.3, 7.6 and 8.3 MPa at 3 d, and 3.5, 6.3, 7.6 and 8.3 MPa at 28 d. These faster strength gains than the reference mortar could be possibly interpreted as there being faster reactions and more hydrates generated in these CCG- and limestone-added systems as the consequence of increased curing temperature. Additionally, it is also interesting to note that the CCGL30 mortars gained comparable compressive strength to the CCGL15 mortars with a curing temperature of 40 °C both at 3 and 7 d, indicating that the compressive strength of the lower clinker system is more sensitive to the curing temperature.

With the curing age increased up to 28 d (Figure 2d), the curing temperature displays limited influence on the compressive strength of reference mortar, which is reflected by the comparable strength values upon increasing the curing temperature from 20 to 40 °C. On the contrary, for different CCGL mortars, their strength values at 40 °C are expected to be higher than at 20 °C, indicating that increasing the curing temperature is still beneficial to developing the compressive strength of CCGL mortars. But the difference in the strength values between 20 and 40 °C appears smaller and smaller, which is possibly related to the great reaction of CCG in this period that makes up for the strength development of mortars with CCG and limestone to some extent.

In order to better disclose the potential mechanism of the compressive strength development of these mortars, the systems of OPC and CCGL30 curing at 20 and 40 °C were selected for the further microstructural analysis.

3.2. XRD Analysis

Figures 3–6 shows the phase assemblages of T20-OPC, T40-OPC, T20-CCGL30 and T40-CCGL30 hydrated from 1 to 28 d, respectively. As observed, the primary clinker phases of C_3S and C_2S are present throughout the hydration process in these four samples, and the main crystalline hydrates of ettringite (AFt) and portlandite (CH) are also precipitated in these samples at the beginning of 1 d (Figure 3) and exist during the whole curing age.

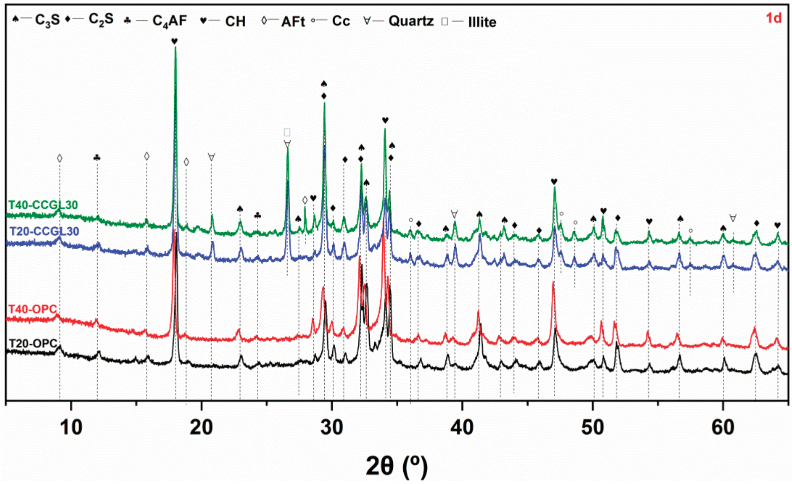

Figure 3. XRD patterns of paste samples cured at 20 and 40 °C at 1 d (C_3S: tricalcium silicate, C_2S: dicalcium silicate, C_4AF: ferrite, CH: portlandite, AFt: ettringite, Cc: calcite).

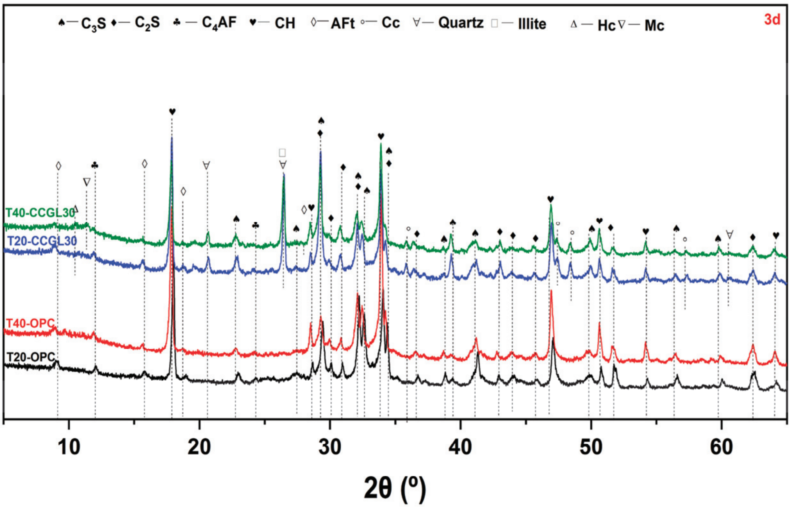

Figure 4. XRD patterns of paste samples cured at 20 and 40 °C at 3 d (C_3S: tricalcium silicate, C_2S: dicalcium silicate, C_4AF: ferrite, CH: portlandite, AFt: ettringite, Cc: calcite).

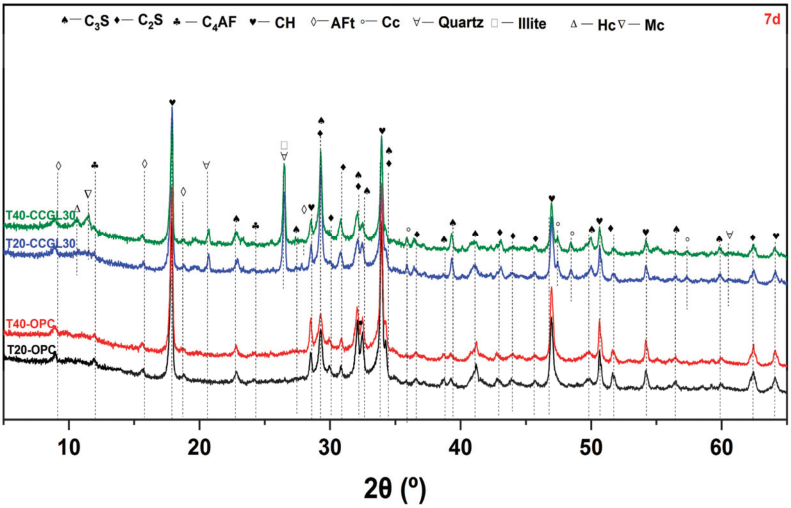

Figure 5. XRD patterns of paste samples cured at 20 and 40 °C at 7 d (C_3S: tricalcium silicate, C_2S: dicalcium silicate, C_4AF: ferrite, CH: portlandite, AFt: ettringite, Cc: calcite).

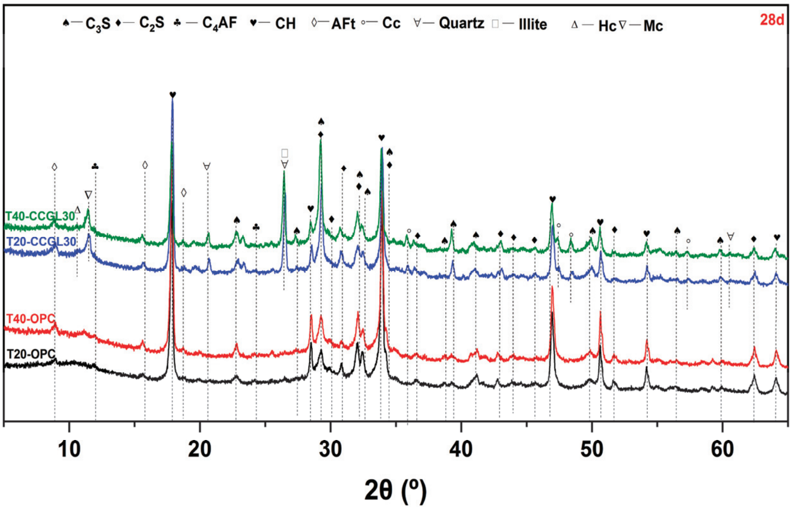

Figure 6. XRD patterns of paste samples cured at 20 and 40 °C at 28 d (C_3S: tricalcium silicate, C_2S: dicalcium silicate, C_4AF: ferrite, CH: portlandite, AFt: ettringite, Cc: calcite).

In order to better compare the influence of curing temperature on cement hydration, the overlapped C_3S and C_2S peak centered at 32.5° 2θ was selected for better comparison. As shown in Figure 3, compared with T20-OPC, the intensity of this peak decreased in T40-OPC, indicating that increasing the curing temperature accelerated cement hydration. Since CH in only precipitated from C_3S and C_2S hydration, the precipitation of CH was also enhanced, as evidenced by the intensity in the characteristic peak of CH centered at 18.0° 2θ also increasing accordingly. These changes were also observed at 3 and 7 d of curing (Figures 4 and 5). However, the difference in the peak intensity centered at 32.5° 2θ is difficult to observe at 28 d (Figure 6), which reflected that increasing the curing temperature up to 40 °C is not effective in enhancing cement hydration.

A similar promotion effect in cement hydration with the increasing curing temperature can also observed in the samples of T20-CCGL30 and T40-CCGL30. Different from T20-OPC and T40-OPC, the phase of hemi-carboaluminate (Hc) with a characteristic peak centered at 32.5° 2θ was observed in T20-CCGL30 at 7 d due to the presence of limestone (Figure 5). After 28 d of curing, the characteristic peak of mono-carboaluminate (Mc) centered at 32.5° 2θ appeared while the peak of Hc was negligible. This resulted from the transformation from Hc to Mc. When the curing temperature increased to 40 °C, both the Hc and Mc peaks started to appear from 3 d. The Hc peak can still be observed at 7 d, but it disappeared at 28 d. This reflected that a higher curing temperature was conducive to not only the formation of Hc and Mc but also the transformation from Hc to Mc. Note that by the comparison of T20-CCGL30, the peak intensity of CH centered at 18.0° 2θ in T40-CCGL30 was also much lower from 3 d onwards, which is because the accelerated reaction of CCG under a higher reaction temperature consumed more CH.

3.3. Thermal Analysis

The TG/DTG curves of all samples at curing ages ranging from 1 to 28 d are illustrated in Figures 7–10. From the DTG results, it can be seen that three major mass loss peaks are observed. The first peak of mass loss, occurring between 40 and 200 °C, primarily results from the dehydration process of calcium silicate hydrate (C-S-H) and ettringite (AFt). The second mass loss peak within the temperature range of 400–500 °C is attributed to the decomposition of portlandite (CH). Lastly, the mass loss occurring between 600 and 800 °C mainly arises from the decarbonation process of $CaCO_3$. In addition, the mass losses in different temperature ranges were also calculated according to TG/DTG curves, and the results are listed in Table 3.

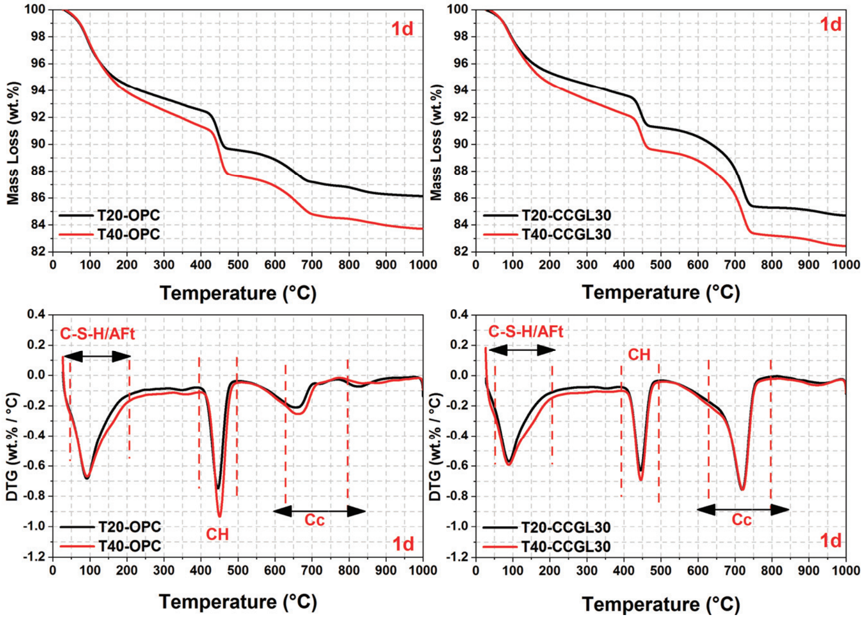

Figure 7. TG-DTG curves of hardened pastes at 1 day.

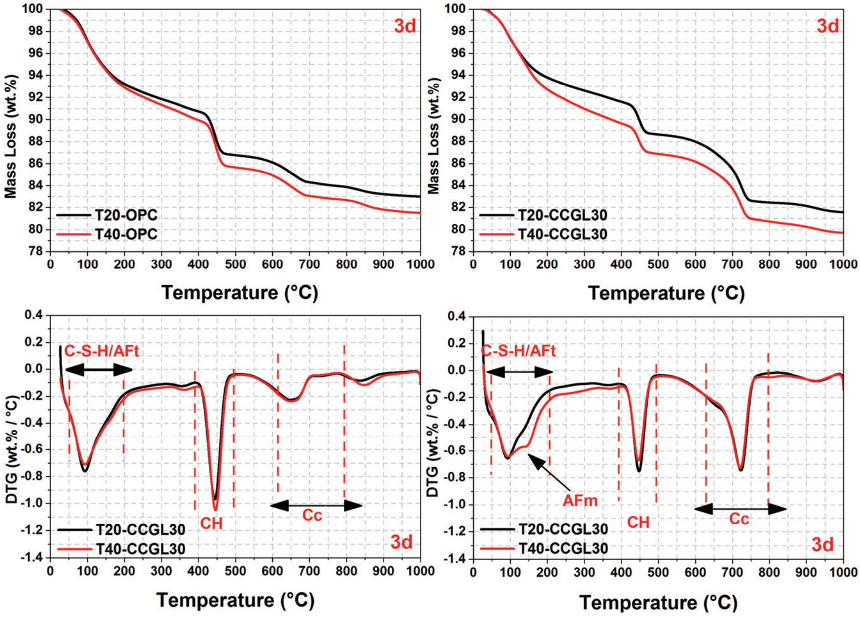

Figure 8. TG-DTG curves of hardened pastes at 3 days.

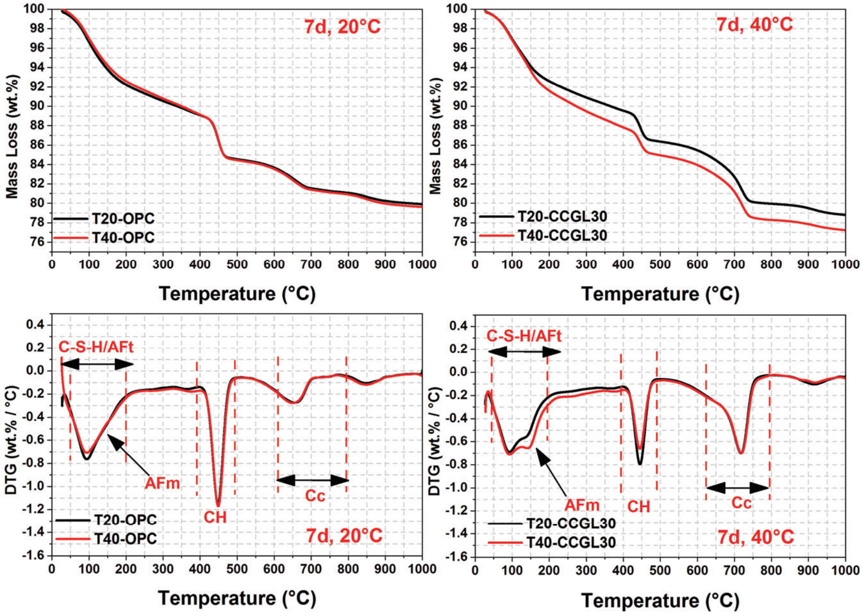

Figure 9. TG-DTG curves of hardened pastes at 7 days.

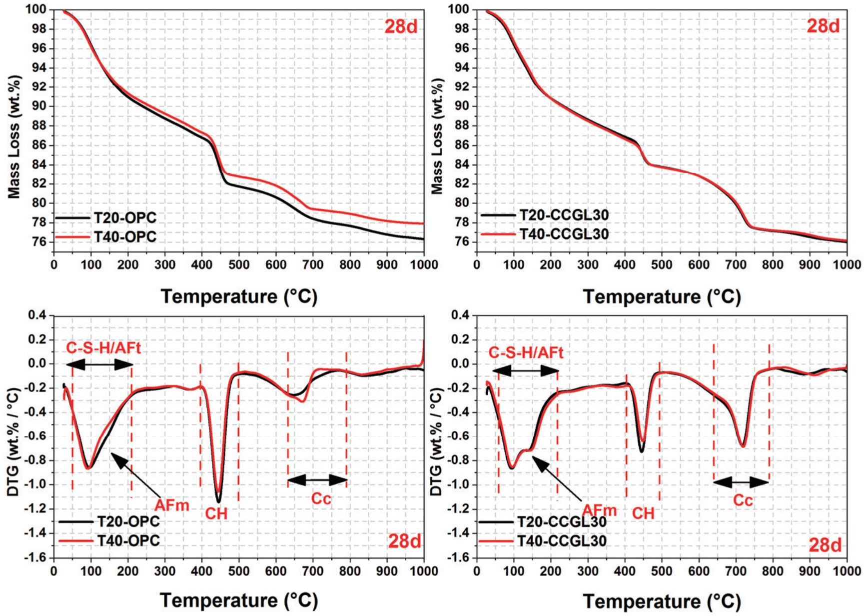

Figure 10. TG-DTG curves of hardened pastes at 28 days.

Table 3. Relative mass loss at different temperature ranges (%).

Curing Age	Stage	OPC		CCGL30	
		20 °C	40 °C	20 °C	40 °C
1 d	40–200 °C	5.41	5.82	4.89	5.93
	400–500 °C	2.97	3.74	2.47	2.79
	40–1000 °C	9.69	11.17	13.9	15.81
3 d	40–200 °C	6.63	6.59	6.58	7.82
	400–500 °C	3.69	4.23	3.04	4.61
	40–1000 °C	11.91	12.17	16.69	17.08
7 d	40–200 °C	6.84	6.23	7.66	8.78
	400–500 °C	4.58	4.73	3.26	2.96
	40–1000 °C	13.13	12.05	18.49	19.48
28 d	40–200 °C	7.94	8.01	9.65	9.82
	400–500 °C	4.42	4.59	3.18	3.01
	40–1000 °C	14.21	13.85	20.62	20.44

As observed in Figures 7–9, the overall mass loss of T40-OPC was much higher than that of T20-OPC from 1 to 3 d, indicating the hydration of cement at the early curing ages was accelerated upon increasing the curing temperature. However, T40-OPC presented a comparable overall mass loss to T20-OPC at 7 d (Figure 10), but it was much lower at 28 d, indicating that the curing temperature has a limited or even negative influence on the hydration of cement upon further increasing the curing age from 7 to 28 d.

As shown in Figure 9, the overall mass loss of CCGL30 cured at 40 °C was still significantly higher than that cured at 20 °C at 7 d. On the contrary, the area of CH in T40-CCGL30 started to be much lower than that in T20-CCGL30 from 3 d, indicating that CH was greatly consumed during this period. It should also be pointed out that the sample of T40-CCGL30 exhibited traces of AFm-type hydrates at 3 d (see Figure 8), which reflected that CCG started to react with limestone to precipitate AFm-type hydration products such as Hc and Mc. These phases were only detected in T20-CCGL30 at 7 d or even later.

This means that the reaction between CCG and limestone was promoted. These findings are consistent with the XRD observations, where increasing the curing temperature not only promoted cement hydration at early ages but also promoted the reaction of CCG, as evidenced by the accelerated consumption of CH and early appearance of AFm phases. The positive effect on the reactions of OPC and CCGL30 systems that resulted from increasing the curing temperature also well explained the compressive strength development of the corresponding mortars, as observed in Figure 2.

3.4. Pore Structure Analysis

The total porosity and pore size distribution of hardened pastes can be obtained based on the test results of MIP analysis. The effects of curing temperature on the pore structure of hardened pastes at 1 d and 28 d are illustrated in Figures 11 and 12, respectively. The total porosity of hardened pastes is listed in Table 4.

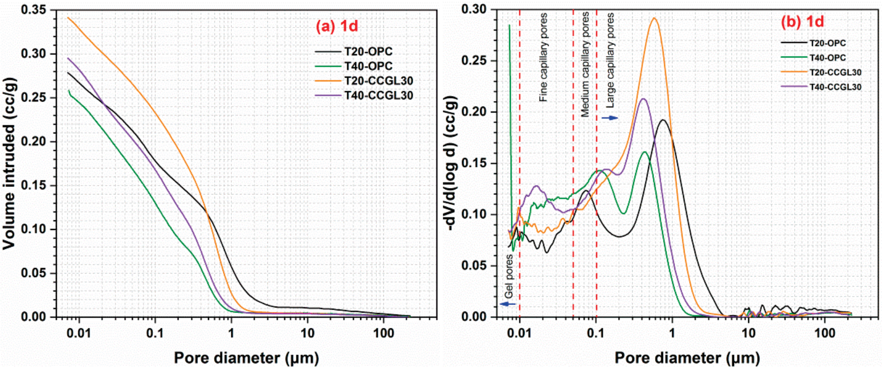

Figure 11. (**a**) Cumulative and (**b**) incremental pore volume of hardened pastes at 1 d.

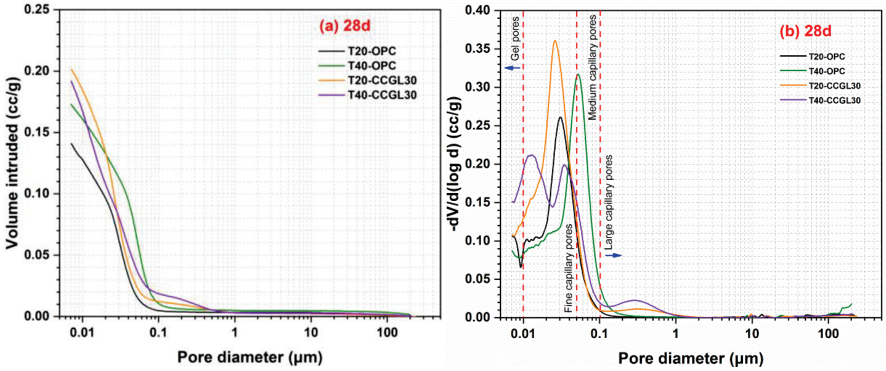

Figure 12. (**a**) Cumulative and (**b**) incremental pore volume of hardened pastes at 28 days.

Table 4. Total porosity of samples (%).

	1 d	28 d
T20-OPC	27.91	14.07
T40-OPC	25.88	19.17
T20-CCGL30	34.18	20.10
T40-CCGL30	29.47	19.14

At 1 d, the total porosity of hardened pastes decreased when the curing temperature was increased in both OPC and CCG systems (see Figure 11a). The increase in temperature promotes the hydration of the system, leading to the formation of more hydration products. As a result, the overall porosity of the system is reduced. The total porosity of the CCG system is higher than that of the OPC system at the same curing temperature, especially for the CCG system cured at 20 °C. This difference can be mainly attributed to the slower reaction kinetics of calcined coal gangue and limestone. Additionally, the total porosity of the CCG system cured at 40 °C is comparable to that of the OPC system cured at 20 °C, indicating that elevating the curing temperature significantly contributes to reducing the total porosity of the CCG system. The pore size distribution of hardened pastes at 1 d is illustrated in Figure 11b. As observed, the pores in hardened pastes can be categorized as gel pores (<0.01 μm), fine capillary pores (0.01–0.05 μm), medium capillary pores (0.05–0.1 μm), and large capillary pores (>0.1 μm). The refinement of the pore structure in the hardened paste is evidently observed with an increase in curing temperature, leading to a shift of the distribution curve from larger pores toward smaller ones.

As shown in Figure 12, unquestionably, the total porosity of hardened cement pastes decreases with the increase in curing age due to the continuous reaction of reactants that filled the pores. Similar to 1 d, the total porosity of the CCG systems decreased upon increasing the curing temperature at 28 d, indicating that a higher curing temperature continued to reduce the porosity of CCG. However, it is worth noting that in the OPC system, increasing the curing temperature leads to an increase in total porosity, which is possibly due to the adverse impact of high-temperature curing on the subsequent structural compaction. Figure 12b shows the pore size distribution of hardened pastes at 28 d. The pores of hardened pastes can also be categorized into four parts. The pore structure at 28 d is significantly finer compared to that of 1 d, which is mainly due to the continuous hydration process in the systems. The pore sizes of all systems are predominantly distributed within the range of fine capillary pores and medium capillary pores. The pore structure of OPC samples cured at 40 °C is more evenly distributed in medium capillary pores compared to that of OPC samples cured at 20 °C, which is consistent with the total porosity of the OPC sample cured at 40 °C being higher than that of the sample cured at 20 °C. The pore size distribution of CCG samples is predominantly concentrated in fine capillary pores. In contrast, the pore size distribution curve of CCG samples cured at 40 °C exhibits a greater shift toward gel pores. The CCG samples demonstrate a favorable pore structure in later stages, and elevating the curing temperature contributes to further refinement of the pore structure.

3.5. SEM Analysis

Figure 13 shows the morphology of T20-OPC, T40-OPC, T20-CCGLS30 and T40-CCGLS30 at 1 d. As shown in Figure 13a, T20-OPC presented loose morphology with many pores left by the free water, while denser morphology with less pores was available in T40-OPC (Figure 13b). Similarly, T40-CCGLS30 also revealed a much more compact structure than T20-CCGLS30. This can be mainly attributed to the increased curing temperature that greatly promoted cement hydration at 1 d, which produced more hydrates and densified the microstructure. These changes are also have significantly positive effects on the pore structures' refinement (Figure 11) and early compressive strength development (Figure 2).

After 28 d of hydration (Figure 14), the continuous cement hydration precipitated more hydrates and forming a connected morphology of T20-OPC and T40-OPC. However, the morphologies of T20-OPC and T40-OPC are comparable, indicating that increased the curing temperature had a limited effect on the microstructure of OPC. On the contrary, the morphology of T40-CCGLS30 is still much denser than that of T20-CCGLS30 in this period, which is mainly due to the promotion effect of the increased curing temperature on CCG reactions that produced more hydrates (C-A-S-H gel, Hc and Mc). This also well explained the higher compressive strength of T40-CCGLS30 than that of T20-CCGLS30 at 28 d (Figure 2).

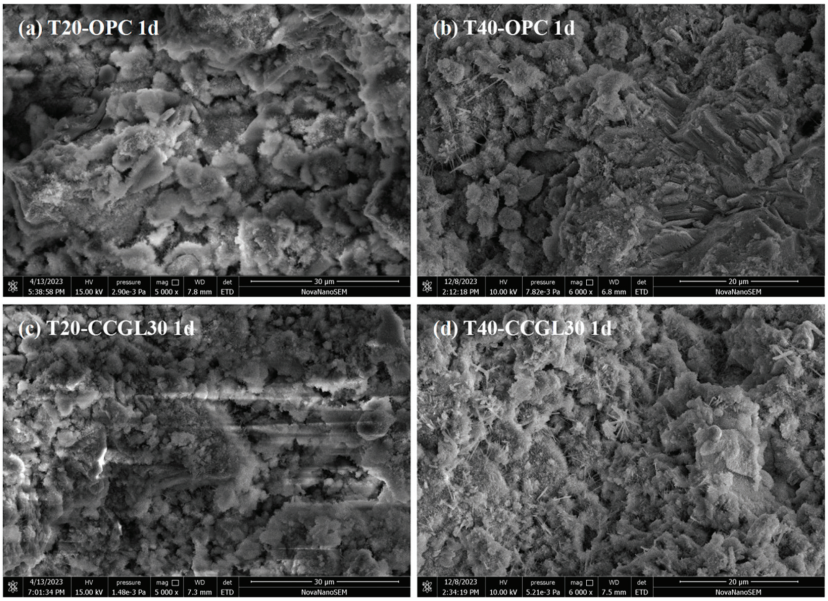

Figure 13. SEM observation of hardened pastes at 1 d.

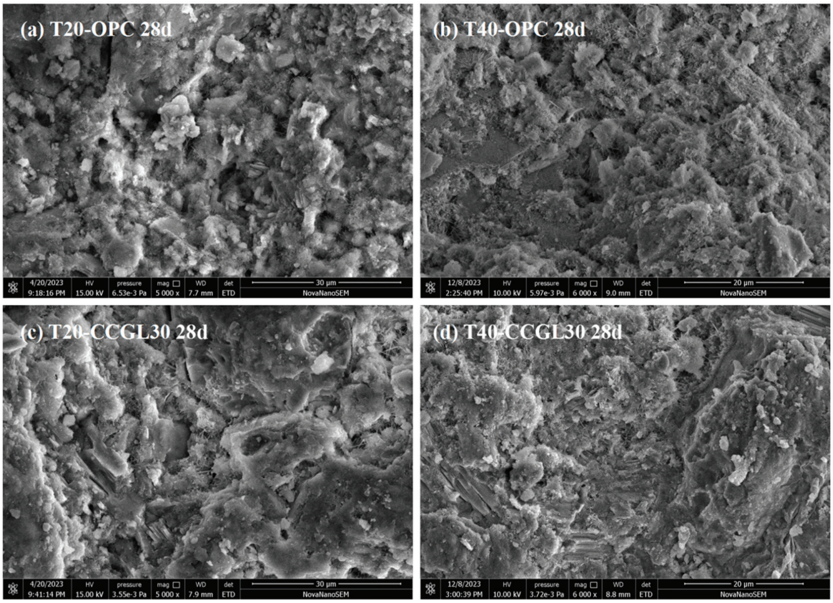

Figure 14. SEM observation of hardened pastes at 28 d.

4. Conclusions

This research investigated the influence of curing temperature on the hydration properties of blended cement with limestone and calcined coal gangue. Based on the results and discussion, the following conclusions can be drawn:

- The compressive strength of the calcined coal gangue–limestone blended cements is effectively enhanced by elevating the curing temperature to 40 °C, particularly in low clinker systems which exhibit greater sensitivity toward temperature.
- In calcined coal gangue–limestone blended cements, increasing the curing temperature not only promotes cement hydration but also facilitates the reaction of CCG, which precipitated more hydrates such as C-A-S-H gel, Hc and Mc.
- The total porosity of the calcined coal gangue–limestone blended cements decreases with increasing curing temperature. At 20 °C, the pore size distribution is mainly concentrated in fine capillary pores. At 40 °C, there is a more pronounced shift toward gel pores observed in the pore size distribution curve.
- The calcined coal gangue–limestone blended cements will exhibit a denser microscopic morphology when the curing temperature is increased.

Author Contributions: W.Z.: Data curation, Writing—original draft. H.Z.: Writing—original draft. Y.H.: Formal analysis. J.W.: Writing—review and editing. J.M.: Writing—review and editing, Supervision. R.J.: Resource, Conceptualization, Data curation. J.S.: Resource, Conceptualization, Supervision. All authors have read and agreed to the published version of the manuscript.

Funding: The authors are grateful for the National Natural Science Foundation of China (52108250), CNBM Technology Innovation Academy, the Key Laboratory of Inorganic Functional Materials and Intelligent Manufacturing of Shandong Province (2021SFGC0903), the Key Research and Development Plan Science and Technology Demonstration Project of Shandong Province “Integrated Innovation and demonstration of new green building materials” (2021SFGC0903), the funding for school-level research projects of Yancheng Institute of Technology (XJR2023053), the special fund project for the Special Fund of Chinese Central Government for Basic Scientific Research Operations in the commonwealth Research Institute (GYZX220301), and the Special Fund of Carbon Peak and Carbon Neutrality Research Institute supported by the Nanjing Institute of Environmental Sciences, Ministry of Ecology and Environment (ZX2023SZY060).

Institutional Review Board Statement: Not applicable.

Informed Consent Statement: Not applicable.

Data Availability Statement: The data used in this study can be required from the corresponding author. The data are not publicly available due to information that could compromise the research participants’ privacy.

Conflicts of Interest: The authors declare no conflict of interest.

References

1. Singh, S.B.; Haskin, N.; Dastgheib, S.A. Coal-based graphene oxide-like materials: A comprehensive review. *Carbon* **2022**, *215*, 118447. [CrossRef]
2. Hao, Y.; Guo, X.; Yao, X.; Han, R.; Li, L.; Zhang, M. Using Chinese coal gangue as an ecological aggregate and its modification: A review. *Materials* **2022**, *15*, 4495. [CrossRef]
3. Li, J.; Wang, J. Comprehensive utilization and environmental risks of coal gangue: A review. *J. Clean. Prod.* **2019**, *239*, 117946. [CrossRef]
4. Zhang, Y.; Ling, T.-C. Reactivity activation of waste coal gangue and its impact on the properties of cement-based materials—A review. *Constr. Build. Mater.* **2020**, *234*, 117424. [CrossRef]
5. Li, L.; Shao, X.; Ling, T.-C. Life cycle assessment of coal gangue composite cements: From sole OPC towards low-carbon quaternary binder. *J. Clean. Prod.* **2023**, *414*, 137674. [CrossRef]
6. Liu, L.; Liu, Q.; Zhang, S.; Li, Y.; Yang, L. The thermal transformation behavior and products of pyrite during coal gangue combustion. *Fuel* **2022**, *324*, 124803. [CrossRef]
7. Jiu, S.; Cheng, S.; Li, H.; Wang, L. Reaction mechanism of metakaolin materials prepared by calcining coal gangue. *Mater. Res. Express* **2021**, *8*, 015508. [CrossRef]
8. Wang, A.; Liu, P.; Mo, L.; Liu, K.; Ma, R.; Guan, Y.; Sun, D. Mechanism of thermal activation on granular coal gangue and its impact on the performance of cement mortars. *J. Build. Eng.* **2022**, *45*, 103616. [CrossRef]
9. Sanchez, M.A.; Garcia, H.L.C.; Molina, W.M.; Guzman, E.M.A.; Acosta, A.A.T.; Ortega, J.M.P. Use of metakaolin or coal gangue as a partial substitution of cement in mechanical performance of PC mortars. *Eur. J. Environ. Civ. Eng.* **2021**, *25*, 502–515. [CrossRef]
10. Guo, Z.; Xu, J.; Xu, Z.; Gao, J.; Zhu, X. Performance of cement-based materials containing calcined coal gangue with different calcination regimes. *J. Build. Eng.* **2022**, *56*, 104821. [CrossRef]

11. Zhang, M.; Li, L.; Yang, F.; Zhang, S.; Zhang, H.; Zhu, Y.; An, J. Thermal activation of high-alumina coal gangue auxiliary cementitious admixture: Thermal transformation, calcining product formation and mechanical properties. *Materials* **2024**, *17*, 415. [CrossRef] [PubMed]
12. Zhou, S.; Dong, J.; Yu, L.; Xu, C.; Jiao, X.; Wang, M. Effect of activated coal gangue in North China on the compressive strength and hydration process of cement. *J. Mater. Civ. Eng.* **2019**, *31*, 04019022. [CrossRef]
13. Yang, J.; Su, Y.; He, X.; Tan, H.; Jiang, Y.; Zeng, L.; Strnadel, B. Pore structure evaluation of cementing composites blended with coal by-products: Calcined coal gangue and coal fly ash. *Fuel Process. Technol.* **2018**, *181*, 75–90. [CrossRef]
14. Yu, L.; Xia, J.; Gu, J.; Zhang, S.; Zhou, Y. Degradation mechanism of coal gangue concrete suffering from sulfate attack in the mine environment. *Materials* **2023**, *16*, 1234. [CrossRef] [PubMed]
15. Wang, A.; Hao, F.; Liu, P.; Mo, L.; Liu, K.; Li, Y.; Cao, J.; Sun, D. Separation of calcined coal gangue and its influence on the performance of cement-based materials. *J. Build. Eng.* **2022**, *51*, 104293. [CrossRef]
16. Ren, B.; Chai, L.; Liu, Y.; Wang, Y. Preparation of high-ductility cement-calcined coal-cangue-powder-composite-based rapid repair material. *Materials* **2023**, *16*, 6049. [CrossRef] [PubMed]
17. Jiu, S.; Wang, M.; Chen, Y.; Chen, J.; Gao, Q. Synthesis and characterization of low-carbon cementitious materials from suspended calcined coal gangue. *Front. Mater.* **2022**, *9*, 982861. [CrossRef]
18. Liu, Y.; Ling, T.-C.; Wang, M.; Wu, Y.-Y. Synergic performance of low-kaolinite calcined coal gangue blended with limestone in cement mortars. *Constr. Build. Mater.* **2021**, *300*, 124012. [CrossRef]
19. Scrivener, K.; Martirena, F.; Bishnoi, S.; Maity, S. Calcined clay limestone cements (LC3). *Cem. Concr. Res.* **2018**, *114*, 49–56. [CrossRef]
20. Antoni, M.; Rossen, J.; Martirena, F.; Scrivener, K. Cement substitution by a combination of metakaolin and limestone. *Cem. Concr. Res.* **2012**, *42*, 1579–1589. [CrossRef]
21. Avet, F.; Scrivener, K. Investigation of the calcined kaolinite content on the hydration of limestone calcined clay cement (LC3). *Cem. Concr. Res.* **2018**, *107*, 124–135. [CrossRef]
22. Lin, R.-S.; Oh, S.; Du, W.; Wang, X.-Y. Strengthening the performance of limestone-calcined clay cement (LC3) using nano silica. *Constr. Build. Mater.* **2022**, *340*, 127723. [CrossRef]
23. Zhang, W.; Zhao, M.; Yang, Z.; Guo, R.; Wang, X.-Y.; Lin, R.-S. Properties of red sandstone-limestone-cement ternary com-posites: Hydration mechanism, microstructure, and high-temperature damage. *Dev. Built Environ.* **2024**, *17*, 100346. [CrossRef]
24. Herath, C.; Gunasekara, C.; Law, D.W.; Setunge, S. Performance of high volume fly ash concrete incorporating additives: A systematic literature review. *Constr. Build. Mater.* **2020**, *258*, 120606. [CrossRef]
25. Emmanuel, A.C.; Bishnoi, S. Influence of clinker replacement and curing temperature on hydration kinetics, strength development, and phase assemblage of fly ash–blended cements. *J. Mater. Civ. Eng.* **2022**, *34*, 04022107. [CrossRef]
26. Pang, X.; Sun, L.; Chen, M.; Xian, M.; Cheng, G.; Liu, Y.; Qin, J. Influence of curing temperature on the hydration and strength development of Class G Portland cement. *Cem. Concr. Res.* **2022**, *156*, 106776. [CrossRef]
27. Bai, S.; Guan, X.; Li, G. Early-age hydration heat evolution and kinetics of Portland cement containing nano-silica at different temperatures. *Constr. Build. Mater.* **2022**, *334*, 127363. [CrossRef]
28. Narmluk, M.; Nawa, T. Effect of fly ash on the kinetics of Portland cement hydration at different curing temperatures. *Cem. Concr. Res.* **2011**, *41*, 579–589. [CrossRef]
29. Shirani, S.; Cuesta, A.; Morales-Cantero, A.; De la Torre, A.G.; Olbinado, M.P.; Aranda, M.A. Influence of curing temperature on belite cement hydration: A comparative study with Portland cement. *Cem. Concr. Res.* **2021**, *147*, 106499. [CrossRef]
30. Shi, M.; Wang, Q.; Zhou, Z. Comparison of the properties between high-volume fly ash concrete and high-volume steel slag concrete under temperature matching curing condition. *Constr. Build. Mater.* **2015**, *98*, 649–655.
31. Bentz, D.P. Activation energies of high-volume fly ash ternary blends: Hydration and setting. *Cem. Concr. Compos.* **2014**, *53*, 214–223. [CrossRef]
32. Sun, J.; Wang, Z.; Chen, Z. Hydration mechanism of composite binders containing blast furnace ferronickel slag at different curing temperatures. *J. Therm. Anal. Calorim.* **2018**, *131*, 2291–2301. [CrossRef]
33. Snellings, R.; Machner, A.; Bolte, G.; Kamyab, H.; Durdzinski, P.; Teck, P.; Zajac, M.; Muller, A.; de Weerdt, K.; Ben Haha, M. Hydration kinetics of ternary slag-limestone cements: Impact of water to binder ratio and curing temperature. *Cem. Concr. Res.* **2022**, *151*, 106647. [CrossRef]
34. *GB/T 17671-2021*; Test Method of Cement Mortar Strength (ISO Method). China Standard Press: Beijing, China, 2021.
35. *GB/T 50081-2019*; Standard for Test Methods of Concrete Physical and Mechanical Properties. China Construction Industry Press: Beijing, China, 2019.

materials

Article

Rheological Properties of Silica-Fume-Modified Bioasphalt and Road Performance of Mixtures

Gui Hou [1,2,3], **Yanhua Xue** [4,5,*], **Zhe Li** [3,4,5] **and Weiwei Lu** [4,5]

[1] Institute of Cold Region Science and Engineering, Northeast Forestry University, Harbin 150040, China; nmgjky2024@sina.com
[2] Northeast Forestry University Engineering Consulting and Design Research Institute, Ltd., Harbin 150040, China
[3] Inner Mongolia Autonomous Region Transportation Science and Development Research Institute, Hohhot 010051, China; nmgjtysbwh@163.com
[4] National Key Laboratory of Green and Long-Life Road Engineering in Extreme Environment (Changsha), Changsha University of Science & Technology, Changsha 410114, China; lww_cs@csust.edu.cn
[5] National Engineering Research Center of Highway Maintenance Technology, Changsha University of Science & Technology, Changsha 410114, China
* Correspondence: xueyanhua_2022@stu.csust.edu.cn

Abstract: The objective of this research is to enhance the high-temperature antirutting and antiaging characteristics of bioasphalt. In this study, silica fume (SF) was selected to modify bioasphalt. The dosage of bio-oil in bioasphalt was 5%, and the dosage of SF was 2%, 4%, 6%, 8%, and 10% of bioasphalt. The high- and low-temperature characteristics, aging resistance, and temperature sensitivity of Bio + SF were evaluated by temperature sweep (TS), the multiple stress creep recovery (MSCR) test, the bending beam rheology (BBR) test, and the viscosity test. Meanwhile, the road behavior of the Bio + SF mixture was evaluated using the rutting test, low-temperature bending beam test, freeze–thaw splitting test, and fatigue test. The experimental results showed that the dosage of SF could enhance the high-temperature rutting resistance, aging resistance, and temperature stability of bioasphalt. The higher the dosage of SF, the more significant the enhancement effect. However, incorporating SF weakened bioasphalt's low-temperature cracking resistance properties. When the SF dosage was less than 8%, the low-temperature cracking resistance of Bio + SF was still superior to that of matrix asphalt. Compared with matrix asphalt mixtures, the dynamic stability, destructive strain, freeze–thaw splitting strength ratio, and fatigue life of 5%Bio + 8%SF mixtures increased by 38.4%, 49.1%, 5.9%, and 68.9%, respectively. This study demonstrates that the development of SF-modified bioasphalt could meet the technical requirements of highway engineering. Using SF and bio-oil could decrease the consumption of natural resources and positively reduce environmental pollution.

Keywords: bio-oil; silica fume; rheological properties; bioasphalt

Citation: Hou, G.; Xue, Y.; Li, Z.; Lu, W. Rheological Properties of Silica-Fume-Modified Bioasphalt and Road Performance of Mixtures. *Materials* **2024**, *17*, 2090. https://doi.org/10.3390/ma17092090

Academic Editor: Simon Hesp

Received: 28 March 2024
Revised: 19 April 2024
Accepted: 23 April 2024
Published: 29 April 2024

1. Introduction

Petroleum asphalt is a nonrenewable resource. However, with the increasing cost of energy and the strong global demand for petroleum resources, it is an inevitable trend to find new binders to modify or replace petroleum asphalt [1]. Amar K. Mohanty, in his study, pointed out that biomass energy sources have attracted the attention of many researchers for their environmental friendliness, wide sources, large storage capacity, low price, and sustainability [2]. Biomass is mainly derived from crop residues, waste oils and fats, plants, animal feces, municipal waste, wood chips, etc. Biomass energy sources can be converted through a series of transformations and eventually become a new green road material with properties similar to those of petroleum asphalt, i.e., bioasphalt [3]. Applying bioasphalt produced from these biomass materials to the road field could enhance the characteristics of asphalt, deal with waste, protect the environment, and develop a sustainable economy [4].

Julian Mills-Beale et al. [5] utilized a swine waste biobinder to prepare bioasphalt and investigated its rheological characteristics and modification mechanism. It was found that pig waste is compatible with asphalt and effectively improves the low-temperature characteristics. However, it reduced the aging resistance and high-temperature stabilization. Lei et al. [6] researched the effect of varying oils on the low-temperature behavior of asphalt. The study findings exhibited that the oil can effectively strengthen the low-temperature characteristics, and the asphalt mixtures have superior low-temperature anticracking characteristics. Sun et al. [7] researched waste-cooking-oil-modified asphalt's mechanical, chemical, and rheological characteristics. Silvia Caro et al. [8] researched the chemical, rheological, and thermodynamic characteristics of bagasse, corn kernel, and rice husk bio-oils on bitumen. Yang et al. [9] used wood in the form of woodchips, sawdust, and shavings to produce bio-oils and investigated the effects on the elemental composition of the asphalt, chemical composition, oxidative aging, and compatibility. Several studies showed that most bioasphalts prepared from various biomass resources could enhance the low-temperature characteristics and degrade mixtures' optimal mixing and compaction temperatures. However, various bio-oils can adversely affect petroleum asphalt's antiaging and high-temperature characteristics [10]. The poor bioasphalt performance at high temperatures restricts biomass asphalt's wide-scale utilization in pavement construction.

Therefore, researchers have compensated for its performance by adding modifiers to biomass asphalt to enhance its high-temperature stabilization and antiaging characteristics. Sara R.M. Fernandes et al. [11] combined waste motor oil and recycled motor oil residues with polymers such as used polyethylene (PE), rubber powder, and styrene–butadiene–styrene block copolymer (SBS) to reduce the use of asphalt. The findings demonstrated that combining waste motor oil products with polymers enhanced the high-temperature characteristics. Lei et al. [12] prepared asphalt mastic using bio-oil and mineral powder filler with different dosages. The findings indicated that adding bio-oil enhanced asphalt mastic's high-temperature stabilization and antideformation ability. Zheng et al. [10] used 4,4′-diphenylmethane diisocyanate (MDI) as an additive to boost the characteristics of wood-based bio-oil asphalt. The findings indicated that wood-based bio-oil asphalt will have strengthened high-temperature characteristics, and the low-temperature characteristics were not weakened. Ju et al. [13] used polyphosphoric-acid-modified castor oil bitumen, and the results showed that the polyphosphoric acid was not weakened. The wood bio-oil asphalt will raise high-temperature characteristics, and the low-temperature characteristics will not be weakened. Peng et al. [14] modified bioasphalt using rock asphalt. Zhao et al. [15] modified bioasphalt using nanomaterials, SBS, styrene–butadiene rubber (SBR), PE, and ethylene vinyl acetate (EVA). The high-temperature characteristics were remarkably enhanced when 7% bio-oil, 5% SBS, and 0.2% nanosilica were used.

Existing studies have found that the modifiers used to enhance bioasphalt performance are mainly organic modifiers. The most widely used are polymers such as SBS and SBR, which have excellent deformation and aging resistance under high-temperature conditions [16]. However, they also have the disadvantages of a cumbersome preparation process, high cost, and difficult storage. In addition to organic modifiers, inorganic modifiers could also effectively enhance the performance of asphalt. Commonly used inorganic modifiers include carbon black, fiber, diatomaceous earth, cement, slaked lime, silica fume, layered silicate, nano calcium carbonate, etc. Sun et al. [17] investigated the effect of carbon black (CB) on asphalt properties. It was found that CB enhances the properties of asphalt, such as its high-temperature characteristics and aging resistance. Zhu et al. [18] researched the effect of the type of layered silicate on the composite ratio of multidimensional nanomaterials (MDNs) in styrene–butadiene–styrene copolymer-modified asphalt (SBSMA). Li et al. [19] explored the effect of surface-modified diatomaceous earth (SMD) on the characteristics of bioasphalt, and the addition of SMD raised the asphalt's characteristics, such as viscosity, softening point, fatigue index, and rutting coefficient. Yadykova et al. [20] modified bioasphalt using montmorillonite and found that montmorillonite significantly raises the characteristics of asphalt, such as elasticity, stiffness, and cohesion. Silica fume (SF), as an admixture for cement or concrete, has the advantages of great strength, abrasion resistance, erosion resistance, and corrosion resistance. Due to its peculiar micropore structure and better adsorption capacity, SF was often used as a modifier in preparing modified asphalt [21,22]. Yang et al. [23] used SF as an asphalt modifier. The findings indicated that SF could enhance asphalt's high-temperature and temperature-affected characteristics. It could enhance the mixture's high-temperature stabilization and water stability. Luo et al. [24] used SF to modify SBS asphalt, and the asphalt's high temperature and water stability were significantly enhanced. Shang et al. [25] analyzed SF-modified asphalt's rheological properties and microstructure before and after aging. Feng et al. [26] revealed that SF could enhance the high-temperature characteristics of asphalt. Yadykova et al. [27] examined the effect of hydrophilic and hydrophobic silica on bio-oil asphalt's rheological properties, cohesion, and adhesion characteristics. Numerous studies have found that SF with a large specific surface area and strong adsorption capacity could usefully strengthen the high-temperature characteristics [28,29].

Therefore, in view of the current situation that bioasphalt's high-temperature characteristics and antiaging are insufficient, SF was used as a modifier to modify bioasphalt in this study. The dosage of bio-oil in bioasphalt was 5%. The dosage of SF was 2–10% of the bioasphalt. A high-speed shear and colloid mill prepared the bio-oil/SF-modified asphalt (Bio + SF). The high- and low-temperature characteristics, temperature stabilization, and antiaging behavior of Bio + SF were investigated by rheological tests. At the same time, the road behavior of Bio + SF mixtures was tested. It provides the experimental basis and technological guidance for applying SF-modified bioasphalt. An experimental flowchart is illustrated in Figure 1.

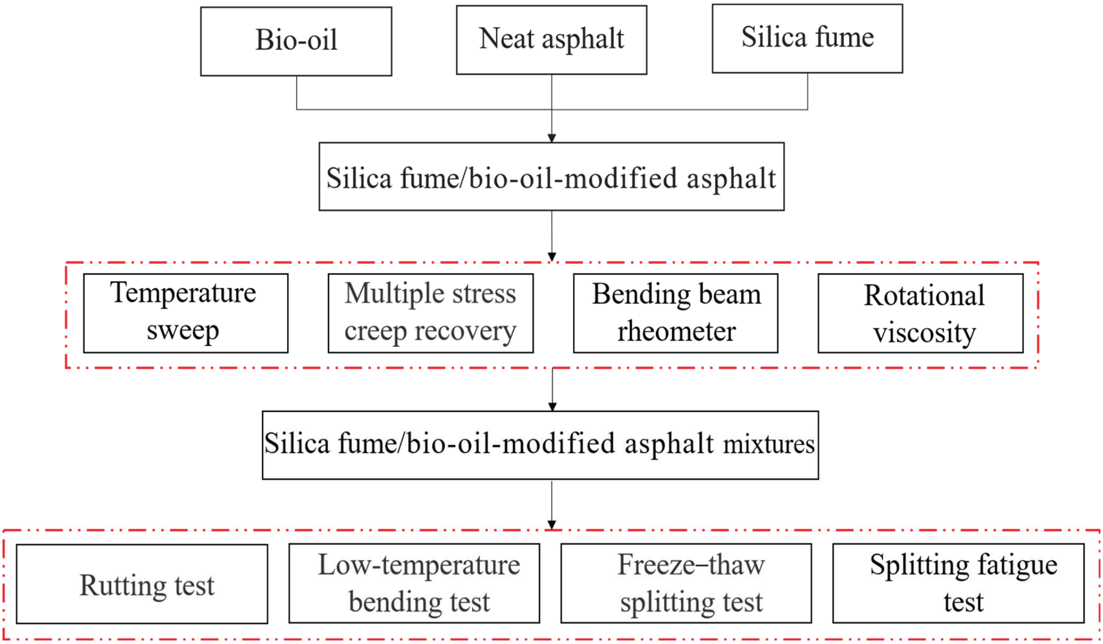

Figure 1. The experimental flowchart.

2. Test Materials and Methods

2.1. Raw Materials

2.1.1. Matrix Asphalt

This study selected the SK-70 model matrix asphalt as the original material. The detailed characteristics are outlined in Table 1.

Table 1. The detailed characteristics of asphalt.

Technical Indexes	Unit	Test Results	Specification Requirements	Test Methods
Penetration (25 °C, 5 s, 100 g)	0.1 mm	67	60~80	ASTM D 5 [30]
Ductility (5 cm/min, 10 °C)	cm	32	≥15	ASTM D 113 [31]
Softening point	°C	48	≥46	ASTM D 36 [32]
Viscosity (60 °C)	Pa·s	219	≥180	ASTM D 4402 [33]
	after RTFOT aging			
Mass loss	%	0.024	≤±0.8	ASTM D 2872 [34]
Residual penetration ratio (25 °C, 5 s, 100 g)	%	67	≥61	ASTM D 5
Ductility (5 cm/min, 10°C)	cm	8	≥6	ASTM D 113

2.1.2. Silica Fume

Qinghai Tongda Company (Xining, China) produced the silica fume (SF) used in this study. The detailed characteristics are depicted in Table 2.

Table 2. SF technical indexes.

Indexes	Results
Appearance	Pale grayish-white powder
SiO_2 content (%)	92.88
PH value	6–8
Whiteness (%)	0.24
Particle size distribution (μm)	0.1–0.3
Specific surface area (m^2/g)	25.37

Notes: The whiteness of SF is defined as its brightness or lightness compared with a standard white reference material.

2.1.3. Bio-Oil

In this study, the bio-oil used was from Jinan Boao Chemical Co., Ltd. (Jinan, China), and was the residue extracted from vegetable oil. The major components were 60–80% fatty acid and vegetable alcohol. The major features of the bio-oil are depicted in Table 3.

Table 3. The major features of bio-oil.

Indicators	Results
Acid value (mgKOH/g)	51
Moisture content (%)	≤0.3
Kinematic viscosity (mm^2/s)	148
Density (g/mL)	0.93
Fatty acids content (%)	65

2.1.4. Aggregates

In this study, the aggregate used was limestone. It was tested according to the JTG E42-2005 [35] specification, and all the indexes satisfied the technical demands of the standard. The specific technical indexes of coarse and fine aggregates are depicted in Tables 4 and 5.

Table 4. Technical specifications of coarse aggregates.

Technical Indicators	Results	Standards
Los Angeles abrasion test (%)	23	≤28
Crushing value (%)	12.1	≤28
Acicular and flaky grain in aggregate (%)	10.3	≤15

Table 5. Technical specifications for fine aggregates.

Technical Indicators	Results	Standards
Water absorption (%)	0.5	≤2.0
Mud content (%)	1.7	≤3
Sand equivalent (%)	69	≥60

2.1.5. Grading Curve

AC-13 grading was selected for this study, and the grading curve is displayed in Figure 2.

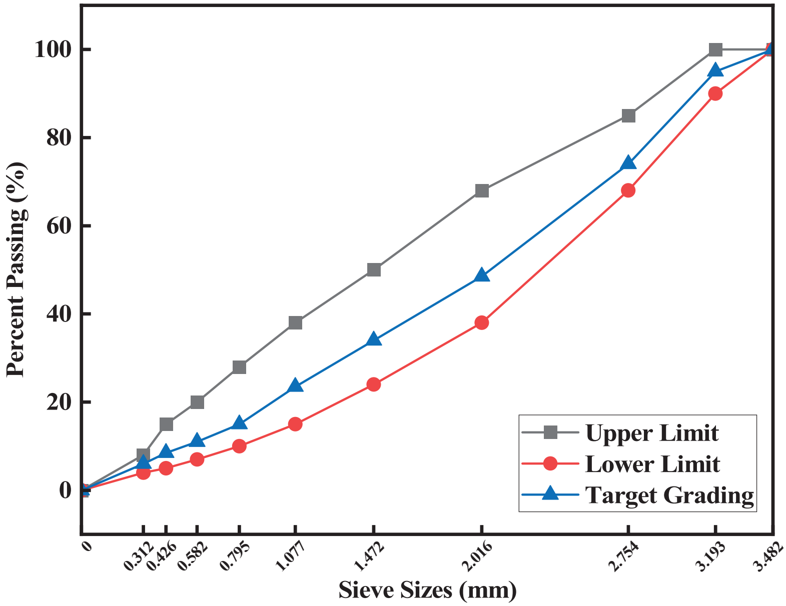

Figure 2. Grading curve.

2.2. Preparation of Bio-Oil/SF-Modified Asphalt

Since SF is a chainlike aggregate from amorphous spheres, it is easily adsorbed to moisture in the air due to its large particle size and large specific surface area. To ensure the SF remained dry during the preparation process, the SF was put into an oven at 105 °C to dry before preparing the modified asphalt. The degree of dispersion of the SF in the asphalt directly affects the performance of modified asphalt. To minimize the phenomenon of SF agglomeration in asphalt, in the preparation of SF/bio-oil-modified asphalt (Bio + SF), an MJ-65 colloid mill was used for dispersion for 3 min at a speed of 2900 r/min. The preparation process of Bio + SF was as follows: First, 400 g of matrix asphalt was put into an oven at 135 °C for 1 h to reach the flow state; then 5% (by mass of asphalt) of bio-oil was incorporated. After premixing using a glass rod, the mixture was sheared at 135 °C and 3000 rpm for 5 min. After shearing, at 180 °C, the predried SF was added to the bioasphalt, dispersed for 3 min using a colloid mill, and mixed at 5000 rpm for 30 min using a high-speed shear. Finally, Bio + SF was obtained. The dosage of SF was 0%, 2%, 4%, 6%, 8%, and 10% of the mass of bioasphalt, respectively. Abbreviations are presented in Table 6.

Table 6. Bio + SF abbreviations.

SF Content	**0%**	**2%**	**4%**	**6%**	**8%**	**10%**
Abbreviation	5%Bio	5%Bio + 2%SF	5%Bio + 4%SF	5%Bio + 6%SF	5%Bio + 8%SF	5%Bio + 10%SF

2.3. Test Methods

2.3.1. Temperature Sweep (TS)

Dynamic shear rheometers were used to perform temperature sweeps according to the AASHTO T 315-20 [36] specification. The temperature range was 52–82 °C, with temperature increments of 6 °C. The test was conducted under stress-controlled mode. The sample diameter was 25 mm, and the thickness was 1 mm. The frequency was 10 rad/s. The original asphalt strain was set to 12%, and the strain after rolling thin-film oven (RTFO) aging was set to 10%.

2.3.2. Multiple Stress Creep Recovery (MSCR)

The MSCR test on asphalt after RTFO was performed according to the AASHTO T350-14 [37] specification. The MSCR test consisted of 0.1 kPa and 3.2 kPa stress levels. A total of 20 cycles were loaded at 0.1 kPa stress, and 10 cycles were loaded at 3.2 kPa stress. The temperature was 58 °C. Three parallel tests were run for each type of asphalt.

2.3.3. Rotational Viscosity

Based on the AASHTO T 316 [38] specification, a Brookfield viscometer performed viscosity tests on unaged asphalt. The test was conducted using a No. 27 rotor. The rotor and sample container were maintained in an oven for 1.5 h. The samples were loaded into a viscometer, held to reach the test equilibrium temperature, and then tested. The torque was maintained between 10% and 98% during the test. The test temperatures were 135 °C, 165 °C, and 175 °C. The rotational speed was 20 r/min at 135 °C. The rotational speed was 50 r/min at 165 °C and 175 °C. After the viscosity value was stabilized, readings were taken at 60 s intervals for 3 consecutive times, and the average value was used as the viscosity measurement value. Each asphalt was tested twice in parallel.

2.3.4. Bending Beam Rheometer (BBR)

The low-temperature rheological characteristics of Bio + SF were tested according to AASHTO T 313-19 [39]. The size of the specimen was 127 mm × 6.35 mm × 12.7 mm. The contact load was 35 ± 10 mN. The test load was 980 ± 50 mN. The test load was constant for 240 s. The temperatures were −12 °C and −18 °C. The strength modulus (S) and creep rate (m) indices for PAV-aged asphalt were obtained. Each asphalt was tested three times in parallel.

2.4. Asphalt Mixture Road Behavior Test

According to the JTG E20-2011 [40] specification, the appropriate mixing and compaction temperatures were selected according to the Brookfield rotational viscosity test. The optimum asphalt–aggregate ratio was obtained using the Marshall test method.

2.4.1. Rutting Resistance at High Temperature

According to the specification of JTG E20-2011 [40], the rutting test was carried out on matrix asphalt mixtures, 5%Bio + 6%SF mixtures, 5%Bio + 8%SF mixtures, and 5%Bio + 10%SF mixtures. The specimen size was 300 mm × 300 mm × 50 mm. The temperature was 60 °C. The contact pressure between the tire and the specimen was 0.7 MPa, and the wheel acted on the specimen 42 times per minute. The rutting deformations d_1 and d_2 at 45 min (t_1) and 60 min (t_2) were taken for the calculation of dynamic stability (DS), as shown in Equation (1).

$$\mathrm{DS} = \frac{42 \times (t_2 - t_1)}{d_2 - d_1} \tag{1}$$

2.4.2. Low-Temperature Anticracking Properties

Based on the specification of JTG E20-2011 [40], a low-temperature bending beam damage test was carried out for matrix asphalt mixtures, 5%Bio + 6%SF mixtures, 5%Bio + 8%SF mixtures, and 5%Bio + 10%SF mixtures. The specimen size was 250 mm × 30 mm × 35 mm, a small beam specimen. The loading rate was 50 mm/min. The temperature was −10 °C. The ultimate bending tensile failure strain (ε) was calculated as in Equation (2):

$$\varepsilon = \frac{6\mathrm{hd}}{\mathrm{L}^2} \tag{2}$$

where L is the diameter of the specimen, mm; h is the height of the midspan section of the specimen, mm; and d is the midspan deflection of the specimen, mm.

2.4.3. Freeze–Thaw Splitting Strength

According to the specification of JTG E20-2011 [40], freeze–thaw splitting tests were conducted on matrix asphalt mixtures, 5%Bio + 6%SF mixtures, 5%Bio + 8%SF mixtures, and 5%Bio + 10%SF mixtures. The specimens of each asphalt mixture were divided into two groups. One group was first treated with a freeze–thaw cycle, and then the two groups of specimens were soaked in a 25 °C water bath for 2 h and then tested for splitting strength separately. The freeze–thaw splitting strength ratio (TSR) formula is presented in (3):

$$\mathrm{TSR} = \frac{\mathrm{R}_{\mathrm{T2}}}{\mathrm{R}_{\mathrm{T1}}} \times 100\% \tag{3}$$

where R_{T1} and R_{T2} are the strength values of the asphalt mixture before and after freezing and thawing; R = 0.006287 P/h, MPa; P is the breaking load, N; and h is the height of the specimen, mm.

2.4.4. Splitting Fatigue

The durability test was tested using the split fatigue test on matrix asphalt mixtures, 5%Bio + 6%SF mixtures, 5%Bio + 8%SF mixtures, and 5%Bio + 10%SF mixtures. The temperature was 15 °C. The stress level was 0.3 MPa. Control mode was selected as stress control. The loading frequency was 10 Hz.

3. Results and Analysis

3.1. TS Analysis

The rutting factor ($G^*/\sin\delta$) is utilized to assess the ability of asphalt to resist irrecoverable deformation during dynamic shear. The larger its value, the more superior the capacity of asphalt to resist deformation [41,42]. Figures 3 and 4 show the rutting factor with temperature curves of matrix asphalt, bioasphalt, and bio-oil/SF with different SF dosages after unaged and short-term aging, respectively.

$G^*/\sin\delta$ decreased with increasing temperature for varying types of asphalt (Figures 3 and 4). Adding bio-oil reduced the $G^*/\sin\delta$ value of asphalt compared with matrix asphalt. The $G^*/\sin\delta$ value of bioasphalt declined by 77.6% compared with matrix bitumen at 52 °C, which substantially weakened the antideformation characteristics of the matrix asphalt. This was attributed to the fact that adding bio-oil increases the asphalt's lightweight component and reduces the asphalt's ability to resist high-temperature deformation [14]. The $G^*/\sin\delta$ of bioasphalt strengthened continuously after incorporating SF into bioasphalt. The $G^*/\sin\delta$ values of bio-oil + SF strengthened by 85.3%, 191.9%, 284.3%, 437.0%, and 591.8% for 2%SF, 4%SF, 6%SF, 8%SF, and 10%SF dosages at 52 °C, respectively. Adding SF enhanced the ability of bioasphalt to prevent permanent distortion. When the amount of SF was 6%, the $G^*/\sin\delta$ value was comparable with matrix asphalt. When the amount of SF was 8%, the antirutting characteristics of bioasphalt at high temperatures were superior to those of matrix asphalt.

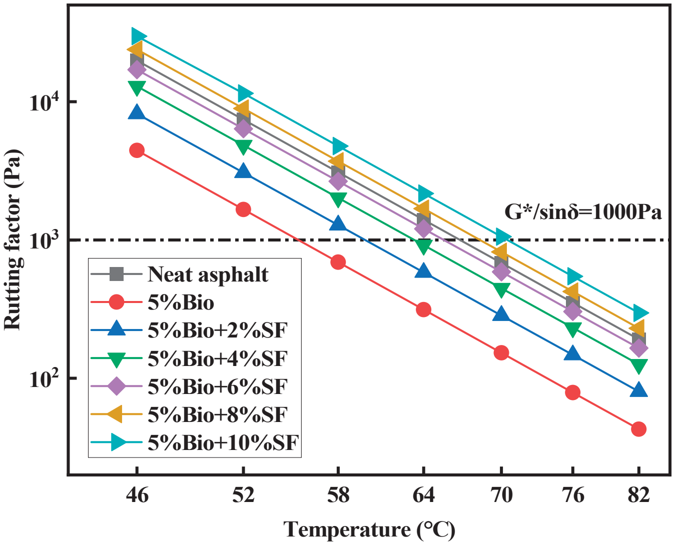

Figure 3. Rutting factor of unaged asphalt.

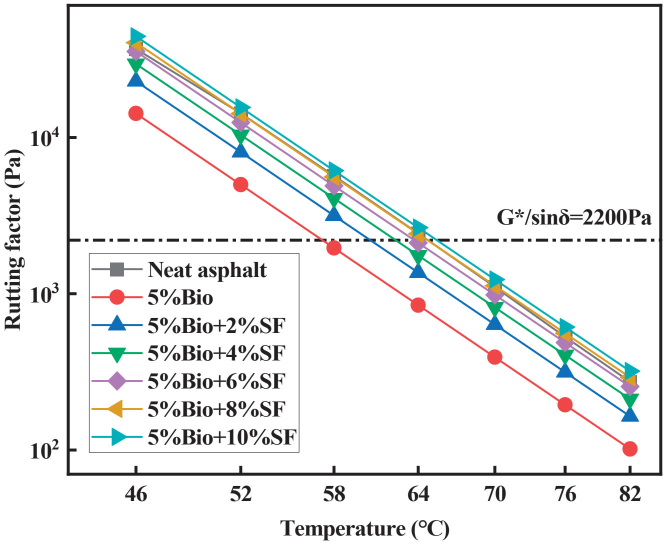

Figure 4. Rutting factors for short-term aged asphalt.

According to the Superpave standard, G*/sinδ is an index of the PG gradation of asphalt at high temperatures. The standard defines that the G*/sinδ of unaged asphalt shall be greater than 1000 Pa. The G*/sinδ of asphalt after short-term aging shall be greater than 2200 kPa. The results of PG grading are depicted in Table 7.

According to the asphalt high-temperature PG results shown in Table 7, SF can effectively promote the capacity of bioasphalt to withstand permanent deformation and enhance its high-temperature stabilization.

Table 7. Asphalt high-temperature PG classification.

Type of Asphalt	High-Temperature Grade
Matrix asphalt	PG64
5%Bio	PG52
5%Bio + 2%SF	PG58
5%Bio + 4%SF	PG58
5%Bio + 6%SF	PG58
5%Bio + 8%SF	PG64
5%Bio + 10%SF	PG64

3.2. Antiaging Performance

The rutting factor aging index (RFAI) was calculated based on the rutting factor test results of original and short-term aged asphalt in the temperature sweep. RFAI is calculated as shown in Equation (4). The lower the RFAI, the more superior the antiaging characteristics [43,44]. The results of RFAI values for different asphalts are shown in Figure 5.

$$\text{RFAI} = \frac{\text{Rutting factor/short} - \text{term aged}}{\text{Rutting factor/unaged}} \quad (4)$$

As illustrated in Figure 5, The RFAI value of bio-asphalt appeared to be increased, with the RFAI elevated by 55.2% compared with the matrix asphalt. Meanwhile, the RFAI value of bio-asphalt continuously decreases after SF incorporation. Compared with 5%Bio, the RFAI values of 5%Bio + 2%SF, 5%Bio + 4%SF, 5%Bio + 6%SF, 5%Bio + 8%SF and 5%Bio + 10%SF decreased by 13.1%, 28.9%, 35.0%, 46.8% and 54.7%, respectively. The resistance to aging of bio-asphalt strengthened with the rise of the SF content. When the SF amount was 8%, bio-asphalt's anti-aging characteristics were better than matrix asphalt. The cause was mainly related to the composition of bio-oil. Bio-oil contains many light components, which easily volatilize in a high-temperature oxygen-containing environment and are gradually converted into heavy components, weakening bio-asphalt's resistance to aging characteristics. Incorporating SF could effectively enhance the force between SF particles and asphalt molecules, creating a stable space network structure and greatly enhancing the cohesion of bio-based materials and matrix asphalt. Then, it strengthened the resistance to aging characteristics of bio-asphalt.

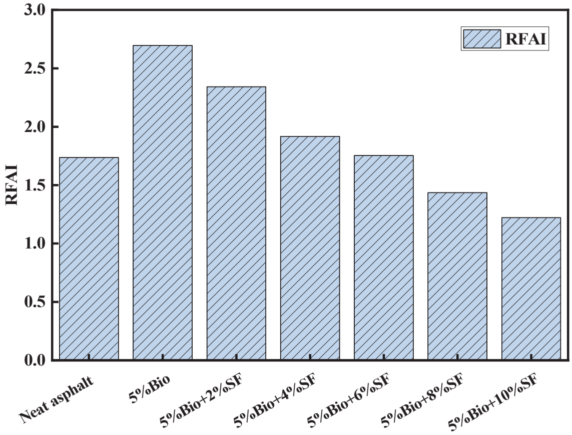

Figure 5. RFAI values for different asphalt types.

3.3. MSCR Analysis

The creep recovery rate (R) and the unrecoverable creep flexibility (Jnr) could be obtained from the MSCR test. The R-value characterizes the resilient composition. The higher the value, the greater the elastic deformation recovery. The Jnr-value characterizes the resistance to permanent deterioration. The lower the value, the greater the antideformation ability at high-temperature terms [16,41]. Figures 6 and 7 display the R-values and Jnr-values of asphalt for stress levels of 0.1 kPa and 3.2 kPa at 58 °C, respectively.

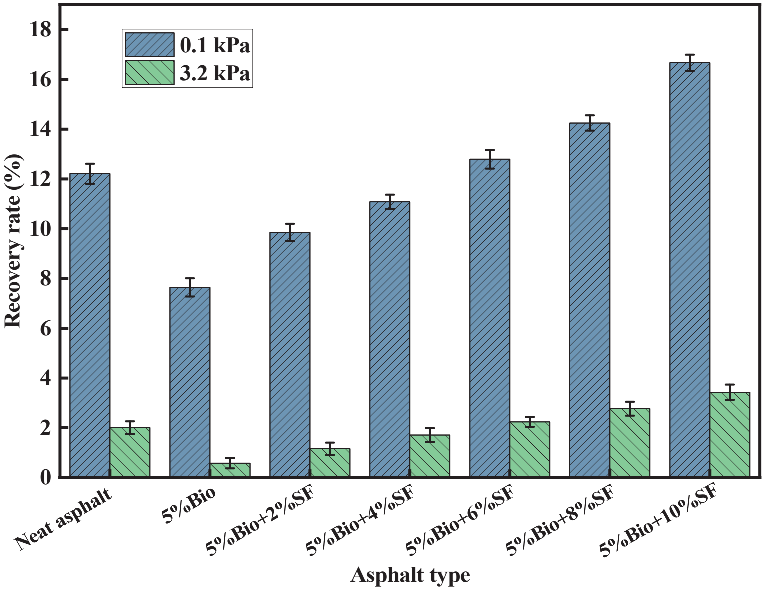

Figure 6. Creep recovery for different asphalt types.

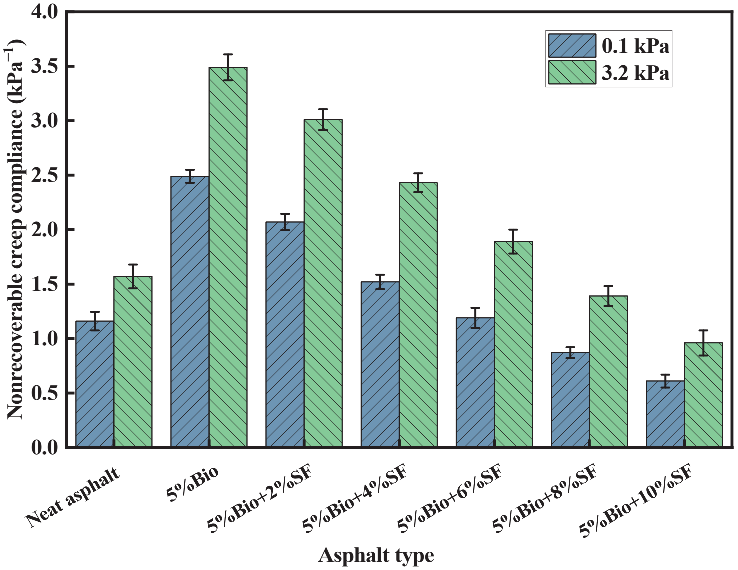

Figure 7. Unrecoverable creep flexibility for different asphalt types.

The R-values of varying asphalt types decline continuously with rising stress (Figure 6). It indicates that an increase in stress level decreases the capacity of asphalt to restore deformation under a high-temperature environment resiliently. The R-value of bioasphalt declined compared with matrix asphalt at the corresponding stress level. The R-value of bioasphalt declined by 37.4% at 0.1 kPa. This was mainly because the bio-oil contained more lightweight components, which reduced the resilient composition of the asphalt, thus reducing the deformation capacity of the asphalt for elastic recovery. SF incorporation strengthened the deformation recovery capacity of bioasphalt under high-temperature conditions. At 0.1 kPa, compared with 5%Bio-oil, the R-values of 5%Bio + 2%SF, 5%Bio + 4%SF, 5%Bio + 6%SF, 5%Bio + 8%SF, and 5%Bio + 10%SF increased by 28.9%, 45.0%, 67.4%, 86.5%, and 118.2%, respectively. When the amount of SF was 6%, the R-value of Bio + SF was similar to that of matrix asphalt. When the amount of SF was more than 6%, the R-value of Bio + SF was significantly larger than that of matrix asphalt, and the deformation capacity of elastic recovery was better than that of matrix asphalt.

The Jnr-values of varying asphalt types increased with increasing stress (Figure 7). The higher the stress level, the bigger the irrecoverable deformation of asphalt under repeated loading. The Jnr-value of bioasphalt was significantly higher than that of matrix asphalt at 0.1 kPa, and the Jnr-value rose by 114.7%. After the incorporation of SF, the Jnr-values of bioasphalt decreased continuously. Compared with that of 5%Bio, the Jnr-values of 5%Bio + 2%SF, 5%Bio + 4%SF, 5%Bio + 6%SF, 5%Bio + 8%SF, and 5%Bio + 10%SF were reduced by 16.9%, 39.0%, 52.2%, 65.1%, and 75.5%, respectively. At 3.2 kPa, the Jnr-value of 5%Bio + 6%SF was similar to that of matrix asphalt. When the dosage of SF was greater than 6%, the Jnr-value of Bio + SF was significantly smaller than that of matrix asphalt, and the resistance to deformation was superior to that of matrix asphalt.

3.4. Viscosity Results Analysis

The viscosity of asphalt is an index for evaluating the ease of pavement construction. Figure 8 displays the viscosity values of varying asphalt types at 135 °C, 165 °C, and 175 °C.

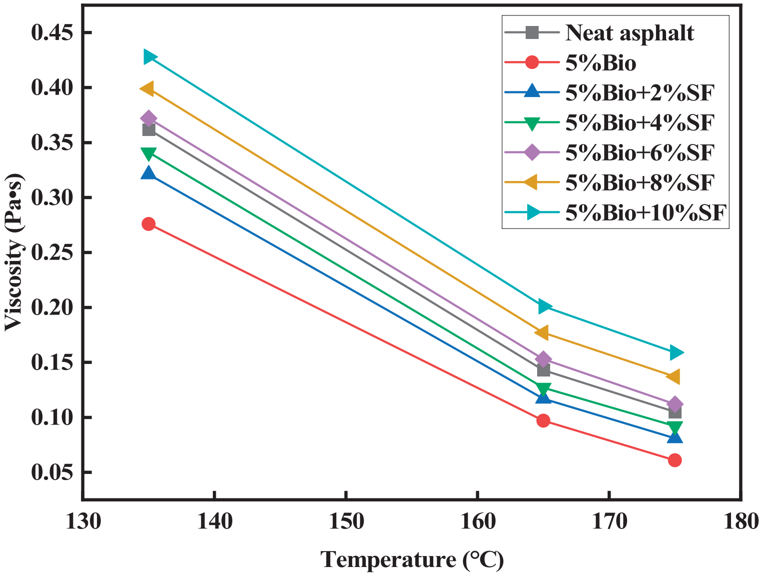

Figure 8. Viscosity test results.

The viscosity values of varying asphalt types declined with increasing temperature (Figure 8). The viscosity of 5%Bio was 0.276 Pa·s at a temperature of 135 °C. The viscosity of bioasphalt declined by 23.8% compared with that of matrix asphalt. After adding SF, bioasphalt viscosity gradually increased, and the deformation resistance was enhanced. Compared with that of 5%Bio, the viscosity values of 5%Bio + 2%SF, 5%Bio + 4%SF, 5%Bio + 6%SF, 5%Bio + 8%SF, and 5%Bio + 10%SF were increased by 16.3%, 23.6%, 34.8%, 44.6%, and 55.1%, respectively. When the SF dosage was 6%, the viscosity of Bio + SF was comparable with the matrix asphalt.

Asphalt binders are susceptible to temperature, and temperature sensitivity is an essential characteristic. Based on the viscosity data of asphalt at 135 °C, 165 °C, and 175 °C, regression analyses were performed for varying asphalt types according to the viscosity–temperature curve equation. The formula is shown in Equation (5) [43].

$$\log(\log(\eta \times 10^3)) = n - m\lg(T + 273.13) \quad (5)$$

In the equation, m is the viscosity–temperature indices VTS. The higher the value, the bigger the characterization of the asphalt material viscosity by temperature and the worse its temperature stability. Figure 9 displays the viscosity–temperature curves of varying asphalts, and the fitting parameters are summarized in Table 8.

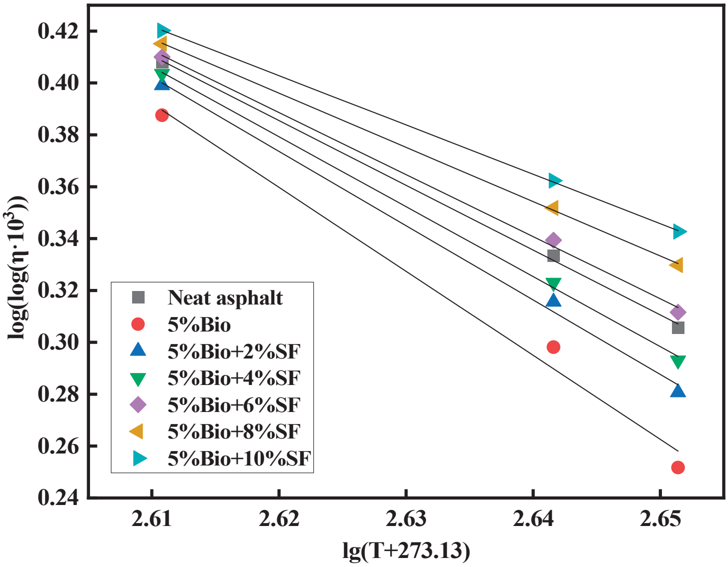

Figure 9. Viscosity–temperature curve.

Table 8. Viscosity–temperature curve fitting parameters.

Type of Asphalt	m	n	R^2
Matrix asphalt	2.497	6.928	0.99
5%Bio	3.239	8.845	0.98
5%Bio + 2%SF	2.866	7.883	0.99
5%Bio + 4%SF	2.696	7.443	0.99
5%Bio + 6%SF	2.392	6.657	0.99
5%Bio + 8%SF	2.092	5.876	0.99
5%Bio + 10%SF	1.901	5.384	0.99

Adding bio-oil diminished the viscosity of asphalt (Figure 9 and Table 8). Adding bio-oil increased the VTS value by 22.9% compared with matrix asphalt, weakening the temperature stability. After adding SF, the VTS value of bioasphalt was reduced with the increase in SF amount, which enhanced temperature stability. The viscosity values of 5%Bio + 2%SF, 5%Bio + 4%SF, 5%Bio + 6%SF, 5%Bio + 8%SF, and 5%Bio + 10%SF decreased by 11.5%, 16.8%, 26.2%, 35.4%, and 41.3%, respectively, compared with 5%Bio. When the SF dosage was 6%, bioasphalt's VTS values were comparable with matrix asphalt's. This was mainly because SF had a large specific area of surface, which enhanced the force of interaction with the asphalt and bio-oil molecules. This led to the formation of a stable space network structure in the asphalt, which enhanced bioasphalt's temperature stabilization.

3.5. Low-Temperature Rheological Characteristics

The S characterizes the resistance of asphalt to loads. The m characterizes the change rate of asphalt stiffness with time. Based on the AASHTO T 313-19 specification, the S-value shall be less than 300 MPa, and the m-value shall be bigger than 0.3 [45–47]. Figures 10 and 11 demonstrate the test results of varying asphalt types.

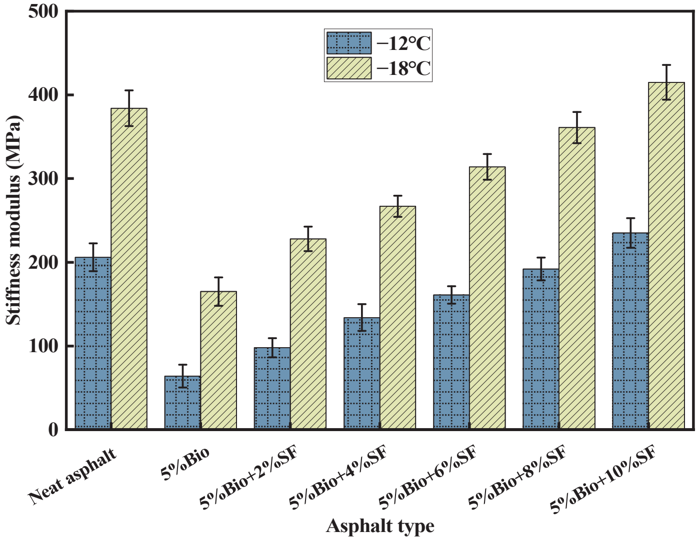

Figure 10. S-values of varying asphalt types.

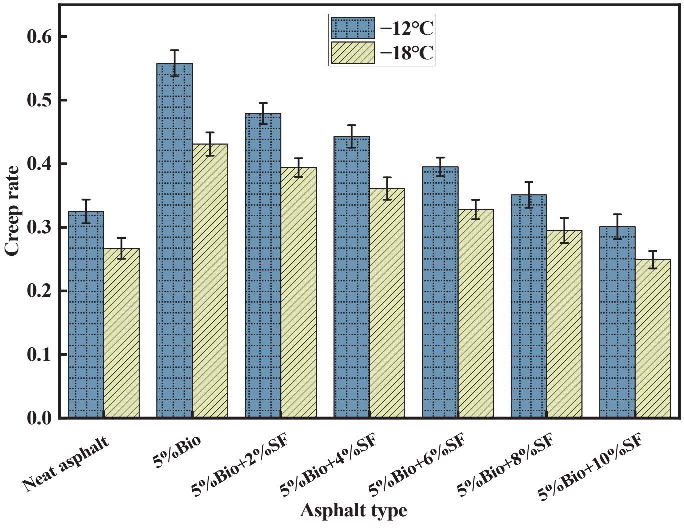

Figure 11. m-Values for varying asphalt types.

The S-values of varying asphalt types increased with decreasing temperature (Figure 10). The lower the temperature, the lower the capacity of asphalt to resist loading. At −12 °C, the S-value of varying asphalt types was less than 300 MPa, which could satisfy the standard request. When the temperature was −18 °C, only the S-values of 5%Bio, 5%Bio + 2%SF, and 5%Bio + 4%SF asphalts could satisfy the standard demand. The S-values of matrix asphalt, 5%Bio + 6%SF, 5%Bio + 8%SF, and 5%Bio + 10%SF were all greater than 300 MPa, and the ability to resist low-temperature loading was significantly reduced. Among them, when the temperature was −18 °C, adding bio-oil minimized the S-value of matrix asphalt with a decrease of 57.0%. The low-temperature antifracture characteristics of bioasphalt were significantly enhanced. This was because bio-oil could supplement the lightweight component and reduce the creep modulus during the aging process of asphalt. When SF was incorporated, compared with 5%Bio, the S-values of 5%Bio + 2%SF, 5%Bio + 4%SF, 5%Bio + 6%SF, 5%Bio + 8%SF, and 5%Bio + 10%SF increased by 38.2%, 61.8%, 90.3%, 118.8%, and 151.5%, respectively. The incorporation of SF diminished the low-temperature behavior of bioasphalt. The S-value of bioasphalt was comparable with that of matrix asphalt when the amount of SF was 8%. This was because the intermolecular interaction between bio-oil, SF, and asphalt was enhanced, and the structure was stabilized after the incorporation of SF. It increased asphalt's modulus, which caused it to crack easily under low-temperature conditions.

The m-values of asphalt decreased with decreasing temperature (Figure 11). This demonstrates that the stress relaxation ability of asphalt diminished when the temperature was reduced, leading to easy cracking of asphalt. The m-value of all seven asphalts was greater than 0.3 at −12 °C, which met the specification. The m-value of matrix asphalt was 0.267 at −18 °C, which did not satisfy the standard demand. The m-value of asphalt strengthened when bio-oil was blended into the matrix asphalt and increased by 61.4% compared with the m-value of matrix asphalt. The m-value of bioasphalt declined markedly after incorporating different amounts of SF into the bioasphalt. Compared with 5%Bio, the m-values of 5%Bio + 2%SF, 5%Bio + 4%SF, 5%Bio + 6%SF, 5%Bio + 8%SF, and 5%Bio + 10%SF showed a decrease of 8.6%, 16.2%, 23.9% 31.6%, and 42.2%, respectively. The m-value of Bio + SF was comparable with that of matrix asphalt when the SF dosage was 8%.

To better estimate the low-temperature anticracking behavior of Bio + SF, the creep recovery rate (m)/strength modulus (S) index was used for comparative analysis. Among them, the greater the m/S is, the more superior the anticracking characteristics of asphalt are, and vice versa [48]. Figure 12 shows the variation pattern of m/S values for asphalt at different temperatures.

As illustrated in Figure 12, the lower the temperature, the higher the m/S value of asphalt. The m/S value of bioasphalt strengthened by 452.6% compared with that of matrix asphalt at −12 °C. Incorporating bio-oil strengthened the anticracking characteristics of matrix asphalt. The m/S value of bioasphalt decreased after SF was incorporated into the bio-asphalt. Compared with 5%Bio, the m/S values of 5%Bio + 2%SF, 5%Bio + 4%SF, 5%Bio + 6%SF, 5%Bio + 8%SF, and 5%Bio + 10%SF decreased by 43.9%, 62.1%, 71.9%, 79.0%, and 85.3%, respectively. The m/S values were ranked as follows: 5%Bio > 5%Bio + 2%SF > 5%Bio + 4%SF > 5%Bio + 6%SF > 5%Bio + 8%SF > matrix asphalt > 5%Bio + 10%SF. SF incorporation weakened the anticracking behavior of bioasphalt. However, for a certain amount of incorporation, the low-temperature behavior of Bio + SF was still better than that of matrix asphalt.

Based on comprehensive G*/sinδ, R, Jnr, RFAI, VTS, m, S, m/S indexes, adding bio-oil reduced the high-temperature stabilization of asphalt, but bioasphalt had superior low-temperature behavior. The incorporation of SF could effectively compensate for the high-temperature antideformation characteristics of bioasphalt and enhance the aging resistance and temperature stability. However, SF will reduce the low-temperature characteristics of bioasphalt. Nevertheless, with a certain amount of SF dosage, the low-temperature behavior of bioasphalt was still superior to matrix asphalt's.

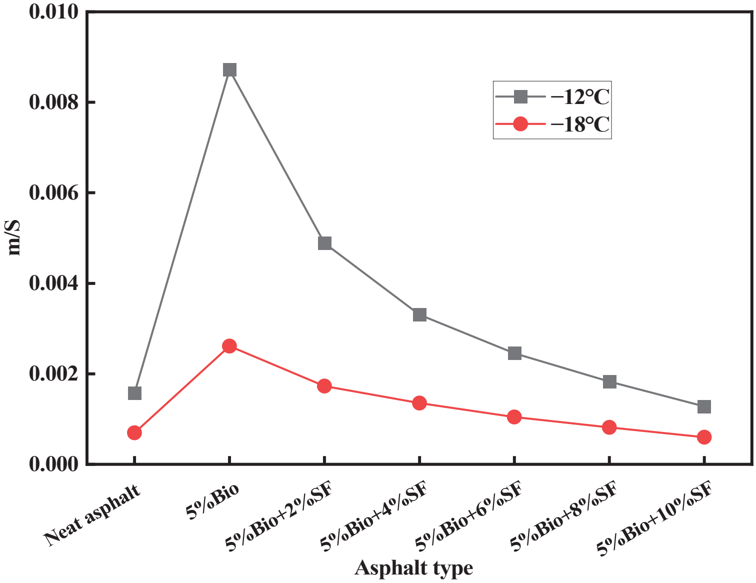

Figure 12. m/S values of varying asphalt types.

3.6. Road Performance

3.6.1. Rutting Resistance at High Temperature

The four asphalt mixtures' dynamic stability (DS) was obtained by high-temperature rutting tests, as shown in Figure 13.

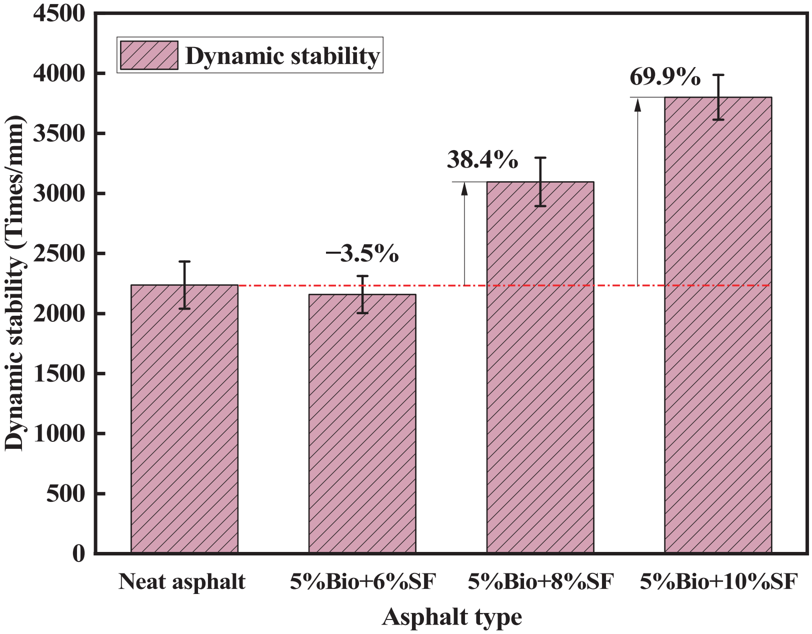

Figure 13. Dynamic stability test results.

According to JTG D50-2006 [49], the DS of an ordinary asphalt mixture should be superior to 1000 times/mm in the hot summer area. The DS of the modified asphalt mixture should be superior to 2800 times/mm. The DS of the matrix asphalt mixture was 2237 events/mm (Figure 13). Compared with the matrix asphalt mixtures, the 5%Bio + 6%SF mixture showed a decrease of 3.5% in dynamic stability. The 5%Bio + 8%SF and 5%Bio + 10%SF mixtures increased by 38.4% and 69.9%, respectively. The DS of bio-oil + SF mixtures with more than 8%SF was more than 2800 times/mm, which met the standard demand and was excellent for the matrix asphalt mixtures. Incorporating SF could effectively strengthen the antirutting characteristics of bioasphalt and asphalt mixtures.

3.6.2. Low-Temperature Anticracking Characteristics

The destructive strain of asphalt mixture specimens under a low-temperature environment is to reflect the capacity of asphalt mixture deformation. The stronger the value, the more superior the capacity of the mixture to deform. Figure 14 displays the results of the destructive strain tests of four asphalt mixtures.

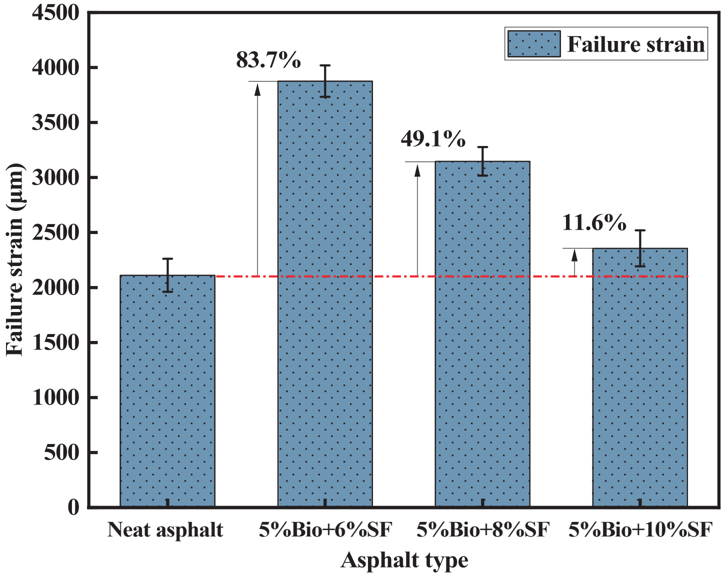

Figure 14. Failure strain test results.

According to JTG D50-2006 [49], the failure strain of ordinary asphalt mixtures is not less than 2000 μm. Modified asphalt mixtures are not smaller than 2500 μm. As illustrated in Figure 14, the failure strain of matrix asphalt mixtures is 2111 μm, which can satisfy the standard demand. After adding bio-oil and SF to the matrix asphalt, the failure strain of the bio-oil + SF mixtures strengthened remarkably, and the deformation resistance of the mixtures was effectively improved. Compared with the matrix asphalt mixtures, the failure strains of 5%Bio + 6%SF, 5%Bio + 8%SF, and 5%Bio + 10%SF mixtures increased by 83.7%, 49.1%, and 11.6%, respectively. The failure strain of 5%Bio + 10%SF modified asphalt with a 10%SF dosage was 2356 μm, which did not satisfy the standard demand for the failure strain of modified asphalt mixtures. The reason was that bio-oil contains more lightweight components, which could effectively reduce the creep modulus of asphalt. Thus, the low-temperature anticracking behavior of bio-oil + SF mixtures can be enhanced. However, incorporating SF enhanced the intermolecular forces, increasing the modulus of bioasphalt, resulting in bioasphalt mixtures being prone to cracking under low-temperature environments. The higher the amount of SF, the poorer the low-temperature behavior of bioasphalt mixtures.

3.6.3. Water Damage Resistance

The freeze–thaw splitting test is an index to assess the water loss resistance of asphalt mixtures. Figure 15 exhibits the results of the freeze–thaw split strength ratio (TSR) of four asphalt mixtures: matrix asphalt, 5%Bio + 6%SF, 5%Bio + 8%SF, and 5%Bio + 10%SF.

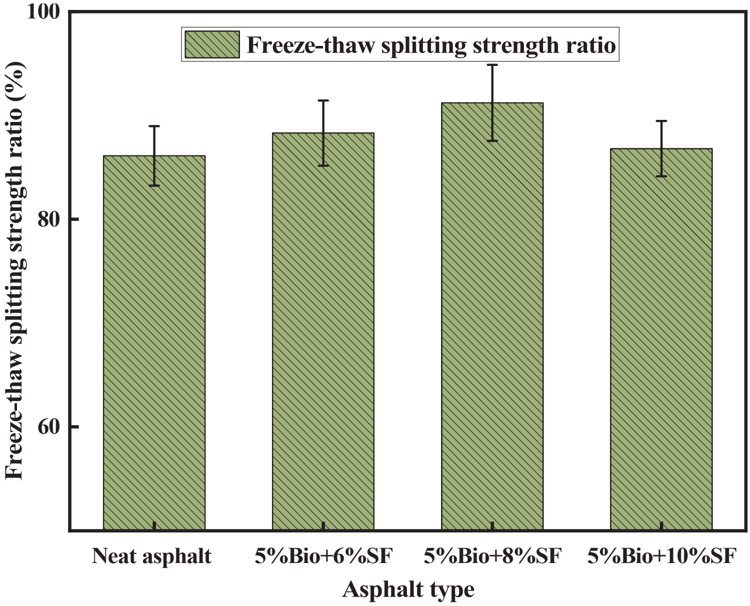

Figure 15. Freeze–thaw splitting strength ratio test results.

According to JTG D50-2006 [49], the TSR of ordinary asphalt mixtures is not smaller than 75%. The modified asphalt mixture is not smaller than 80%. As shown in Figure 15, the TSR of the matrix asphalt mixture was 86.1%, which satisfies the standard demand. The TSRs of 5%Bio + 6%SF, 5%Bio + 8%SF, and 5%Bio + 10%SF mixtures were increased by 2.6%, 5.9%, and 0.8% compared with that of the matrix asphalt mixture, respectively, which satisfy the standard demand. This was because incorporating SF can enhance the adhesion between asphalt and mineral material, enhancing the water damage resistance of bio-oil + SF mixtures.

3.6.4. Fatigue Life

Fatigue life is an essential parameter for evaluating the durability of asphalt mixtures. Figure 16 exhibits the fatigue life test results of four asphalt mixtures for matrix asphalt, 5%Bio + 6%SF, 5%Bio + 8%SF, and 5%Bio + 10%SF.

As demonstrated in Figure 16, the fatigue life of bio-oil + SF mixtures was greater than the matrix asphalt mixtures at the 0.3 MPa stress level. Compared to the fatigue life of the matrix asphalt mixtures, the fatigue life of 5%Bio + 6%SF, 5%Bio + 8%SF and 5%Bio + 10%SF mixtures increased by 17.9%, 68.9% and 7.0%, respectively. The incorporation of SF resulted in a remarkably enhanced fatigue life of bio-asphalt.

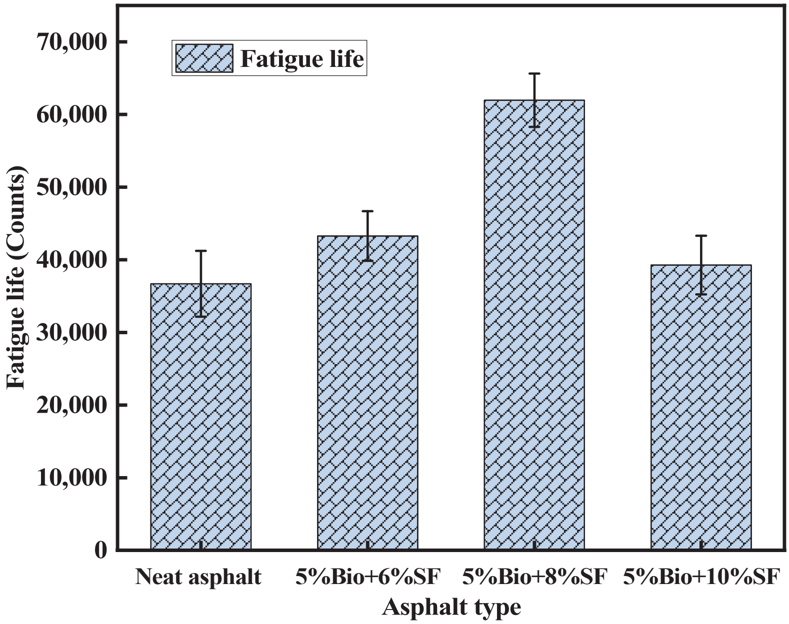

Figure 16. Fatigue life test results.

4. Conclusions

This study developed bio-oil + SF, and TS, MSCR, viscosity, and BBR tests investigated the high- and low-temperature characteristics of bio-oil + SF. Meanwhile, the road behavior of bio-oil + SF mixtures was examined using a high-temperature stabilization test, flexural creep test, split freeze–thaw test, and fatigue test. The main conclusions were drawn:

(1) Incorporating bio-oil strengthened the low-temperature characteristics of matrix asphalt. However, bio-oil significantly reduced the high-temperature characteristics of matrix asphalt.

(2) The G*/sinδ, R, and Jnr indexes showed that adding SF could improve resistance to the permanent deformation of bioasphalt at high temperatures. The RFAI and VTS indexes showed that adding SF improved bioasphalt's aging resistance and temperature stability.

(3) The m, S, and m/S indexes at −12 °C and −18 °C indicated that the rise in the dosage of SF weakened the low-temperature characteristics of bioasphalt. However, when the dosage of SF was less than 8%, the low-temperature characteristics of bio-oil + SF were still superior to those of matrix asphalt.

(4) The high-temperature stabilization, low-temperature anticracking, water damage resistance, and fatigue durability of bio-oil + SF mixtures were superior to those of matrix asphalt mixtures. The best road behavior was shown by 5%Bio + 8%SF mixtures.

(5) The test results of SF-modified bioasphalt and mixtures provided a specific scientific basis for the green and efficient application of bio-oil and SF. However, this study lacks an analysis of the SF + bio-oil mechanism. The next step will continue to explore the micromechanism of SF-modified bioasphalt and its practical engineering applications.

Author Contributions: G.H.: conceptualization, resources, data curation, writing—original draft. Y.X.: software, validation, formal analysis, writing—reviewing and editing. Z.L.: writing—reviewing and editing, conceptualization, formal analysis, methodology, validation. W.L.: methodology, conceptualization, validation, formal analysis. All authors have read and agreed to the published version of the manuscript.

Funding: This research received no external funding.

Data Availability Statement: Some or all data, models, or codes generated or used during the study are available from the corresponding author by request.

Conflicts of Interest: Author Gui Hou was employed by the company Northeast Forestry University Engineering Consulting and Design Research Institute, Ltd. The remaining authors declare that the research was conducted in the absence of any commercial or financial relationships that could be construed as a potential conflict of interest.

References

1. Zhang, Y.; Si, C.; Fan, T.; Zhu, Y.; Li, S.; Ren, S.; Lin, P. Research on the optimal dosage of Bio-Oil/Lignin composite modified asphalt based on rheological and Anti-Aging properties. *Constr. Build. Mater.* **2023**, *389*, 131796. [CrossRef]
2. Mohanty, A.K.; Vivekanandhan, S.; Pin, J.-M.; Misra, M. Composites from renewable and sustainable resources: Challenges and innovations. *Science* **2018**, *362*, 536–542. [CrossRef] [PubMed]
3. Wang, J.; Lv, S.; Liu, J.; Peng, X.; Lu, W.; Wang, Z.; Xie, N. Performance evaluation of aged asphalt rejuvenated with various bio-oils based on rheological property index. *J. Clean. Prod.* **2023**, *385*, 135593. [CrossRef]
4. Wang, H.; Jing, Y.; Zhang, J.; Cao, Y.; Lyu, L. Preparation and performance evaluation of swine manure bio-oil modified rubber asphalt binder. *Constr. Build. Mater.* **2021**, *294*, 123584. [CrossRef]
5. Mills-Beale, J.; You, Z.; Fini, E.; Zada, B.; Lee, C.H.; Yap, Y.K. Aging Influence on Rheology Properties of Petroleum-Based Asphalt Modified with Biobinder. *J. Mater. Civ. Eng.* **2014**, *26*, 358–366. [CrossRef]
6. Zhang, L.; Bahia, H.; Tan, Y. Effect of bio-based and refined waste oil modifiers on low temperature performance of asphalt binders. *Constr. Build. Mater.* **2015**, *86*, 95–100. [CrossRef]
7. Sun, Z.; Yi, J.; Huang, Y.; Feng, D.; Guo, C. Properties of asphalt binder modified by bio-oil derived from waste cooking oil. *Constr. Build. Mater.* **2016**, *102*, 496–504. [CrossRef]
8. Caro, S.; Vega, N.; Husserl, J.; Alvarez, A.E. Studying the impact of biomodifiers produced from agroindustrial wastes on asphalt binders. *Constr. Build. Mater.* **2016**, *126*, 369–380. [CrossRef]
9. Yang, X.; Mills-Beale, J.; You, Z. Chemical characterization and oxidative aging of bio-asphalt and its compatibility with petroleum asphalt. *J. Clean. Prod.* **2017**, *142*, 1837–1847. [CrossRef]
10. Zheng, W.; Wang, H.; You, Z.; Shao, L.; Golroo, A.; Chen, Y. Mechanism and rheological characterization of MDI modified Wood-Based Bio-Oil asphalt. *Constr. Build. Mater.* **2021**, *309*. [CrossRef]
11. Fernandes, S.R.M.; Silva, H.M.R.D.; Oliveira, J.R.M. Developing enhanced modified bitumens with waste engine oil products combined with polymers. *Constr. Build. Mater.* **2018**, *160*, 714–724. [CrossRef]
12. Lei, Y.; Wang, H.; Chen, X.; Yang, X.; You, Z.; Dong, S.; Gao, J. Shear property, high-temperature rheological performance and low-temperature flexibility of asphalt mastics modified with bio-oil. *Constr. Build. Mater.* **2018**, *174*, 30–37. [CrossRef]
13. Ju, Z.; Ge, D.; Wu, Z.; Xue, Y.; Lv, S.; Li, Y.; Fan, X. The performance evaluation of high content bio-asphalt modified with polyphosphoric acid. *Constr. Build. Mater.* **2022**, *361*. [CrossRef]
14. Lv, S.; Peng, X.; Liu, C.; Qu, F.; Zhu, X.; Tian, W.; Zheng, J. Aging resistance evaluation of asphalt modified by Buton-rock asphalt and bio-oil based on the rheological and microscopic characteristics. *J. Clean. Prod.* **2020**, *257*, 120589. [CrossRef]
15. Zhao, X.; Zang, G.; Gong, J.; Ren, J. Study on preparation and pavement properties of highperformance modified bio-asphalt binder. *J. Shandong Univ. Technol.* **2020**, *34*, 28–32. [CrossRef]
16. Xue, Y.; Liu, C.; Lv, S.; Ge, D.; Ju, Z.; Fan, G. Research on rheological properties of CNT-SBR modified asphalt. *Constr. Build. Mater.* **2022**, *361*, 129587. [CrossRef]
17. Sun, C.; Hao, R.; Sun, H.; Lu, T.; Tang, Q.; Wu, Y.; Wang, Y. Investigation on chemically modified carbon black in enhancing asphalt performance. *Case Stud. Constr. Mater.* **2023**, *19*, e02488. [CrossRef]
18. Zhu, C.; Zhang, H.; Zhang, Y. Influence of layered silicate types on physical, rheological and aging properties of SBS modified asphalt with multi-dimensional nanomaterials. *Constr. Build. Mater.* **2019**, *228*, 116735. [CrossRef]
19. Li, Y.; He, T.; Tang, J. Performance evaluation of asphalt binders incorporating surface-modified diatomite and bio-oil: A value-added utilization of natural resource. *Case Stud. Constr. Mater.* **2024**, *20*, e02988. [CrossRef]
20. Yadykova, A.Y.; Ilyin, S.O. Bitumen improvement with bio-oil and natural or organomodified montmorillonite: Structure, rheology, and adhesion of composite asphalt binders. *Constr. Build. Mater.* **2023**, *364*, 129919. [CrossRef]
21. Jia, X. Study on Microstructure, Action Mechanismand Mixture Performance of Inorganicmicropowder Modified Asphalt. Ph.D. Thesis, Chongqing Jiaotong University, Chongqing, China, 2022. [CrossRef]
22. Zheng, X.; Xu, W.; Feng, H.; Cao, K. High and Low Temperature Performance and Fatigue Properties of Silica Fume/SBS Compound Modified Asphalt. *Materials* **2020**, *13*, 4446. [CrossRef]
23. Song, Y. Study on Silice Fume for Modified Asphalt by Indoor Experiment. Master's Thesis, Beijing University of Technology, Beijing, China, 2008.
24. Luo, Z. The Preparation and Performance Study of Silica Fume/SBS Composite Modifiedasphalt and Its Mixture. Master's Thesis, Lanzhou University of Technology, Lanzhou, China, 2014.
25. Shang, W.; Zhan, B. Investigation of aging kinetics of silica fume modified asphalt. *J. Hefei Univ. Technol.* **2015**, *38*, 534–537.

26. Feng, H.; Xu, W.; Ji, W. The analysis on rheological properties ofsilicon powder/SBS compositemodified asphalt base on dynamic shear test. *J. Guangxi Univ.* **2019**, *44*, 191–196. [CrossRef]
27. Yadykova, A.Y.; Ilyin, S.O. Rheological and adhesive properties of nanocomposite bitumen binders based on hydrophilic or hydrophobic silica and modified with bio-oil. *Constr. Build. Mater.* **2022**, *342*, 127946. [CrossRef]
28. Khudair, A.Z.A.; Abdulzahra, M.Z.; Hamza, A.H. Effect of Silica fume on Cold Mix Asphalt Mixture. *IOP Conf. Ser. Mater. Sci. Eng.* **2020**, *737*, 012147. [CrossRef]
29. Cao, K. Study on Road Performance of the Silica Fume/SBS Composite Modified Asphalt Mixture. Master's Thesis, Northeast Forestry University, Harbin, China, 2019. [CrossRef]
30. *ASTM D 5-05*; Standard Test Method for Penetration of Bituminous Materials. American Society for Testing and Materials: West Conshohocken, PA, USA, 2005.
31. *ASTM D 113-99*; Standard Test Method for Ductility of Bituminous Materials. American Society for Testing and Materials: West Conshohocken, PA, USA, 1999.
32. *ASTM D 36-06*; Standard Test Method for Softening Point of Bitumen (Ring-and-Ball Apparatus). American Society for Testing and Materials: West Conshohocken, PA, USA, 2006.
33. *ASTM D 4402*; Standard Test Method for Viscosity Determination of Asphalt at Elevated Temperatures Using a Rotational Viscometer. American Society for Testing and Materials: West Conshohocken, PA, USA, 2012.
34. *ASTM D 2872*; Test Method for Effect of Heat and Air on a MovingFilm of Asphalt (Rolling Thin-Film Oven Test). American Society for Testing and Materials: West Conshohocken, PA, USA, 2022.
35. *JTG E42-2005*; Test Methods of Aggregate for Highway Engineering. Research Institute of Highway Ministry of Transport: Beijing, China, 2005; p. 147P.;A4. Available online: https://kns.cnki.net/kcms/detail/detail.aspx?FileName=SCSD000005041126&DbName=SCSD (accessed on 24 September 2013).
36. *AASHTO T 315-20*; Standard Method of Test for Determining the Rheological Properties of Asphalt Binder Using a Dynamic Shear Rheometer (DSR). American Association of State and Highway Transportation Officials: Washington, DC, USA, 2020.
37. *AASHTO T 350-14*; Multiple Stress Creep Recovery (MSCR) Test of Asphalt Binder Using a Dynamic Shear Rheometer (DSR). American Association of State and Highway Transportation Officials: Washington, DC, USA, 2014.
38. *AASHTO T 316*; Standard Method of Test for Viscosity Determination of Asphalt Binder Using Rotational Viscometer. American Association of State and Highway Transportation Officials: Washington, DC, USA, 2022.
39. *AASHTO T 313-19*; Standard Method of Test for Determining the Flexural Creep Stiffness of Asphalt Binder Using the Bending Beam Rheometer (BBR). American Association of State and Highway Transportation Officials: Washington, DC, USA, 2019.
40. *JTG E20-2011*; Standard Test Methods of Bitumen and Bituminous Mixtures for Highway Engineering. Research Institute of Highway Ministry of Transport: Beijing, China, 2011; p. 373P.;A4.
41. Xue, Y.; Liu, C.; Qu, J.; Lv, S.; Ju, Z.; Ding, S.; An, H.; Ren, K. Research on pavement performance of recycled asphalt mixture based on separation technology of asphalt and aggregate in RAP. *Constr. Build. Mater.* **2023**, *393*, 132103. [CrossRef]
42. Liang, B.; Zhang, H.; Liu, Z.; Liao, W. Research progress on properties of fiber modified asphalt mixture. *J. China Foreign Highw.* **2023**, *43*, 1–16. [CrossRef]
43. Liu, C.; Zhao, B.; Xue, Y.; He, Y.; Ding, S.; Wen, Y.; Lv, S. Synchronous method and mechanism of asphalt-aggregate separation and regeneration of reclaimed asphalt pavement. *Constr. Build. Mater.* **2023**, *378*, 131127. [CrossRef]
44. Huang, J.; Yan, K.; Wang, M.; Zhang, X. Enhancing rheological and aging performance of matrix asphalt through thermoplastic phenol-formaldehyde resin-based intercalated clay nanocomposites: Mechanisms and effects. *Constr. Build. Mater.* **2024**, *411*, 134351. [CrossRef]
45. Chang, J. Influence of Different Waste Oils on Rheological Properties of Aged SBS Asphalt. *J. Highw. Transp. Res. Dev.* **2023**, *40*, 33–40.
46. Ye, X.; Zou, X.; Tian, F. Study on lnfluence of Ultraviolet Radiation Aging on Rheological Properties of SBs-MCR Modified Asphalt. *J. China Foreign Highw.* **2022**, *42*, 236–240. [CrossRef]
47. Xue, Y.; Liu, C.; Shi, Q.; Ju, Z.; Fan, G.; Zhang, C.; Lv, S. Road performance and mechanism of Hot in-place recycling asphalt mixture modified by direct-to-plant SBS. *Constr. Build. Mater.* **2024**, *416*, 135122. [CrossRef]
48. Liu, S.; Cao, W.; Shang, S.; Qi, H.; Fang, J. Analysis and application of relationships between low-temperature rheological performance parameters of asphalt binders. *Constr. Build. Mater.* **2010**, *24*, 471–478. [CrossRef]
49. *JTG D50-2006*; Specifications for Design of Highway Asphalt Pavement. Zhongjiao Highway Planning and Design Institute: Beijing, China, 2006; p. 143P.;A4. Available online: https://kns.cnki.net/kcms/detail/detail.aspx?FileName=SCSD000005136705&DbName=SCSD (accessed on 24 September 2013).

materials

Article

Preparation and Hydration Properties of Sodium Silicate-Activated Municipal Solid Waste Incineration Bottom Ash Composite Ground-Granulated Blast Furnace Slag Cementitious Materials

Juan Deng [1], Guoxiong Wu [1,2,*], Yuchao Xia [1,*] and Li Liu [3]

[1] School of Civil Engineering, Chongqing Jiaotong University, Chongqing 400074, China; juandeng@mails.cqjtu.edu.cn
[2] Department of Transportation and Municipal Engineering, Chongqing Jianzhu College, Chongqing 400072, China
[3] School of He Hai, Chongqing Jiaotong University, Chongqing 400074, China
* Correspondence: wgx_ph.d@163.com (G.W.); xiayuchao@cqjtu.edu.cn (Y.X.)

Abstract: The production of municipal solid waste incineration bottom ash (MSWIBA) is substantial and has the potential to replace cement, despite challenges such as complex composition, uneven particle size distribution, and low reactivity. This paper employs sodium silicate activation of MSWIBA composite Ground-granulated Blast Furnace slag (GGBS) to improve the reactivity in preparing composite cementitious materials. It explores the hydration performance of the composite cementitious materials using isothermal calorimetric analysis, Fourier-transform infrared (FTIR) spectroscopy, XRD physical diffraction analysis, and SEM tests. SEM tests were used to explore the hydration properties of the composite gelling. The results show that with an increase in MSWIBA doping, the porosity between the materials increased, the degree of hydration decreased, and the compressive strength decreased. When the sodium silicate concentration increased from 25% to 35%, excessive alkaline material occurred, impacting the alkaline effect. This inhibited particle hydration, leading to a decrease in the degree of hydration and, consequently, the compressive strength. The exothermic process of hydration can be divided into five main stages; quartz and calcite did not fully participate in the hydration reaction, while aluminum did. The vibrational peaks of Si-O-Ti (T = Si and Al) were present in the material. The vibrational peaks of XRD, FTIR, and SEM all indicate the presence of alumosilicate network structures in the hydration products, mainly N-A-S-H and C-A-S-H gels.

Keywords: MSWIBA; sodium silicate-activated; hydration properties; hydration process

Citation: Deng, J.; Wu, G.; Xia, Y.; Liu, L. Preparation and Hydration Properties of Sodium Silicate-Activated Municipal Solid Waste Incineration Bottom Ash Composite Ground-Granulated Blast Furnace Slag Cementitious Materials. *Materials* **2024**, *17*, 2406. https://doi.org/ 10.3390/ma17102406

Academic Editor: Miguel Ángel Sanjuán

Received: 15 April 2024
Revised: 9 May 2024
Accepted: 14 May 2024
Published: 17 May 2024

1. Introduction

Solid waste production is enormous and many countries face serious issues with municipal solid waste (MSW) and environmental pollution. Selecting high-temperature incineration to treat MSW is the most effective way to reduce volume [1,2]. In general, MSW incineration treatment can reduce its mass by 70% and its volume by 90% [2,3], while the rate of unburned ash in the ash residue is 0.7–2%. The residual rates of MSWIBA and fly ash generation from MSW incineration are approximately 20% and 2% [4], respectively. Even after incineration, a large amount of MSW incineration bottom ash (MSWIBA) is still generated [5].

The rapid development of modern society requires alternative materials for sustainable development [6]. Provis pointed out that alkali-activated materials offer real possibilities to improve the sustainability of civil construction [7]. Ordinary Portland cement (OPC) consumes a considerable amount of non-renewable resources, as its production process accounts for approximately 8–10% of anthropogenic CO_2 emissions [8–10]. When using reactive alkali materials in concrete production, the CO_2 emissions are approximately 3.6 times lower than in conventional concrete production [11]. Several studies have shown that MSWIBA is potentially chemically active and can be blended with GGBS as a potential replacement material for cement through the action of alkali exciters [12].

MSWIBA is characterized by an unstable source, complex composition, non-uniform particle size distribution, and low reactivity, so it is necessary to adopt an activation treatment method to address the difficulties and problems of MSWIBA in engineering utilization [13]. Numerous scholars have explored the effect of MSWIBA at different blending levels on cement mortar or cement and found that bottom slag reduces the slump value [5,13–21]. In contrast, the opposite trend was observed when used as a cement substitute. The 28-day compressive strength of the latter was similar to or slightly higher than that of the control mixture (without the addition of MSWIBA) [22,23]. Lin et al. prepared cubic specimens to test the compressive strength of hardened slurries of cementitious materials made from slag and cement by melting MSWIBA into the slag and grinding it into powder. The results showed that the 28- and 90-day compressive strengths of the specimens were 84~90% and 95~110% of ordinary cement specimens, respectively [22,24,25]. The effect of Al_2O_3 on MSWIBA, by melting the mixture into slag and pulverizing it to replace part of the cement, has some merit [22,26].

Alkali excitation technology uses alkali exciters to activate the potential activity in MSWIBA and convert it into a material with gelling properties [27]. MSWIBA includes a large number of active components, such as silicon and aluminum, which have the potential to be alkali-activated [25]. The material undergoes hydration during the alkali activation process, the most critical chemical reaction being that between the aluminosilicate powder and the alkali exciter to produce a hardened slurry with high strength [25,27]. According to P. Kryvenko [28], the resulting geopolymer network consists of SiO_4 and AlO_4 tetrahedra, both with oxygen atoms attached, and the negative charges are balanced by positive ions (e.g., K^+, Na^+, Ca^{2+}, and Li^+) in the cavity framework [27,29,30]. The secondary binder products formed during alkali activation (including layered double hydroxides in the alkali-activated slag) are essential in determining the final properties of the material [7].

MSWIBA has a relatively stable (crystalline) chemical structure and low reactivity when in contact with water; when used as a cementitious material, it needs to be activated to improve its properties. The most common activation treatments for this purpose are physical milling activation treatment and activation treatment using alkaline substances [17,31].

The most common alkali activators are sodium hydroxide (NaOH) and sodium silicate (Na_2SiO_3, water glass) [32,33]. It is suggested that for alkali-activated slag cementitious materials, sodium silicate should be used [34,35], taking into consideration factors such as the molar concentration, the solution–binder ratio (s/b), and alkalinity [32,36,37].

In this paper, we used sodium silicate as an alkali activator and considered different ratios of Na_2SiO_3, NaOH, and MSWIBA to prepare alkali-activated materials. We used isothermal calorimetric analysis, Fourier-transform infrared (FTIR) spectroscopy, XRD physical phase diffraction analysis, and SEM, among other tests, to explore the hydration properties of composite cementation research. This aimed to promote the harmless disposal of MSWIBA and waste reuse, reduce the amount of cement, achieve energy saving and emission reduction, and promote the comprehensive reuse of the MSWIBA of this solid waste. These efforts provide theoretical references for the treatment of and application of MSWIBA.

2. Methods

2.1. Experimental Materials

2.1.1. MSWIBA and GGBS

The MSWIBA was generated by the waste incineration company Chongqing Tongxing in China Chongqing using the German Martin SITY2000 reverse thrust tilting grate technology to burn the MSW from the Chongqing area and obtain the residue. After incineration, the ferrous metal was washed, magnetically selected, and then crushed by a crusher after natural drying in the stockpile plant.

The MSWIBA was processed in a muffle furnace at a high temperature of 1000 °C for three hours and then ground by a planetary ball mill for 30 min to improve its reactivity.

By weighing 2~3 g of pre-treated MSWIBA degassed in a vacuum environment at 110 °C for 16 h using a fully automated specific surface and pore size analyzer (Quantachrome Instruments, Inc. nova-4000, Boynton Beach, FL, USA) for testing and by putting MSWIBA under an analytical temperature of −196 °C and a relative pressure interval of P/P0 = 0.01~0.995, low-pressure N2 adsorption/desorption isotherms of MSWIBA after incineration were obtained.

The treated MSWIBA was tested using the BET method to obtain a specific surface area of 1.705 m^2g^{-1} and an average pore size of 3.388 nm. The particle size distribution of the period analyzed by the laser particle sizing instrument is shown in Figure 1.

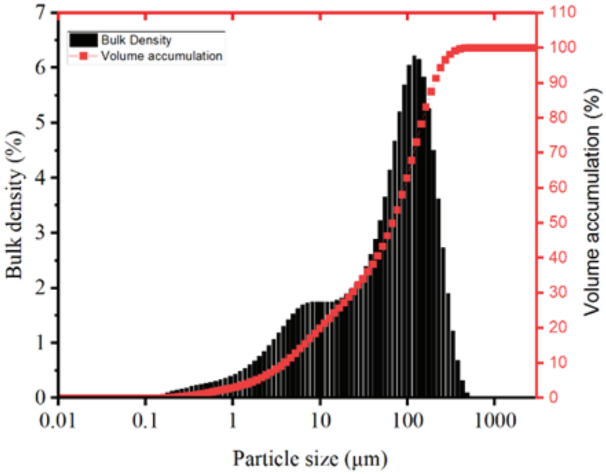

Figure 1. MSWIBA particle size distribution.

Using an X-ray fluorescence spectrometer (Rigaku Corporation, Co. ZSX Primus III+, Tokyo, Japan) on the MSWIBA and S95 GGBS, the chemical composition of the MSWIBA was determined, as shown in Table 1. According to the National Standards of China definition of the Ground-granulated Blast Furnace slag (GGBS) for Cement [38], the alkalinity index of the MSWIBA, expressed as the alkalinity index (Mo = (CaO + MgO)/(SiO_2 + AL_2O_3)), was approximately 0.68, while an Mo < 1 indicates acidic GGBS.

Table 1. The main chemical compositions of MSWIBA and GGBS (wt%).

Oxides	SiO_2	CaO	Al_2O_3	Fe_2O_3	P_2O_5	Na_2O	MgO	SO_3	K_2O
MSWIBA	37.79	28.60	9.34	5.94	5.22	3.25	2.74	2.33	1.52
GGBS	30.49	40.83	15.26	0.32	0.02	0.49	8.50	2.08	0.45

In this paper, S95 Ground-granulated Blast Furnace slag (GGBS) was selected and its density was obtained through experimental measurements, with a loss on burning of 0.84% and a water content of 0.45%. The 7-day activity index was 84.20% and Mo = (CaO + MgO)/(SiO_2 + AL_2O_3) = 1.08, indicating alkalinity according to the National Standards of China [39].

2.1.2. Sodium Silicate

Liquid sodium silicate, also known as water glass, was used in this paper as an AR analytically pure product with a modulus of 2.25, a Baume degree of 43.5, a density of 1.51 g/mL, a Na_2O content of 13.75 w%, a silica SiO_2 content of 29.99 w%, and a transparency ≥85 w%. It was produced by China Jiashan County Yourui Refractories Co. China, Jiaxing, to which 2 w% NaOH white homogeneous granular solid (Xilong Science Co. China, Chongqing) was added.

2.1.3. Other Materials

ISO reference sand was used for the tests, composed of natural round siliceous sand with a SiO_2 content of no less than 98%, meeting the requirements of National Standards of China [40]. Except for the isothermal calorimetry experiment, which used deionized water, the other experiments used tap water.

2.2. Methods

2.2.1. Material Mixing

According to the results of previous experiments, five groups of mixing ratios were selected for comparative analysis, as shown in Table 2. According to the total amounts of MSWIBA, GGBS, and sodium silicate alkali components, along with the amount of water added, the water–cement ratio (W/B) was fixed at 0.50 for the preparation of the slurry. The MSWIBA content was the lowest in the B5S25 experimental group, while the B29S25, B29S15, and B29S35 experimental groups had the highest contents, followed by B17S25. The sodium silicate content was the highest in the B29S35 experimental group, followed by B5S25, while B29S15 had the lowest content.

Table 2. The main chemical compositions of MSWIBA and GGBS (wt%).

Number	MSWIBA	Sodium Silicate	GGBS	W/C
B5S25	5	25	70	0.5
B29S25	29	25	46	0.5
B17S25	17	25	58	0.5
B29S15	29	15	56	0.5
B29S35	29	35	36	0.5

2.2.2. Experimental Methods

1. Compressive strength

According to the Test Procedure for Cement and Concrete in Highway Engineering and Test Method for Strength of Cementitious Sand (ISO Method) [40], the compressive and flexural strengths of cementitious sand are determined by molding. The size of the steel–plastic specimen was in accordance with the requirements of JC/T726, with the inner length of the test specimen being 40 × 40 × 160 mm. The specimen and the test specimen were cured in a standard curing room for 20 to 23 h. After 20 to 23 h of curing, the specimen was demolded with a machine. After demolding, the compressive and flexural strengths of the specimens were tested according to the curing requirements until the specified age. According to the molding specification, after being maintained in a standard maintenance room for 3 and 28 days, the different alkali excitation ratios of the MSWIBA composite cementitious cemented sand specimens were measured.

2. Isothermal calorimetry experiment

The heat of hydration of the composite slurry was determined using a TAM Air isothermal calorimeter produced by TA Instruments, Inc. (New Castle, DE, USA). The test time was 7 days, the calorimeter temperature was 20 °C, the water–cement ratio (W/B) was 0.5, and the material composition was consistent with Table 2. Before the experiment, the slurry was thoroughly mixed and poured into the isothermal calorimeter. After exothermic stabilization (30 min), the experimental results were recorded.

3. Hydration product analysis

The net slurry was prepared according to the Chinese national standard (GB/T1346-2011). All of the powdered materials (i.e., the GGBS and alkali components) were mixed, and then water was continuously stirred in until a homogeneous slurry was formed. The AASC slurry was hydrated at 20 ± 2 °C and 95 ± 5 RH for 3, 7, and 28 days. The AASC samples were then pulverized into small pieces and soaked in anhydrous ethanol for three days to stop hydration.

The samples were then dried in an oven at 55 °C for 48 h, crushed to make small pieces, and then vacuum processed. The microscopic morphology of the different materials was observed using a scanning electron microscope. Elemental analysis was conducted using a scanning electron microscope and an energy spectrometer. Some of the small pieces were crushed and milled for 15 to 20 min and passed through a 200 mesh square hole sieve to carry out the XRD, SEM, and FTIR spectroscopy tests.

This paper used an X-ray diffractometer (Bruker, D8Advance, Karlsruhe, Germany) to analyze the physical phase, set-hardened net paste, and mortar of the raw materials. The operating parameters of the instrument were Cu target, Kα rays, λ = 0.015 nm, X-ray generation power = 3 kw, and step size = 0.02°. The retrieved physical phases were analyzed using Jade 6.5 and HighScore Plus (3.0.5) for mineral structure analysis software. The 2023 database in X′Pert HighScore software (3.0.5) was compared to determine the crystalline phase of the material by analyzing the different peaks in the XRD pattern and comparing them with known crystal structures [41].

The molecular structure and vibrational modes of the composite cementitious materials were tested using an FTIR spectrometer utilizing a diffuse reflectance technique, which permits the incoming beam to be reflected from the ground sample to the overhead mirror, where diffusely scattered light is collected and measured in the detector.

The surface morphology of the cementite samples was observed via field emission group scanning electron microscopy (SEM) using a scanning electron microscope (Carl Zeiss AG Co. ZEISS supra55, Germany, Oberkochen), and the samples were prepared in the form of blocks with a surface area of approximately 0.5 cm^2 and a thickness of approximately 1 mm. One side of the block was polished with sandpaper to facilitate bonding on the sample stage, and the other was left untreated for observation.

3. Results and Discussion

3.1. Mechanical Properties

3.1.1. Mechanical Properties of Different MSWIBA Doping Levels

Figure 2 shows the compressive strength of the materials with different dosing ratios. The changes in compressive strength are evident. Before the reaction, the compressive strength at 3d is approximately half that at 28d. During the third reaction stage, a significant quantity of unreacted silicate mineral particles exists in the material, which means that with the increase in hydration reaction time, the degree of hydration reaction increases and compressive strength improves. In the experimental group B5S25, the 3d and 28d compressive strengths were 47.4 and 70.8 Mpa, respectively, with the highest compressive strengths. Compared with B29S25 and B17S25, with 17% and 29% MSWIBA, the 3d and 28d compressive strengths show decreasing tendencies with the increase in MSWIBA and the 3d compressive strengths reduce by 26.6% and 26.8%, respectively. The 28d compressive strengths decrease by 11.0% and 16.5%. It shows that with the increase in MSWIBA, many MSWIBA particles in the early stage of hydration of the unreacted particles increased, while the porosity between the material decreased. Hydration decreases and the compressive strength decreases with the increase in MSWIBA.

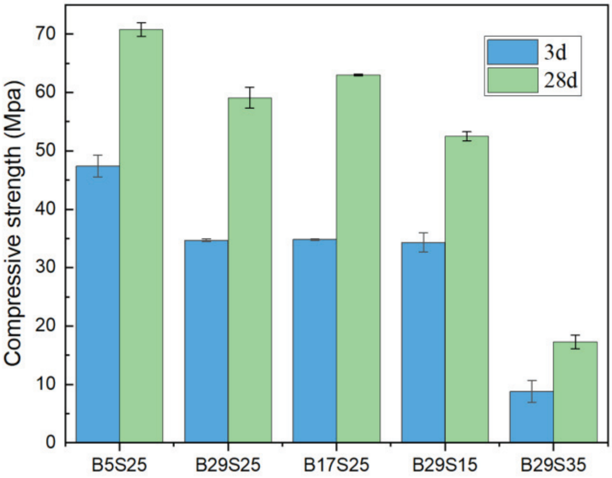

Figure 2. Compressive strength of MSWIBA GGBS composite cementitious materials activated by sodium silicate.

3.1.2. Mechanical Properties of Different Sodium Silicate Dosages

Figure 2 shows that the 3- and 28-day compressive strengths of 15% sodium silicate and the 29% MSWIBA experimental group B29S15 were 34.3 and 52.5 Mpa, respectively. The 3- and 28-day compressive strengths of B29S25 were the highest compared to B29S15 and B29S35, which increased by 1.2% and 12.6% compared to B29S15. The compressive strengths of the B29S35 experimental group were the lowest, only 8.8 and 17.3 Mpa, i.e., 74.3% and 67.0% lower than B29S25, respectively. This means that while sodium silicate increased from 15% to 25%, the alkaline material also increased, enhancing the hydration of sodium silicate particles in the alkaline environment. Consequently, the degree of hydration reaction increased, the porosity decreased and promoted the generation of hardened slurry with strength, and the compressive strength increased. When the sodium silicate increased from 25% to 35%, the alkaline material became excessive, resulting in over-alkalinity. This inhibited the hydration of particles, causing a decrease in the degree of hydration reaction and the compressive strength.

3.2. Hydration Process

3.2.1. Cumulative Heat

Figure 3a shows the cumulative exothermic curves of the four groups of materials with different ratios, from which it can be seen that the cumulative exothermic hydration time of each group increased with the increase in hydration reaction time. Additionally, with exothermic hydration, the mechanical compressive strength of the material also increased. The amount of exothermic hydration for B29S35 was significantly lower than that of the other experimental groups, as was its mechanical compressive strength. B29S15 exhibited the most significant amount of exothermic hydration and its mechanical compressive strength performed better, much higher than that of B29S35 and lower than that of the other experimental groups. The differences between B29S15 and B5S25 were minor, as shown in Figure 3b. Comparisons can be made that show that, approximately 1.5 h before and 24 h after the reaction, the exothermic hydration of B29S15 was slightly higher than that of B5S25, whereas in between, the exothermic hydration of B5S25 was somewhat higher. The amount of exothermic hydration was marginally higher.

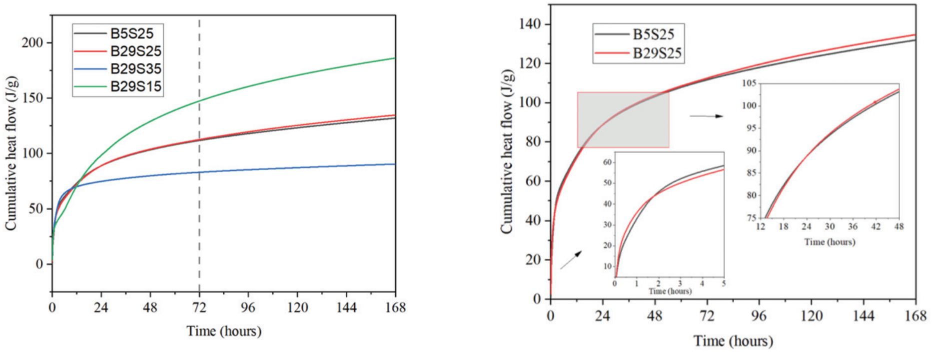

(**a**) (**b**)

Figure 3. (**a**) Cumulative heat diagrams; (**b**) Cumulative heat for B5S25 and B29S25.

3.2.2. Heat Flow

Figure 4 shows the calorimetric response and the exothermic process measured using isothermal calorimeter tests, summarized as follows.

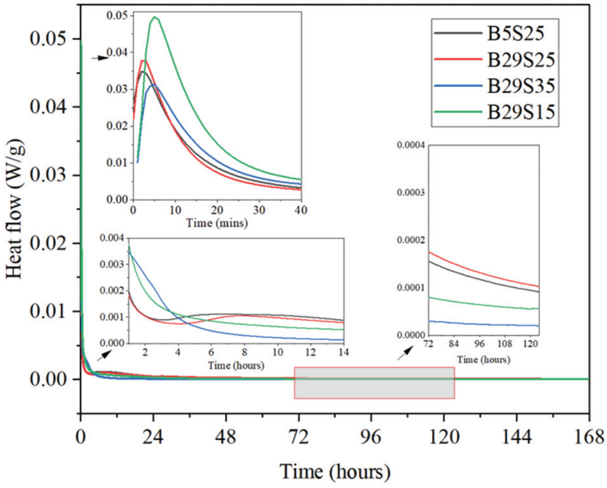

Figure 4. Heat flow diagrams of MSWIBA GGBS composite cementitious material activated by sodium silicate.

The hydration process was roughly divided into five phases. An initial induction phase, an induction phase, an acceleration phase, a deceleration phase, and a steady state phase [42]. The materials did not undergo an apparent initial induction or have an induction period and there was a prominent exothermic peak at the beginning of hydration.

The first stage is the initial induction period; this initial stage is a transient state in which the mixed GGBS dissolves rapidly. At this time, the aluminum silicate precursor gradually dissolves and is destroyed, forming an unstable iso-phase [42,43].

The second phase is the induction phase, which proceeds from the initial induction phase. At this point, the Ca^{2+} in the cementitious materials dissolves with the alkali activator, causing the ionic concentration mixing solution to become too high and the dissolution of the aluminosilicates to be inhibited [42].

The third phase, the accelerated phase, ranges from 10 min to 2–3 h; at this time, with the dissolution of the alkali activator, the concentration of OH- in the solution increases and the activity of MSWIBA and GGBS is activated, under which hydration and polymerization reactions take place to produce gel products such as (N)C-A-S-H.

The fourth phase is deceleration, ranging from 2~3 h to 24 h; at this time, the hydration rate starts to slow down with the increase in hydration products because the surface of MSWIBA and GGBS particles is gradually covered by the hydration products, which reduces the contact area [42].

Phase 5 is the steady state stage, which occurs beyond 24 h. The hydration rate is relatively low and stable, which is called the stabilization period. At this time, the cementitious material gradually hardens from the paste, the hydration reaction forms a hardened slurry, and the pore structure becomes stable [42].

3.2.3. Hydration Exothermic Equivalent Age Modeling

The heat of hydration was expressed using hyperbolic form [22], as shown in the following Equation (1):

$$Q(t) = Q_{\max} t/(n+t) \tag{1}$$

where n is the heat of hydration at half of the age. The above equation can be rewritten in the following form, as shown in the following Equation (2):

$$\frac{t}{Q(t)} = \frac{n}{Q_{\max}} + \frac{\mathrm{t}}{Q_{\max}} \tag{2}$$

First, the ratio $t/Q(t)$ was chosen as the vertical coordinate and t as the horizontal coordinate for a graph. Then, a fitting analysis was performed to obtain the slope of the line as $1/Qmax$ and the line intercept in the vertical coordinate as $n/Qmax$, leading to the value of n. This critical parameter helped us accurately describe the hydraulic exothermic process.

The equations can be obtained by calculation using *Qmax*. Figure 5 shows the hydration and heat release models of B5S25 and B29S25, as shown in Equations (3) and (4), respectively.

$$Q(t) = \frac{10{,}000t}{86.2 + 6.00089t} \tag{3}$$

$$Q(t) = \frac{10{,}000t}{90.8 + 5.85017t} \tag{4}$$

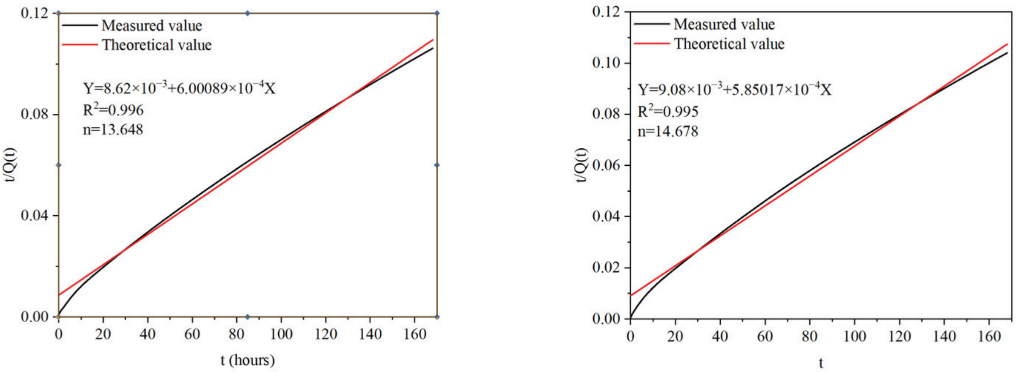

(**a**) (**b**)

Figure 5. (**a**) Model parameter-solving diagram for B5S25; (**b**) model parameter-solving diagram for B29S25.

Figure 6 illustrates the cumulative heat release of the material, as predicted by the hydration heat release model, alongside the accumulated heat release measured during testing. It can be seen from the figure that with an increase in the MSWIBA content, the total amount of accumulated heat release decreased and the theoretical value became less than the test value during the heat release. The difference did not change much in the 60 h before the heat release of hydration. After 72 h, the difference increased with time and the degree fitting degree worsened in the late stage of hydration heat release.

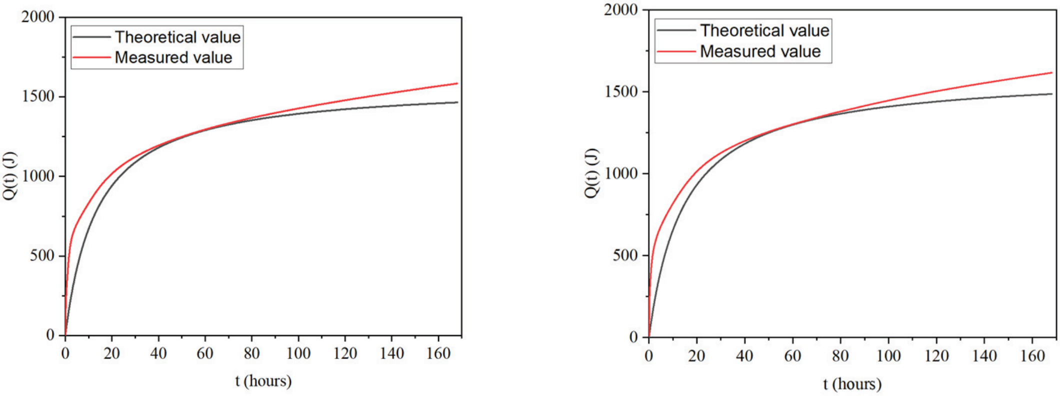

(**a**) (**b**)

Figure 6. (**a**) Comparison between the theoretical and measured values for B5S25; (**b**) comparison between the theoretical and measured values for B29S25.

3.3. Hydration Products and Properties

3.3.1. XRD Analysis

Figure 7a,b compares the ratios of the three materials after 3 and 28 days of curing B5S25 and B29S25. Compared to the XRD test curves of the raw materials, the X-ray diffraction peaks of the alkali-activated MSWIBA were relatively small in angle, indicating the formation of a new amorphous gel [44]. The broader diffraction peaks were mainly associated with the amorphous material of the feedstock and the newly formed amorphous gels of the reaction products. Using XRD analysis, it is difficult to identify and differentiate amorphous N-A-S-H and C-A-S-H gels. The quartz and mullite crystals in the MSWIBA were not fully involved in the reaction during the hydration process. They demonstrated distinct diffraction peaks in the XRD patterns.

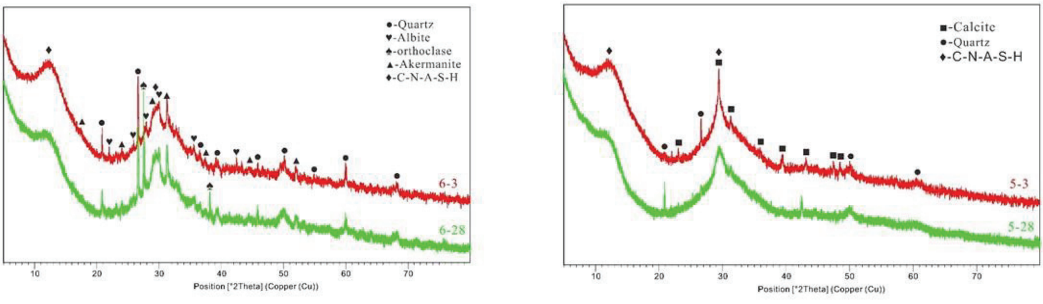

(**a**) (**b**)

Figure 7. (**a**) XRD posotion patterns of B5S25; (**b**) XRD posotion patterns of B29S25.

In contrast, the difference between specimen peaks was relatively small at three days, indicating that adding MSWIBA weakened the early hydration of the alkali-stimulated composite collodion materials [44]. In addition, the trend of high to low is consistent with the results of the mechanical properties of the slurry. A comparison of the plots of specimen B5S25 showed that the amount of hydration products increased with the length of hydration [44]. The XRD plots of group B29S25 showed changes in the physical phases after 3 and 28 days of curing. The MSWIBA content increased from 5% to 29% and the physical phases of the main hydration products in the gelling system were similar. However, an increase in the diffraction peaks of the new and firmer phases was found.

In conclusion, the physical phases of quartz and calcite were observed in the XRD patterns of the two sets of diagrams. As the hydration process proceeded, the quartz and calcite contents decreased, suggesting that these two substances transformed into different substances during the hydration process. The reduction in quartz and calcite indicates that these two substances are involved in the hydration reaction and the primary substances of the hydration reaction are similar. The C-A-S-H peaks of the 28-day groups were higher than the corresponding positions of the 7-day peaks, which indicates that the degree of hydration reaction was higher.

3.3.2. Fourier-Transform Infrared (FTIR) Analysis

FTIR spectroscopy was used to obtain the structural characteristics. Figure 8 shows the structure of the functional groups of B5S25, in which an O-H telescopic vibrational absorption peak at 3464 cm^{-1} can be observed, generated by the telescopic vibration of H-O-H in water [31]. There was also an O-H bending vibration peak at 1651 cm^{-1}, generated by the bending vibration of O-H in water. These peaks indicate the amount of chemically bound water in the alkali-activated MSWIBA GGBS binder. The higher intensity of the peaks indicates the presence of more chemically bound water in the binder [43]. Moreover, no distinct or sharp bands associated with the stretching vibration of the OH single bond in $Ca(OH)_2$ were observed at 3644 cm^{-1}, whereas the presence of the absorption band material of the Al(Mg)Si-OH phase was seen in the infrared spectral map of the MSWIBA at 3620 cm^{-1}. This indicates that the aluminosilicate in MSWIBA actively participates in the hydration reaction process during alkali activation, thus eliminating the vibrations of Al(Mg)Si-OH [31,45]. This suggests that the alkaline chemical environment plays a crucial role in reducing the crystallinity of quartz in MSWIBA and domestic waste incineration GGBS.

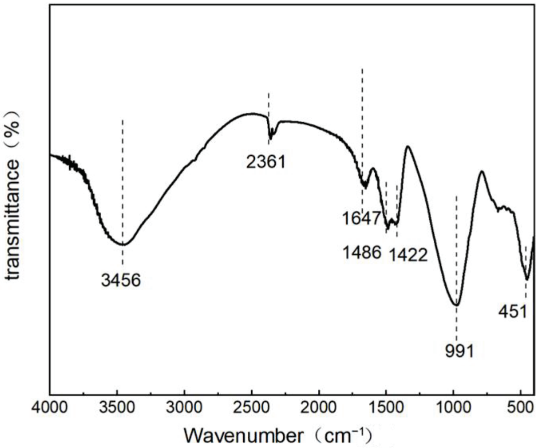

Figure 8. FTIR spectrum of B5S25.

The absorption peak at 1420 cm^{-1} resulted from the C-C stretching vibration caused by the symmetric stretching vibration of CO_3^{2-} at 3464 cm^{-1}, which accompanied a broad water peak with low intensity. This indicates that water occupied a certain proportion of the sample, suggesting that the binder contained a higher amount of chemically bound water. In the range of 600 to 1200 cm^{-1}, vibrational peaks with Si-O-Ti (T = Si and Al) were observed, indicating that an aluminosilicate network structure existed in all of the hydration products. This suggests that the aluminosilicates in the bottom GGBS of domestic waste incineration actively participate in the hydration reaction process during the alkali activation of the production process of bottom GGBS in domestic waste incineration. The results show that the samples were present in the C-A-S-H and calcium alumina, which is consistent with the X-ray diffraction and SEM-EDS analysis results.

3.3.3. Scanning Electron Microscopy

According to previous results, amorphous gels usually consist of C-A-S-H and N-A-S-H gels coexisting in alkali-activated GGBS/systems and the analyses showed the presence of N-A-S-H gels, C-(A)-S-H gels, and some unreacted MSWIBA and GGBS particles. These components showed a disordered lattice structure and excellent compatibility [31,46,47], indicating that sodium silicate's content significantly influenced the surface morphology and structure of the composite gelling material.

As can be seen from Figure 9a–c, the samples in groups B29S15, B29S35, and B29S25 have multiple microcracks due to drying shrinkage. Among them, the width and number of microcracks on the surface of B29S35 were significantly higher than that of B29S15 and there were few microcracks in B29S25. This is because when the alkali exciter dosage is 15%, it cannot provide enough alkaline material. Consequently, the activity of the gelling system is insufficient and the particles cannot react sufficiently, resulting in lower strength and a loose micro-morphology, indicating the presence of many unhydrated particles. When the alkali exciter content was increased to 25%, the activity of the gelling system increased, thus promoting the hydration reaction effect, allowing the particles to become fully dissolved and hydrated. As per the figure, the micrograph of the B29S25 specimen shows dense characteristics, with the hydration reaction products tightly wrapped around the unreacted substrate particles. At the same time, the substrate is well compacted and no apparent microcracks were found, resulting in excellent performance in terms of the compressive properties of the hardened slurry. When the alkali exciter dosage exceeded 25% to 35%, it was in excess, inhibiting the occurrence of the hydration reaction. Therefore, a large number of particles were exposed and they were not sufficiently hydrated to generate a crystalline phase. The loose morphology of B29S35 with a vast number of microcracks can be seen in Figure 9b.

The dense amorphous gel phase C-(A)-S-H with large-size silicate particles can be seen in Figure 9d–f, in which B29S35 had the most and B29S35 the least. In Figure 9e, a network-like gel phase can be seen and the 35% alkali stimulant dosing of B29S35 contained a large number of unhydrated particles compared to B29S25, which also had partially exposed and unhydrated particles. The 28-day compressive strength of the B29S35 sample was only approximately one-third of that of B29S25. Many needle- and rod-like AFt crystals can be seen in Figure 9f, enhancing the interconnection with the C-A-S-H gel.

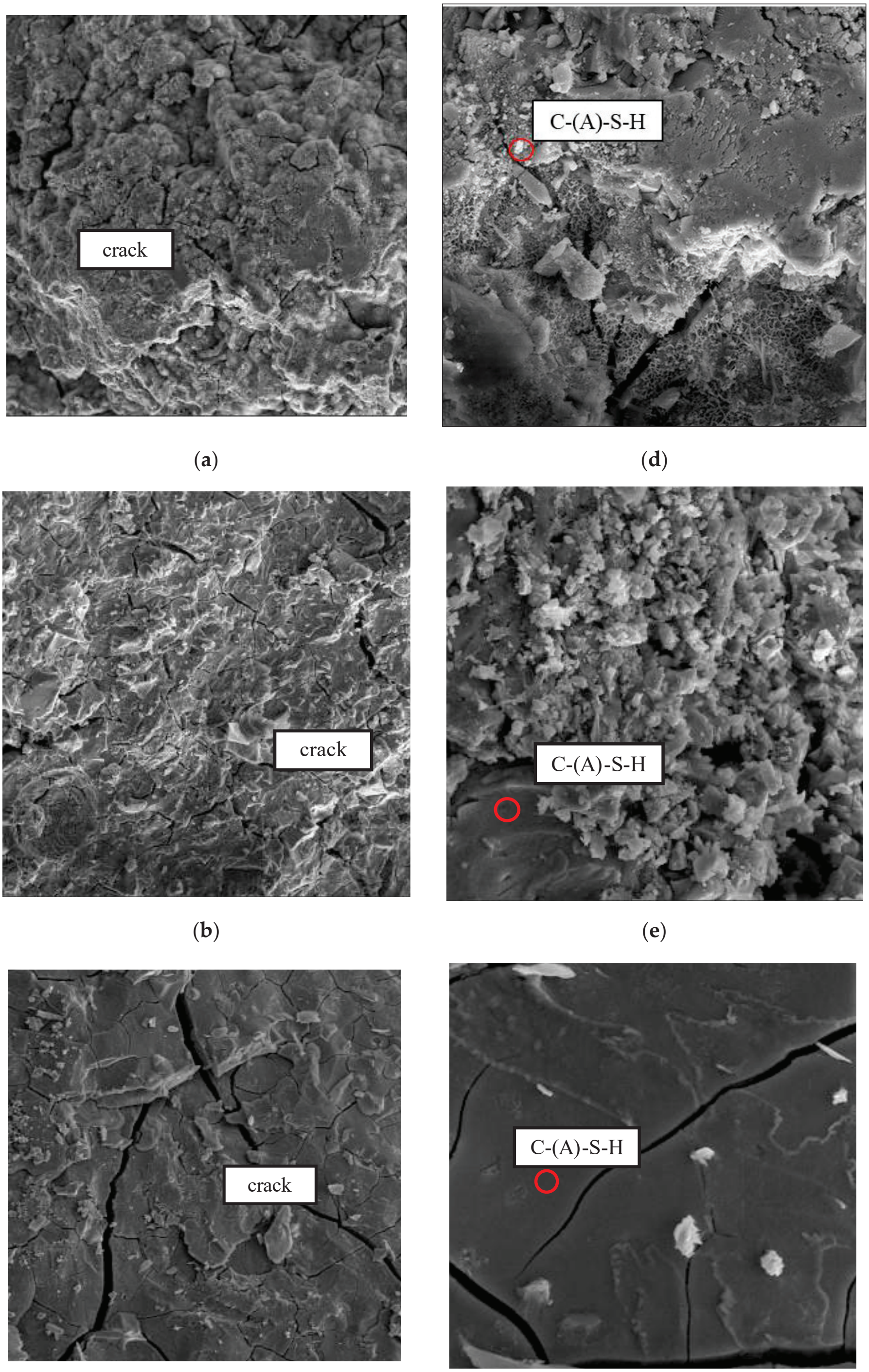

(**a**) (**d**)

(**b**) (**e**)

(**c**) (**f**)

Figure 9. (**a**,**d**) SEM observation of B29S15 at 28 days; (**b**,**e**) SEM observation of B29S35 at 28 days; (**c**,**f**) SEM observation of B29S25 at 28 days.

The results of this study show that the performance of the micro-morphological characteristics and compressive strength test results is consistent with the alkalinity of the alkali exciter, being one of the very important factors in the formation of MSWIBA composite cementitious materials and the final hydration products. With an increase in alkali exciter dosage from 15% to 25%, the increase in alkali exciters significantly promoted the conversion of free alkali to bonded alkali and the stimulation of the activator was enhanced, which helped the hydration reaction occur. A more hydrated crystalline phase was generated and the strength of the cementitious system improved. When the alkali exciter dosage increased from 25% to 35%, the alkali exciter dosage became excessive, resulting in an over-alkali effect, reducing the stimulation ability of the activator, and inhibiting the hydration reaction. Additionally, there were a large number of unhydrated particles and the microscopic morphology showed that the product was very loose, with a large number of microcracks, resulting in a significant decrease in compressive strength.

4. Summary

This research investigated the preparation and hydration properties of the sodium silicate activation of MSWIBA–GGBS composite cementitious materials, leading to the following conclusions.

The compressive strength decreased with an increase in MSWIBA. When the sodium silicate content was below 25%, the compressive strength exhibited an increasing trend with higher silicate levels. However, when the content was above 25%, the compressive strength decreased as the silicate level increased.

The hydration process can be divided into five phases. The heat is reduced with the increase in MSWIBA and the hyperbolic form is modeled as less than the test value.

As the hydration process proceeded, the quartz and calcite contents decreased, and activated aluminum participated in the hydration reaction. The XRD, FTIR, and SEM results showed that there was an aluminosilicate network structure in the hydration products, mainly N-A-S-H and C-A-S-H gels.

Author Contributions: Validation, J.D.; Formal analysis, J.D.; Investigation, J.D.; Writing—original draft, J.D.; Writing—review & editing, G.W.; Supervision, G.W.; Project administration, G.W.; Funding acquisition, Y.X. and L.L. Writing review and editing, Y.X.; Methodology, Y.X.; Visualization Y.X.; Writing—review & editing Formal Analysis, L.L. All authors have read and agreed to the published version of the manuscript.

Funding: This research received no external funding.

Institutional Review Board Statement: Not applicable.

Informed Consent Statement: Not applicable.

Data Availability Statement: Data are contained within the article.

Conflicts of Interest: The authors declare no conflict of interest.

References

1. Silva, R.V.; de Brito, J.; Lynn, C.J.; Dhir, R.K. Environmental impacts of the use of bottom ashes from municipal solid waste incineration: A review. *Resour. Conserv. Recycl.* **2019**, *140*, 23–35. [CrossRef]
2. Barros, R.M. 4-Municipal solid waste ash. In *Sustainable Concrete Made with Ashes and Dust from Different Sources*; Siddique, R., Belarbi, R., Eds.; Woodhead Publishing: Cambridge, UK, 2022; pp. 93–177.
3. Stegemann, J.A.; Schneider, J.; Baetz, B.W.; Murphy, K.L. Lysimeter washing of MSW incinerator bottom ash. *Waste Manag. Res.* **1995**, *13*, 149–165. [CrossRef]
4. Liu, J.; Wang, Z.; Li, Z.; Xie, G.; Zhang, W.; Jin, H.; Xing, F. Investigation of the cyclic separation of dioxins from municipal solid waste incineration fly ash by using fat. *J. Clean. Prod.* **2024**, *450*, 141840. [CrossRef]
5. Joseph, A.M.; Snellings, R.; Van den Heede, P.; Matthys, S.; De Belie, N. The Use of Municipal Solid Waste Incineration Ash in Various Building Materials: A Belgian Point of View. *Materials* **2018**, *11*, 141. [CrossRef] [PubMed]
6. You, Z.; Mills-Beale, J.; Yang, X.; Dai, Q. *Alternative Materials for Sustainable Transportation*; Michigan Department of Transportation: St. Joseph, MI, USA, 2012.
7. Provis, J.L. Geopolymers and other alkali activated materials: Why, how, and what? *Mater. Struct.* **2014**, *47*, 11–25. [CrossRef]

8. Ali, M.B.; Saidur, R.; Hossain, M.S. A review on emission analysis in cement industries. *Renew. Sustain. Energy Rev.* **2011**, *15*, 2252–2261. [CrossRef]
9. Wang, J.; Zhai, Z.; Jing, Y.; Zhang, C. Influence analysis of building types and climate zones on energetic, economic and environmental performances of BCHP systems. *Appl. Energy* **2011**, *88*, 3097–3112. [CrossRef]
10. González-Torres, M.; Pérez-Lombard, L.; Coronel, J.F.; Maestre, I.R.; Yan, D. A review on buildings energy information: Trends, end-uses, fuels and drivers. *Energy Rep.* **2022**, *8*, 626–637. [CrossRef]
11. Alves, B.I.; Marvila, M.T.; Linhares Júnior, J.A.; Vieira, C.M.; Alexandre, J.; de Azevedo, A.R. Alkaline Activation of Binders: A Comparative Study. *Materials* **2024**, *17*, 667. [CrossRef]
12. Gao, X.; Yuan, B.; Yu, Q.L.; Brouwers, H.J.H. Characterization and application of municipal solid waste incineration (MSWI) bottom ash and waste granite powder in alkali activated slag. *J. Clean. Prod.* **2017**, *164*, 410–419. [CrossRef]
13. Tang, P.; Chen, W.; Xuan, D.; Zuo, Y.; Poon, C.S. Investigation of cementitious properties of different constituents in municipal solid waste incineration bottom ash as supplementary cementitious materials. *J. Clean. Prod.* **2020**, *258*, 120675. [CrossRef]
14. Yamaguchi, N.; Nagaishi, M.; Kisu, K.; Nakamura, Y.; Ikeda, K. Preparation of monolithic geopolymer materials from urban waste incineration slags. *J.-Ceram. Soc. Jpn.* **2013**, *121*, 847–854. [CrossRef]
15. Łach, M.; Mierzwiński, D.; Korniejenko, K.; Mikuła, J.; Hebda, M. Geopolymers as a material suitable for immobilization of fly ash from municipal waste incineration plants. *J. Air Waste Manag. Assoc.* **2018**, *68*, 1190–1197. [CrossRef]
16. Peceño, B.; Luna-Galiano, Y.; Varela, F.; Alonso-Fariñas, B.; Leiva, C. Study of a Fire-Resistant Plate Containing Fly Ashes Generated from Municipal Waste Incinerator: Fire and Mechanical Characteristics and Environmental Life Cycle Assessment. *Materials* **2024**, *17*, 1813. [CrossRef]
17. Vilarinho, I.S.; Guimarães, G.; Labrincha, J.A.; Seabra, M.P. Development of Eco-Mortars with the Incorporation of Municipal Solid Wastes Incineration Ash. *Materials* **2023**, *16*, 6933. [CrossRef]
18. Malaiškienė, J.; Spudulis, E.; Stonys, R. The Effect of Milled Municipal Solid Waste Incineration Bottom Ash on Cement Hydration and Mortar Properties. *Materials* **2023**, *16*, 2528. [CrossRef]
19. Thomas, M.; Ślosarczyk, A. Effect of Municipal Solid Waste Slag on the Durability of Cementitious Composites in Terms of Resistance to Freeze–Thaw Cycling. *Materials* **2023**, *16*, 626. [CrossRef]
20. Poranek, N.; Łaźniewska-Piekarczyk, B.; Lombardi, L.; Czajkowski, A.; Bogacka, M.; Pikoń, K. Green Deal and Circular Economy of Bottom Ash Waste Management in Building Industry—Alkali (NaOH) Pre-Treatment. *Materials* **2022**, *15*, 3487. [CrossRef]
21. Czop, M.; Łaźniewska-Piekarczyk, B. Use of Slag from the Combustion of Solid Municipal Waste as a Partial Replacement of Cement in Mortar and Concrete. *Materials* **2020**, *13*, 1593. [CrossRef] [PubMed]
22. Lin, K.L.; Lin, D.F. Hydration characteristics of municipal solid waste incinerator bottom ash slag as a pozzolanic material for use in cement. *Cem. Concr. Compos.* **2006**, *28*, 817–823. [CrossRef]
23. Lynn, C.J.; Dhir, R.K.; Ghataora, G.S. Municipal incinerated bottom ash characteristics and potential for use as aggregate in concrete. *Constr. Build. Mater.* **2016**, *127*, 504–517. [CrossRef]
24. Pouhet, R.; Cyr, M. Carbonation in the pore solution of metakaolin-based geopolymer. *Cem. Concr. Res.* **2016**, *88*, 227–235. [CrossRef]
25. Ryu, G.S.; Lee, Y.B.; Koh, K.T.; Chung, Y.S. The mechanical properties of fly ash-based geopolymer concrete with alkaline activators. *Constr. Build. Mater.* **2013**, *47*, 409–418. [CrossRef]
26. Huang, G.; Ji, Y.; Li, J.; Hou, Z.; Jin, C. Use of slaked lime and Portland cement to improve the resistance of MSWI bottom ash-GBFS geopolymer concrete against carbonation. *Constr. Build. Mater.* **2018**, *166*, 290–300. [CrossRef]
27. Xiaolong, Z.; Shiyu, Z.; Hui, L.; Yingliang, Z. Disposal of mine tailings via geopolymerization. *J. Clean. Prod.* **2021**, *284*, 124756. [CrossRef]
28. Krivenko, P.; Pushkareva, E.; Chirkova, V. Processes of the calcium silicate hydration in the presence of alkali-metal compounds. *Izv. Vyss. Uchebnykh Zaved. Khimiya I Khimicheskaya Tekhnologiya* **1985**, *28*, 70–74.
29. Provis, J.L.; Duxson, P.; Van Deventer, J.S.J. *Geopolymer Technology and the Search for a Low-CO_2 Alternative to Concrete*; American Institute of Chemical Engineers: Salt Lake City, UT, USA, 2007.
30. Davidovits, J. Geopolymers and geopolymeric materials. *J. Therm. Anal.* **1989**, *35*, 429–441. [CrossRef]
31. Moussadik, A.; Ouzoun, F.; Ez-zaki, H.; Saadi, M.; Diouri, A. Mineralogical study of a binder based on alkali-activated coal gangue. *Mater. Today Proc.* **2023**. [CrossRef]
32. Setlak, K.; Mikuła, J.; Łach, M. Application of Industrial Waste Materials by Alkaline Activation for Use as Geopolymer Binders. *Materials* **2023**, *16*, 7651. [CrossRef]
33. Kwek, S.Y.; Awang, H.; Cheah, C.B.J.M. Influence of liquid-to-solid and alkaline activator (Sodium silicate to sodium hydroxide) ratios on fresh and hardened properties of alkali-activated palm oil fuel ash geopolymer. *Materials* **2021**, *14*, 4253. [CrossRef]
34. Sun, K.; Peng, X.; Wang, S.; Zeng, L.; Ran, P.; Ji, G.J.C.; Materials, B. Effect of nano-SiO_2 on the efflorescence of an alkali-activated metakaolin mortar. *Constr. Build. Mater.* **2020**, *253*, 118952. [CrossRef]
35. Adeleke, B.O.; Kinuthia, J.M.; Oti, J.; Pirrie, D.; Power, M. Mechanical and Microstructural Investigation of Geopolymer Concrete Incorporating Recycled Waste Plastic Aggregate. *Materials* **2024**, *17*, 1340. [CrossRef]
36. Sirotti, M.; Delsaute, B.; Staquet, S. New Experimental Evidence for Drying Shrinkage of Alkali-Activated Slag with Sodium Hydroxide. *Materials* **2023**, *16*, 5659. [CrossRef]

37. Naqi, A.; Delsaute, B.; Königsberger, M.; Staquet, S. Effect of Solution-to-Binder Ratio and Alkalinity on Setting and Early-Age Properties of Alkali-Activated Slag-Fly Ash Binders. *Materials* **2023**, *16*, 373. [CrossRef]
38. *GB/T 203-2008*; Granulated Blastfurnace Slag Used for Cement Production. National Cement Standardization Committee: Beijing, China, 2008.
39. *GB/T 18046-2017*; Ground Granulated Blast Furnace Slag Used for Cement, Mortar and Concrete. National Cement Standardization Committee: Beijing, China, 2017.
40. *GB/T 17671-2021*; Test Method of Cement Mortar Strength (ISO Method). National Standards—State Administration for Market Supervision and Administration: Beijing, China, 2021.
41. Asadizadeh, M.; Hedayat, A.; Tunstall, L.; Gonzalez, J.A.V.; Alvarado, J.W.V.; Neira, M.T. The impact of slag on the process of geopolymerization and the mechanical performance of mine-tailings-based alkali-activated lightweight aggregates. *Constr. Build. Mater.* **2024**, *411*, 134347. [CrossRef]
42. Zhao, J.; Long, B.; Yang, G.; Cheng, Z.; Liu, Q. Characteristics of alkali-activated slag powder mixing with seawater: Workability, hydration reaction kinetics and mechanism. *Case Stud. Constr. Mater.* **2022**, *17*, e01381. [CrossRef]
43. Zhang, X.; Wang, W.; Zhang, Y.; Gu, X. Research on hydration characteristics of OSR-GGBFS-FA alkali-activated materials. *Constr. Build. Mater.* **2024**, *411*, 134321. [CrossRef]
44. Huang, G.; Yang, K.; Sun, Y.; Lu, Z.; Zhang, X.; Zuo, L.; Feng, Y.; Qian, R.; Qi, Y.; Ji, Y.; et al. Influence of NaOH content on the alkali conversion mechanism in MSWI bottom ash alkali-activated mortars. *Constr. Build. Mater.* **2020**, *248*, 118582. [CrossRef]
45. Mitrović, A.; Zdujić, M. Preparation of pozzolanic addition by mechanical treatment of kaolin clay. *Int. J. Miner. Process.* **2014**, *132*, 59–66. [CrossRef]
46. Li, B.; Liu, Z.; Sun, Q.; Yang, L. Preparation of alkali-activated nickel slag-based cemented tailings backfill: Workability, strength characteristics, localized deformation and hydration mechanism. *Constr. Build. Mater.* **2024**, *411*, 134639. [CrossRef]
47. Ahmad, M.R.; Qian, L.-P.; Fang, Y.; Wang, A.; Dai, J.-G. A multiscale study on gel composition of hybrid alkali-activated materials partially utilizing air pollution control residue as an activator. *Cem. Concr. Compos.* **2023**, *136*, 104856. [CrossRef]

materials

MDPI

Article

The Effects of Hydroxypropyl Methyl Cellulose and Metakaolin on the Properties of Self-Compacting Solidified Soil Based on Abandoned Slurry

Liang Tang [1], Kaijian Huang [1,*], Gong Shen [2], Yixin Miao [2] and Jiansheng Wu [3]

[1] College of Civil Engineering, Nanjing Forestry University, Nanjing 210037, China; 13770663211@163.com
[2] Wuxi Communications Construction Engineering Group Co., Ltd., Wuxi 214000, China
[3] Nanjing Kegong Coal Science and Technology Research Co., Ltd., Nanjing 210037, China
* Correspondence: huangkaijian@njfu.edu.cn; Tel.: +86-138-1386-6459; Fax: +86-025-84498336

Abstract: As a new type of backfill material, Self-compacting solidified soil (SCSS) takes the abandoned slurry of cast-in-place piles after dewatering and reduction as the main raw material, which brings a problem of coordinating the working performance with the mechanical property under the condition of high mobility. In this paper, hydroxypropyl methyl cellulose (HPMC) and metakaolin were introduced as additives to solve this problem. First, the workability and mechanical properties of SCSS were regulated and optimized by means of the water seepage rate test, the flowability test, and the unconfined compressive strength test. Second, this study also used X-ray diffraction (XRD) and scanning electron microscopy (SEM) to investigate the effects of HPMC and metakaolin on the physical phase and microstructure of SCSS. In this way, the results showed that there was a significant impact on the flowability of SCSS, that is, when the dosage reached 0.3%, the water seepage rate of SCSS was reduced to less than 1%, and the compressive strength at 7 days reached its peak. At the same time, HPMC weakened the strength growth of SCSS in the age period of 7 days to 14 days. However, the addition of metakaolin promoted its compressive strength. XRD analysis showed that the additives had no significant effects on the physical phases. And, from the SEM results, it can be seen that although the water-retaining effect of HPMC makes hydration of cement more exhaustive, more ettringite (AFt) can be observed in the microstructure. In addition, it can be observed that the addition of metakaolin can generate more hydrated calcium silicate (C-S-H) due to the strong surface energy possessed by metakaolin. As a result of the above factors, SCSS filled the voids between particles and improved the interface structure between particles, thus enhanced the compressive strength.

Keywords: self-compacting solidified soil; workability; compressive strength; hydroxypropyl methylcellulose; metakaolin

Citation: Tang, L.; Huang, K.; Shen, G.; Miao, Y.; Wu, J. The Effects of Hydroxypropyl Methyl Cellulose and Metakaolin on the Properties of Self-Compacting Solidified Soil Based on Abandoned Slurry. *Materials* **2024**, *17*, 2960. https://doi.org/10.3390/ma17122960

Academic Editor: Evangelos J. Sapountzakis

Received: 6 May 2024
Revised: 5 June 2024
Accepted: 14 June 2024
Published: 17 June 2024

1. Introduction

During the construction of highways, railways, bridges, tunnels, and other infrastructure projects, a significant volume of slurry is utilized in the drilling process of cast-in-place piles. This slurry serves multiple purposes, including safeguarding equipment, stabilizing well walls, suspending drilling cuttings, and facilitating their removal from the hole [1]. However, the properties of the slurry gradually deteriorate over time, and once it ceases to meet the required standards, it is discarded. Consequently, a substantial quantity of discarded slurry inevitably accumulates during engineering construction [2]. These discarded muds contain substantial quantities of sand, crushed stone minerals, and various chemical additives, exhibiting a moisture content ranging from 30 to 300% [3]. Characterized by high viscosity, high moisture content, strong fluidity, and low strength, this mixture poses significant challenges for disposal. Traditionally, these muds have been dumped in large-scale landfills, leading to prolonged processing cycles, elevated costs, and potential soil erosion and damage [4–7]. When soil conditions are characterized by physical factors such as hardness and dryness, chemical factors including hypoxia and salinity, as well as biological factors like initial infection by disease organisms, plant growth is threatened. However, these marginal lands tend to nurture unique species, and research results from reference [8] indicate that species obtained from marginal lands have high potential as raw materials for the production of solid biofuels. Furthermore, the poor permeability of these engineering sludges renders them difficult to dewater and solidify naturally [9]. Consequently, the adoption of appropriate treatment methods is crucial not only for environmental protection but also for fostering the healthy and sustainable growth of the engineering industry [10,11].

Previous studies have primarily focused on recycling systems, classification, and disposal strategies for abandoned mud [12–15]. However, there is a paucity of research exploring the transformation of abandoned mud into novel materials. Currently, the utilization of mud discarded from bored piles primarily involves its conversion into cement-based construction materials [16–21], volcanic ash-based materials [22–24], fine aggregates [25–27], and brick materials [28,29]. Luis et al. [22] investigated the potential of water treatment sludge (WTS) for the development of supplementary cementitious materials (SCM). The results confirmed that WTS calcined at 600 °C possesses significant potential for producing SCM. Qian et al. [27] examined the feasibility of partially replacing sand with excess excavated soil to prepare controlled low-strength materials (CLSM). Their findings revealed that an increase in soil content leads to a reduction in the strength, fluidity, water stability, and frost resistance of CLSM. Guo et al. [28] utilized blast furnace slag to stabilize excavated soft soil for use in reclamation projects. Their results showed that the combination of blast furnace slag and lime effectively inhibits sample expansion and enhances the consolidation coefficient. Nevertheless, these resource utilization methods often encounter challenges such as high energy consumption and costs. Self-compacting solidified soil (SCSS) represents a novel type of engineering backfill material that is environmentally adaptive and leverages waste materials. Its advantages, including pumpability, high fluidity, and adjustable strength, address several limitations associated with traditional backfilling methods. Given that the slurry discarded from cast-in-place piles contains a substantial amount of water, converting it into SCSS through coagulation and dewatering treatment could effectively address the challenges related to its disposal and reuse. This approach offers notable economic and ecological benefits, making it a promising direction for future research and implementation.

Traditional solidified soil faces challenges due to high water content and poor cohesion, leading to poor flowability and excessive water permeability. For self-compacting solidified soil (SCSS) to have good self-flowing filling performance, its flowability should exceed 200 mm. Water permeability should not exceed 2% to prevent post-construction settlement. Research suggests that additives like hydroxypropyl methyl cellulose (HPMC), thermal mixed rubber, and polypropylene thickener can enhance water retention and thickening in cement-based materials, potentially improving SCSS performance [30–32]. Cellulose ether, specifically hydroxypropyl methyl cellulose (HPMC), effectively enhances both water retention and flowability in cement-based materials [32,33]. As the most widely used cellulose ether [34]. HPMC's robust water retention capabilities facilitate the hydration of cement, leading to significant improvements in the mechanical strength and adhesive properties of the slurry [35,36]. Patural [33] conducted a study on the rheological and water retention properties of mortar influenced by cellulose. At a dosage of 0.27%, cellulose exhibited remarkable thickening and water retention capabilities, with the water retention capacity increasing proportionally with molecular weight. Yang et al. [37] examined the impact of HPMC on cement-based grout properties. Their findings revealed that HPMC enhanced the aggregation of grout particles, resulting in an increase in compressive strength from 2.58 to 3.59 MPa after 28 days. Bulichen et al. [38] investigated the water retention mechanism of methyl hydroxyethyl cellulose (MHEC) and discovered that at low dosages, MHEC retained water primarily by adsorbing water molecules. On the other hand, metakaolin, a mineral additive, has been shown to influence the flowability and mechanical properties of self-compacting solidified soil. Khan et al. [39] conducted a study to investigate the impact of metakaolin content on the flowability and mechanical properties of cement-based composites. Their findings revealed that the introduction of metakaolin significantly reduced the flowability of these composites, while also exerting a negative influence on their compressive strength. Yu et al. [40] delved into the performance of metakaolin-modified concrete. Their results indicated that, at a water-cement ratio of 0.6, an increase in metakaolin content led to a decrease in concrete flowability and a corresponding increase in compressive strength. These results provide important insights into the role of HPMC and metakaolin in modifying the performance characteristics of cement-based materials. In our current study, lime and cement were employed to solidify the dehydrated slurry, resulting in the production of self-compacting solidified soil. To further enhance the water seepage properties of this material, hydroxypropyl methylcellulose (HPMC) was introduced. We systematically investigated the effects of both HPMC and metakaolin on the flowability and mechanical properties of the self-compacting solidified soil. Additionally, we analyzed the underlying mechanisms through the examination of phase composition and microscopic morphology. Our aim is to provide valuable insights and guidance for the optimal preparation of self-compacting solidified soil. To tackle the difficulty in regulating the workability and mechanical properties of self-compacting stabilized soil, this research aims to improve its usability. Not only will this bring substantial environmental benefits, but it also holds the potential for significant economic gains.

2. Experiment

2.1. Experimental Materials

This experiment used abandoned slurry from a certain road and bridge project in Wuxi, Jiangsu Province, China which consists of water as the liquid phase with sand, clay, metakaolin, and chemical reagents as the solid phase. After coagulation and dewatering, the moisture content of the slurry decreased to 63.8%, and the pH value decreased to 7.0.

The cement used in the experiment is P.O 42.5 ordinary Portland cement, and its performance indicators are shown in Table 1.

Table 1. Performance index of cement.

Density/ $(g\cdot cm^{-3})$	Fineness (80 μm)/%	Specific Surface Area/$(m^2\cdot kg^{-1})$	Compressive Strength/MPa		Flexural Strength/MPa	
			3d	28d	3d	28d
3.11	2.6	375	23.8	48.9	5.5	9.2

The chemical composition of quicklime and metakaolin with a particle size of 1250 mesh is shown in Tables 2 and 3.

Table 2. Chemical composition of quicklime.

Component	CaO	MgO	CO_2	SO_2
content/%	79	3	2	1

Table 3. Chemical composition of metakaolin.

Component	SiO_2	Al_2O_3	Fe_2O_3	TiO_2	K_2O	MgO	CaO
content/%	52.1	44.6	0.8	1.2	0.4	0.17	0.12

HPMC was selected with viscosities of 100,000 mPa·s and 200,000 mPa·s, denoted as HPMC–10 and HPMC–20, respectively. The molecular structure and performance parameters are shown in Figure 1 and Tables 4 and 5.

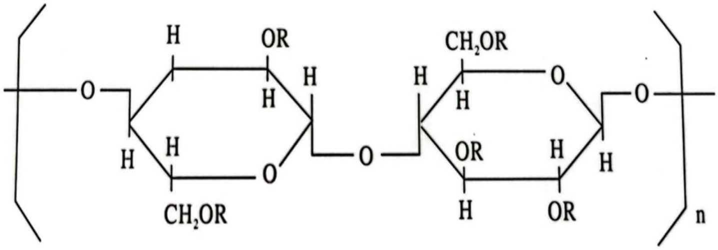

Figure 1. Molecular structure diagram of HPMC.

Table 4. HPMC–10 Basic parameters.

Name	Average Molecular Weight	Viscosity/mPa·s	Ash Content	Methoxy Content	Hydroxypropyl Content
				%	
HPMC	100,000	105,100	5	22.2	10

Table 5. HPMC–20 Basic parameters.

Name	Average Molecular Weight	Viscosity/mPa·s	Ash Content	Methoxy Content	Hydroxypropyl Content
				%	
HPMC	200,000	192,000	5	29.5	12

2.2. Methods

2.2.1. Preparation, Curing, and Mix Design of Specimens

First, this experiment required a certain amount of abandoned slurry, which was coagulated and dewatered, and the mass of each solidifying agent according to the experimental plan needed to be calculated, weighed accurately, and mixed well. Then, the blades and mixing drum of the cement slurry mixer had to be wiped with a clean damp cloth before the experiment. Next, the abandoned slurry had to adding into the mixing drum and gradually mixed with the solidifying agent while stirring. At this step, the soil was stirred for 3 to 5 min, and casted into a 40 mm 40 mm 40 mm standard cubic mold, and the surface scrape flat with a scraper when the slurry becomes homogeneous. Lastly, the mold with the sample was put into a standard curing box for 24 h of curing, then demolded. After demolding, the sample continued to cure in the curing box for 7 days, 14 days, and 28 days. The curing box was set to standard curing conditions: temperature (20 ± 2) °C, humidity 95% [41].

In this experiment, the mix design is shown in Table 6.

Table 6. Mix design.

Name	Cement	Quicklime	Metakaolin	HPMC
Add quantity/%	16	15	3 6 9 12 /	0.1 0.2 0.3 0.4 0.5

2.2.2. Water Bleeding Rate

The water seepage rate is a key indicator reflecting the resistance to segregation and the stability of solidified soil. The experiment was conducted with six sets of samples. When testing the water seepage rate, refer to JTG 3420-2020 "Test Code for Cement and Cement Concrete in Highway Engineering" (Chinese Standard) [42]. The solidified soil sample was placed in a beaker and allowed to stand. Every 15 min, the water seeped out from the surface of the solidified soil had to be extract by a dropper, and was measured with the mass as m. The calculation formula for the water seepage rate is as follows:

$$B = (m/M) \times 100\%$$

In the formula: B is the water seepage rate (%) at a certain time, m is the mass (g) of water seepage after a certain time, M is the mass (g) of the original water.

2.2.3. Flowability

The flowability is the main indicator for evaluating the workability of self-compacting solidified soil. In this study, the test method specified in the "Test Methods for Air-Entrained Mortar and Air-Entrained Grout" developed by the Japan Road Association was used [43]. For the HPMC experiments, six sets of samples were prepared, while for the metakaolin experiments, five sets of samples were utilized. The test apparatus was a hollow glass cylinder with an inner diameter of 80 mm and a height of 80 mm. In this experiment, the first step was placing the test cylinder on a smooth glass plate. After the self-compacting solidified soil was mixed, the mixture poured into the cylinder slowly. Then, the cylinder was measured its maximum spread diameter and vertical diameter when it was lifted slowly and evenly. The average of the two values was taken as the flowability of the solidified soil.

2.2.4. Unconfined Compressive Strength

The compressive strength test method follows the standard JGJ/T 70-2009 "Standard Test Methods for Basic Performance of Building Mortars" (Chinese Standard) [44]. For the HPMC experiments, six sets of samples were prepared, while for the metakaolin experiments, five sets of samples were utilized. The test is conducted by a universal testing machine produced by Shenzhen WANCE Testing Machine Co., Ltd. (Shenzhen, China), loading at a rate of 1 mm/s until failure.

$$\mathrm{f_{cu}} = \frac{\mathrm{P}}{\mathrm{A}}$$

In the formula: $\mathrm{f_{cu}}$ is the uniaxial compressive strength of the cement soil, MPa; P is the failure load, KN; A is the cross-sectional area of the specimen, mm^2.

Requirements for processing test results: The arithmetic mean of the measured values from three test pieces shall be taken as the average unconfined compressive strength of the test group. If the difference between the maximum or minimum measured value and the median value exceeds 15% of the median, both the maximum and minimum values should be discarded, and the median value should be taken as the compressive strength of the test group. If the difference between the two measured values and the median exceeds 15% of the median, the test results of the group are invalid, and new samples need to be prepared.

2.2.5. Microscopic Analysis

The solidified soil samples were analyzed for phase composition by a combination multi-functional X-ray diffractometer (Rigaku Corporation, Tokyo, Japan). The microstructure of the solidified soil specimens was analyzed by environmental scanning electron microscopy.

3. Results and Discussion

3.1. The Effect of HPMC on the Bleeding Rate of Self-Compacting Solidified Soil

From Figures 2 and 3, it is evident that the blank control group, devoid of HPMC (HPMC content of 0%), presents a strikingly high water seepage rate in the self-compacting solidified soil. The water seepage rate had already escalated to 15.1% when the SCSS was mixed for 5 min. Subsequently, the seepage rate continued its upward trajectory, and ultimately stabilizing after 90 min. So, the water seepage rate of the solidified soil without

HPMC peaked at 29.1 % finally, and it marked a substantial 94% surge compared to the initial rate observed at 5 min. Such a significant and sustained increase in water seepage rate is clearly unacceptable for practical engineering applications, highlighting the critical need for additives like HPMC to effectively mitigate this issue.

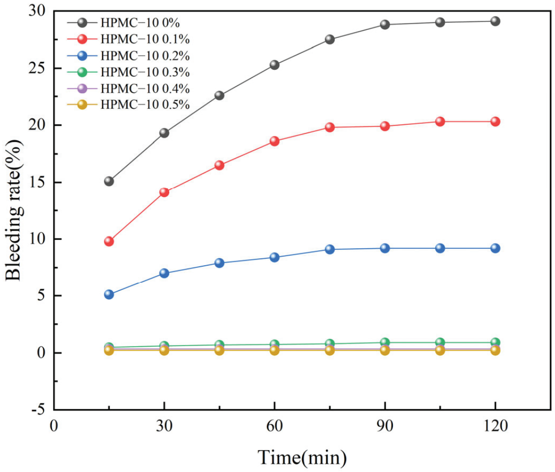

Figure 2. Bleeding rate of soil solidified with different dosages of HPMC–10.

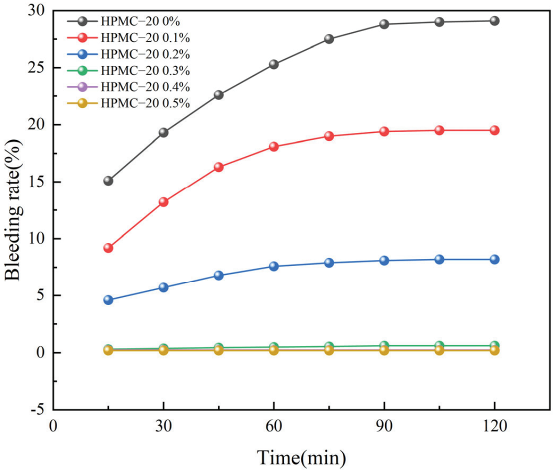

Figure 3. Bleeding rate of soil solidified with different dosages of HPMC–20.

The water seepage of SCSS had an obvious decrease when incorporated 0.1% HPMC into the solidified soil. Specifically, the inclusion of HPMC–10 resulted in a reduced water seepage rate of 9.8% within 5 min, marking a decrease of 35.1% compared to the control group. Similarly, the addition of HPMC–20 further decreased the water seepage rate to 9.2% within the same time frame, representing a 39.1% reduction. The difference in reduction between the two types of HPMC was relatively minor. Beyond 75 min, the water seepage rates in both cases began to stabilize, ultimately settling at 20.3% for HPMC–10 and 19.5% for HPMC–20. Compared to the blank control group, this stabilization represented a 30% and 33% reduction in water seepage rate. However, it is evident that the water seepage problem remains significant, indicating the need for further optimization or the exploration of alternative solutions to achieve more satisfactory results.

As the HPMC content rose further, the water seepage rate of the solidified soil demonstrated a consistent decrease. When the HPMC content attained 0.3%, the water seepage of SCSS with two types of molecular weights of HPMC reduced to less than 1%. The water seepage rate remained stable even over time. Specifically, the water seepage rate for HPMC–10 settled at 0.92% finally, while HPMC–20 was even lower at 0.63%. Upon further increased the HPMC content SCSS to 0.5%, the final water seepage rates for it with two types of molecular weights of HPMC were exceptionally low in values at 0.21% and 0.22%, this is similar to the findings reported by Yang et al. [37]. These results clearly demonstrated that HPMC is highly effective in reducing the water seepage rate of SCSS. Additionally, the water seepage of SCSS could be decreased when using HPMC, and a slight edge in performance is evident with HPMC–20, this is in line with the results reported in reference [32].

HPMC possesses long molecular chains adorned with numerous hydroxyl and ether groups. When these chains encounter water molecules, they establish hydrogen bonds [31,45], effectively sequestering the water either internally within the molecular chains or externally on their surface, which referred as the "bound water effect" [46]. Furthermore, the ether bonds present on the molecular chains have the ability to form attachments with calcium ions situated on the surface of cement particles. This allows a single cellulose molecule to adsorb multiple cement particles, leading to a phenomenon known as the "cement particle bonding effect." The combined influence of these two effects results in a reduction of free water within the solidified soil slurry. Consequently, the water seepage rate of the slurry is significantly decreased [47]. Based on a comprehensive analysis of test results, it has been determined that the water seepage issue in SCSS could be addressed by introduced an HPMC content of 0.3%.

3.2. The Influence of HPMC and Metakaolin on the Flowability of Self-Compacting Solidified Soil

3.2.1. The Impact of HPMC on the Flowability of Self-Compacting Solidified Soil

Figure 4 illustrates that as the content of HPMC with varying molecular weights rises, the flowability of self-compacting solidified soil initially improves but then gradually decreases. Notably, the influence of HPMC–20, with its higher molecular weight, is more pronounced on the flowability compared to HPMC–10. Without HPMC, the SCSS exhibited significant stratification, with a thinner slurry around the edges and cluster in the center, and resulted in poor flowability. However, the addition of 0.1% HPMC noticeably enhanced the flowability of the self-compacting soil, even it was a slow growth in flowability.

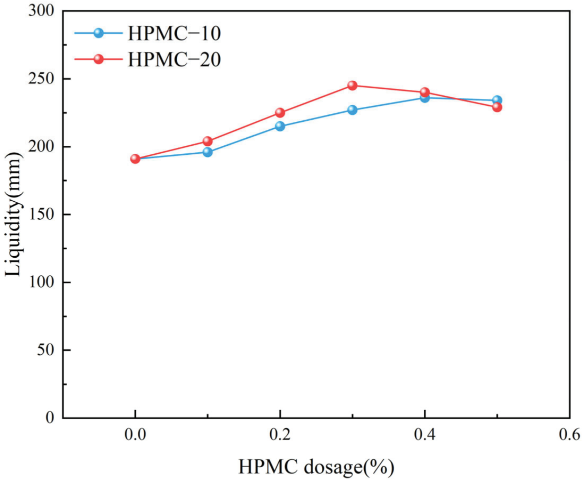

Figure 4. The effect of HPMC dosage on the flowability of self compacting solidified soil.

The content of HPMC increases, the flowability of the SCSS gradually improves, and the stratification phenomenon has diminished with the middle slurry collapsing towards the periphery. Figure 4 clearly demonstrates that the impact of different molecular weights of HPMC on flowability widens as the content rises. Specifically, the flowability peaks when 0.3% HPMC–20 is used, while for HPMC–10, the peak is observed at 0.4% content. Figure 5 further illustrates the significant improvement in slurry flowability, with the SCSS containing HPMC–10 achieving a flowability of 236 mm and that with HPMC–20 reaching 245 mm.

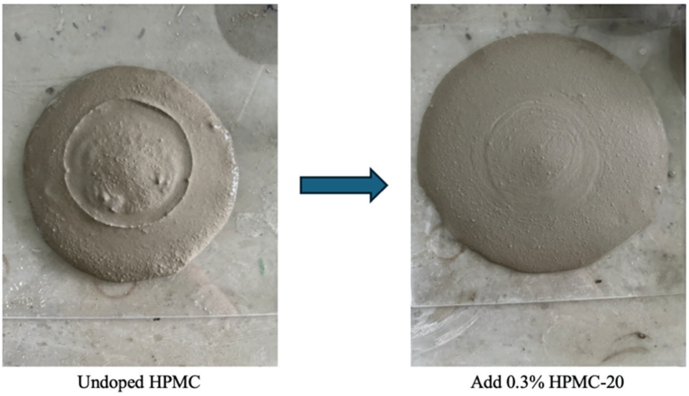

Figure 5. Liquidity test.

However, when the content of HPMC exceed a certain level, the flowability of the SCSS tends to decrease. This is due to the excessive viscosity caused by a high concentrations of HPMC, which in turn hinders the soil's ability to flow smoothly [48].

3.2.2. The Effect of Metakaolin on the Flowability of Self-Compacting Solidified Soil

Figure 6 reveals a distinct trend: as the content of metakaolin gradually increases, the flowability of the SCSS decreases, this is in agreement with the findings reported in reference [39]. Notably, as the content of metakaolin increases 3%, the flowability of SCSS has diminished by approximately 5%. When the metakaolin content reaches 12%, the flowability significantly has decreased from 245 mm to 192 mm. This observation underscores the significant impact of metakaolin on reducing the flowability of SCSS.

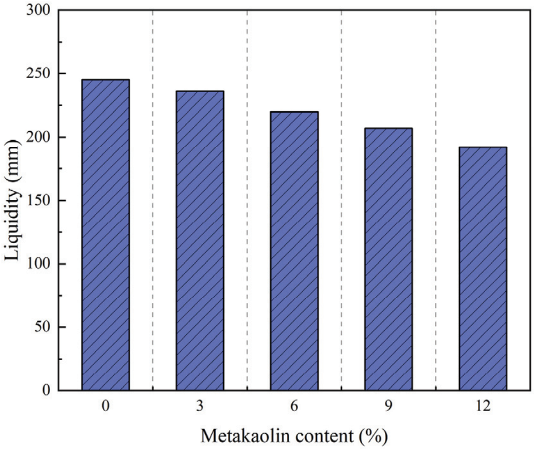

Figure 6. The effect of metakaolin content on the flowability of self compacting solidified soil.

Decrease in the flowability of SCSS upon the addition of metakaolin is primarily attributed to two key factors. Firstly, metakaolin possesses a lamellar structure and exhibits a small particle size, enabling it to adsorb a significant amount of water. Secondly, the presence of hydrophilic minerals in metakaolin contributes to the overall viscosity of the solidified soil. The combination of these two factors enhances the viscosity of the soil, leading to a reduction in its flowability [49].

3.3. The Effect of HPMC and Metakaolin on the Compressive Strength of Self-Compacting Solidified Soil

3.3.1. The Impact of HPMC on the Compressive Strength of Self-Compacting Solidified Soil

The thickening and water retention effects of high molecular weight thickeners significantly enhance the workability and stability of SCSS. Nevertheless, the addition of these thickeners may potentially affect the strength properties of SCSS. Figure 7 illustrates the impact of various dosages of HPMC–10 and HPMC–20 on the compressive strength of SCSS after 7 days.

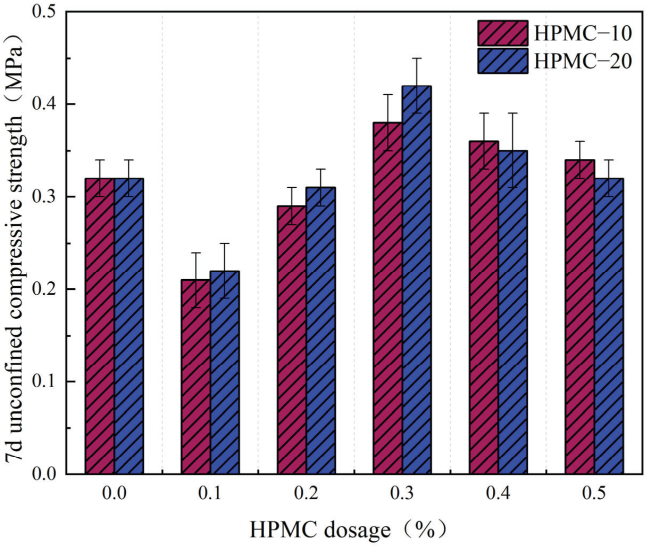

Figure 7. The effect of HPMC dosage on the compressive strength of solidified soil.

From the above figure, it is observable that the compressive strength of SCSS initially decreases and subsequently increases with the augmentation of HPMC dosage, this result is consistent with the findings reported in reference [37]. Notably, the strength attains its maximum at a dosage of 0.3%. Specifically, the strength of HPMC–10 reaches 0.38 MPa, indicating a 19% elevation compared to the baseline control group (0.32 MPa). More significantly, HPMC–20 demonstrates a strength of 0.42 MPa, reflecting a substantial 31% increase over the control. This underscores the preponderance of high molecular weight HPMC in augmenting the strength of solidified soil compared to its low molecular weight variant.

However, SCSS begins to decline once the HPMC dosage surpasses 0.3%. Specifically, the strength of the SCSS with HPMC–10 diminishes by 11% compared to its peak, while the strength of the solidified soil with HPMC–20 decreases by 24% when both of them at a dosage of 0.5%. This decrement in strength can be attributed to two factors. Firstly, an excessive amount of HPMC can lead to an increase in free water within SCSS. As this water evaporates, the structural integrity of SCSS will be weakened when it leaves behind pores, which is caused by the stress concentration. Secondly, the introduction of HPMC also brings about an increase in bubbles. The viscosity of the solidified soil rises when the dosage is high, impeding the effective diffusion and elimination of these internal bubbles [50,51]. And this reduction in compactness further contributes to the decrease in strength [37]. Taken together, these factors explain the observed decline in strength when the HPMC dosage exceeds optimal levels.

Figures 8 and 9 show the variation of the strength of solidified soil with different HPMC dosages over time. The following trends can be clearly observed from the above figures: the control group had the highest strength increase from 7 to 14 days, reaching 0.17 MPa. The solidified soil with the highest HPMC dosage shows the greatest strength increase from 7 to 14 days, with a strength of 0.13 MPa for 0.3% HPMC–10, but still lower than the control group. In contrast, the strength increase is minimal for the 0.5% dosage of HPMC–20, which is 0.07 MPa during the same period, also lower than the control group, A similar phenomenon was also observed in reference [52]. Additionally, the strength increase of the control group from 14 to 28 days was 0.09 MPa, while the strength increases for different dosages of HPMC–10 and HPMC–20 solidified soil during the same period remained at around 0.08 MPa, showing a trend similar to that of the control group.

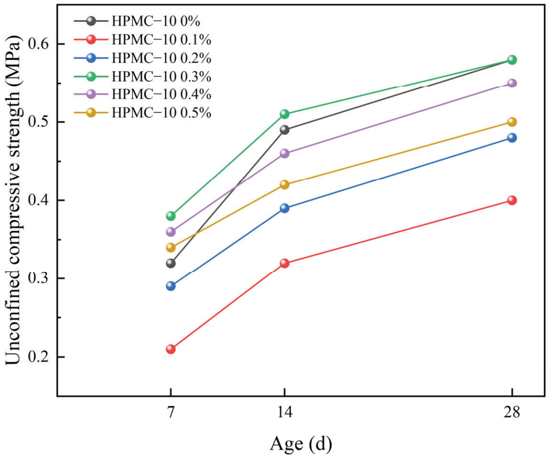

Figure 8. Changes in strength of solidified soil with different HPMC–10 dosages over time.

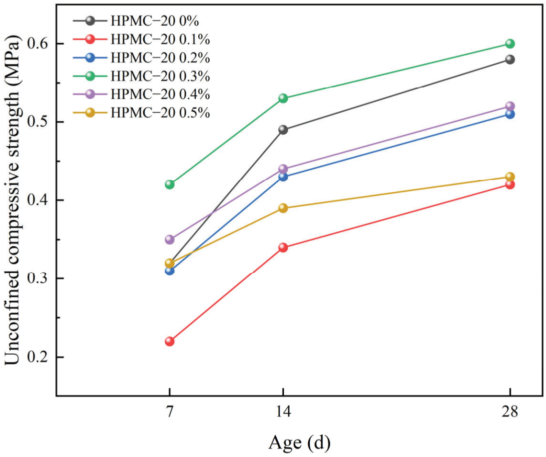

Figure 9. Changes in strength of solidified soil with different HPMC–20 dosages over time.

Based on this experiment, it can be deduced that the addition of HPMC hinders the strength development of self-compacting solidified soil during the initial 7 to 14 days of curing. However, from 14 to 28 days, the impact of HPMC on strength growth appears to be insignificant [50]. Furthermore, it is noteworthy that high molecular weight HPMC exerts a more pronounced influence on this trend.

3.3.2. The Effect of Metakaolin on the Compressive Strength of Self-Compacting Solidified Soil

This experiment maintains a constant dosage of HPMC–20 at 0.3% while varying the metakaolin content when assessing the impact of various curing ages of metakaolin on the compressive strength of SCSS.

Figure 10 illustrates the 7-day unconfined compressive strength of self-compacting solidified soil across various metakaolin dosages. Evidently, as the metakaolin dosage increases, the compressive strength of the soil also rises consistently. This result is identical to that reported in literature [40]. Notably, the compressive strength reaches 0.82 MPa when the metakaolin dosage attains 9%, surpassing the blank control group by a substantial 95%. This significant enhancement suggests that metakaolin supplementation is an effective means to boost the compressive strength of self-compacting solidified soil. And, the magnitude of this increase scales with the amount of metakaolin added.

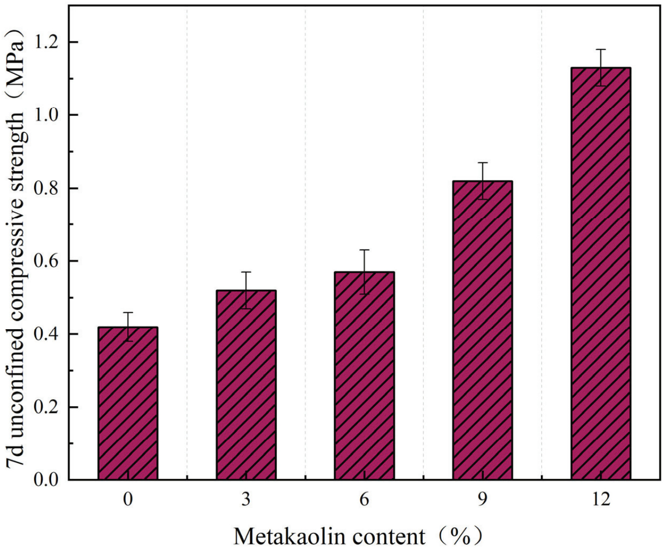

Figure 10. The effect of metakaolin content on the compressive strength of solidified soil.

Figure 11 demonstrates the compressive strength development of self-compacting solidified soil at varying ages and metakaolin dosages. Compared to the blank control group, which exhibits a strength growth of 0.11 MPa from 7 to 14 days and 0.07 MPa from 14 to 28 days, the groups with metakaolin supplementation display superior growth rates. Specifically, the metakaolin-added groups show that the lowest strength growth is 0.15 MPa from 7 to 14 days and 0.12 MPa from 14 to 28 days. The strength growth curves apparently show that the slopes of the metakaolin-containing groups are slightly steeper than those of the control, indicating that metakaolin significantly accelerates the strength growth rate of self-compacting solidified soil.

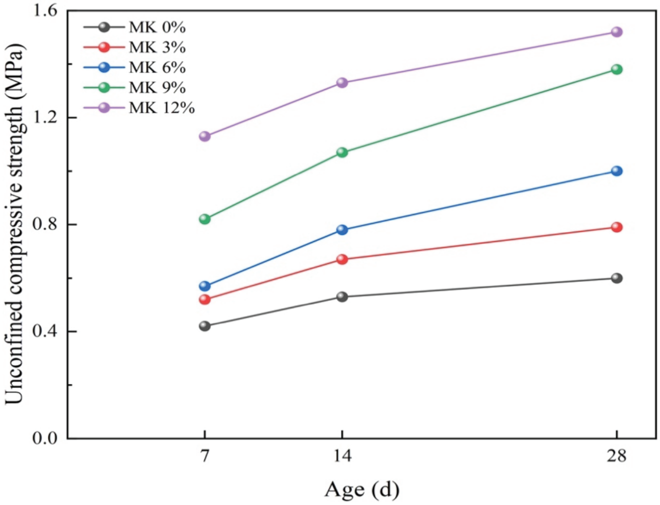

Figure 11. Figure of strength variation of solidified soil with age under different metakaolin contents.

3.4. The Effects of HPMC and Metakaolin on the Phase Composition

Figure 12 presents the XRD spectra of self-compacting solidified soil with varying ratios after 7 days of curing. A, B, and C correspond to the blank group, 0.3% HPMC, and 0.3% HPMC + 3% metakaolin, respectively.

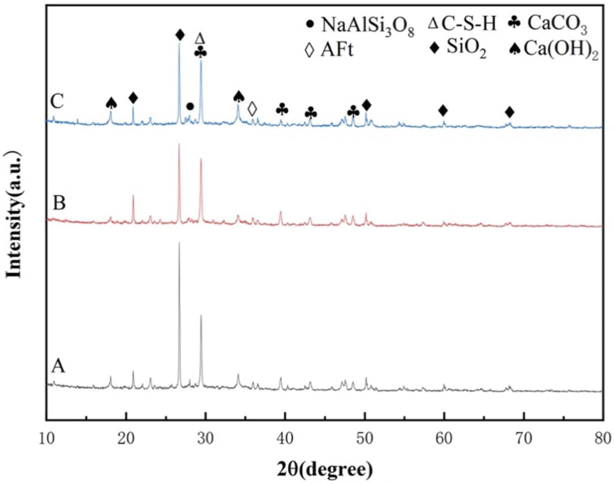

Figure 12. XRD spectra of solidified soil with different proportions at 7 d age.

The spectra reveal the presence of SiO_2, $CaCO_3$, sodium feldspar $NaAlSi_3O_8$, $Ca(OH)_2$, hydrated calcium silicate C-S-H, and ettringite AFt in all three groups. Figure 12 shows that the diffraction peaks of the SCSS remain largely unchanged across different ratios, even if the addition of HPMC and metakaolin alter the phase composition of SCSS. During the hydration process, cement produces $Ca(OH)_2$ and hydrated calcium silicate C-S-H gel, while quicklime reacts with water and atmospheric carbon dioxide to form $CaCO_3$. These are the primary sources of strength in the self-compacting solidified soil. And, it is obviously that the SiO_2 peak decreases upon the addition of HPMC. This indicates that a greater quantity of active SiO_2 is participating in the hydration reaction, leading to the formation of hydrated calcium silicate C-S-H gel and other substances [47]. Furthermore, the addition of metakaolin results in a slight strengthening of the hydrated calcium silicate C-S-H gel diffraction peak. This enhancement is attributed to the secondary hydration reaction between the active SiO_2 in metakaolin and the hydration product $Ca(OH)_2$ of cement. This reaction continuously generates hydrated calcium silicate C-S-H gel, thereby enhancing the hydration efficiency of cement.

3.5. The Effects of HPMC and Metakaolin on the Microstructure

Figure 13 presents the SEM image of self-compacting solidified soil with varying ratios after 7 days of curing.

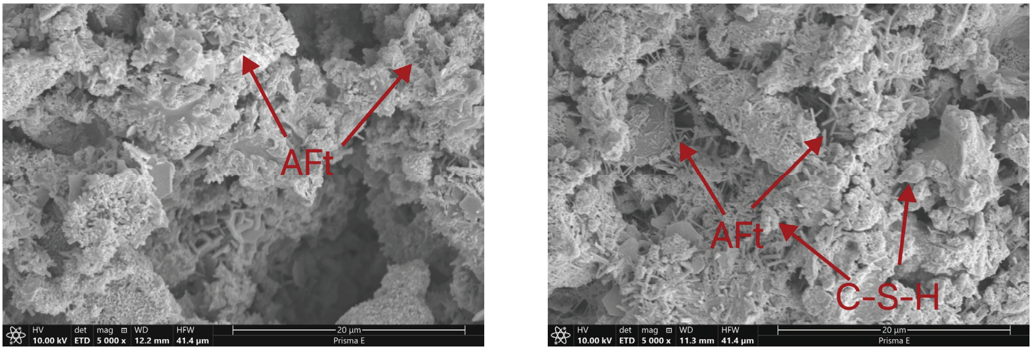

(**a**) Blank group (**b**) Add HPMC

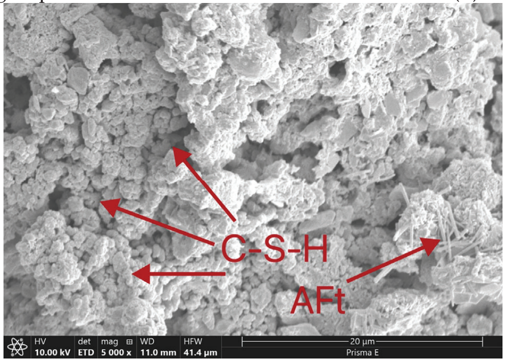

(**c**) Add HPMC and metakaolin

Figure 13. SEM images of cured soil.

From Figure 13a, it is evident that the blank control group reveals the presence of needle-like ettringite (AFt) and flocculent hydrated calcium silicate (C-S-H) gel when magnified 5000 times [53]. And, these are the primary hydration products of cement within the solidifying agent. It also shows that the gel products are interconnect and envelope the soil particles which constituting the primary source of strength for the solidified soil. Nevertheless, a notable observation from the figure is that the sample lacking additives exhibits a relatively high porosity throughout its structure.

After comparing Figure 13b, it is observed that the addition of 0.3% HPMC-20 significantly reduces the porosity in the solidified slurry sample while increasing the formation of needle-like ettringite (AFt). This is attributed to the water retention properties of HPMC, which gradually releases moisture from the slurry to the surface or air. And, the presence of free water in the solidified soil slurry extend and promote cement hydration. The expansion property of ettringite effectively fills pores, enhancing the compactness and strength of the solidified soil.

Compared with Figure 13c, SCSS shows enhanced compactness and effectively reduced porosity when it takes an addition of 3% metakaolin. The amount of flocculent hydrated calcium silicate (C-S-H) gels within the soil increases significantly. Metakaolin's fractured chemical bonds and high surface energy promote reactions with calcium hydroxide on cement and clay particle surfaces. These reactions not only refine the particle interfaces but also incorporate additional C-S-H gels, improving the internal pore structure. Since the particles of metakaolin are smaller than the cement particles, these are able to fill in the gaps between the cement particles and the clay particles to reduce the interparticle spaces. Additionally, small amounts of needle-like AFt can be seen in filling interparticle spaces. These factors collectively contribute to a denser structure and higher compressive strength in the metakaolin-reinforced solidified soil [37].

4. Conclusions

This study conducted indoor experiments to investigate the effects of HPMC and metakaolin on the properties of self-compacting solidified soil. The following key findings and conclusions were obtained:

(1) Hydroxypropyl methylcellulose (HPMC) effectively reduced the bleeding rate of the soil. At an HPMC content of 0.3%, the bleeding rate was successfully brought down to less than 1%. Additionally, higher molecular weight HPMC exhibited a superior water retention capacity. Simultaneously, HPMC enhanced the fluidity of the soil, with a more significant impact observed with higher molecular weights. Specifically, peak fluidity was achieved when the content of HPMC-10 reached 0.4% and HPMC-20 reached 0.3%. However, beyond these optimal contents, the fluidity began to decline. Conversely, metakaolin had a negative impact on fluidity, with increasing metakaolin content leading to a continuous decrease in fluidity.

(2) HPMC significantly influenced the compressive strength of the solidified soil. Both molecular weights of HPMC maximized the compressive strength at a dosage of 0.3%. Exceeding this dosage resulted in a decrease in strength, with a more pronounced effect for the higher molecular weight variant. Furthermore, HPMC attenuated the strength growth of the soil between 7 and 14 days, while having minimal impact on strength growth from 14 to 28 days. On the other hand, metakaolin effectively boosted the compressive strength of the soil and facilitated strength growth throughout the entire curing period.

(3) Neither HPMC nor metakaolin had a notable effect on the phase composition of the self-compacting solidified soil. However, the water-retaining property of HPMC facilitated more thorough hydration of cement, leading to the observation of increased ettringite in the microstructure. Meanwhile, metakaolin, due to its high surface energy, reacted with calcium hydroxide on the surface of cement and clay particles, resulting in distinct microstructural changes.

Author Contributions: Methodology, K.H.; Conceptualization, K.H.; Resources, G.S.; Investigation, L.T. and G.S.; Writing—original draft, L.T.; Supervision, Y.M. and J.W.; Validation, Y.M. and J.W. All authors have read and agreed to the published version of the manuscript.

Funding: This research received no external funding.

Institutional Review Board Statement: Not applicable.

Informed Consent Statement: Not applicable.

Data Availability Statement: Data are contained within the article.

Conflicts of Interest: Authors Gong Shen and Yixin Miao was employed by the company "Wuxi Communications Construction Engineering Group Co., Ltd.". Author Jianshen Wu was employed by the company "Nanjing Kegong Coal Science and Technology Research Co., Ltd.". The remaining authors declare that the research was conducted in the absence of any commercial or financial relationships that could be construed as a potential conflict of interest.

References

1. Zhu, H.; Sun, H.; Wang, F.; Zou, J.; Fan, J. Preparation of chitosan-based flocculant for high density waste drilling mud solid–liquid separation. *J. Appl. Polym. Sci.* **2012**, *125*, 2646–2651. [CrossRef]
2. Fang, K.; Zhang, Z.-M.; Liu, J.-C. Pollution of construction waste slurry and prevention measures. *Chin. J. Geotech. Eng.* **2011**, *33*, 238–241.
3. Ryu, Y.-M.; Kwon, Y.-S.; Kim, T.-H.; Lee, I.-M. Slurry Clogging Criteria for Slurry Shield Tunnelling in Highly Permeable Ground. *KSCE J. Civ. Eng.* **2019**, *23*, 2784–2793. [CrossRef]
4. Lang, L.; Chen, B.; Chen, B. Strength evolutions of varying water content-dredged sludge stabilized with alkali-activated ground granulated blast-furnace slag. *Constr. Build. Mater.* **2021**, *275*, 122111. [CrossRef]
5. Dong, C.-Q.; Zhang, R.-J.; Zheng, J.-J.; Jiang, W.-H. Strength behavior of dredged mud slurry treated jointly by cement, metakaolin and flocculant. *Appl. Clay Sci.* **2020**, *193*, 105676. [CrossRef]
6. Lang, L.; Chen, B.; Li, N. Utilization of lime/carbide slag-activated ground granulated blast-furnace slag for dredged sludge stabilization. *Mar. Georesour. Geotechnol.* **2021**, *39*, 659–669. [CrossRef]
7. Lang, L.; Song, C.; Xue, L.; Chen, B. Effectiveness of waste steel slag powder on the strength development and associated micro-mechanisms of cement-stabilized dredged sludge. *Constr. Build. Mater.* **2020**, *240*, 117975. [CrossRef]
8. Kamperidou, V.; Terzopoulou, P.; Barboutis, I. Marginal lands providing tree-crop biomass as feedstock for solid biofuels. *Biofuels Bioprod. Biorefining* **2021**, *15*, 1395–1405. [CrossRef]
9. Bo, M.W.; Choa, V.; Chu, J.; Arulrajah, A.; Horpibulsuk, S. Laboratory investigation on the compressibility of Singapore marine clays. *Mar. Georesources Geotechnol.* **2017**, *35*, 847–856. [CrossRef]
10. Wu, Y.; Lu, Y.; Niu, K.; Sun, D. Experimental study on solid-liquid separation of construction waste slurry by additive agent-combined vacuum preloading. *Chin. J. Geotech. Eng.* **2016**, *38*, 1365–1373. [CrossRef]
11. Chang, I.; Im, J.; Cho, G.-C. Introduction of microbial biopolymers in soil treatment for future environmentally-friendly and sustainable geotechnical engineering. *Sustainability* **2016**, *8*, 251. [CrossRef]
12. Wu, L.; Zhan, L.; Zhang, S.; Song, X.; Lu, J.; Wang, Y. Decision analysis on disposal of large quantities of excavated soft soil in abandoned mines using a Bayesian network. *Int. J. Min. Reclam. Environ.* **2022**, *36*, 419–442. [CrossRef]
13. Huang, T.; Kou, S.; Liu, D.; Li, D.; Xing, F. A BIM-GIS-IoT-Based system for excavated soil recycling. *Buildings* **2022**, *12*, 457. [CrossRef]
14. Guo, Q.; Zhan, L.; Shen, Y.; Wu, L.; Chen, Y. Classification and quantification of excavated soil and construction sludge: A case study in Wenzhou, China. *Front. Struct. Civ. Eng.* **2022**, *16*, 202–213. [CrossRef]
15. Wang, J.-N.; Xu, H.; Zhan, L.-T.; Li, S.-Z.; Wang, L.-N. Stability satisfied design and construction of excavated soil dumps in a soft soil region in China. *Front. Earth Sci.* **2022**, *9*, 822511. [CrossRef]
16. Lafhaj, Z.; Samara, M.; Agostini, F.; Boucard, L.; Skoczylas, F.; Depelsenaire, G. Polluted river sediments from the North region of France: Treatment with Novosol® process and valorization in clay bricks. *Constr. Build. Mater.* **2008**, *22*, 755–762. [CrossRef]
17. Zhang, N.; Zhang, H.; Schiller, G.; Feng, H.; Gao, X.; Li, E.; Li, X. Unraveling the Global Warming Mitigation Potential from Recycling Subway-Related Excavated Soil and Rock in China Via Life Cycle Assessment. *Integr. Environ. Assess. Manag.* **2021**, *17*, 639–650. [CrossRef] [PubMed]
18. Abadel, A.A.; Alghamdi, H.; Alharbi, Y.R.; Alamri, M.; Khawaji, M.; Abdulaziz, M.A.M.; Nehdi, M.L. Investigation of alkali-activated slag-based composite incorporating dehydrated cement powder and red mud. *Materials* **2023**, *16*, 1551. [CrossRef] [PubMed]
19. Wang, Q.; Chu, H.; Shi, W.; Jiang, J.; Wang, F. Feasibility of preparing self-compacting mortar via municipal solid waste incineration bottom ash: An experimental study. *Arch. Civ. Mech. Eng.* **2023**, *23*, 251. [CrossRef]
20. Wang, Q.; Chu, H.; Jiang, J.; Zhu, B. Enhancing mechanical performance and durability of high strength mortar with incineration bottom ash via Al_2O_3 micro-powder: An experimental study. *J. Build. Eng.* **2024**, *89*, 109268. [CrossRef]
21. Chu, H.; Wang, Q.; Zhang, W. Optimizing ecological ultra-high performance concrete prepared with incineration bottom ash: Utilization of Al_2O_3 micro powder for improved mechanical properties and durability. *Constr. Build. Mater.* **2024**, *426*, 136152. [CrossRef]
22. de Godoy, L.G.G.; Rohden, A.B.; Garcez, M.R.; Da Dalt, S.; Gomes, L.B. Production of supplementary cementitious material as a sustainable management strategy for water treatment sludge waste. *Case Stud. Constr. Mater.* **2020**, *12*, e00329. [CrossRef]
23. Priyadharshini, P.; Ramamurthy, K.; Robinson, R. Sustainable reuse of excavation soil in cementitious composites. *J. Clean. Prod.* **2018**, *176*, 999–1011. [CrossRef]
24. Wasim, M.; Abadel, A.; Bakar, B.A.; Alshaikh, I.M. Future directions for the application of zero carbon concrete in civil engineering—A review. *Case Stud. Constr. Mater.* **2022**, *17*, e01318. [CrossRef]
25. Priyadharshini, P.; Ramamurthy, K.; Robinson, R. Excavated soil waste as fine aggregate in fly ash based geopolymer mortar. *Appl. Clay Sci.* **2017**, *146*, 81–91. [CrossRef]
26. Priyadharshini, P.; Ramamurthy, K.; Robinson, R. Reuse potential of stabilized excavation soil as fine aggregate in cement mortar. *Constr. Build. Mater.* **2018**, *192*, 141–152. [CrossRef]
27. Qian, J.; Hu, Y.; Zhang, J.; Xiao, W.; Ling, J. Evaluation the performance of controlled low strength material made of excess excavated soil. *J. Clean. Prod.* **2019**, *214*, 79–88. [CrossRef]
28. Ding, G.; Xu, J.; Wei, Y.; Chen, R.; Li, X. Engineered reclamation fill material created from excavated soft material and granulated blast furnace slag. *Resour. Conserv. Recycl.* **2019**, *150*, 104428. [CrossRef]

29. Ren, H.-M.; Liu, W.-B. Macro and micro analysis of shear strength of solidified silty soils with different phosphogypsum content. *Sci. Adv. Mater.* **2020**, *12*, 1824–1832. [CrossRef]
30. Üzer, E.; Plank, J. Impact of welan gum stabilizer on the dispersing performance of polycarboxylate superplasticizers. *Cem. Concr. Res.* **2016**, *82*, 100–106. [CrossRef]
31. Ma, B.; Peng, Y.; Tan, H.; Lv, Z.; Deng, X. Effect of polyacrylic acid on rheology of cement paste plasticized by polycarboxylate superplasticizer. *Materials* **2018**, *11*, 1081. [CrossRef] [PubMed]
32. Pourchez, J.; Peschard, A.; Grosseau, P.; Guyonnet, R.; Guilhot, B.; Vallée, F. HPMC and HEMC influence on cement hydration. *Cem. Concr. Res.* **2006**, *36*, 288–294. [CrossRef]
33. Patural, L.; Marchal, P.; Govin, A.; Grosseau, P.; Ruot, B.; Deves, O. Cellulose ethers influence on water retention and consistency in cement-based mortars. *Cem. Concr. Res.* **2011**, *41*, 46–55. [CrossRef]
34. Bülichen, D.; Plank, J. Water retention capacity and working mechanism of methyl hydroxypropyl cellulose (MHPC) in gypsum plaster—Which impact has sulfate? *Cem. Concr. Res.* **2013**, *46*, 66–72. [CrossRef]
35. Govin, A.; Bartholin, M.-C.; Biasotti, B.; Giudici, M.; Langella, V.; Grosseau, P. Modification of water retention and rheological properties of fresh state cement-based mortars by guar gum derivatives. *Constr. Build. Mater.* **2016**, *122*, 772–780. [CrossRef]
36. Zhang, G.; He, R.; Lu, X.; Wang, P. Early hydration of calcium sulfoaluminate cement in the presence of hydroxyethyl methyl cellulose. *J. Therm. Anal. Calorim.* **2018**, *134*, 1429–1438. [CrossRef]
37. Yang, L.; Jia, H.; Jiao, H.; Dong, M.; Yang, T. The Mechanism of Viscosity-Enhancing Admixture in Backfill Slurry and the Evolution of Its Rheological Properties. *Minerals* **2023**, *13*, 1045. [CrossRef]
38. Bülichen, D.; Kainz, J.; Plank, J. Working mechanism of methyl hydroxyethyl cellulose (MHEC) as water retention agent. *Cem. Concr. Res.* **2012**, *42*, 953–959. [CrossRef]
39. Khan, M.I.; Abbas, Y.M.; Fares, G.; Alqahtani, F.K. Flowability and Strength Characteristics of Binary Cementitious Systems Containing Silica Fume, Fly Ash, Metakaolin, and Glass Cullet Powder. *Materials* **2023**, *16*, 6436. [CrossRef]
40. Yu, Z.; Zhang, T.; Deng, Y. The micro-facial characteristics and mechanical behavior of metakaolin and steel fibers modified concrete at high fluidity. *Case Stud. Constr. Mater.* **2022**, *16*, e01019. [CrossRef]
41. Gu, Y.; Zhang, P.; Dong, W.; Sun, Q.; Yao, G.; Lv, R. Research on the preparation and properties of GBFS-based mud solidification materials. *Constr. Build. Mater.* **2024**, *423*, 135900. [CrossRef]
42. *JTG 3420-2020*; Test Code for Cement and Cement Concrete in Highway Engineering. China Construction Industry Press: Beijing, China, 2020.
43. Japanese Road Corporation Test Methods. *Test Methods for Air-Entrained Mortar and Air-Entrained Grout*; Japanese Road Corporation: Osaka, Japan, 1990.
44. *JGJ/T 70-2009*; Basic Experimental Performance Standards for Construction Mortar. China Construction Industry Press: Beijing, China, 2009.
45. Petit, J.-Y.; Wirquin, E. Evaluation of various cellulose ethers performance in ceramic tile adhesive mortars. *Int. J. Adhes. Adhes.* **2013**, *40*, 202–209. [CrossRef]
46. Khayat, K.H. Viscosity-enhancing admixtures for cement-based materials—An overview. *Cem. Concr. Compos.* **1998**, *20*, 171–188. [CrossRef]
47. Chen, N.; Wang, P.; Zhao, L.; Zhang, G. Water Retention Mechanism of HPMC in Cement Mortar. *Materials* **2020**, *13*, 2918. [CrossRef]
48. Ding, Z.; Wang, X.; Sanjayan, J.; Zou, P.X.W.; Ding, Z.-K. A Feasibility Study on HPMC-Improved Sulphoaluminate Cement for 3D Printing. *Materials* **2018**, *11*, 2415. [CrossRef] [PubMed]
49. Güneyisi, E.; Gesoğlu, M. Properties of self-compacting mortars with binary and ternary cementitious blends of fly ash and metakaolin. *Mater. Struct.* **2008**, *41*, 1519–1531. [CrossRef]
50. Xu, C.; Wang, D.; Wang, H.; Hu, J.; Zhu, X.; Zhang, Y. Effect of partially hydrolyzed polyacrylamide on the solution and foam properties of sodium alcohol ether sulfate. *Colloids Surf. A Physicochem. Eng. Asp.* **2018**, *556*, 51–60. [CrossRef]
51. She, W.; Du, Y.; Miao, C.; Liu, J.; Zhao, G.; Jiang, J.; Zhang, Y. Application of organic-and nanoparticle-modified foams in foamed concrete: Reinforcement and stabilization mechanisms. *Cem. Concr. Res.* **2018**, *106*, 12–22. [CrossRef]
52. Zhang, Q.; Qiu, J.; Jiang, H.; Kong, X.; Guo, Z.; Xiang, J.; Sun, X. Effect of hydroxypropyl methyl cellulose on coarse tailings cemented backfill: Rheology, stability, strength and microstructure. *Constr. Build. Mater.* **2024**, *425*, 136042. [CrossRef]
53. Xiang, J.; Qiu, J.; Zheng, P.; Sun, X.; Zhao, Y.; Gu, X. Usage of biowashing to remove impurities and heavy metals in raw phosphogypsum and calcined phosphogypsum for cement paste preparation. *Chem. Eng. J.* **2023**, *451*, 138594. [CrossRef]

materials

MDPI

Article

Bending Fatigue Properties of Ultra-High Toughness Cementitious Composite (UHTCC)

Pengju Wang [1], Kaijian Huang [1,*], Gong Shen [2], Yixin Miao [2] and Jiansheng Wu [3]

[1] College of Civil Engineering, Nanjing Forestry University, Nanjing 210037, China; 18251851497@163.com
[2] Wuxi Communications Construction Engineering Group Co., Ltd., Wuxi 214000, China; gongshen0526@163.com (G.S.); yixinmiao269@163.com (Y.M.)
[3] Nanjing Kegong Coal Science and Technology Research Co., Ltd., Nanjing 210037, China; wujiansheng@njsjy.com
* Correspondence: huangkaijian@njfu.edu.cn; Tel.: +86-138-13866459; Fax: +86-025-84498336

Abstract: Ultra-High Toughness Cementitious Composite (UHTCC) represents a composite material meticulously engineered on the foundation of micromechanical principles. The multi-crack cracking and strain-hardening characteristics of UHTCC enable it to be applied to orthotropic steel decks to control the crack width. Different from most studies which only focus on hybrid fiber or fatigue characteristics, this paper studies the influence of hybrid fiber content on static mechanical properties, flexural toughness, and flexural fatigue characteristics of UHTCC under different stress levels. The compressive and flexural strength, bending toughness, and fatigue damage of UHTCC under different fiber ratios were compared, and the fatigue properties of hybrid fiber UHTCC were verified. The results reveal that hybrid fiber exerts a more pronounced effect on toughness, augmenting the maximum folding ratio by 23.7%. Single-doped steel fiber UHTCC exhibits a characteristic strain-softening phenomenon attributable to inadequate fiber content, whereas the bending toughness index of hybrid fiber UHTCC surpasses that of SF1.5P0 by 18.6%. Under low-stress conditions, UHTCC demonstrates a nearly threefold increase in bending fatigue life with a mere 1% steel fiber content, while the influence of polyvinyl alcohol (PVA) fiber on fatigue life is more significant: with an increase of only 1/5 volume content, the fatigue life increased by 29.8%, reaching a maximum increase of 43.2% at 1/4 volume content. Furthermore, the fatigue damage accumulation curve of UHTCC follows a three-stage inverted S-shaped trajectory. The inclusion of PVA fiber facilitates early initiation of stable cracking during the fatigue failure process, thereby advancing the entire strain stability development stage and mitigating external load forces through the proliferation of micro-cracks. Consequently, compared to SF1P0, the ε_0 of SF1P5 experiences a significant increase, reaching 143.43%.

Keywords: Ultra-High Toughness Cementitious Composite; toughness; bending fatigue characteristics; fatigue damage

Citation: Wang, P.; Huang, K.; Shen, G.; Miao, Y.; Wu, J. Bending Fatigue Properties of Ultra-High Toughness Cementitious Composite (UHTCC). *Materials* **2024**, *17*, 3128. https://doi.org/10.3390/ma17133128

Academic Editor: Miguel Ángel Sanjuán

Received: 6 May 2024
Revised: 19 June 2024
Accepted: 20 June 2024
Published: 26 June 2024

1. Introduction

Compared with the flexible paving layer, the rigid paving layer, represented by cement-based materials, significantly improves stress conditions within the paving layer. Consequently, the adoption of rigid paving layers to address steel bridge deck paving issues has emerged as a research focal point [1–4]. Tong [5] conducted experiments and utilized finite element models to perform parametric analyses. Both experimental and simulated results indicate that UHTCC layers substantially enhance the toughness and durability of composite bridge floor structures. Wang [6] investigated various peg spacings and longitudinal reinforcement ratios to analyze the deformation and cracking characteristics of composite structures. It was observed that the cracking stresses $\sigma_{0.05}$ and $\sigma_{0.1}$ of UHTCC steel bridge panels were 58.6% to 216.8% and 58.9% to 213.5% higher, respectively, than those of ordinary steel concrete bridge panels.

The road and bridge structures are subjected to various loads, and when the stress reaches the limit, deformation occurs, leading to fatigue failure [7–10]. UHTCC exhibits a similar fatigue failure phenomenon as ordinary concrete, albeit with differing fatigue life and characteristics [11–14]. This disparity has spurred scholarly investigation into the fatigue performance of UHTCC [15–17], particularly focusing on bending fatigue characteristics, which has yielded fruitful results [18–22]. Ma [7] reinforced RC beams with steel plates and UHTCC, finding that the bending resistance of RC beams containing a UHTCC layer and steel plate was more than double that of the control group. After 200,000 and 2 million fatigue loads, the residual bearing capacity was 96.2% and 94.2% of the static load test, respectively. Regarding the optimization of the composite material itself, aside from altering the composition of the binding material [23,24], a method more suited to the design mechanism of UHTCC involves focusing on the fiber material [25–27]. This includes mixing fibers with varying stiffness, elastic modulus, or scale to enable different fibers to function optimally at different stress stages, thereby enhancing the mechanical properties of the composite materials [28,29]. Yang [30] developed a multi-scale reinforcement system using millimeter-level PE fiber, micro-scale calcium carbonate whisker, and nano-scale carbon nanotubes as externally doped fibers. The results indicated that calcium carbonate whisker exerted the greatest influence on compressive strength, while polyethylene fiber had the greatest impact on bending and tensile strength. When the contents of the three additives were 1.55%, 2.17%, and 0.154% respectively, the composite material exhibited optimal comprehensive performance.

As mentioned above, all the studies only focus on hybrid fibers or fatigue properties, and the exploration of hybrid fiber UHTCC is insufficient. This paper aims to improve the static mechanical properties of UHTCC, study its bending fatigue properties, explore the effect of hybrid fiber content on the static mechanical properties and high cycle fatigue characteristics of UHTCC, optimize the mix ratio design of composite materials, and play a certain guiding role for practical engineering.

2. Materials and Experiment

2.1. Experimental Materials

The materials used in this work are P·O 42.5 ordinary silicate cement (Conch, Anhui, China), silica ash (Langtian, Sichuan, China) with an apparent density of 1290 kg/m^3 and a specific surface area of 21,500 m^2/kg, standard sand (Iso, Xiamen, China), tap water, polycarboxylate superplasticizer (Nanjing, China), and stabilizer produced by Germany Mingling Chemical (Essen, Germany). Short straight copper-coated steel fiber and PVA fiber (Shandong, China)were vital in this study. PVA fiber and steel fiber have large differences in elastic modulus and physical size. The mechanical properties of the two fibers were obtained through a drawing test and physical property test, as shown in Tables 1 and 2.

Table 1. Basic properties of steel fiber.

Length (mm)	Equivalent Diameter (mm)	Density (kg/m^3)	Fusing Point (°C)	Tensile Strength (MPa)
13.12	0.20	7800	1200	2868

Table 2. Performance parameters of polyvinyl alcohol.

Length (mm)	Equivalent Diameter (um)	Density (g/cm^3)	Initial Modulus (MPa)	Elongation at Break (%)	Breaking Strength (MPa)
12	15	0.9	35.7×10^3	19.47	1589

2.2. Methods

The research group has already conducted relevant research [31]. In addition, some more mature studies also provide guidance for the experimental design of this paper [32,33]. The specific mixing ratio adopted in this paper is shown in Table 3. The mass fraction of the cementation material is 10%; the volume content of steel fiber is0%, 1.0%, and 1.5%; the volume content of steel fiber of blended fiber UHTCC is 1.0%; and the volume content of PVA fiber is 1/5, 1/4 and 1/3 of the former, respectively. They are named SF0P0, SF1P0, SF1.5P0, SF1P5, SF1P4, and SF1P3.

Table 3. Benchmark mix ratio.

Cementing Material	Water–Binder Ratio	Sand Binder Ratio	Water Reducer (%)	Stabilizer (%)
1	0.22	1.0	0.7	0.4

By referring to relevant specifications [34,35], specimens for flexural strength, compressive strength, and three-point bending fatigue tests were prepared. The sample sizes and number of each group are shown in Table 4. The specimen pouring molding is shown in Figure 1. The mold is released after 28 days of maintenance under standard conditions.

Table 4. Specimen size.

Test	Specimen Size	Number of Specimens
Flexural and compressive tests	160 mm × 40 mm × 40 mm	3
Three-point bending test	380 mm × 65 mm × 50 mm	4
Bending fatigue test	380 mm × 65 mm × 50 mm	6

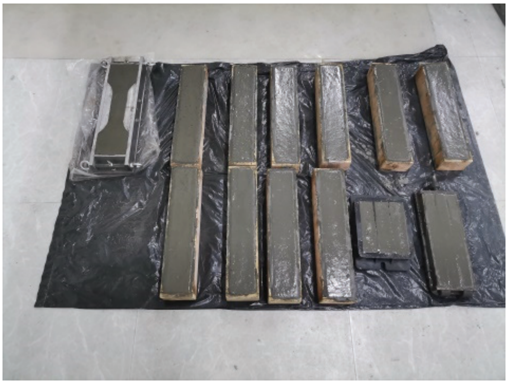

Figure 1. Specimen molding.

In this paper, the data results were processed by Origin software (9.90.225), a compressive and bending strength testing machine was used for the strength test, and the static load test data of three-point bending were obtained from the CMT4204 electronic universal testing machine (Sansi Eternal Technology, Ningbo, China). Finally, the bending fatigue test was carried out by a pneumatic servo universal material testing machine (Sansi Eternal Technology, Ningbo, China), as shown in Figure 2.

In the fatigue test, the static load strength is the average value of the four test blocks in each mixing ratio, and the parameters selected for the fatigue life are the loading frequency of 5 Hz. Thus, the loading frequency does not affect the fatigue life measured by the fatigue test [31]. The loading waveform is selected as a sine wave. Another parameter of the fatigue test is the stress level, that is, the ratio of the maximum stress during the cycle to the static load strength, taking 0.6 and 0.7. The strain data in the fatigue test were obtained from the DH5922 strain testing system, as shown in Figure 3. Considering the large discreteness of the fatigue test, three parallel samples were prepared for each group of tests, and their average values were taken as the final fatigue life results.

Figure 2. Pneumatic servo universal material testing machine.

Figure 3. DH5922 strain test system.

3. Results and Discussion

3.1. Influence of Fiber Content on Static Mechanical Properties

UHTCC strength test results are shown in Figure 4. Compared with SF0P0, the compressive strength of SF1P0 increases by 2.2%, and it increases by only 0.5% when steel fiber is added to 1.5% volume content. It can be observed that the enhancement of compressive strength with single-doped steel fiber tends to saturate near 1.0% volume content while playing a pivotal role in improving bending strength. The flexural strength of SF1P0 and SF1.5P0 increases by 16.8% and 27.6%, respectively. The impact of steel fiber on UHTCC compressive strength manifests primarily in two aspects. Firstly, it reinforces the matrix and restrains the transverse deformation of UHTCC specimens. Secondly, it bridges micro-cracks that develop continuously alongside cracks during compression failure, effectively resisting external stresses.

Throughout this process, continuous adhesive slip occurs between the steel fiber and the matrix, thereby enhancing the compressive strength of the specimen to a certain extent. However, owing to the low water–binder ratio employed in this study, the compressive strength of the specimen itself is relatively high, resulting in an insignificant increase in compressive strength from the addition of steel fiber, especially when the distribution of high-volume doped steel fiber is excessively concentrated (as depicted in Figure 5).

This concentration forms a low bonding strength interface between the fiber and the matrix, slowing the growth of compressive strength. Simultaneously, as the volume content increases, the number of steel fibers per unit volume increases while the average spacing between fibers decreases. This phenomenon leads to the increase in steel fibers at cracks in the UHTCC matrix, where they can better distribute and transfer stress, thereby delaying crack development and improving flexural strength. Moreover, during the process of pulling out steel fiber, overcoming the bonding force between the matrix and the fiber requires additional work and consumes more energy. Macroscopically, it is evident that within a certain range, a higher steel fiber content results in a more pronounced improvement in the folding effect.

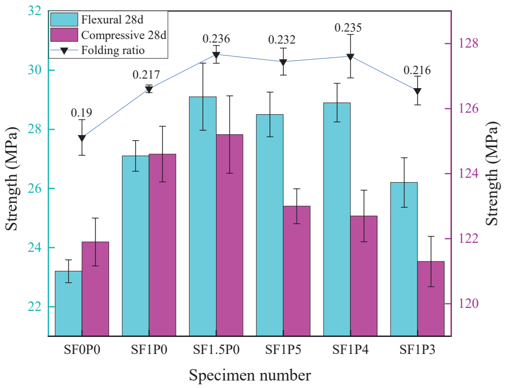

Figure 4. Effect of fiber content on mechanical properties of UHTCC.

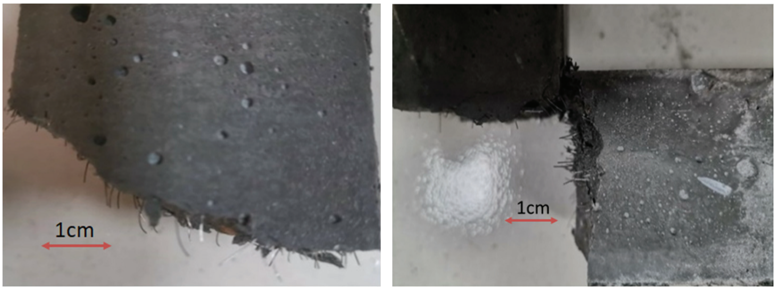

(**a**) (**b**)

Figure 5. Section of steel fiber distribution. (**a**) Even distribution of steel fibers. (**b**) Uneven distribution of steel fibers.

The enhancement of UHTCC's mechanical properties through the incorporation of PVA fiber is constrained. On the foundation of a 1.0% steel fiber content, the introduction of PVA fiber leads to a maximum 6.6% increase in bending strength, a growth rate lower than that observed with SF1.5P0. Additionally, the inclusion of PVA fiber induces a slight reduction in compressive strength, primarily attributed to its flexible nature and low elastic modulus. The mechanism of action involves densification of the structure through self-filling. Excessive PVA fiber content or inadequate dispersion leads to aggregation within the cement matrix, forming agglomerates that create weaker interfacial transition zones, thus diminishing compressive strength. During UHTCC specimen formation, fibers establish a stable framework within the cement matrix, effectively mitigating external loads. Upon structural damage, such as fracture or pull-out of steel fibers, substantial energy is dissipated, thereby suppressing crack propagation. Notably, the hydrophilic properties of PVA fiber significantly mitigate cracks induced by water evaporation and hydration, thereby enhancing concrete bending strength. However, the analysis of experiment results presented herein suggests the superior efficacy of singly doped steel fiber.

The flexographic ratio, representing the ratio of flexographic strength to compressive strength, serves as an indicator of material toughness. Analysis of the data depicted in Figure 4 reveals a comparable increase in the folding ratio of the two fibers within the specimen. Relative to the undoped fiber, SF1P0 exhibits a 14.2% rise in the bending ratio. Upon introduction of PVA fiber, the bending ratio peaks at 0.235 for SF1P4, marking a 23.7% surge, akin to the impact observed with SF1.5P0. However, given the slightly lower quantity of PVA fiber compared to steel fiber, the hybrid fiber demonstrates enhanced toughening properties. Compared with Huang's research [28], the compressive strength of the specimen prepared in this paper is insufficient, but under the condition of less fiber content, the bending strength of the specimen is more than 40% higher than the maximum value of 20.3 MPa of the former.

3.2. Effect of Fiber Content on Flexural Toughness

The load-deflection curves obtained from the three-point bending toughness test are plotted in Figure 6. The bending toughness index TIF is obtained according to the area enclosed by the curve and the X-axis to represent the bending toughness [36]. The specific data are shown in Table 5.

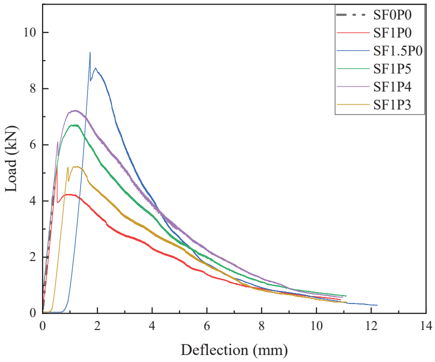

Figure 6. Deflection-load curve.

Table 5. Bending toughness data of UHTCC.

Specimen Number	SF0P0	SF1P0	SF1.5P0	SF1P5	SF1P4	SF1P3
Cracking Deflection (mm)	0.42	0.53	1.74	1.20	1.21	1.26
Flexural toughness index (J)	0.98	20.68	28.45	30.37	33.74	22.74

As depicted in Figure 6, the loading process of specimens reveals distinctive development trajectories in various UHTCCs. Notably, the curve representing SF0P0 exhibits a singular upward trend, indicative of brittle fracture. Conversely, the inclusion of steel fiber alters the behavior, as observed in the SF1P0 curve, which manifests three distinct stages. In the initial ascent, the specimen undergoes early loading, wherein the load sustained by the specimen escalates alongside deflection. Upon reaching a critical deflection threshold, the specimen experiences cracking. Transitioning into the yield phase, the presence of steel fiber mitigates rapid fracture, prolonging the specimen's structural integrity. Cracks induced during this phase influence deflection, leading to fluctuations in load. In the subsequent descent phase, the deflection-induced separation between steel fibers and the matrix, coupled with crack propagation, contributes to load diminishment. Additionally, the analysis of the figure reveals that the maximum load in the rising section surpasses that in the yielding section. This discrepancy is attributed to inadequate steel fiber content, leading to a rapid decline in load between the rising and yielding sections. This decline aligns with the typical curve characteristics observed in strain softening of conventional steel fiber concrete [37]. The curve trajectories of SF1.5P0 and SF1P0 exhibit similar patterns, albeit with a more moderate decline observed between the rising and yield sections in the latter. The cracking deflection of the specimen experiences a significant surge from 0.53 mm to 1.74 mm, marking a 228% increase. Additionally, the bending toughness index escalates from 20.68 J to 28.45 J, denoting a 37.6% increment. These findings underscore that, despite the strain softening phenomenon, when compared to the SF0P0 specimen, the cracking deflection escalates by 314%, and the bending toughness index increases by more than 28-fold.

There is no abrupt transition between the ascending and yielding segments of the blended fiber curve, showcasing the characteristic strain-hardening properties of UHTCC. This observation, when coupled with the data in Table 5, reveals that the maximum cracking deflection of the mixed fiber specimen falls short compared to that of the singly doped steel fiber specimen, registering a decrease of 27.6% compared to SF1.5P0. This discrepancy primarily arises from the larger size and higher elastic modulus of steel fibers, which exert a more pronounced influence on macro-level crack suppression. Consequently, within a defined range, higher steel fiber content correlates with increased cracking deflection. Conversely, when a specific volume of PVA fiber is introduced, the bending toughness index of SF1P4 surpasses that of SF1.5P0 by 18.6%. This enhancement stems from the bridge and crack resistance properties inherent in PVA fibers, which impede the propagation of fine cracks surrounding the initial crack and restrict crack width expansion within a limited scope. Consequently, achieving failure through bending in the specimen necessitates greater force and entails increased energy consumption during the load failure process, thus resulting in a numerically higher bending toughness index for the hybrid fiber specimen.

Additionally, as the relative volume content of PVA fiber increases from 1/5 to 1/3, there is a mere 5% rise in the cracking deflection of the specimen, juxtaposed with a notable 25.1% decline in the bending toughness index. Furthermore, in the case of SF1P0, the augmentation of PVA fiber initially escalated the toughening effect before undergoing a subsequent decline, attributed to the poor dispersion of PVA fiber. Upon excessive addition of PVA fiber to the composite material, a mere 5% increase in the cracking deflection of the specimen is observed alongside a significant 25.1% decrease in the bending toughness index. This phenomenon is exacerbated by severe fiber clumping, posing challenges not only in micro-crack suppression post specimen formation but also in deteriorating the operational efficacy of the composite material. Such clumping also accounts for the diminished flowability of the specimen during the pouring process, further underscoring the adverse effects of excessive PVA fiber content.

3.3. Effect of Fiber Content on Bending Fatigue Properties

Factors such as the non-uniformity of concrete materials and the randomness of the fatigue process result in large discreteness of the measured data in the fatigue test. In order to obtain results that are not too conservative and more consistent with the actual project, this paper selects the density function of Weibull distribution to represent the distribution law of fatigue life N of UHTCC from the perspective of probability [38], and Weibull variable is represented by N_ξ. Fatigue life N under the condition of a given survival rate P is calculated, as shown in Equation (1) [38].

$$P\left(N_\xi > N\right) = \int_N^\infty f(N)\mathrm{d}N = \exp\left[-\left(\frac{N-N_0}{N_a-N_0}\right)^b\right] \tag{1}$$

In the equation, N_0 is the minimum fatigue life, N_a is the characteristic fatigue life, and b is the Weibull shape parameter. For a simple operation, $N_0 = 0$ is usually assumed to obtain the Weibull distribution of two parameters, and the natural logarithm is applied to both sides of the equation to obtain Equation (2) [38].

$$\ln\left[\ln\left(\frac{1}{P}\right)\right] = b\ln N - b\ln N_a \tag{2}$$

The above two formulas are theoretical equations for the study of concrete fatigue. Traffic requires high cycle fatigue of pavement materials, so this paper uses a 0.6 stress level to study the high cycle fatigue characteristics of UHTCC at low-stress levels, and the average bending fatigue life of each group is shown in Table 6.

Table 6. Bending fatigue life of UHTCC.

Specimen Number	SF0P0	SF1P0	SF1.5P0	SF1P5	SF1P4	SF1P3
Mean fatigue life (times)	264,132	1,037,359	1,248,526	1,346,539	1,485,994	1,391,845

In this paper, there are three groups of UHTCC fatigue life tests for each ratio, and the assigned probability P according to the Weibull distribution is 0.75, 0.50, and 0.25. The linear fitting analysis of UHTCC fatigue life data is shown in Figure 7. The relevant parameters of the linear regression equation obtained by fitting are shown in Table 7.

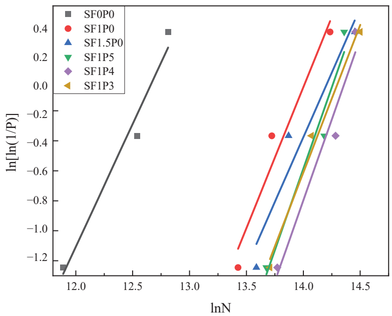

Figure 7. Weibull distribution test of fatigue life.

Table 7. Linear regression equation-related parameters.

Specimen Number	SF0P0	SF1P0	SF1.5P0	SF1P5	SF1P4	SF1P3
Regression coefficient $\hat{a}$	−20.7894	−26.3432	−24.5201	−31.0026	−31.0606	−28.2101
Regression coefficient $\hat{b}$	1.6400	1.8785	1.7244	2.1724	2.1615	1.9712
R^2	0.9450	0.9041	0.8625	0.9164	0.9139	0.9739

As shown in Table 6, SF0P0 specimens experience a sudden brittle fracture, attributed to the short fatigue life of undoped steel fibers. Introducing 1% steel fibers extends fatigue life by nearly threefold, while for SF1.5P0, the increase is still notable at 20.4%. Notably, the addition of PVA fibers enhances fatigue life significantly, with a 29.8% increase at 1/5 volume addition, peaking at a 43.2% increase at 1/4 volume addition. Furthermore, as indicated in Table 7, the correlation coefficient R^2 consistently hovers around 0.9, indicating a high degree of linear regression fit. The bending fatigue life of the composite material predominantly conforms to the Weibull distribution, as supported by the analysis of these parameters.

In the bending fatigue test, the maximum stress manifests within the mid-span of the specimen, where the initial crack propagates along the surface, culminating in fracture failure. This paper focuses on documenting the initiation time of cracks to assess the behavior of band cracks during composite fatigue failure. Given the minute nature of the initial cracks, both sides of the span are moistened with a wet cloth, and recording commences upon the detection of micro-cracks absorbing water. At stress levels of 0.6 and 0.7, recordings are taken, respectively, every 1 h and 0.5 h following the test initiation, and the fatigue life corresponding to crack formation time is computed. Additionally, this paper introduces the split working time ratio, as defined by Equation (3).

$$R = \frac{N - T}{N} \times 100\% \quad (3)$$

In the equation, R is the proportion of working time with cracking, N is the fatigue life of the specimen, and T is the initial cracking time. According to the formula, the working time ratio of each group of specimens with band cracks was calculated as shown in Figure 8.

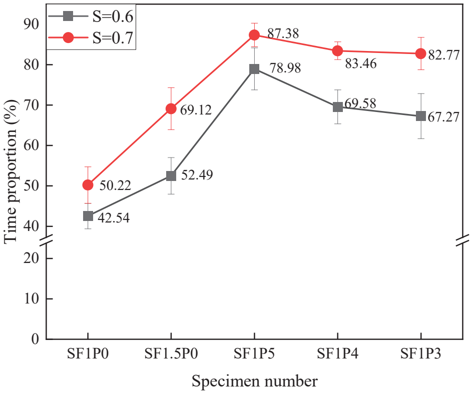

Figure 8. Proportion of UHTCC cracking working time under different stress levels.

Based on the analysis depicted in Figure 8, under different stress levels, the time for the initial crack to appear decreases, and R also increases with the increase in stress level. This phenomenon arises due to the escalation of the maximum load across the span with increasing stress levels, resulting in earlier cracking of the specimen and bearing of greater stress through the formation of fine cracks. Moreover, the augmentation of stress level leads to varying increments in the *R* value across different specimens. Particularly noteworthy is the most pronounced average increase observed in SF1.5P0 at 16.63%, followed closely by SF1P3 at 15.5%. This trend can be attributed to the inclusion of fibers, notably PVA fibers, which not only bolstered toughness but also fortified the capacity to restrict micro-crack expansion, consequently expanding the crack space within composite materials. This augmentation facilitates earlier cracking of the material to withstand higher loads. Throughout testing, it can be observed that the cracking of UHTCC with single-doped steel fiber under load was distinctly visible, as illustrated in Figure 9, whereas the cracking observed in hybrid fiber configurations appeared more subtle, as depicted in Figure 10. This phenomenon has also occurred in other studies [39].

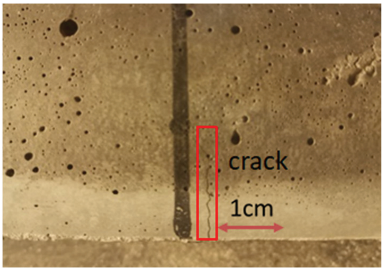

Figure 9. Cracks in single-doped steel fiber UHTCC under load.

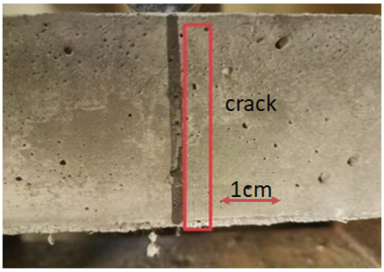

Figure 10. Cracks in mixed fiber UHTCC under load.

3.4. Bending Fatigue Damage Analysis

When subjected to bending fatigue loads, internal defects within concrete gradually propagate, accumulating damage until eventual failure. The progression of concrete fatigue damage unfolds in two discernible stages, contingent upon the emergence of macroscopic cracks. Initially, in the absence of macroscopic cracks, damage accrues through the expansion of micro-cracks within the cement matrix, as well as through fiber tension and frictional interactions with the matrix. Upon reaching a critical threshold, macroscopic damage manifests in concrete, resulting in the appearance of macroscopic cracks. Subsequently, in the second stage, post macro-crack formation, the damage primarily ensues from the extension and enlargement of the micro-crack zone within the concrete, alongside the progression of macroscopic cracks.

Given the remarkable attributes of UHTCC and their extensive fatigue testing period, this paper delves into the accumulation process of fatigue damage during the initial stage when the stress level is 0.7. Commencing from the onset of loading until the emergence of macroscopic cracks, the strain gauge positioned on the underside of the specimen fractures. This observation extends and elaborates upon the previously recorded time for the inception of micro-cracks, facilitating an evaluation of the material's operational efficacy concerning crack development. Employing the symbol 'D' to signify the extent of damage and structural degradation, a defined range [0, 1] characterizes its magnitude. A value of 0 indicates the absence of fatigue-induced damage, while 1 denotes its presence. Leveraging the data acquired on the bottom strain of the specimen throughout the experimentation, a D-ε curve is constructed to scrutinize the correlation between UHTCC damage accumulation and strain, drawing on the Miner linear cumulative damage theory [40], as depicted in Figure 11. The maximum strain values portrayed in the figure represent the peak strains recorded at the specimen's bottom during each cycle, as measured by the strain gauge.

The D-ε curve is nonlinearly fitted by a cubic polynomial to describe the damage and strain relationship of the whole fatigue process of UHTCC. When D = 0, there is no damage to the concrete, and the initial strain ε_0 exists. Failure occurs when D = 1, and the ultimate strain ε_f exists. Table 8 below shows the fatigue damage fitting equation and related parameters.

As can be seen from Table 8, R^2 represents the correlation coefficient of the fitted curve. The correlation of the fitted equations in the table is all greater than 0.9, indicating that the curve-fitting effect is relatively good. As depicted in Figure 11, the overall trajectory of the curve exhibits an inverted S-shaped developmental pattern, delineated into three discernible stages. The initial phase represents a period of rapid development wherein cyclic loading initiates, prompting the emergence of initial defects within the concrete and subsequent rapid strain accumulation. Following this, the progression enters a phase characterized by stable development, wherein the damage increment sustains steady growth at a relatively constant rate. Subsequently, the trajectory transitions into an intense development stage, marked by a sharp escalation in fatigue strain concurrent with the evolution of damage until internal damage accumulation reaches its critical threshold, thereby placing the concrete in an unstable condition, culminating in failure. In comparison with SF0P0, the incorporation of fiber into UHTCC induces notable alterations. Firstly, during the initial stage, the ε_0 value exhibits a diminutive magnitude but experiences accelerated development. This phenomenon stems from the fact that damage accumulation during this phase primarily arises from the expansion of initial defects within the concrete, a process effectively mitigated by the presence of fibers. Secondly, the introduction of fibers imparts a measure of toughness to UHTCC, thereby fostering a sustained upward trend in strain during the subsequent stage. Additionally, owing to the toughening influence of fibers, the ε_f value of UHTCC experiences a significant augmentation, registering an increase of up to 188.4%.

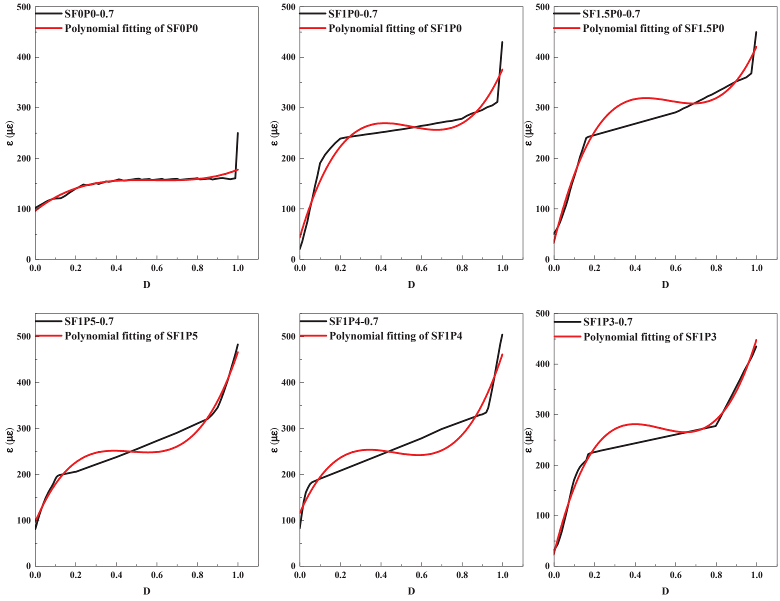

Figure 11. D-ε curve of UHTCC.

Table 8. D-ε fatigue damage equation.

Specimen Number	Fatigue Damage Equation	R^2	ε_0 (με)	ε_f (με)
SF0P0-0.7	$\varepsilon = 262.28D^3 - 379.32D^2 + 178.99D + 99.52$	0.9869	99.52	161.47
SF1P0-0.7	$\varepsilon = 1430.70D^3 - 2853.68D^2 + 1781.96D + 39.35$	0.9059	39.35	398.33
SF1.5P0-0.7	$\varepsilon = 1618.98D^3 - 2956.68D^2 + 1726.26D + 32.02$	0.9054	32.02	420.58
SF1P5-0.7	$\varepsilon = 1038.12D^3 - 2265.67D^2 + 1597.43D + 95.79$	0.9616	95.79	465.67
SF1P4-0.7	$\varepsilon = 996.28D^3 - 2296.80D^2 + 1646.49D + 114.86$	0.9505	114.86	460.83
SF1P3-0.7	$\varepsilon = 1620.52D^3 - 3262.98D^2 + 2067.65D + 22.25$	0.9713	22.25	447.44

Quantitatively, the ratio of cycles corresponding to the conclusion of the first stage and the completion of the second stage to the total number of cycles was designated as k_1 and k_2, respectively. The comparative analysis reveals that the hybrid fiber UHTCC exhibits a relatively large k value, indicating a balanced progression across various UHTCC strain stability development stages. However, the inclusion of PVA fiber enables earlier engagement in structural reinforcement during the fatigue failure process of specimens, advancing the overall strain stability development phase. Compared with the data in the table, it is found that the initial strain increases significantly after adding PVA fiber. The inherent characteristics of PVA fiber dictate an earlier transition of specimens into the multi-crack failure mode to counteract external loading [18,20]. Consequently, the ε_0 of SF1P0 and SF1P5 experiences a significant increase of 143.43%, while SF1P4 records an increase of 191.89%, albeit at a decelerated pace. Conversely, the ε_0 of SF1P3 registers a notable decline, dropping even lower than SF1P0. This phenomenon arises from the incorporation of excessive PVA fiber, leading to a proliferation of initial defects. Although this results in greater inhibition of micro-crack expansion during the initial stage, it concurrently compromises various material properties, culminating in the emergence of dense cracks at lower strains. Nevertheless, the inclusion of PVA fiber significantly elevates the ε_f of the specimens, with SF1P5 showing a 16.9% increase compared to SF1P0.

4. Conclusions

In this paper, flexural and compressive strength tests, three-point bending static tests, and fatigue tests are carried out on fiber UHTCC with different contents to explore the influence of hybrid fiber content on the static mechanical properties and high-cycle fatigue characteristics of UHTCC, and the following conclusions are reached.

1. The hybrid fiber specimens obtained the same toughness as the single-doped steel fiber specimens with less fiber content. PVA fiber exerts a profound influence on both enhancing toughness and augmenting crack deflection in composite materials. The flexural toughness index of hybrid fiber UHTCC surpasses that of SF1.5P0 by up to 18.6%.
2. At a low-stress level, the fatigue life of PVA fiber increases more significantly, which reaches the highest increase of 43.2% at SF1P4. The working time ratio of UHTCC band cracks increases with the increase in stress level. The effect of hybrid fibers can be attributed to the suppression of various cracks in the matrix at various stages and the enhancement of the cracking space of the composite materials.
3. Incorporating mixed PVA fiber triggers early activation, facilitating stable cracking during the fatigue failure progression of specimens. This early activation advances the strain stability development phase and mitigates external load through the formation of additional micro-cracks. Consequently, the initial strain ε_0 of SF1P5 is 143.43% higher than that of SF1P0. Compared with single-doped steel fiber, the ultimate strain of hybrid fiber specimen increases by 16.9%.

Author Contributions: Conceptualization, K.H.; Methodology, K.H. and J.W.; Formal analysis, P.W. and G.S.; Resources, Y.M.; Data curation, G.S., Y.M. and J.W.; Writing—original draft, P.W.; Writing—review & editing, P.W. and K.H. All authors have read and agreed to the published version of the manuscript.

Funding: This research received no external funding.

Institutional Review Board Statement: Not applicable.

Informed Consent Statement: Not applicable.

Data Availability Statement: The original contributions presented in the study are included in the article, further inquiries can be directed to the corresponding author.

Conflicts of Interest: Authors Gong Shen and Yixin Miao were employed by the company Wuxi Communications Construction Engineering Group Co., Ltd. Author Jiansheng Wu was employed by the company Nanjing Kegong Coal Science and Technology Research Co., Ltd. The remaining authors declare that the research was conducted in the absence of any commercial or financial relationships that could be construed as a potential conflict of interest.

References

1. Fan, J.; Gou, S.; Ding, R.; Zhang, J.; Shi, Z. Experimental and analytical research on the flexural behaviour of steel–ECC composite beams under negative bending moments. *Eng. Struct.* **2020**, *210*, 110309. [CrossRef]
2. Li, Q.; Wang, G.; Tong, J.; Xu, S. Flexural capacity of steel-UHTCC (ultra-high toughness cementitious composite) bridge deck considering different shear connection degrees. *Adv. Struct. Eng.* **2022**, *25*, 1907–1922. [CrossRef]
3. Zhang, C.; Guan, X.; Tian, J.; Li, Y.; Lyu, J. Corrosion resistance of RC/UHTCC beams with various healing promoters in marine environment. *Cem. Concr. Compos.* **2022**, *131*, 104604. [CrossRef]

4. Xu, S.; Xie, H.; Li, Q.; Hong, C.; Liu, J.; Wang, Q. Bending performance of RC slabs strengthened by CFRP sheets using sprayed UHTCC as bonding layer: Experimental study and theoretical analysis. *Eng. Struct.* **2023**, *292*, 116575. [CrossRef]
5. Tong, J.; Chen, Y.; Li, Q.; Xu, S.; Chen, T.; Gao, W. Experimental and Numerical Study of Transversal Flexural Behavior on Steel Ultrahigh-Toughness Cementitious Composite Bridge Decks. *J. Bridge Eng.* **2023**, *28*, 04023044. [CrossRef]
6. Wang, G.; Tong, J.; Li, Q.; Xu, S.; Dai, J. Flexural Performance and Design of Steel-UHTCC Composite Bridge Decks with Different Composite Degrees under Hogging Moments. *J. Struct. Eng.* **2023**, *149*, 04023023. [CrossRef]
7. Ma, X.; Liu, L. Fatigue properties of RC beams reinforced with ECC layer and steel plate. *Constr. Build. Mater.* **2023**, *372*, 130799. [CrossRef]
8. Riyar, R.L.; Bhowmik, S. Fatigue behaviour of plain and reinforced concrete: A systematic review. *Theor. Appl. Fract. Mech.* **2023**, *125*, 103867. [CrossRef]
9. He, H.; Liang, X.; Shang, J.; Long, Y. Experimental study on residual mechanical properties after cyclic loading of steel-concrete composite-laminated beams. *Case Stud. Constr. Mater.* **2023**, *19*, e02257. [CrossRef]
10. Liang, L.; Liu, C.; Cui, Y.; Li, Y.; Chen, Z.; Wang, Z.; Yao, Z. Characterizing fatigue damage behaviors of concrete beam specimens in varying amplitude load. *Case Stud. Constr. Mater.* **2023**, *19*, e02305. [CrossRef]
11. Cui, T.; Ning, B.; Shi, X.; Li, J. Flexural fatigue behavior of hybrid steel-polypropylene fiber reinforced high-strength lightweight aggregate concrete. *Constr. Build. Mater.* **2023**, *377*, 131079. [CrossRef]
12. Ferreira, E.; Sotoudeh, P.; Svecova, D. Fatigue life of plain concrete subjected to low frequency uniaxial stress reversal loading. *Constr. Build. Mater.* **2024**, *411*, 134247. [CrossRef]
13. Guo, C.; Li, J. A fast fatigue life estimation method for concrete based on the energy dissipation approach. *Int. J. Fatigue* **2023**, *177*, 107948. [CrossRef]
14. Kumar, B.; Sharma, A.; Ray, S. Characterization of crack-bridging and size effect on ultra-high performance fibre reinforced concrete under fatigue loading. *Int. J. Fatigue* **2024**, *182*, 108158. [CrossRef]
15. Huang, B.; Li, Q.; Xu, S.; Zhou, B. Tensile fatigue behavior of fiber-reinforced cementitious material with high ductility: Experimental study and novel PSN model. *Constr. Build. Mater.* **2018**, *178*, 349–359. [CrossRef]
16. Li, H.; Xu, S. Rate dependence of ultra high toughness cementitious composite under direct tension. *J. Zhejiang Univ.-Sci. A* **2016**, *17*, 417–426. [CrossRef]
17. Zhao, X.; Yu, X.; Cai, L.; Peng, Q.; Wu, H.; Zhou, F. The effects of tensile strain rate on the dynamic tensile behavior of ultra high toughness cementitious composite. *J. Build. Eng.* **2023**, *68*, 106199. [CrossRef]
18. Huang, B.; Li, Q.; Xu, S.; Zhang, L. Static and fatigue performance of reinforced concrete beam strengthened with strain-hardening fiber-reinforced cementitious composite. *Eng. Struct.* **2019**, *199*, 109576. [CrossRef]
19. Huang, B.; Dai, J.; Weng, K.; Zhu, J.; Shah, S.P. Flexural performance of UHPC–concrete–ECC composite member reinforced with perforated steel plates. *J. Struct. Eng.* **2021**, *147*, 04021065. [CrossRef]
20. Li, Q.; Luo, A.; Hong, C.; Wang, G.; Yin, X.; Xu, S. Fatigue behavior of short-headed studs embedded in Ultra-high Toughness Cementitious Composites (UHTCC). *Eng. Struct.* **2024**, *300*, 117194. [CrossRef]
21. Xu, S.; Lyu, Y.; Xu, S.; Li, Q. Enhancing the initial cracking fracture toughness of steel-polyvinyl alcohol hybrid fibers ultra high toughness cementitious composites by incorporating multi-walled carbon nanotubes. *Constr. Build. Mater.* **2019**, *195*, 269–282. [CrossRef]
22. Zhang, X.; Liu, G.; Shen, Z.; Gao, Y.; Zhou, H.; Wang, Z. A comprehensive study on the effect of reinforcing methods on the flexural behaviour of Concrete-RUHTCC composite beams. *Eng. Struct.* **2023**, *292*, 116524. [CrossRef]
23. Zhang, Z.; Liu, S.; Yang, F.; Weng, Y.; Qian, S. Sustainable high strength, high ductility engineered cementitious composites (ECC) with substitution of cement by rice husk ash. *J. Clean. Prod.* **2021**, *317*, 128379. [CrossRef]
24. Kim, M.; Oh, T.; Yoo, D. Mechanical performance of ultra-high-performance strain-hardening cementitious composites according to binder composition and curing conditions. *Arch. Civ. Mech. Eng.* **2022**, *22*, 63. [CrossRef]
25. Liu, T.; Bai, R.; Chen, Z.; Li, Y.; Yang, Y. Tailoring of polyethylene fiber surface by coating silane coupling agent for strain hardening cementitious composite. *Constr. Build. Mater.* **2021**, *278*, 122263. [CrossRef]
26. Lao, J.; Xu, L.; Huang, B.; Dai, J.; Shah, S.P. Strain-hardening Ultra-High-Performance Geopolymer Concrete (UHPGC): Matrix design and effect of steel fibers. *Compos. Commun.* **2022**, *30*, 101081. [CrossRef]
27. Ma, K.; Deng, H.; Guo, X.; Yin, J.; Zhao, Y. The investigating on mechanical properties of engineered cementitious composites with high ductility and low cost. *J. Build. Eng.* **2022**, *57*, 104873. [CrossRef]
28. Huang, B.; Zhu, J.; Weng, K.; Li, V.C.; Dai, J. Ultra-high-strength engineered/strain-hardening cementitious composites (ECC/SHCC): Material design and effect of fiber hybridization. *Cem. Concr. Compos.* **2022**, *129*, 104464. [CrossRef]
29. Tinoco, M.P.; de Andrade Silva, F. Repair of pre-damaged RC beams using hybrid fiber reinforced strain hardening cementitious composites. *Eng. Struct.* **2021**, *235*, 112081. [CrossRef]
30. Yang, B.; Wang, C.; Chen, S.; Qiu, K.; Jiang, J. Optimisation of the Mechanical Properties and Mix Proportion of Multiscale-Fibre-Reinforced Engineered Cementitious Composites. *Polymers* **2023**, *15*, 3531. [CrossRef]
31. Qin, Y.; Huang, K.; Wang, Y.; Wang, A.; Wu, J. Study on mechanical and shrinkage properties of ultra-high strength cement-based composites. *Concr. Cem. Prod.* **2020**, *3*, 1–5. [CrossRef]

32. Chu, H.; Wang, Q.; Zhang, W. Optimizing ecological ultra-high performance concrete prepared with incineration bottom ash: Utilization of Al_2O_3 micro powder for improved mechanical properties and durability. *Constr. Build. Mater.* **2024**, *426*, 136152. [CrossRef]
33. Chu, H.; Wang, Q.; Gao, L.; Jiang, J.; Wang, F. An approach of producing Ultra-High-Performance concrete with high elastic modulus by Nano-Al_2O_3: A preliminary study. *Materials* **2022**, *15*, 8118. [CrossRef]
34. *GB/T 17671-2021*; Test Method of Cement Mortar Strength (ISO Method). Standardization Administration: Beijing, China, 2021.
35. *ASTMC1609/C1609M-2005*; Standard Test Method for Flexural Performance of Fiber-Reinforced Concrete (Using Beam With Third-Point Loading). American Society for Testing and Materials: West Conshohocken, PA, USA, 2005.
36. Shui, F.; Su, J.; Huang, J.; Li, Y.; Qian, W. Research on Flexural Properties and Flexural Toughness Evaluation Method of Steel Fiber Reinforced Cementitious Composites under Polar Low Temperatures. *Adv. Civ. Eng.* **2024**, *2024*, 1137438. [CrossRef]
37. Park, S.H.; Kim, D.J.; Ryu, G.S.; Koh, K.T. Tensile behavior of ultra high performance hybrid fiber reinforced concrete. *Cem. Concr. Compos.* **2012**, *34*, 172–184. [CrossRef]
38. Zhao, D.; Kong, W.; Song, X. Statistical Analysis for Fatigue Life of Concrete. *Key Eng. Mater.* **2008**, *385*, 285–288. [CrossRef]
39. Xu, L.; Huang, B.; Li, V.C.; Dai, J. High-strength high-ductility Engineered/Strain-Hardening Cementitious Composites (ECC/SHCC) incorporating geopolymer fine aggregates. *Cem. Concr. Compos.* **2022**, *125*, 104296. [CrossRef]
40. Christensen, R.M. An evaluation of linear cumulative damage (Miner's Law) using kinetic crack growth theory. *Mech. Time-Depend. Mater.* **2002**, *6*, 363–377. [CrossRef]

materials

Article

The Research Effects of Variable Temperature and Early Strength Agent on the Mechanical Properties of Cement-Stabilized Macadam

Yanhua Xue [1,2], Dongdong Ge [1,2,*], Songtao Lv [1,2], Hui Wei [1,2], Weiwei Lu [1,2] and Liangchen Peng [1,2]

[1] National Key Laboratory of Green and Long-Life Road Engineering in Extreme Environment (Changsha), Changsha 410114, China; xueyanhua_2022@stu.csust.edu.cn (Y.X.); lst@csust.edu.cn (S.L.); wh@csust.edu.cn (H.W.); lww_cs@csust.edu.cn (W.L.); plc@stu.csust.edu.cn (L.P.)
[2] Xiangjiang Laboratory, Changsha 410114, China
* Correspondence: dge1@csust.edu.cn

Abstract: In cold regions with high daily temperature gradients (>20 °C), the durability of cement-stabilized macadam (CSM) base materials is poor and prone to cracking. To effectively reduce the cracking of semi-rigid base layers in cold regions with high daily temperature gradients and extend fatigue life, this study focused on cracking and fatigue characteristics of CSM with a 10% commercial early strength agent (ESA) added by the external mixing method under different curing conditions. The ESA was manufactured by Jiangsu Subote New Materials Co., Ltd. (Nanjing, China). The curing conditions were divided into variable temperature (0–20 °C) and standard temperature (20 °C). CSM curing was carried out through a programmable curing box. The research results indicated that the variable temperature curing conditions reduced the strength and fatigue resistance of CSM and accelerated the modulus attenuation rate of CSM. At the same time, the drying shrinkage of CSM was greater. The temperature shrinkage coefficient and strain of CSM under variable temperature conditions were smaller than those under standard temperature conditions. The effect of variable temperature conditions on the cracking and durability of CSM could not be ignored in cold regions. Compared to standard temperature curing conditions, the indirect tensile strength of CSM reduced by 31.04% under variable temperature conditions, the coefficient of variation increased by 2.97 times, and the discrete type significantly increased. Compared with CSM without ESA, the dry and temperature shrinkage strains of CSM with 10% ESA were reduced by 24.65% and 26.10%, respectively. At a stress level of 0.6, compared to standard temperature curing conditions, the fatigue life of CSM decreased by 97.19% under variable temperature conditions. Under variable temperature conditions, the fatigue life of CSM with 10% ESA increased by 196 times compared to 0% ESA. Adding ESA enhanced the anti-shrinkage cracking, strength, and durability of CSM under variable temperatures. ESA incorporation effectively compensated for the weakened characteristics of CSM under variable temperature conditions. The study proposed a practical approach for boosting the durability of CSM in cold environments.

Keywords: cement-stabilized macadam; variable temperature curing condition; early strength agent; shrinkage characteristics; fatigue damage characteristics

Citation: Xue, Y.; Ge, D.; Lv, S.; Wei, H.; Lu, W.; Peng, L. The Research Effects of Variable Temperature and Early Strength Agent on the Mechanical Properties of Cement-Stabilized Macadam. *Materials* **2024**, *17*, 3720. https://doi.org/10.3390/ma17153720

Academic Editor: Francisco Agrela

Received: 11 June 2024
Revised: 5 July 2024
Accepted: 24 July 2024
Published: 27 July 2024

1. Introduction

Cement-stabilized macadam (CSM) has the benefits of high strength, excellent integrity, good water stability, and frost resistance [1–4]. As a base material, CSM can decrease the tensile stress at the bottom of the asphalt surface layer. It can also ensure the stability of the roadbed [5]. CSM is a mixture of cement and water added to macadam with a gradation. The rate of cement hydration directly affects the strength of CSM. In low-temperature environments (<20 °C), the hydration reaction rate of cement is slow, which is not conducive to the formation of strength [6,7]. Therefore, the formation of CSM strength is highly susceptible to the influence of environmental temperature [8,9].

Tian et al. [9] observed that when the curing temperature of CSM increased from 5 °C to 10 °C, the 7-day flexural strength increased by 214.3%. When the temperature increased from 10 °C to 20 °C, the 7-day bending tensile strength increased by 157.1%. Soriano et al. and Ryou et al. [10–12] pointed out that under low-temperature conditions, an ice interlayer would be generated in the concrete, leading to the fracture of the hydration product gel. At the same time, the freezing of water molecules will generate expansion stress, causing deterioration of the internal interface transition zone of the concrete and loosening of the cement structure, reducing the macroscopic mechanical characteristics of concrete. Ma et al. [13–15] observed the effects of different curing temperatures on the mechanical characteristics of CSM, covering unconfined compressive strength, flexural strength, and compressive rebound modulus. This study found that under normal low-temperature conditions, the cement hydration reaction rate of CSM was slow or even stopped, and the durability was poor.

For areas with year-round low temperatures, large temperature differences between day and night, and high water evaporation in cold regions, CSM base materials were more prone to damage [13,16]. During construction in cold regions of China with high daily temperature gradients (>20 °C) in summer, CSM had a fast and large evaporation rate of water, which could lead to drying shrinkage and cracking [17]. The temperature gradient during the curing process could cause temperature stress to exceed the strength formed during its curing period, making it prone to temperature shrinkage and cracking. He et al. [18] conducted a core sample investigation on the road surface of the existing roads in Qinghai Tibet and found that most of the core samples were loose and even showed a high number of non-load-type cracks. Therefore, improving the durability of CSM in cold regions with high daily temperature gradients was of great significance.

Current researchers and scholars have paid much attention to the influence of constant-temperature curing on the characteristics of CSM materials in cold regions with high daily temperature gradients, with the temperature mainly concentrated in the range of −5–20 °C [19]. However, the average temperature in July and August was only 6 °C for the cold regions with high daily temperature gradients, and negative temperatures often occur at night [16]. When the region was in the best construction season, the temperature difference between day and night remained relatively large. Therefore, variable temperature curing of CSM according to the temperature variation in the cold regions with high daily temperature gradients could explore the performance evolution of CSM in harsh environments more realistically [20].

Meanwhile, reducing the cracking of semi-rigid base layers in the cold regions with high daily temperature gradients was crucial for extending the durability of pavements [21–24]. The study showed that incorporating an early strength agent (ESA) into CSM accelerated the hydration reaction rate of cement, effectively boosted the strength of CSM, and enabled CSM to meet the specification strength requirements at low-temperature conditions. Hang et al. [25–27] investigated composite low-temperature ESA's influence on concrete strength under a 5 °C low-temperature environment. The study found that composite low-temperature ESA significantly raised the early strength of concrete in low-temperature conditions, and the later strength would not decrease. Wang et al. [28] studied the shrinkage characteristics of CSM using ESA. The study found that at the 8% ESA (mixture of single early strength agents Z1, Z2, and Z3 and expansion agent P) dosage, the dry shrinkage coefficient of CSM decreased by 11.2% compared to CSM without adding early strength materials. Tian et al. [29] studied the mechanical, fatigue, and shrinkage characteristics of CSM using ESA. The results shown that ESA significantly boosted the strength, fatigue resistance, and cracking resistance of CSM. Xiong and Lin et al. [30–33] used different types of ESA to investigate the characteristics enhancement of CSM. Sheng et al. [19] studied the shrinkage characteristics of CSM by combining ESA and brucite fiber.

The incorporation of ESA remarkably boosted the strength, frost resistance, shrinkage cracking, and fatigue characteristics of CSM. However, the existing study focused on the laboratory constant curing temperature, and the effect of ESA on the cracking resistance and fatigue characteristics of CSM under the variable temperature environment in the cold regions with high daily temperature gradients was unclear. Therefore, this study adopted an ESA, based on a variable temperature curing environment, to study the effects of curing conditions on the dry shrinkage, temperature shrinkage, indirect tensile strength, and indirect tensile fatigue behavior of CSM with ESA. The modulus decay equation of CSM was established to study the fatigue damage law of CSM.

2. Materials and Methods

2.1. Raw Materials

According to the basis of previous research [20], this study used PC42.5 cement, and the main technical specifications are illustrated in Table 1. The aggregate type is limestone, and the characteristics indicators are illustrated in Table 2. The ESA is manufactured by Jiangsu Subote New Materials Co., Ltd. (Nanjing, China), and the key technical indexes are illustrated in Table 3. The gradation of CSM used in this study is illustrated in Figure 1.

Table 1. Technical indexes of cement.

Property		Results	Requirement	Standard Deviation
Setting time	Initial setting time/min	270	≥180	9.3
	Final setting time/min	395	≥360, ≤180	12.1
3D compressive strength/MPa		23.8	≥3.5	3.69
3D flexural strength/MPa		4.9	≥17	1.45

Table 2. Limestone characteristics indicators results.

Property	Requirement	Coarse Aggregate Test Results				Standard Deviation	Test Method
		19~ 31.5 mm	9.5~ 19.5 mm	4.75~ 9.5 mm	0~ 4.75 mm		
Crushing value/%	≤26%	21.3	18.9	-	-	3.61	T 0316-2005 [34]
Gross volume relative density/(g/cm^3)	Actual measurement records	2.230	2.730	2.607	2.589	0.59	T 0316-2005 [34]
Apparent density/(g/cm^3)	Actual measurement records	2.821	2.763	2.731	2.692	0.93	T 0312-2005 [34]
Water absorption rate/%	Actual measurement records	0.4	0.6	1.3	-	0.69	T 0312-2005 [34]
Liquid limit/plasticity index of particles less than 0.6 mm	Liquid limit ≤ 28%	23%				2.46	T 0118-2005 [34]
	Plasticity index ≤ 9	3.2				1.03	T 0118-2005 [34]

Table 3. Characteristics indexes of ESA.

Property	Test Results	Standard Deviation
Appearance status	Powder	-
1.18 mm sieve residue (%)	≤0.05	0.014
Setting time difference (min)	≤30	2.45
24 h cement paste strength ratio (%)	≥125	16.16

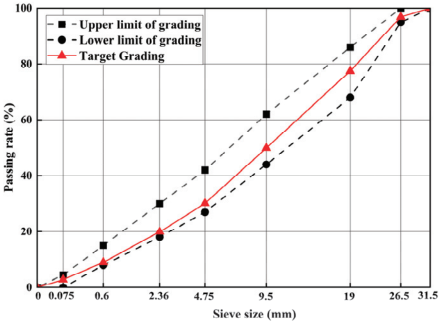

Figure 1. Gradation design of CSM.

2.2. *Preparation of Sample*

The specimens were prepared with a cement content of 4.5% [20,35]. The optimal moisture content of CSM obtained through the compaction test was 5.5%, and the maximum dry density was 2.405 g/cm^3. The dosage of ESA was 10% of the cement dosage [20].

This study used vibration mixing to prepare CSM. The preparation process was as follows: First, the weighed aggregate was added into the mixing pot. Then, it was mixed with water for 90 s in advance, and then cement was incorporated and stirred for 90 s to ensure uniform distribution [20]. Finally, Φ150 mm × 150 mm cylindrical specimens and 400 mm × 100 mm × 100 mm beam specimens were compacted by the vibratory compactor. The specimens were demolded after 12 h to obtain the CSM specimens.

2.3. *Curing Condition*

According to previous research, a programmable curing box was used for variable temperature curing, and the parameters of variable temperature curing are illustrated in Table 4 [20].

Table 4. Variable temperature curing parameters.

Indicator	Ranges					
Temperature	15~20 °C	20~15 °C	15~5 °C	5~0 °C	0~5 °C	5~15 °C
Duration	4 h	4 h	4 h	6 h	3 h	3 h

The CSM specimens were demolded into plastic bags and placed into a programmable curing chamber. Using the standard temperature curing room as the control group, the temperature in the standard temperature curing room was 20 °C, and the humidity was 95%. The abbreviation of CSM is illustrated in Table 5.

Table 5. Abbreviation of CSM.

Curing Condition	ESA Content	
	0%	10%
Standard temperature curing	ST0%	ST10%
Variable temperature curing	VT0%	VT10%

2.4. *Test Methods*

2.4.1. Temperature Shrinkage Test

Based on specification JTG E51-2009 [36], after curing the beam specimen for 7 days and soaking it in water for the last 1 day, the specimen was dried in a 105 °C oven for 10–12 h until it reached a stable weight (quality change less than 0.05%). After measuring the length of the specimen, it was placed on a shrinkage tester and the dial gauge was adjusted. The temperature range of the experiment was −30~60 °C. At the beginning of the experiment, the temperature was raised to 60 °C, and every 10 °C was a stage of gradual cooling, with a cooling rate of 0.5 °C/min. The temperature shrinkage strain and temperature shrinkage coefficient were calculated by Equations (1) and (2).

$$\varepsilon_i = \frac{l_i - l_{i+1}}{L_0} \tag{1}$$

$$\alpha_i = \frac{\varepsilon_i}{t_i - t_{i+1}} \tag{2}$$

In the formula, ε_i represents the temperature shrinkage strain. α_i represents the temperature shrinkage coefficient. l_i represents the average value (mm) of the sum of the readings on the dial gauge for the *i*-th temperature range. t_i represents the *i*-th temperature range set by the temperature control program (°C). L_0 represents the initial length of the specimen (mm).

2.4.2. Drying Shrinkage Test

Based on specification JTG E51-2009 [36], the beam specimens were cured for 7 days and soaked in water on the last day. After soaking in water, the specimen was dried and the length and mass were measured. The experiment was conducted in a drying shrinkage box with a temperature of 20 ± 1 °C and a humidity of 60 ± 5%. The CSM specimens were divided under each scheme into two groups, with one group of specimens placed on a shrinkage tester to examine for shrinkage deformation. Another group was placed in a drying shrinkage box to examine the drying shrinkage water loss rate. Then, the specimen was placed in a drying chamber and its length and mass were measured daily. After the experiment, the specimen was placed in an oven and heated to a stable weight (quality change less than 0.05%). The water loss rate, shrinkage strain, and dry shrinkage coefficient were calculated by Equations (3)–(7).

$$w_i = (m_i - m_{i+1})/m_p \tag{3}$$

$$\delta_i = \left(\sum_{j=1}^{4} X_{i,j} - \sum_{j=1}^{4} X_{i+1,j} \right)/2 \tag{4}$$

$$\varepsilon_i = \delta_i / l \tag{5}$$

$$\alpha_{di} = \varepsilon_i / w_i \tag{6}$$

$$\alpha_d = \frac{\sum \varepsilon_i}{\sum w_i} \tag{7}$$

In the formula, w_i represents the *i*-th water loss rate. δ_i represents the *i*-th drying shrinkage. ε_i represents the *i*-th dry shrinkage strain. α_{di} represents the *i*-th drying shrinkage coefficient. α_d represents the total shrinkage coefficient. m_i represents the mass of the standard specimen measured for the *i*-th time (g). $X_{i,j}$ represents the reading of the *j*-th dial gauge at the *i*-th test (mm). l represents the length of the standard specimen (mm). m_p represents the mass of the standard specimen after drying (g).

2.4.3. Indirect Tensile Strength (ITS) Test

ITS is an essential parameter in the structural design of semi-rigid base materials, which can represent crack resistance under load. According to specification JTG E51-2009 [36], ITS tests were conducted on cylindrical specimens with standard and variable temperature curing for 28 days on a universal testing machine. The loading rate was 1 mm/min. The ITS of the specimen was calculated by Equation (8).

$$R = 0.004178\frac{P}{h} \tag{8}$$

In the formula, R represents the ITS of the specimen (Mpa). P represents the maximum pressure at which the specimen fails (N). *h* represents the height of the specimen after immersion in water (mm).

2.4.4. Indirect Tensile Fatigue Test

The cylindrical specimen was cured for 28 days and the test was conducted after soaking in water for the last 1 day. The surface of the specimen was polished smooth with sandpaper, and two strain sensors were pasted on both sides of the specimen. A strain sensor horizontally measures tensile strain. Another strain sensor measures compressive strain, as illustrated in Figure 2. Indirect tensile fatigue tests were conducted on specimens with strain sensors installed.

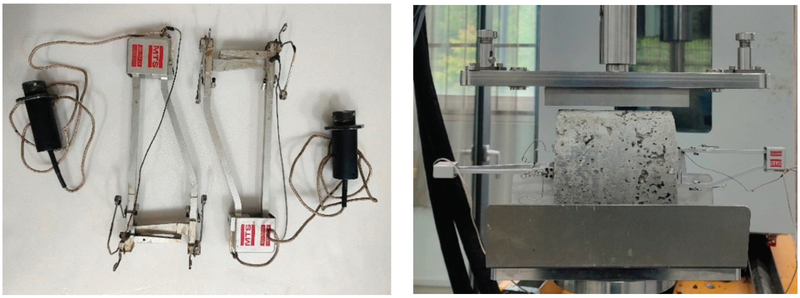

(**a**) Strain sensor (**b**) Specimens with strain sensors installed

Figure 2. Indirect tensile fatigue test.

2.4.5. Indirect Tensile Modulus

The stress state of the sample in the indirect tensile test is illustrated in Figure 3 [37]. The calculation formula of Brazilian discs was commonly used for indirect tensile tests. According to elasticity, the force distribution at any point T (x, y) inside the disk can be calculated as illustrated in Equation (9).

$$\begin{cases} \sigma_x = \frac{2P}{\pi L}\left(\frac{\sin^2\theta_1\cos\theta_1}{r_1} + \frac{\sin^2\theta_2\cos\theta_2}{r_2}\right) - \frac{2P}{\pi DL} \\ \sigma_y = \frac{2P}{\pi L}\left(\frac{\cos^3\theta_1}{r_1} + \frac{\cos^3\theta_2}{r_2}\right) - \frac{2P}{\pi DL} \\ \sigma_{xy} = \frac{2P}{\pi L}\left(\frac{\sin\theta_1\cos^2\theta_1}{r_1} - \frac{\sin\theta_2\cos^2\theta_2}{r_2}\right) \end{cases} \tag{9}$$

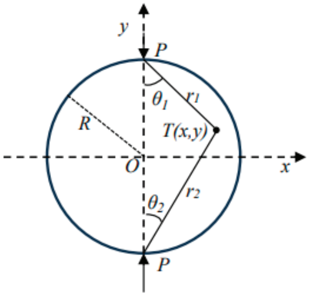

Figure 3. Schematic diagram.

In the formula, P is the load (N), L is the length (thickness) of the cylindrical specimen (mm), and D is the diameter of the cylindrical specimen (mm).

Chen et al. [38,39] derived the tensile and compressive modulus equations in indirect tensile fatigue testing based on the strain gauge testing method, as illustrated in Equation (10).

$$\begin{cases} E_x = \frac{4P}{\pi L} \times \frac{ab+cd\mu^2}{b\Delta\mu-\mu d\Delta v} \\ E_y = \frac{4P}{\pi L} \times \frac{ab+cd\mu^2}{\mu c\Delta\mu+a\Delta v} \end{cases} \tag{10}$$

Among them:

$$\begin{cases} a = \frac{Dl}{D^2+l^2} - \arctan\frac{l}{D} + \frac{l}{2D} \\ b = \frac{l}{2D} - \ln\frac{D-l}{D+l} \\ c = \frac{l}{2D}; \Delta\mu = \varepsilon_\mu l; \Delta v = \varepsilon_v l \\ d = \frac{Dl}{D^2+l^2} + \arctan\frac{l}{D} - \frac{l}{2D} \end{cases} \tag{11}$$

ε_μ and ε_v represent the horizontal and vertical strains of the specimen tested by the strain sensor. l is the initial distance between the two ends of the strain sensor (50 mm).

3. Shrinkage Test Results and Discussion

3.1. Analysis of Temperature Shrinkage Results

The confidence intervals for the temperature shrinkage strains and the temperature shrinkage coefficients are displayed in Figure 4.

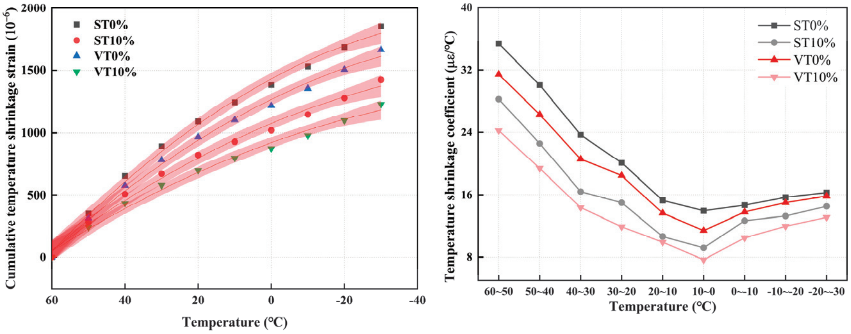

(**a**) Cumulative temperature shrinkage strain (**b**) Temperature shrinkage coefficient

Figure 4. Temperature shrinkage results of CSM.

As illustrated in Figure 4a, the cumulative temperature shrinkage strain of ST0%, ST10%, VT0%, and VT10% continues to increase with the temperature decrease. The cumulative temperature shrinkage strains of ST0%, ST10%, VT0%, and VT10% are 1851.06 με, 1425.55 με, 1664.76 με, and 1230.18 με, respectively. Adding ESA can reduce the temperature shrinkage strain of CSM. Incorporating 10% ESA reduces the temperature shrinkage strain by 22.99% and 26.10% in standard and variable temperature curing environments, respectively. Under variable temperature curing conditions, the temperature shrinkage strain of CSM was less. Compared with ST0%, the temperature shrinkage strain of VT0% was reduced by 10.06%.

As illustrated in Figure 4b, the temperature shrinkage coefficients of ST0%, ST10%, VT0%, and VT10% show a trend of first reducing and then growing with the decline in temperature and reaching the lowest point within the range of 0–10 °C. The reason may be that as the temperature decreases, the thermal motion of pore water molecules in CSM weakens, the molecular spacing decreases, the attraction increases, and the surface tension increases. This effect leads to specimen volume shrinkage. The surface tension in the early cooling stage was high, causing significant temperature shrinkage deformation and temperature shrinkage coefficient reduction. The surface tension reduces as the temperature declines, and the temperature shrinkage coefficient gradually reduces. When the temperature is less than 0 °C, the pore water freezes, causing volume expansion and offsetting some shrinkage deformation, increasing the temperature shrinkage coefficient [40]. Under variable temperature curing conditions, compared with CSM with 0% ESA, CSM with 10% ESA showed a 22.94% decrease in the temperature shrinkage coefficient at 50–60 °C. At 50–40 °C, it decreased by 24.46%. At 40–30 °C, it reduced by 25.94%. At 30–20 °C, it reduced by 27.75%. At 20–10 °C, it reduced by 27.71%. At 10–0 °C, it reduced by 28.21%. At −10–0 °C, it reduced by 27.79%. At −20–−10 °C, it decreased by 27.04%. At −30–−20 °C, it decreased by 26.10%. As the temperature gradually decreases from high temperature, the effect of ESA on the temperature shrinkage coefficient of CSM shows a trend of first increasing and then decreasing. ESA has the greatest impact within the temperature range of 0–20 °C, and the decrease in temperature shrinkage coefficient is the most significant.

3.2. Analysis of Drying Shrinkage Test Results

The changes in water loss rate, dry shrinkage strain, and dry shrinkage coefficient with time of CSM are illustrated in Figures 5 and 6. Statistical analysis of the water loss rate is illustrated in Table 6.

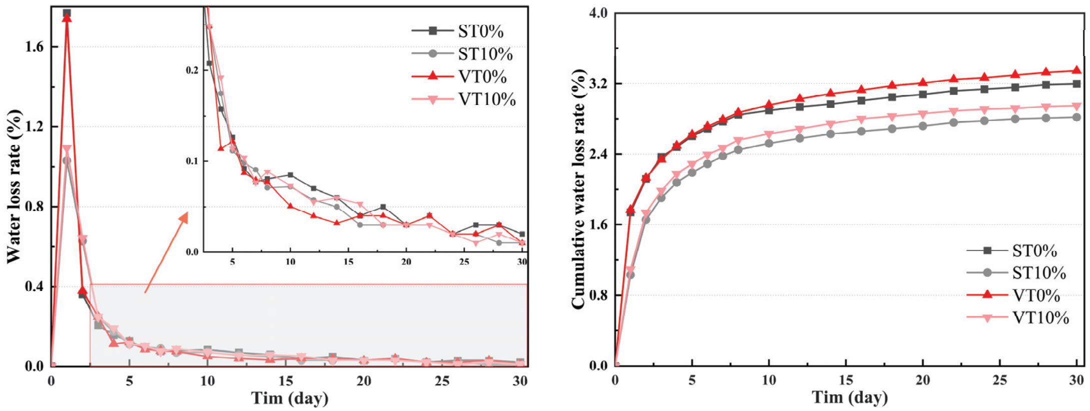

(**a**) Water loss rate (**b**) Cumulative water loss rate

Figure 5. Water loss rate of CSM.

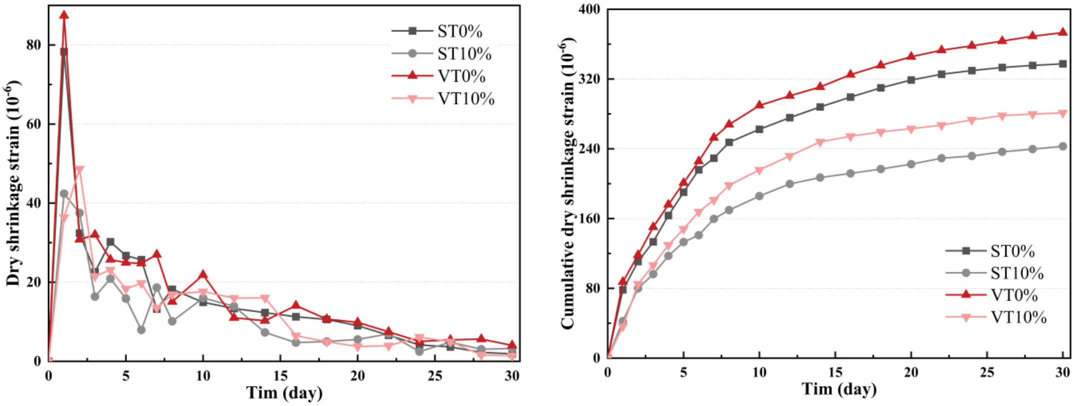

(**a**) Dry shrinkage strain (**b**) Cumulative dry shrinkage strain

Figure 6. Dry shrinkage strain test results of CSM.

Table 6. Statistical analysis of water loss rate.

Time (Day)	ST0%		ST10%		VT0%		VT10%	
	Average Value	Variance	Average Value	Variance	Average Value	Variance	Average Value	Variance
0	0	0	0	0	0	0	0	0
2	0.36	0.000107	0.63	0.000184	0.38	0.000181	0.64	0.000186
4	0.15	0.000059	0.17	0.000037	0.11	0.000065	0.19	0.000094
6	0.09	0.000036	0.10	0.000064	0.09	0.000071	0.10	0.000039
8	0.08	0.000068	0.07	0.000058	0.08	0.000091	0.09	0.000058
10	0.08	0.000072	0.07	0.000063	0.05	0.000064	0.07	0.000064
12	0.07	0.000091	0.06	0.000024	0.04	0.000082	0.06	0.000039
14	0.06	0.000083	0.05	0.000081	0.03	0.000047	0.06	0.000031
16	0.04	0.000101	0.03	0.000047	0.04	0.000059	0.05	0.000064
18	0.05	0.000076	0.03	0.000039	0.04	0.000038	0.03	0.000061
20	0.03	0.000058	0.03	0.000057	0.03	0.000021	0.03	0.000038
22	0.04	0.000069	0.04	0.000069	0.04	0.000019	0.03	0.000075
24	0.02	0.000066	0.02	0.000076	0.02	0.000033	0.02	0.000060
26	0.03	0.000090	0.02	0.000073	0.02	0.000031	0.01	0.000035
28	0.03	0.000046	0.01	0.000042	0.03	0.000067	0.02	0.000066
30	0.02	0.000052	0.01	0.000034	0.01	0.000051	0.01	0.000055

As illustrated in Figure 5, the water loss rate of CSM showed an increase and then a fall with time and gradually tended to stabilize. The cumulative water loss rate of CSM rose continuously with time and gradually stabilized in the later stage of the experiment. The main reason was that in the early stage of the drying shrinkage test, the water lost was mainly free water filled in the pores of CSM, which is abundant and easy to evaporate, so the water loss rate increased rapidly. In the later stage of the experiment, the internal moisture of CSM was mainly adsorbed water and interlayer water, which were difficult to evaporate. Therefore, the water loss rate of CSM would decrease and tend to stabilize.

After adding ESA, the water loss rate of CSM significantly decreased. The cumulative water loss rates of ST0% and VT0% were greater than ST10% and VT10%, respectively. This may be because ESA accelerated cement hydration, and consuming free water and some capillary water in CSM reduces the water loss rate of ST10% and VT10%. The cumulative water loss rates of VT0% and VT10% were higher than ST0% and ST10%, respectively. It may be that the cement hydrates slower and consumes less water under variable temperature conditions. More water was evaporated in the dry shrinkage test session. The statistical results of the water loss rate show that the discreteness of the drying shrinkage test of CSM under different health conditions is relatively small.

As illustrated in Figure 6, the variation in drying shrinkage strain of CSM with time was consistent with the law of water loss rate. In the early stage of the experiment, the drying shrinkage strain was relatively large, and in the later stage, the shrinkage strain gradually stabilized. After 30 days of shrinkage, the cumulative shrinkage strains of ST0%, ST10%, VT0%, and VT10% were 373.15 με, 242.87 με, 337.46 με, and 281.17 με, respectively. Compared to ST0% and VT0%, the cumulative shrinkage strain of ST10% and VT10% decreased by 28.03% and 24.65%, respectively. Adding ESA can diminish the dry shrinkage strain of CSM [41].

Compared to ST0% and ST10%, the cumulative shrinkage strain of VT0% and VT10% increased by 10.58% and 15.77%, respectively. Under variable temperature conditions, the drying shrinkage of CSM was greater. This may be because the variable temperature conditions inhibit cement hydration, produce fewer hydration products, and consume less water, so the faster the water evaporates in the test stage, the greater the drying shrinkage deformation. Related studies have also confirmed that the shrinkage deformation of CSM was greater under low-temperature conditions [19], and adding ESA can enhance the shrinkage characteristics of the CSM under low temperature.

Figure 7 illustrates that the cumulative drying shrinkage coefficients of ST0%, ST10%, VT0%, and VT10% were 105.52%, 86.16%, 111.49%, and 95.30%, respectively. Compared with ST0% and VT0%, the shrinkage coefficients of ST10% and VT10% were reduced by 19.36% and 16.19%. This indicates that ESA significantly impacts the shrinkage coefficient of CSM under different temperatures.

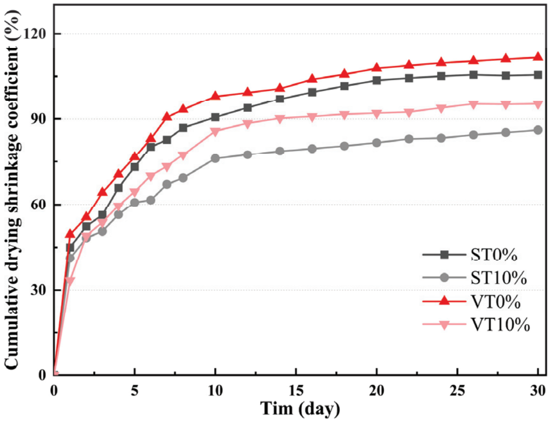

Figure 7. Cumulative drying shrinkage coefficient of CSM.

4. Results and Discussion of Strength and Fatigue Tests

4.1. ITS Analysis

The results of ITS of CSM are illustrated in Table 7.

Table 7. ITS test results.

	ITS (MPa)			Average Value (MPa)	Coefficient of Variation (%)
	1	2	3		
ST0%	0.837	0.761	0.799	0.799	3.85
ST10%	1.042	1.164	1.224	1.143	6.62
VT0%	0.554	0.472	0.627	0.551	11.45
VT10%	0.883	0.947	0.808	0.879	6.46

As illustrated in Table 6, the ITS values of ST0% and ST10% were significantly higher than those of VT0% and VT10%. The variable temperature curing environment was not conducive to forming CSM strength. Compared to ST0%, the ITS of ST10% increased by 43.38%. Compared to VT0%, the ITS of VT10% increased by 60.36%. The incorporation of ESA raised the ITS of CSM in different curing conditions. The coefficient of variation results shown that the intensity variability of VT0% was the highest. The coefficient of variation increased by 2.97 times. The performance of CSM was more discrete in variable temperature curing environments. After adding ESA under variable temperature conditions, the coefficient of variation of the ITS results of CSM decreased, indicating that the addition of ESA can effectively improve the discrete strength of CSM under variable temperature conditions.

4.2. Fatigue Characteristics

Different stress levels are selected for fatigue testing based on the ITS results. The fatigue specimen is illustrated in Figure 8. The fatigue results are illustrated in Table 8.

(**a**) Specimens (**b**) Specimens after fatigue failure

Figure 8. Fatigue test.

Table 8. Fatigue test results.

	Indirect Tensile Strength (MPa)	Stress Level (MPa)	Stress Ratio	Fatigue Life			Average Value
				1	2	3	
ST0%	0.799	0.4	0.50	151,407	270,604	215,586	212,532
		0.5	0.63	27,969	44,512	22,217	31,566
		0.6	0.75	6368	4274	3469	4704
		0.7	0.88	908	322	721	650
ST10%	1.143	0.6	0.52	173,616	233,324	137,908	181,616
		0.7	0.61	28,124	49,702	22,339	33,388
		0.8	0.70	5811	7181	14616	9203
		0.9	0.79	1046	1403	2948	1799
VT0%	0.551	0.3	0.54	142,927	74,708	101,628	106,421
		0.4	0.73	8269	9475	5038	7594
		0.5	0.91	2019	1014	867	1300
		0.6	1.09	184	56	156	132
VT10%	0.879	0.5	0.57	152,807	177,146	109,533	146,495
		0.6	0.68	21,252	24,526	31,969	25,916
		0.7	0.80	4009	6040	4710	4920
		0.8	0.91	745	585	1010	780

As illustrated in Table 7, the fatigue life of CSM diminishes continuously with the increase in stress level. When the stress level is 0.6 MPa, the fatigue lives of ST0%, ST10%, VT0%, and VT10% were 4704, 181,616, 132, and 25,916, respectively. The fatigue life of ST0% was 35 times that of VT0%. The fatigue life of ST10% was seven times that of VT10%. The fatigue life of CSM was significantly reduced under a variable temperature curing environment. Adding ESA raised the durability of CSM under variable temperature conditions.

According to the fatigue test results, fatigue curve fitting was performed on CSM with different stress levels and stress ratios. The fitting results are illustrated in Figures 9 and 10. The fatigue equation and related parameters are illustrated in Tables 9 and 10.

Parameters a and b can reflect the fatigue characteristics of CSM. Among them, the larger the value of a, the superior the fatigue resistance of CSM. The larger the value of b, the more significant the impact of stress changes on the fatigue life of CSM.

The fatigue life of CSM has a very strong correlation with stress levels and stress ratios [42]. Compared to the stress level, the R^2 in the fatigue equation of CSM based on the stress ratio was higher. The degree of fatigue equation fitting for CSM based on the stress ratio was better. The a-values order for CSM under different stress levels or ratios was ST10% > VT10% > ST0% > VT0%. Among them, VT0% has the smallest a-value.

Table 9. Fatigue equation parameters of CSM under different stress ratios.

	a	*b*	Fatigue Equation	R^2
ST0%	8.70	−6.75	$\lg N_f = 8.70 - 6.75\sigma/S$	0.979
ST10%	9.23	−7.64	$\lg N_f = 9.23 - 7.64\sigma/S$	0.957
VT0%	7.83	−5.30	$\lg N_f = 7.83 - 5.30\sigma/S$	0.973
VT10%	8.94	−6.64	$\lg N_f = 8.94 - 6.64\sigma/S$	0.990

Table 10. Fatigue equation parameters of CSM under different stress levels.

	a	*b*	Fatigue Equation	R^2
ST0%	1.27	−10.36	$\lg N_f = 1.27 - 10.36\lg\sigma$	0.970
ST10%	2.72	−11.36	$\lg N_f = 2.75 - 11.36\lg\sigma$	0.955
VT0%	0.06	−9.55	$\lg N_f = 0.06 - 9.550\lg\sigma$	0.970
VT10%	1.89	−11.05	$\lg N_f = 1.89 - 11.05\lg\sigma$	0.983

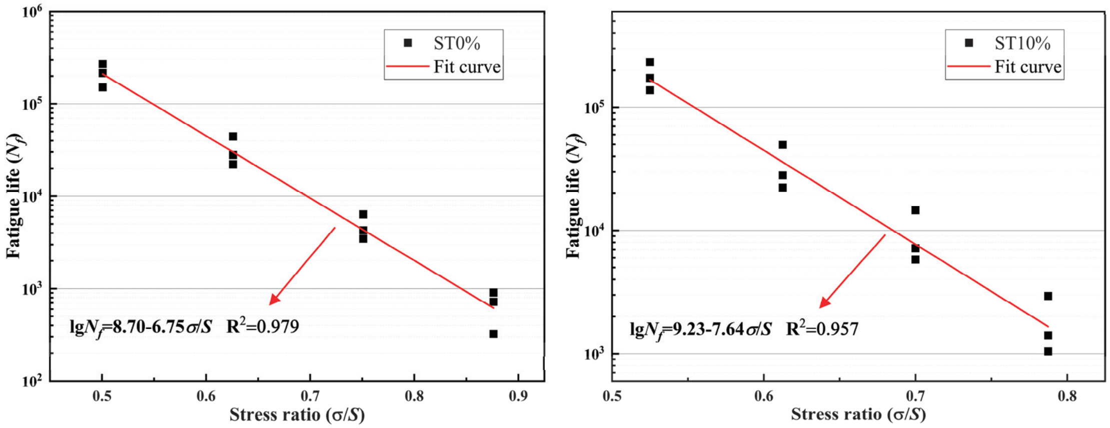

(**a**) ST0% (**b**) ST10%

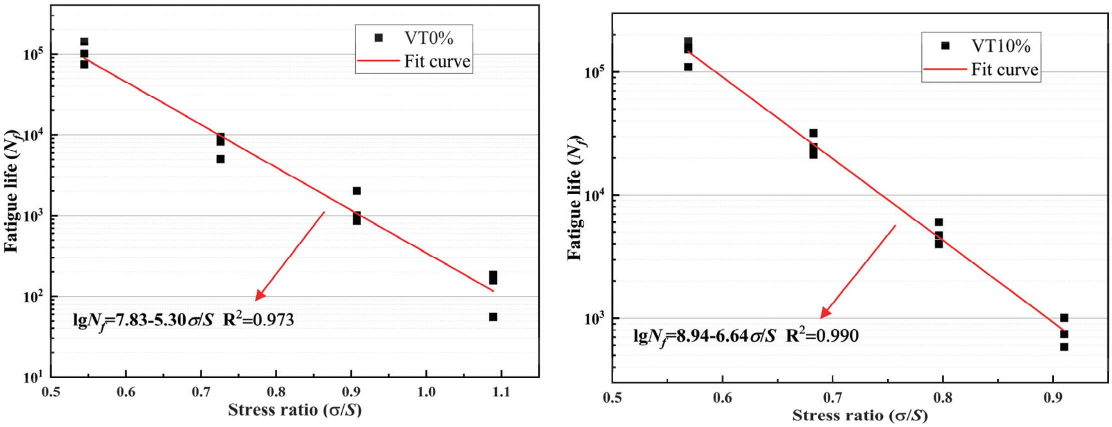

(**c**) VT0% (**d**) VT10%

Figure 9. Fatigue curves of CSM with different stress ratios.

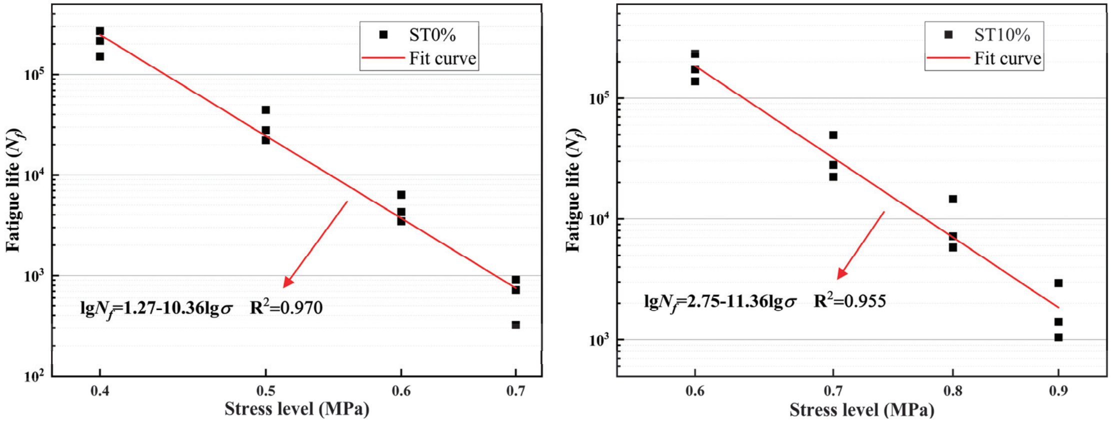

(**a**) ST0% (**b**) ST10%

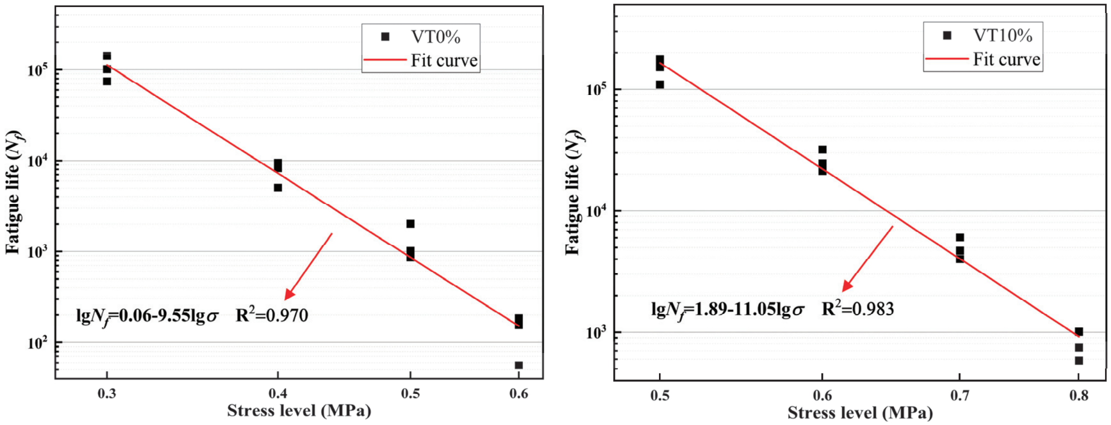

(**c**) VT0% (**d**) VT10%

Figure 10. Fatigue curves of CSM at different stress levels.

Under the same curing conditions, the fatigue life of CSM with 10% ESA added was significantly larger than that of CSM without ESA added, and the coefficient *a* was also significantly increased. ESA greatly boosted the fatigue life of CSM. This was primarily because the incorporation of ESA significantly accelerated the cement hydration reaction rate and the strength formation rate of CSM, thereby improving the fatigue resistance of the CSM. On the other hand, the fatigue life and coefficient *a*-value of the specimens under standard temperature environments are greater than those under variable temperature environments. The durability of CSM under variable temperature was inferior to that of standard temperature, and the incorporation of ESA greatly boosted the fatigue resistance of CSM in variable temperature conditions.

4.3. Test Methods

A modulus value can be obtained for each load cycle when conducting indirect tensile fatigue tests. Due to the large amount of fatigue test data, this study used Python software programming to process the data, calculate the modulus, and analyze the modulus decay of CSM.

4.3.1. Determination of the Indirect Tensile Initial Modulus Value

The indirect tensile initial modulus (E0) of CSM specimens was usually taken as the modulus (MPa) after 50 loading cycles. However, considering that the fatigue life of CSM varies greatly at different stress levels, this method was prone to deviation. This study selected the average value of 10 moduli near $N/N_f = 0.01$ as the indirect tensile initial modulus to improve the accuracy of the data. Tables 11–14 summarize the initial values of CSM.

Table 11. Initial values of modulus for ST0%.

Stress Level (MPa)	Number	E_0 (MPa)	Average Value (MPa)	Coefficient of Variation (%)
0.4	1	27,365	26,920	4.23
	2	28,037		
	3	25,358		
0.5	1	30,777	30,557	2.81
	2	29,414		
	3	31,479		
0.6	1	32,105	32,383	5.41
	2	30,390		
	3	34,655		
0.7	1	39,442	35,755	7.40
	2	34,460		
	3	33,362		

Table 12. Initial values of modulus for ST10%.

Stress Level (MPa)	Number	E_0 (MPa)	Average Value (MPa)	Coefficient of Variation (%)
0.6	1	33,599	35,241	4.67
	2	34,635		
	3	37,489		
0.7	1	38,445	39,850	3.41
	2	39,417		
	3	41,689		
0.8	1	43,106	44,411	7.98
	2	49,252		
	3	40,875		
0.9	1	51,956	46,680	8.82
	2	41,912		
	3	46,173		

Table 13. Initial values of modulus for VT0%.

Stress Level (MPa)	Number	E_0 (MPa)	Average Value (MPa)	Coefficient of Variation (%)
0.3	1	12,384	10,855	10.54
	2	10,547		
	3	9634		
0.4	1	12,482	12,578	11.97
	2	14,467		
	3	10,784		
0.5	1	16,258	16,158	6.36
	2	17,364		
	3	14,852		
0.6	1	18,344	20,529	8.24
	2	22,463		
	3	20,779		

Table 14. Initial values of modulus for VT10%.

Stress Level (MPa)	Number	E_0 (MPa)	Average Value (MPa)	Coefficient of Variation (%)
0.5	1	33,162	30,895	6.91
	2	28,036		
	3	31,486		
0.6	1	33,193	34,413	3.29
	2	35,921		
	3	34,125		
0.7	1	39,048	37,349	5.28
	2	38,414		
	3	34,585		
0.8	1	41,302	45,221	5.72
	2	45,151		
	3	49,210		

As illustrated in Tables 11–14, the coefficient of variation of the indirect tensile initial modulus of CSM ranges from 3.41% to 11.97%, with relatively small variability. The indirect tensile initial modulus of CSM rises with the increase in stress level. The modulus of CSM was significantly affected by different curing environments and ESA content. The initial modulus of ST0% ranges from 26,900 to 35,800 MPa. The indirect tensile initial modulus of ST10% ranges from 32,200 to 46,700 MPa. The indirect tensile initial modulus of VT0% was between 10,800 and 20,600 MPa; the initial modulus of VT10% was between 30,800–42,600 MPa. At a stress level of 0.6 MPa, the average initial modulus values of ST0%, ST10%, VT0%, and VT10% were 32,383 MPa, 35,241 MPa, 20,529 MPa, and 34,413 MPa, respectively. It can be seen that variable temperature curing conditions have an adverse effect on the dynamic modulus of CSM. After adding 10% ESA, the stiffness of CSM significantly improved.

4.3.2. Determination of the Indirect Tensile Critical Modulus Value

In fatigue testing, the modulus of the specimen will gradually decrease with the application of cyclic load. The average modulus of the first five cycles before the end of fatigue testing was mainly used as the critical modulus value (E_{min}). CSM is a brittle material whose modulus was significantly affected by stress and was prone to fracture under high stress. The average modulus of the five cycles before the end of the fatigue test was taken as the critical value, and there was a high degree of variability. To reduce the discreteness of experimental data, the tangent line to the point corresponding to $N/N_f = 0.5$ on the modulus decay curve and the straight line at $N/N_f = 1$ were utilized, and the intersection of the angular bisector of the intersection of the two lines and the modulus decay curve was chosen to be the fatigue modulus critical value [43], which is illustrated in Figure 11.

In the formula, E_0 is the initial modulus of the specimen, and E is the remaining modulus of the specimen after the load was applied. Point A is the point corresponding to the tangent on the fatigue modulus decay curve. Point B is the intersection point between the tangent of the point corresponding to N/N_f = 0.5 on the fatigue modulus decay curve and the straight line at N/N_f = 1. α the bisector angle between two intersecting lines.

The critical modulus values of CSM at different stress levels are illustrated in Tables 15–18.

As illustrated in Tables 15–18, the coefficient of variation of the critical modulus of CSM ranges from 0.77% to 16.49%, with relatively small variability. The critical modulus value of CSM reduces as the stress level grows. The modulus of CSM was significantly affected by environments and ESA content. The critical modulus value of ST0% was between 9500 and 13,600 MPa, ST10% was between 9400 and 21,000 MPa, VT0% was between 3400 and 6000 MPa, and VT10% was between 10,000 and 18,000 MPa. At a stress level of 0.6 MPa, the average critical values of modulus for ST0%, ST10%, VT0%, and VT10% are 11,230 MPa, 21,094 MPa, 3418 MPa, and 15,636 MPa, respectively. Under the same dosage of ESA, the critical value of the modulus of CSM in a variable temperature curing environment was lower than that in a standard temperature curing environment. After adding 10% ESA, the critical modulus values of the CSM under different curing conditions all increased.

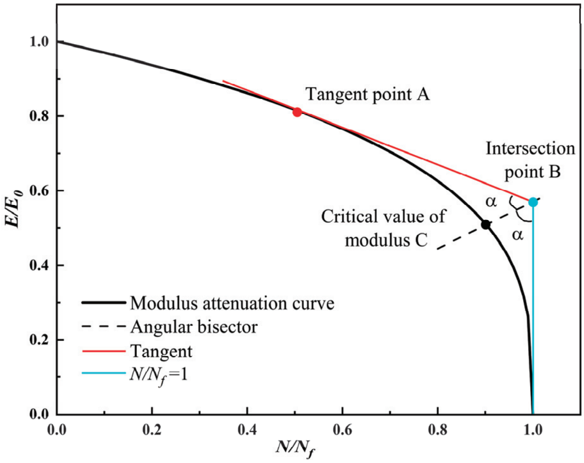

Figure 11. Schematic diagram of modulus critical point.

Table 15. Critical values of modulus for ST0%.

Stress Level (MPa)	Number	E_{min} (MPa)	Average Value (MPa)	Coefficient of Variation (%)
0.4	1	13,235	13,536	4.99
	2	14,472		
	3	12,901		
0.5	1	14,534	14,648	3.13
	2	15,258		
	3	14,151		
0.6	1	11,174	11,230	11.97
	2	9612		
	3	12,905		
0.7	1	10,591	9585	9.31
	2	8422		
	3	9741		

Table 16. Critical values of modulus for ST10%.

Stress Level (MPa)	Number	E_{min} (MPa)	Average Value (MPa)	Coefficient of Variation (%)
0.6	1	21,581	21,094	4.99
	2	21,424		
	3	20,278		
0.7	1	21,773	20,331	3.13
	2	21,794		
	3	17,427		
0.8	1	16,817	17,060	11.97
	2	17,142		
	3	17,221		
0.9	1	14,764	9418	9.31
	2	7482		
	3	6008		

Table 17. Critical values of modulus for VT0%.

Stress Level (MPa)	Number	E_{min} (MPa)	Average Value (MPa)	Coefficient of Variation (%)
0.3	1	6931	6017	10.81
	2	5469		
	3	5652		
0.4	1	5665	5575	6.00
	2	5933		
	3	5128		
0.5	1	5085	5140	0.77
	2	5174		
	3	5162		
0.6	1	2853	3418	20.61
	2	2989		
	3	4411		

Table 18. Critical values of modulus for VT10%.

Stress Level (MPa)	Number	E_{min} (MPa)	Average Value (MPa)	Coefficient of Variation (%)
0.5	1	18,746	18,098	2.57
	2	17,678		
	3	17,871		
0.6	1	14,432	15,636	8.19
	2	15,067		
	3	17,410		
0.7	1	12,182	13,232	10.82
	2	12,258		
	3	15,256		
0.8	1	10,487	10,589	16.49
	2	8503		
	3	12,777		

4.3.3. Analysis of Fitting Results for Modulus Decay of CSM

The compression modulus ratio and fatigue life ratio of CSM were fitted, and the modulus decay model parameters are illustrated in Tables 19–22. The modulus decay of ST0%, ST10%, VT0%, and VT10% is illustrated in Figures 12–15.

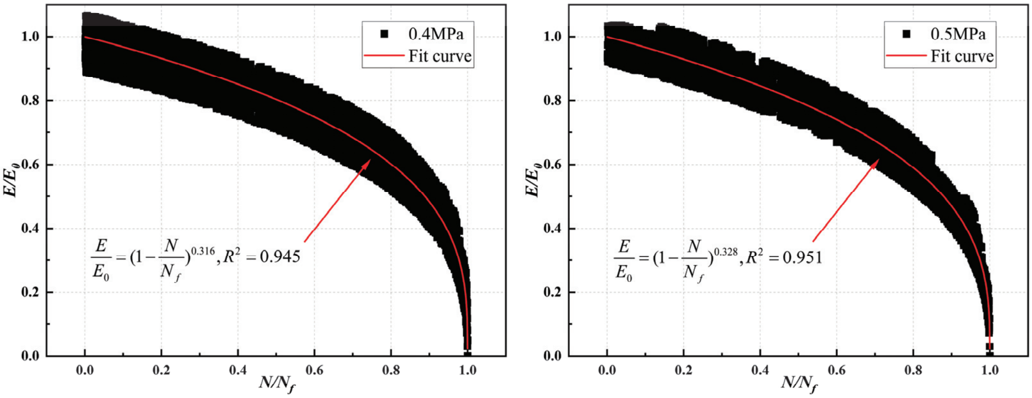

(**a**) 0.4 MPa

(**b**) 0.5 MPa

Figure 12. *Cont.*

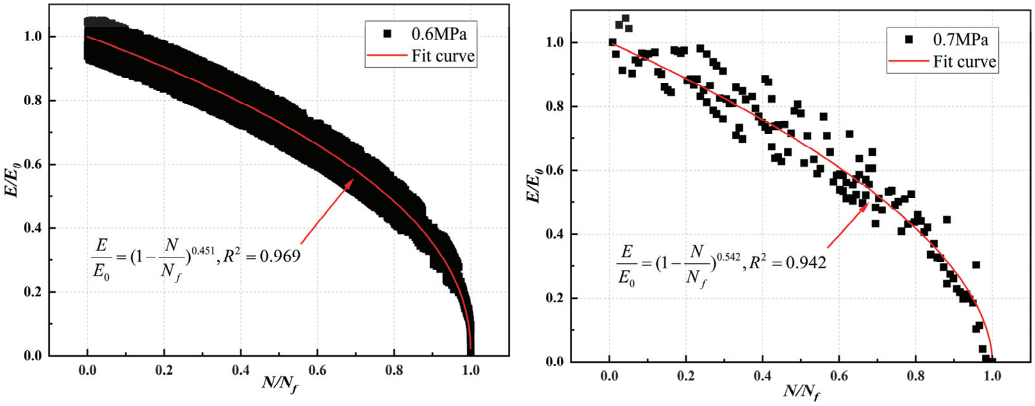

(**c**) 0.6 MPa

(**d**) 0.7 MPa

Figure 12. Modulus decay of ST0% under different stress levels.

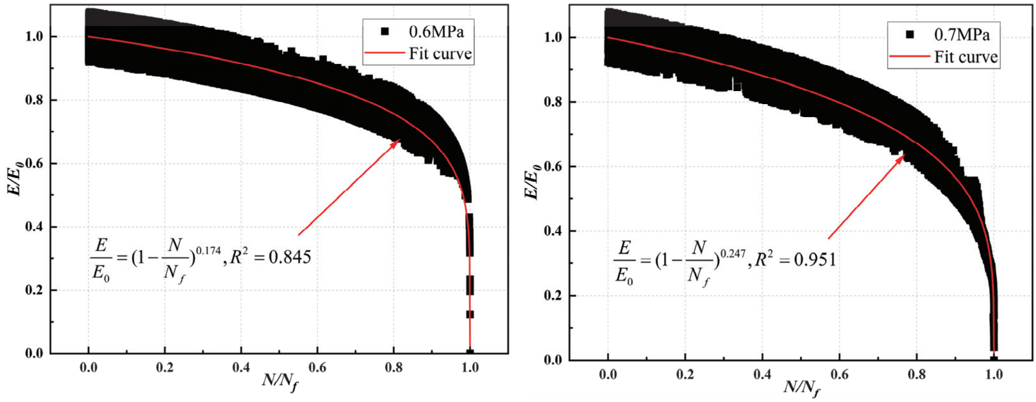

(**a**) 0.6 MPa (**b**) 0.7 MPa

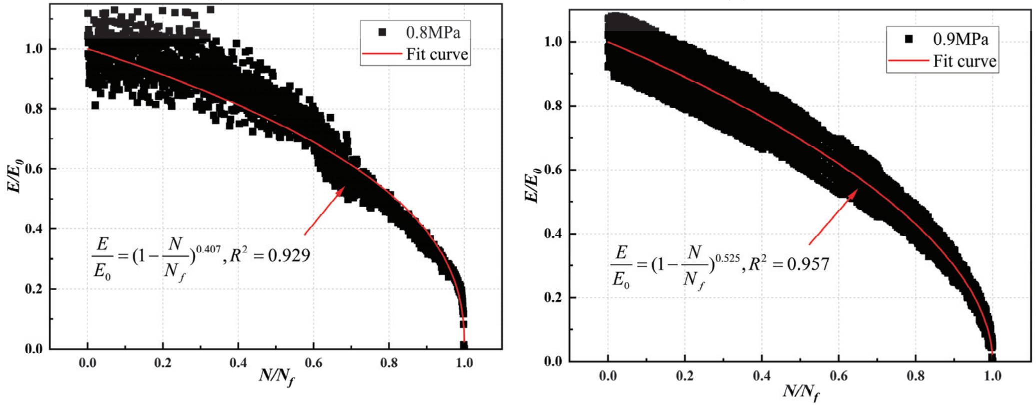

(**c**) 0.8 MPa (**d**) 0.9 MPa

Figure 13. Modulus decay of ST10% under different stress levels.

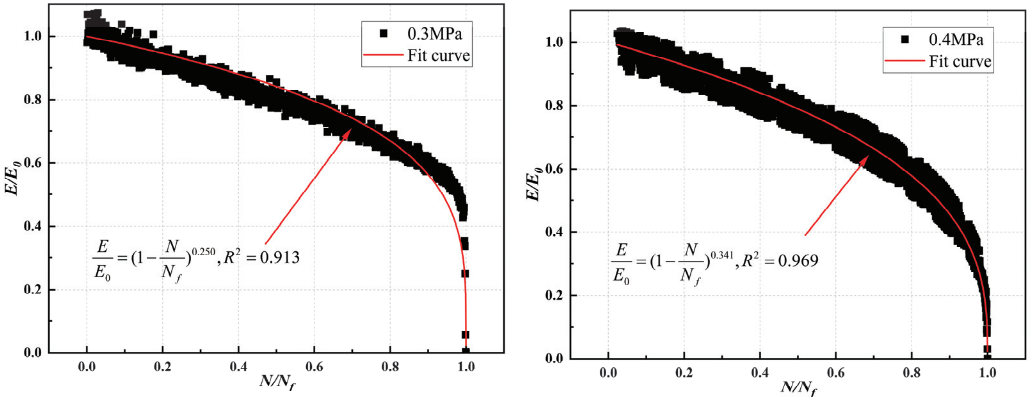

(**a**) 0.3 MPa

(**b**) 0.4 MPa

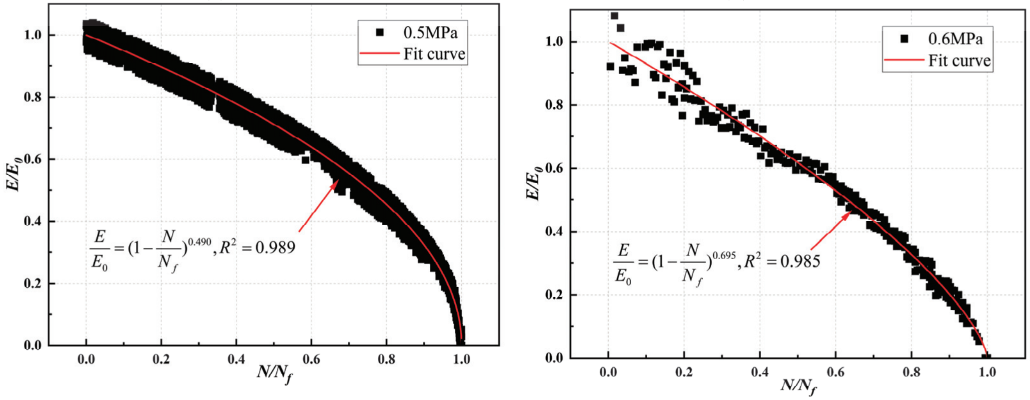

(**c**) 0.5 MPa

(**d**) 0.6 MPa

Figure 14. Modulus decay of VT0% under different stress levels.

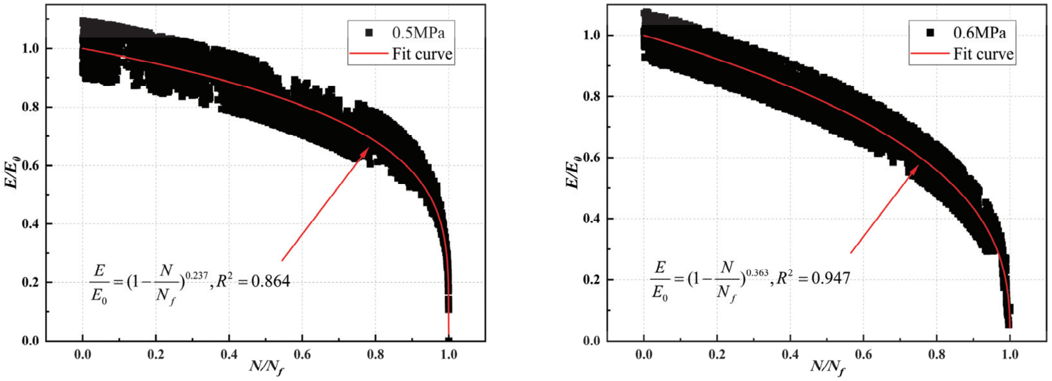

(**a**) 0.5 MPa

(**b**) 0.6 MPa

Figure 15. *Cont.*

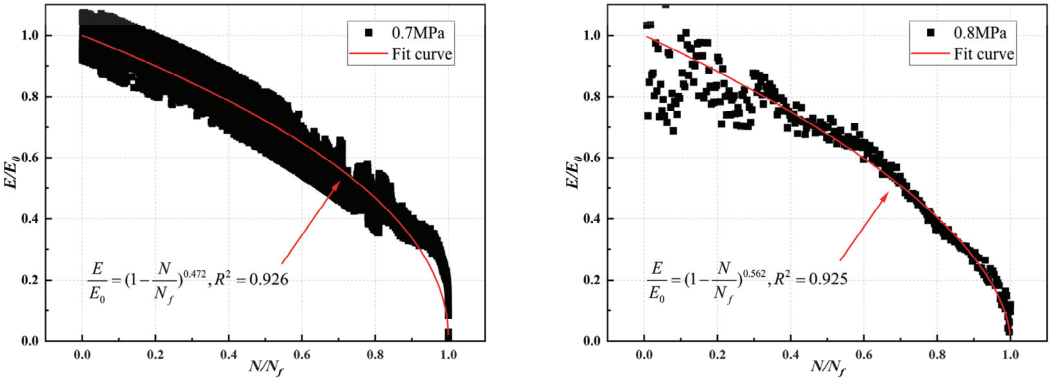

(**c**) 0.7 MPa (**d**) 0.8 MPa

Figure 15. Modulus decay of VT10% under different stress levels.

Table 19. Modulus decay model parameters for ST0%.

Stress Level (MPa)	Stress Ratio (t)	Number	m-Value	R^2	m-Average Value	m-Standard Deviation	Coefficient of Variation (%)
0.4	0.501	1 2 3	0.316 0.289 0.291	0.945 0.921 0.955	0.299	0.012	4.11
0.5	0.626	1 2 3	0.328 0.287 0.349	0.951 0.943 0.927	0.321	0.026	8.01
0.6	0.751	1 2 3	0.451 0.486 0.423	0.969 0.954 0.939	0.453	0.026	5.69
0.7	0.876	1 2 3	0.542 0.572 0.514	0.942 0.919 0.901	0.543	0.024	4.36

Table 20. Modulus decay model parameters for ST10%.

Stress Level (MPa)	Stress Ratio (t)	Number	m-Value	R^2	m-Average Value	m-Standard Deviation	Coefficient of Variation (%)
0.6	0.525	1 2 3	0.174 0.206 0.156	0.845 0.914 0.892	0.179	0.021	11.57
0.7	0.612	1 2 3	0.247 0.258 0.301	0.951 0.946 0.936	0.269	0.023	8.67
0.8	0.700	1 2 3	0.407 0.451 0.376	0.929 0.903 0.947	0.411	0.031	7.48
0.9	0.787	1 2 3	0.525 0.661 0.735	0.957 0.938 0.952	0.640	0.087	13.57

Table 21. Modulus decay model parameters for VT0%.

Stress Level (MPa)	Stress Ratio (t)	Number	m-Value	R^2	m-Average Value	m-Standard Deviation	Coefficient of Variation (%)
0.3	0.544	1 2 3	0.250 0.287 0.231	0.913 0.907 0.871	0.256	0.023	9.08
0.4	0.726	1 2 3	0.341 0.387 0.325	0.969 0.948 0.930	0.351	0.026	7.49
0.5	0.907	1 2 3	0.490 0.507 0.453	0.989 0.934 0.916	0.483	0.023	4.66
0.6	1.089	1 2 3	0.695 0.738 0.614	0.985 0.920 0.917	0.682	0.051	7.53

Table 22. Modulus decay model parameters for VT10%.

Stress Level (MPa)	Stress Ratio (*t*)	Number	*m*-Value	R^2	*m*-Average Value	*m*-Standard Deviation	Coefficient of Variation (%)
0.5	0.569	1 2 3	0.237 0.197 0.246	0.864 0.942 0.936	0.227	0.021	9.40
0.6	0.683	1 2 3	0.363 0.389 0.331	0.947 0.923 0.910	0.361	0.024	6.57
0.7	0.796	1 2 3	0.472 0.492 0.431	0.926 0.921 0.902	0.465	0.025	5.46
0.8	0.910	1 2 3	0.562 0.647 0.553	0.925 0.911 0.935	0.587	0.042	7.21

Tables 19–22 show that the modulus decay curves of CSM were similar at different stress levels. Under load, the internal structure of the specimen was gradually damaged, and the modulus gradually decreased until it failed. This indicated that the damage of CSM was a non-linear accumulation process. However, the curing temperature and ESA affected the internal damage process of CSM. The larger the value of *m*, the faster the modulus attenuation, indicating more internal damage to CSM under the same load. Tables 19–22 show that the rate of CSM modulus attenuation was related to the stress level. As the stress level increased, the CSM modulus decay fitting parameter *m*-value gradually increased, and the CSM modulus decay rate increased.

At a stress level of 0.6 MPa, the modulus decay curve parameters m for ST0%, ST10%, VT0%, and VT10% were 0.453, 0.179, 0.682, and 0.361, respectively. Under the same curing conditions, ST0% and VT0% values were significantly higher than those of ST10% and VT10%. CSM without ESA addition had greater damage under load and a faster performance degradation rate. Adding 10% ESA to CSM improved its fatigue resistance. The *m*-value of CSM under variable temperature was lower than that under standard temperatures. The primary reason was that under variable temperature conditions, the cement hydration rate in CSM was slow, the strength formation of CSM was slow, the adhesion between colloids was poor, and it was easy to cause damage under load.

5. Conclusions

This study investigated the influence of temperature on temperature shrinkage, drying shrinkage, indirect tensile strength, fatigue, and modulus characteristics of CSM with ESA. The conclusions obtained were as follows:

(1) The variable temperature curing conditions adversely affected the drying shrinkage characteristics of CSM. After adding 10% ESA, the drying shrinkage coefficient of CSM decreased by 16.19%. Adding ESA effectively accelerates cement hydration, consumes free water and capillary water in CSM, and effectively improves the anti-shrinkage cracking performance of CSM. However, compared to ST0%, the temperature shrinkage coefficient of VT0% decreased by 10.06%. The variable temperature curing conditions improved the temperature shrinkage characteristics of CSM;

(2) Compared with a standard temperature curing environment, under a variable temperature curing environment, the strength and fatigue life at 0.6 MPa of CSM decreased by 31.04% and 97.19%, respectively. The modulus decay curve parameters at 0.6 MPa increased by 51.21%. The variable temperature curing environment weakened the strength and fatigue resistance of CSM and accelerated the rate of modulus decay. The addition of ESA significantly boosted the durability of CSM under variable temperature conditions;

(3) The variable temperature service environment and the addition of ESA will significantly affect the durability of CSM. In cold regions with high daily temperature gradients, it is necessary to consider the effect of variable temperature conditions on the characteristics of CSM;

(4) The incorporation of ESA compensates for the weakened characteristics of CSM under variable temperature conditions and is a practical approach to boost CSM characteristics in cold regions with high daily temperature gradients (>20 °C).

This study only focuses on specific ESA and variable temperature conditions. In the future, more types of ESA and more severe service conditions can be considered to affect the characteristics of CSM.

Author Contributions: Y.X.: conceptualization, resources, writing—original draft, data curation, writing—reviewing and editing. D.G.: software, validation, formal analysis, writing—reviewing and editing, funding acquisition. S.L.: writing—reviewing and editing, funding acquisition, project administration. H.W.: conceptualization, validation, formal analysis, writing—reviewing and editing. W.L.: methodology, writing—reviewing and editing, software, validation, formal analysis. L.P.: visualization, investigation, formal analysis, writing—reviewing and editing. All authors have read and agreed to the published version of the manuscript.

Funding: This manuscript is based upon work supported by the National Natural Science Foundation of China (Nos. 52225806, 52078063, 52108398), the Major Program of Xiangjiang Laboratory (22XJ01009), and the Science Foundation for the Excellent Youth Scholars of Hunan Province Education Department (23B0322). Any opinions, findings, and conclusions or recommendations expressed in this material are those of the authors and do not necessarily reflect the views of the funders.

Institutional Review Board Statement: Not applicable.

Informed Consent Statement: Not applicable.

Data Availability Statement: Some or all data, models, or codes generated or used during the study are available from the corresponding authors by request.

Conflicts of Interest: The authors declare that they have no known competing financial interests or personal relationships that could have appeared to influence the work reported in this paper.

References

1. Sun, X.; Wu, S.; Yang, J.; Yang, R. Mechanical properties and crack resistance of crumb rubber modified cement-stabilized macadam. *Constr. Build. Mater.* **2020**, *259*, 119708. [CrossRef]
2. Zhang, J.; Bai, J.; Wang, S. Fatigue damage evolution rule of cement stabilized macadam used in pavement's base course at different curing time. *Constr. Build. Mater.* **2022**, *325*, 126827. [CrossRef]
3. Qiu, Y.; Zhang, L. Optimization study on indoor vibratory compaction curves of cement stabilized macadam. *J. China Foreign Highw.* **2023**, *43*, 189–194. [CrossRef]
4. Shu, H.; Tang, Z.; Zhang, Y.; Bu, X.; Liang, D. Effect of basalt fiber on strength of water-stabilized macadam base. *J. China Foreign Highw.* **2024**, 1–8. Available online: https://link.cnki.net/urlid/43.1363.u.20240126.1842.015 (accessed on 5 July 2024).
5. Zhao, X.; Dong, Q.; Chen, X.; Gu, X.; Wang, L. Mesoscale Cracking of Cement-treated Composites with lnitial Defects. *China J. Highw. Transp.* **2020**, *33*, 230–239. [CrossRef]
6. Zeng, X.; Ma, C.; Long, G.; Dang, H.; Xie, Y. Hydration kinetics of cement composites with different admixtures at low temperatures. *Constr. Build. Mater.* **2019**, *225*, 223–233. [CrossRef]
7. Liu, J.; Zhao, L.; Chi, L.; Luo, G.; Li, T.; Cai, S. Effect of multilayer graphene oxide on the hydration and early mechanical strength of cement mortar in low temperature. *Constr. Build. Mater.* **2023**, *364*, 129997. [CrossRef]
8. Duan, Y.; Wang, Q.; Zhang, R.; Chen, C.; Zhang, S. Strength Growth of High Strength Concrete and Its Degree of Hydration under Low Temperature(3 °C). *Bull. Chin. Ceram. Soc.* **2016**, *35*, 12–18. [CrossRef]
9. Tian, Y.; Ma, B.; Wang, D.; Wei, S. Flexural Tensile Characteristics of Cement-StabilizedMacadam in Cold Plateau Regions. *Bull. Chin. Ceram. Soc.* **2015**, *34*, 2569–2573. [CrossRef]
10. Soriano, L.; Monzó, J.; Bonilla, M.; Tashima, M.M.; Payá, J.; Borrachero, M.V. Effect of pozzolans on the hydration process of Portland cement cured at low temperatures. *Cem. Concr. Compos.* **2013**, *42*, 41–48. [CrossRef]
11. Ryou, J.-S.; Lee, Y.-S. Use of tabletting & coating accelerator for the prevention of early-frost of concrete in cold weather. *Cold Reg. Sci. Technol.* **2013**, *87*, 1–5. [CrossRef]
12. Ryou, J.-S.; Lee, Y.-S. Properties of early-stage concrete with setting-accelerating tablet in cold weather. *Mater. Sci. Eng. A* **2012**, *532*, 84–90. [CrossRef]
13. Ma, B.; Liu, P.; Li, N.; Wang, D. Study of compressive properties of cement stabilized macadam in cold plateau regions. *J. Hefei Univ. Technol. (Nat. Sci.)* **2015**, *38*, 1518–1523.
14. Zhou, Q.; Ye, W.; Yang, B.; Wu, X. Analysis of Low Temperature Strength and Drying Shrinkage Characteristics of Cement Stabilized Macadam. *Bull. Chin. Ceram. Soc.* **2016**, *35*, 948–952. [CrossRef]

15. Mi, L. Study on the Influence of Loads during Constryction and Curing Period on the Damage to Cement-Stabilized Macadam Base. Master's Thesis, Harbin Institute of Technology, Harbin, China, 2015.
16. Sha, A.; Ma, B.; Wang, H.; Hu, L.; Mao, X.; Zhi, X.; Chen, H.; Liu, Y.; Ma, F.; Liu, Z.; et al. Highway constructions on the Qinghai-Tibet Plateau: Challenge, research and practice. *J. Road Eng.* **2022**, *2*, 1–60. [CrossRef]
17. Remišová, E.; Decký, M.; Podolka, L.; Kováč, M.; Vondráčková, T.; Bartuška, L. Frost Index from Aspect of Design of Pavement Construction in Slovakia. *Procedia Earth Planet. Sci.* **2015**, *15*, 3–10. [CrossRef]
18. He, Z.; Fang, H. Discussion on Pavement Construction Technology of Qinghai Tibet Highway. In Proceedings of the Fourth International Road and Airport Pavement Technology Conference, Kunming, China, 23–25 April 2002; pp. 437–441.
19. Sheng, Y.; Jia, H.; Sun, S.; Guan, B.; Zhou, H.; Fang, J.; Liu, Q. Experimental Study on Performance of Early Strength and LowShrinkage Cement Stabilized Macadam at Different Temperatures. *Bull. Chin. Ceram. Soc.* **2019**, *38*, 3215–3220+3228. [CrossRef]
20. Xue, Y.; Ge, D.; Lv, S.; Ju, Z.; Wang, J.; Xian, J.; Peng, L. Effect of mechanical properties and microscopic mechanism of cement-stabilized macadam under variable temperature environment with early strength agent. *Case Stud. Constr. Mater.* **2024**, *20*, e03310. [CrossRef]
21. Ma, Y.; Gu, J.; Li, Y.; Li, Y. The bending fatigue performance of cement-stabilized aggregate reinforced with polypropylene filament fiber. *Constr. Build. Mater.* **2015**, *83*, 230–236. [CrossRef]
22. Li, W.; Lang, L.; Lin, Z.; Wang, Z.; Zhang, F. Characteristics of dry shrinkage and temperature shrinkage of cement-stabilized steel slag. *Constr. Build. Mater.* **2017**, *134*, 540–548. [CrossRef]
23. Li, H.; Sun, J.; Cui, C.; Zhao, Q.; Hu, Y.; Shen, R.; Guan, M. Cement-stabilized large-sized steel slag base course based on vibration compaction method: Mechanical properties, shrinkage properties, and numerical simulation. *Constr. Build. Mater.* **2023**, *404*, 133298. [CrossRef]
24. Xia, X.; Han, D.; Ma, Y.; Zhao, Y.; Tang, D.; Chen, Y. Experiment investigation on mix proportion optimization design of anti-cracking stone filled with cement stabilized macadam. *Constr. Build. Mater.* **2023**, *393*, 132136. [CrossRef]
25. Zhang, F.; Bai, Y.; Cai, Y.; Chen, B.; Ning, F. Early Hydration and Microstructure of Cement Pastes Mixed with Low-Temperature Early Strength Accelerator at 5 °C. *J. Chin. Ceram. Soc.* **2020**, *48*, 211–221. [CrossRef]
26. Zhang, F.; Bai, Y.; Cai, Y.; Chen, B.; Ning, F. Properties and Early Strength Mechanism of Compound Early Strength Accelerator at 5 °C. *J. Tongji Univ. (Nat. Sci.)* **2019**, *47*, 1609–1617.
27. Zhang, F.; Bai, Y.; Cai, Y. Effect of new type temperature early strength accelerator on the strength and durability of concrete. *Concrete* **2021**, *6*, 98–102+111.
28. Wang, L.; Shen, A.; Lyu, Z.; Guo, Y.; He, Z.; Mou, G.; Wei, Z. Rapid regeneration cement-stabilized macadam: Preparation; mechanical properties, and dry shrinkage performance. *Constr. Build. Mater.* **2022**, *341*, 127901. [CrossRef]
29. Tian, J.; Chen, S.; Peng, B. Road performance of aggregate mixture stabilized by super rapid strengthening cement. *J. Chang. Univ. (Nat. Sci. Ed.)* **2003**, *5*, 24–27. [CrossRef]
30. Xiong, R.; Yang, X.; Fang, J.; Xu, A.; Sheng, Y.; Guan, B.; Yang, F.; Qiu, M. Mechanical Property of Ultra early strength Cement Stabilized Macadam in Alpine Region. *Mater. Rep.* **2015**, *29*, 542–545.
31. Lin, M.; Zheng, X.; Song, Y. Experimental Study of Early Strength Cement Stabilized Macadam Materialfor Improving Frost Resistance. *Bull. Chin. Ceram. Soc.* **2015**, *34*, 475–480. [CrossRef]
32. Song, Y.-L.; Wang, Y.-D.; Ding, N. Influence of an Early-Strength Agent on the Frost Resistance of a Cement-Stabilized Material. *J. Highw. Transp. Res. Dev. (Engl. Ed.)* **2016**, *10*, 27–33. [CrossRef]
33. Vedernikov, A.; Tucci, F.; Carlone, P.; Gusev, S.; Konev, S.; Firsov, D.; Akhatov, I.; Safonov, A. Effects of pulling speed on structural performance of L-shaped pultruded profiles. *Compos. Struct.* **2021**, *255*, 112967. [CrossRef]
34. *JTG E42-2005*; Test Methods of Aggregate for Highway Engineering. Highway Research Institute of Ministry of Transport: Beijing, China, 2005.
35. Wang, S.; Lv, S.; Pan, Q.; Wang, P.; Deng, W.; Zhang, B.; Lei, D. Investigation on strength and fatigue performance of cement-stabilized macadam under three-dimensional stress state at different ages and cement dosages. *Constr. Build. Mater.* **2024**, *435*, 136686. [CrossRef]
36. *JTG E51-2009*; Test Methods of Materials Stabilized with Inorganic Binders for Highway Engineering. Highway Research Institute of Ministry of Transport: Beijing, China, 2009.
37. Gong, F.; Li, X. Analytical algorithm to estimate tensile modulus in brazilian disk splitting tests. *Chin. J. Rock Mech. Eng.* **2010**, *29*, 881–891.
38. Chen, D. Normalization of Fatigue Characteristics of Asphalt Mixtures under Different Stress States. Master's Thesis, Changsha University of Science and Technology, Changsha, China, 2017. [CrossRef]
39. Lv, S.; Li, Y.P.; Liu, C.C.; Zheng, J.L. Synchronous testing method for tensile and compressive moduli of asphalt mixture based on splitting test. *China J. Highw. Transp.* **2017**, *10*, 1–7+16. [CrossRef]
40. Jiangdong, C.; Zhenquan, J. Analysis of the effect of saturation of deep clayey soil on freezing construction in Wanfu well field. *Coal Eng.* **2009**, *1*, 90–93.
41. Zheng, X.; Yu, P.; Xie, Y.; Zeng, Z.; Li, S.; Liu, J. Research status of hydrated calcium silicate early strength. *Concrete* **2021**, *10*, 119–123.

42. Decky, M.; Papanova, Z.; Juhas, M.; Kudelcikova, M. Evaluation of the Effect of Average Annual Temperatures in Slovakia between 1971 and 2020 on Stresses in Rigid Pavements. *Land* **2022**, *11*, 764. [CrossRef]
43. Li, J. Normalization of Fatigue Characteristics of Cement Stabilized Macadam under Different Loading Modes. Master's Thesis, Changsha University of Science and Technology, Changsha, China, 2019. [CrossRef]

MDPI AG
Grosspeteranlage 5
4052 Basel
Switzerland
Tel.: +41 61 683 77 34

Materials Editorial Office
E-mail: materials@mdpi.com
www.mdpi.com/journal/materials

MDPI

Academic Open
Access Publishing

mdpi.com

ISBN 978-3-7258-2858-6